

UNITED STATES AIR FORCE
SUMMER RESEARCH PROGRAM -- 1997
GRADUATE STUDENT RESEARCH PROGRAM FINAL REPORTS

VOLUME 10A

WRIGHT LABORATORY

RESEARCH & DEVELOPMENT LABORATORIES

5800 Uplander Way

Culver City, CA 90230-6608

Program Director, RDL
Gary Moore

Program Manager, AFOSR
Major Linda Steel-Goodwin

Program Manager, RDL
Scott Licoscas

Program Administrator, RDL
Johnetta Thompson

Program Administrator, RDL
Rebecca Kelly

Submitted to:

AIR FORCE OFFICE OF SCIENTIFIC RESEARCH

Bolling Air Force Base

Washington, D.C.

December 1997

20010321 078

ARM 01-06-1276

REPORT DOCUMENTATION PAGE			Form Approved
<small>Public reporting burden for this collection of information is estimated to average 1 hour per response, including the time for reviewing instructions, searching existing data sources, gathering and maintaining the data needed, and completing and reviewing the collection of information. Send comments regarding this burden estimate or any other aspect of this collection of information, including suggestions for reducing this burden, to Washington Headquarters Services, Directorate for Information Operations and Reports, 1215 Jefferson Davis Highway, Suite 1204, Arlington, VA 22202-4302, and to the Office of Management and Budget, Paperwork Project, Washington, DC 20503.</small>			AFRL-SR-BL-TR-00- 0765
1. AGENCY USE ONLY (Leave blank)	2. REPORT DATE December, 1997	3.	
4. TITLE AND SUBTITLE 1997 Summer Research Program (SRP), Graduate Student Research Program (GSRP), Final Reports, Volume 10A, Wright Laboratory		5. FUNDING NUMBERS F49620-93-C-0063	
6. AUTHOR(S) Gary Moore			
7. PERFORMING ORGANIZATION NAME(S) AND ADDRESS(ES) Research & Development Laboratories (RDL) 5800 Uplander Way Culver City, CA 90230-6608		8. PERFORMING ORGANIZATION REPORT NUMBER	
9. SPONSORING/MONITORING AGENCY NAME(S) AND ADDRESS(ES) Air Force Office of Scientific Research (AFOSR) 801 N. Randolph St. Arlington, VA 22203-1977		10. SPONSORING/MONITORING AGENCY REPORT NUMBER	
11. SUPPLEMENTARY NOTES			
12a. DISTRIBUTION AVAILABILITY STATEMENT Approved for Public Release		12b. DISTRIBUTION CODE	
13. ABSTRACT (Maximum 200 words) The United States Air Force Summer Research Program (USAF-SRP) is designed to introduce university, college, and technical institute faculty members, graduate students, and high school students to Air Force research. This is accomplished by the faculty members (Summer Faculty Research Program, (SFRP)), graduate students (Graduate Student Research Program (GSRP)), and high school students (High School Apprenticeship Program (HSAP)) being selected on a nationally advertised competitive basis during the summer intersession period to perform research at Air Force Research Laboratory (AFRL) Technical Directorates, Air Force Air Logistics Centers (ALC), and other AF Laboratories. This volume consists of a program overview, program management statistics, and the final technical reports from the GSRP participants at the Wright Laboratory.			
14. SUBJECT TERMS Air Force Research, Air Force, Engineering, Laboratories, Reports, Summer, Universities, Faculty, Graduate Student, High School Student		15. NUMBER OF PAGES	
		16. PRICE CODE	
17. SECURITY CLASSIFICATION OF REPORT Unclassified	18. SECURITY CLASSIFICATION OF THIS PAGE Unclassified	19. SECURITY CLASSIFICATION OF ABSTRACT Unclassified	20. LIMITATION OF ABSTRACT UL

GENERAL INSTRUCTIONS FOR COMPLETING SF 298

The Report Documentation Page (RDP) is used in announcing and cataloging reports. It is important that this information be consistent with the rest of the report, particularly the cover and title page. Instructions for filling in each block of the form follow. It is important to **stay within the lines** to meet **optical scanning requirements**.

Block 1. Agency Use Only (*Leave blank*).

Block 2. Report Date. Full publication date including day, month, and year, if available (e.g. 1 Jan 88). Must cite at least the year.

Block 3. Type of Report and Dates Covered. State whether report is interim, final, etc. If applicable, enter inclusive report dates (e.g. 10 Jun 87 - 30 Jun 88).

Block 4. Title and Subtitle. A title is taken from the part of the report that provides the most meaningful and complete information. When a report is prepared in more than one volume, repeat the primary title, add volume number, and include subtitle for the specific volume. On classified documents enter the title classification in parentheses.

Block 5. Funding Numbers. To include contract and grant numbers; may include program element number(s), project number(s), task number(s), and work unit number(s). Use the following labels:

C - Contract
G - Grant
PE - Program
Element

PR - Project
TA - Task
WU - Work Unit
Accession No.

Block 6. Author(s). Name(s) of person(s) responsible for writing the report, performing the research, or credited with the content of the report. If editor or compiler, this should follow the name(s).

Block 7. Performing Organization Name(s) and Address(es). Self-explanatory.

Block 8. Performing Organization Report Number. Enter the unique alphanumeric report number(s) assigned by the organization performing the report.

Block 9. Sponsoring/Monitoring Agency Name(s) and Address(es). Self-explanatory.

Block 10. Sponsoring/Monitoring Agency Report Number. (*If known*)

Block 11. Supplementary Notes. Enter information not included elsewhere such as: Prepared in cooperation with....; Trans. of....; To be published in.... When a report is revised, include a statement whether the new report supersedes or supplements the older report.

Block 12a. Distribution/Availability Statement. Denotes public availability or limitations. Cite any availability to the public. Enter additional limitations or special markings in all capitals (e.g. NOFORN, REL, ITAR).

DOD - See DoDD 5230.24, "Distribution Statements on Technical Documents."

DOE - See authorities.

NASA - See Handbook NHB 2200.2.

NTIS - Leave blank.

Block 12b. Distribution Code.

DOD - Leave blank.

DOE - Enter DOE distribution categories from the Standard Distribution for Unclassified Scientific and Technical Reports.

Leave blank.

NASA - Leave blank.

NTIS -

Block 13. Abstract. Include a brief (*Maximum 200 words*) factual summary of the most significant information contained in the report.

Block 14. Subject Terms. Keywords or phrases identifying major subjects in the report.

Block 15. Number of Pages. Enter the total number of pages.

Block 16. Price Code. Enter appropriate price code (*NTIS only*).

Blocks 17. - 19. Security Classifications. Self-explanatory. Enter U.S. Security Classification in accordance with U.S. Security Regulations (i.e., UNCLASSIFIED). If form contains classified information, stamp classification on the top and bottom of the page.

Block 20. Limitation of Abstract. This block must be completed to assign a limitation to the abstract. Enter either UL (unlimited) or SAR (same as report). An entry in this block is necessary if the abstract is to be limited. If blank, the abstract is assumed to be unlimited.

PREFACE

Reports in this volume are numbered consecutively beginning with number 1. Each report is paginated with the report number followed by consecutive page numbers, e.g., 1-1, 1-2, 1-3; 2-1, 2-2, 2-3.

Due to its length, Volume 10A is bound in two parts, 10A and 10B. Volume 10A contains #1-17. Volume 10B contains reports #18-35. The Table of Contents for Volume 10 is included in all parts.

This document is one of a set of 16 volumes describing the 1997 AFOSR Summer Research Program. The following volumes comprise the set:

<u>VOLUME</u>	<u>TITLE</u>
1	Program Management Report
	<i>Summer Faculty Research Program (SFRP) Reports</i>
2A & 2B	Armstrong Laboratory
3A & 3B	Phillips Laboratory
4A & 4B	Rome Laboratory
5A , 5B & 5C	Wright Laboratory
6	Arnold Engineering Development Center, United States Air Force Academy and Air Logistics Centers
	<i>Graduate Student Research Program (GSRP) Reports</i>
7A & 7B	Armstrong Laboratory
8	Phillips Laboratory
9	Rome Laboratory
10A & 10B	Wright Laboratory
11	Arnold Engineering Development Center, Wilford Hall Medical Center and Air Logistics Centers
	<i>High School Apprenticeship Program (HSAP) Reports</i>
12A & 12B	Armstrong Laboratory
13	Phillips Laboratory
14	Rome Laboratory
15B&15B	Wright Laboratory
16	Arnold Engineering Development Center

GSRP FINAL REPORT TABLE OF CONTENTS

i-xi

1. INTRODUCTION	1
2. PARTICIPATION IN THE SUMMER RESEARCH PROGRAM	2
3. RECRUITING AND SELECTION	3
4. SITE VISITS	4
5. HBCU/MI PARTICIPATION	4
6. SRP FUNDING SOURCES	5
7. COMPENSATION FOR PARTICIPATIONS	5
8. CONTENTS OF THE 1995 REPORT	6

APPENDICIES:

A. PROGRAM STATISTICAL SUMMARY	A-1
B. SRP EVALUATION RESPONSES	B-1

GSRP FINAL REPORTS

SRP Final Report Table of Contents

Author	University/Institution Report Title	Armstrong Laboratory Directorate	Vol-Page
MR Benedict N Arrey	Univ of Texas at San Antonio , San Antonio , TX Identification and Quantitation of N-menthyl-1-(3,4 Methylendioxyphenyl)-2- Butanamine Together wiht	AL/AOT	7- 1
MS JoAnne E Bates	University of North Dakota , Grand Forks , ND A Way to Condense the Time Consuming Procedure of Cognitive Task Analysis	AL/HRCT	7- 2
MR Brandon B Boke	Trinity University , San Antonio , TX Effects of Brain Temperature on Fatigue in Rats due to maximal Exercise an Millimeter Microwave Radi	AL/OER	7- 3
MS Constance R Buford	Alabama A&M University , Normal , AL Assessment of Coagulant Agents on The Reduction of Aqueous Film Forming Foam (AFFF) in Wastewater	AL/OEB	7- 4
MS Dawn D Burnett	Wright State University , Dayton , OH The Effects of Individual Differences and Team Processed ofn Team Member Schema Similarity and Task	AL/CFHI	7- 5
MR Bradley E Collie	Arizona State University , Mesa , AZ Perception of Velocity as a Function of the Oculomotor State of the Eyes	AL/HRA	7- 6
MR Gerald W DeWolfe	Univ of Texas at Austin , Austin , TX Investigation and Validation of Submaximal Cycle Ergometry Protocols Used to Assess the Aerobic Capa	AL/PSP	7- 7
Kea U Duckenfield	The Virginia Institute of Marine Science , Gloucester Point , VA Direct Measurment of DNAPL/Water Contact Area in the Subsurace: One-And three-Dimensional Studies	AL/EQL	7- 8
MR Phillip T Dunwoody	University of Georgia , Athens , GA The Effects of Task Structure on Cognitive Organizing Principles: Implicatins	AL/CFTO	7- 9
MR Daniel X Hammer	Univ of Texas at Austin , Austin , TX Measurement of Dispersive Curves for Ocular Media by white-light Interferometry	AL/OEO	7- 10
MS Catherine R Harrison	Univ of Illinois Urbana/Champaign , Champaign , IL Gender effects in Wayfinding Strategy: Implications for Teamand Individual Trainging	AL/HRCC	7- 11

SRP Final Report Table of Contents

Author	University/Institution Report Title	Armstrong Laboratory Directorate	Vol-Page
MS Laura J Hott	Wright State University , Dayton , OH Examination of an Organizational Climate Measure and the Relationship with Grievances and Turnover	AL/HRG	7- 12
MS Vanessa D Le	Univ of Texas at Austin , Austin , TX A Clearance Study of Nitrotyrosine From a Prostate Cancer Cell Line	AL/OER	7- 13
MS Kavita Mahajan	Trinity University , San Antonio , TX the Effect of 2.06 GHz Microwave Irraditation on The Permeability of the Blood Brain Barrier	AL/OER	7- 14
MR Thomas R Mertz (Jr.)	Univ of Scranton , Scranton , PA Protocol for Development of Amplicons for a Rapid & Efficient Method of Genotyping Hepatitis C Virus	AL/AOEL	7- 15
MR Michael J Miller	Texas A & M Univ-College Station , College Station , TX An Psycholmetric Examination of the Multidimensional work ethic Profile among Air Force enlisted per	AL/HRCF	7- 16
MR Miguel A Moreno	Arizona State University , Tempe , AZ The Effect of Size Disparity on Perception of Surface Slant in Steroscopic Moving Images	AL/HRA	7- 17
MR Brian W Moroney	University of Cincinnati , Cincinnati , OH The Role of Multi-Modal Adaptive Interfaces in Providing Flight Path Guidance	AL/CFHI	7- 18
MR Randy J Mueller	University of Connecticut , Storrs , CT Desorption and Biodegradation of Dinitrotoluenes in Aged soils	AL/EQL	7- 19
MR Mark A Murphy	Ohio University , Athens , OH Implementation of Freflex/merlin Teleoperation	AL/CFBA	7- 20
MS Cynthia J Musante	North Carolina State U-Raleigh , Raleigh , NC Well-Posedness for a Class of Nonlinear Distributed Parameter Models wiht Time Delay Arising in Adva	AL/OES	7- 21
MR David C Powell	The College of William and Mary , Gloucester , VA Investigaatioon of the Iron-Beaaring Phases of the Columbus AFB Aquifer	AL/EQL	7- 22

SRP Final Report Table of Contents

Author	University/Institution Report Title	Armstrong Laboratory Directorate	Vol-Page
MR Christopher S Schreiner	Miami University , Oxford , OH The Effect of Visual Similarity and Reference Frame Alignment on the Recognition of Military Aircraft	AL/HRCT	7- 23
MR John N Sempeles	University of Florida , Gainesville , FL OH Radical Reaction Rate Constant & Product Study of 2-Propoxyethanol	AL/EQL	7- 24
MS Julie A Stiles-Shipley	Bowling Green State University , Bowling Green , OH The Effects of Observation and Training Schedule on The Acquisition of a complex Computer Based	AL/HRCT	7- 25
MR Robert S Tannen	University of Cincinnati , Cincinnati , OH Integrating Multisensory Displays for an Adaptive Target Leading Interface	AL/CFHP	7- 26
MR Paul J Taverna	Tulane University , New Orleans , LA A Preliminary Examination of ECL Activity Geared Toward a CD+2 Sensor	AL/EQL	7- 27
MR James M Tickner	Univ of Scranton , Scranton , PA Molecular typing of Candida Parasilosis Via Amplified Fragment Length Polymorphism and Repetitive S	AL/AOEL	7- 28
MS Deanne L Westerman	Case Western Reserve Univ , Cleveland , OH A Test of the Misattributed-Activation Hypothesis of the Revelatin Effect in Memory	AL/HRCC	7- 29

SRP Final Report Table of Contents

Author	University/Institution Report Title	Phillips Laboratory Directorate	Vol-Page
MR Joshua C Bienfang	University of New Mexico , Albuquerque , NM Frequency Stabilization of an Nd; Yag Laser	AFRL/DEL _____	8- 1
MR Marc L Breen	Tulane University , New Orleans , LA A Study of Defects and Dark Current Mechanisms in Triple-Junction GaInP2/GaAs/Ge Photovoltaic Cells	PL/VTV _____	8- 2
MR Jerome T Chu	University of Florida , Gainesville , FL The Characterization of High Performance Quantum Well Infrared Photodetectors for Low Background O	PL/VTMR _____	8- 3
MR Theodore S Elicker	University of N. C.- Charlotte , Charlotte , NC Simulation and Modeling of Nanoelectronic Materials	PL/VTMR _____	8- 4
MR Jeffery M Ganley	University of New Mexico , Albuquerque , NM A Preliminary Study of the Causes of Spring-IN in A Unidirectional Carbon Fiber/EPOXY Composite	PL/VTV _____	8- 5
Johnelle L Koriath	Univ of Texas at Dallas , Richardson , TX A Preliminary analysis of Stacked blumleins Used in Pulsed power Devices	PL/WSQ _____	8- 6
Kelly K Lau	Univ of Texas at Arlington , Arlington , TX Experimental Validation of Three-Dimensional Reconstruction of Inhomogeneity Images in turbid Media	PL/LIMI _____	8- 7
MS Ruthie D Lyle	Polytechnic University , Farmingdale , NY A Quasi-Particle Analysis of Amplitude Scintillation	PL/GPS _____	8- 8
MR Shaun L Meredith	Massachusetts Inst of Technology , Cambridge , MA Research on Plasma Diagnostics for Versatile Toroidal Facility: Gridded energy Analyzers	PL/GPS _____	8- 9

SRP Final Report Table of Contents

Author	University/Institution Report Title	Phillips Laboratory Directorate	Vol-Page
MR Eric J Paulson	Univ of Colorado at Boulder , Boulder , CO A Study of Atomospheric Perturbations On a Suborbital Space Plane Skipping Trajectory	AFRL/PR _____	8- 10
MR Christopher W Peters	Univ of Michigan , Ann Arbor , MI A New "Technique Used to Dertemine the Time Evolutin of The Frequency in Heterodyne Systems	PL/WSQN _____	8- 11
MR Michael J Rowlands	Massachusetts Inst of Technology , Cambridge , MA Ducted Whistler waves and Emissions in the Laboratory and the Ionosphere	PL/GPS _____	8- 12
MS Lorena L Sanchez	University of New Mexico , Albuquerque , NM A Preliminary Study of the Effects of Process Conditions on Curvature in Graphite/EPoxy Pultruded Ro	PL/VTV _____	8- 13
MR John H Schilling	Univ of Southern California , Los Angeles , CA "A Study of Alternate Propellants for Pulsed Plasma Thrusters	PL/RKEE _____	8- 14
IR Kenneth F Stephens II	University of North Texas , Denton , TX Investigation of an Explosively Formed Fus Using Mach2	AFRL/DEH _____	8- 15
IS Jane A Vladimer	Boston University , Boston , MA Low Latitude Ionospheric Tec Measured by Nasa Topex	PL/GPS _____	8- 16
IR Michael V Wood	Pennsylvania State University , University Park , PA Characterization of Spatial Light Modulator For Application to real-time Hlography	PL/LIMS _____	8- 17
IR Mark C Worthy	Univ of Alabama at Huntsville , Huntsville , AL Library of the Natural Frequency Responses for Cylindrical & Rectangular Shaped Plastic Mines	PL/WSQW _____	8- 18
IR John Yoon	University of Florida , Gainesville , FL Simulating Transient Temperature Distributions in Optically Pumped Multilayer Laser Structures	PL/LIDA _____	8- 19

SRP Final Report Table of Contents

Author	University/Institution Report Title	Rome Laboratory Directorate	Vol-Page
MR Tony M Adami	Ohio University , Athens , OH	RL/C3	9- 1
MR Richard S Andel	SUNY Binghamton , Binghamton , NY Visual Target Tracking and Extraction from a Sequence of Images	RL/IRRE	9- 2
MR Patrick M Garrity	Central Michigan University , Mt. Pleasant , MI An Examination of Java and CORBA Security	RL/CA-II	9- 3
MR Walter I Kaechele	Rensselaer Polytechnic Instit , Troy , NY Operational Analysis of an Actively Mode-Locked Fiber Laser	RL/OCPA	9- 5
MR William J Kostis	Cornell University , Ithaca , NY	RL/OCSS	9- 6
MS Helen Lau	Syracuse University , Syracuse , NY A Simulati9n Study on a Partitioning Procedure for Radar Signal processing Problems	RL/OCSS	9- 7
MR Myron R Mychal	Illinois Inst of Technology , Chicago , IL Simulaton of a Robust Locally Optimum Receiver in Correlated Noise Using Autoregressive Modeling	RL/C3BB	9- 8
MS Maryanne C Nagy	SUNY OF Tech Utica , Utica , NY	RL/IWT	9- 9
DR Luke J Olszewski	Georgia Southern University , Statesboro , GA Software Veification Guide Using PVS	RL/ERDD	9- 12
MR Charles M Palmer	George Washington University , Washington , DC A Technique for locating and characterizing crystalline regions in simulated solids	RL/ERDR	9- 10
MR Dsunte L Wilson	Brown University , Providence , RI System-Level Hardware/Software Partitioning of Heterogeneous Embedded Systems	RL/ERDD	9- 11

SRP Final Report Table of Contents

Author	University/Institution Report Title	Wright Laboratory Directorate	Vol-Page
MR Mark L Adams	Auburn University , Auburn , AL A Study of Laser Induced Plasma Damage of Thin Metal Foils	WL/MNMF _____	10- 1
MR James T Belich	Bethel College , St. Paul , MN Contribution of a scene Projecotr's Non-Uniformity to a test Article's output Image Non-Uniformity	WL/MNGI _____	10- 2
MR Jason W Bitting	Louisiana State University , Baton Rouge , LA Visualization and Two-Color Digital PIV Measurements in Circular and Square Coaxial Nozzles	WL/POSC9 _____	10- 3
MR Lawrence L Brott	University of Cincinnati , Cincinnati , OH Synthesis of a Novel Second Order Nonlinear Optical Polymer	WL/MLBP _____	10- 4
MS Danielle E Brown	Wright State University , Dayton , OH An Experimental and Computational Analysis of the Unsteady Blade Row Potential Interaction in a Tran	WL/POTF _____	10- 5
MS Angela M Cannon	Pennsylvania State University , University Park , PA the Synthesis of a Protected Carboxylic Acid Derivative for Attachment To C60	WL/MLPJ _____	10- 6
MR Charles C Conklin	Florida State University , Tallahassee , FL Vision Algorithms For Military Image Processing	WL/MNMF _____	10- 7
MR Mitchell G Dengler	University of Missouri - Rolla , Rolla , MO	WL/MLIM _____	10- 8
MR James D Drummond	University of Cincinnati , Cincinnati , OH Invesstigation of Conductive Cladding Layers for Improved Polimg in Non-Linear Optical Polymer waveg	WL/MLPO _____	10- 9
MR Gary W Dulaney	Brown University , Providence , RI Computer Simulation of Fire Suppression in Aircraft Engine Nacelles	WL/FIVS _____	10- 10

SRP Final Report Table of Contents

Author	University/Institution Report Title	Wright Laboratory Directorate	Vol-Page
MR Robert L Parkhill	Oklahoma State University , Stillwater , OK Organically modified Silicate Films as Corrosion Resistant Treatments for 2024-T3 Aluminum Alloy	WL/MLBT _____	10- 23
MS Annie R Pearce	Georgia Inst of Technology , Atlanta , GA Cost-Based Risk Prediction and Identification of Project Cost Drives Using Artificial neural Network	WL/FIVC- _____	10- 24
MR Dax B Pitts	University of Cincinnati , Cincinnati , OH A Study of Intra-Class Variability in ATR Systems	WL/AACR _____	10- 25
MR Jonathan M Protz	Massachusetts Inst of Technology , Cambridge , MA An LPV Controller for a Tailless Fighter Aircraft Simulation	WL/FIGC _____	10- 26
MR Jason E Riggs	Clemson University , Clemson , SC	WL/MLPJ _____	10- 27
MR Thomas W Scott	University of Missouri - Rolla , Rolla , MO Iso-Octane and N-Heptane Laminar Flame Numerical Study	WL/POPS _____	10- 28
MR Steven R Stanfill	University of Florida , Gainesville , FL A study of HRR Super Resolution Analysis for Possible ATR Performance Enhancement	WL/AACR _____	10- 29
Adedokun W Sule-Koiki	Howard University , Washington , DC Detection Techniques use in Forward-Lookeng Radar Signal A Literature Review	WL/AAMR _____	10- 30
MR Robert M Taylor	Purdue University , West Lafayette , IN Rapid Modeling for Aircraft Design Synthesis	WL/FIBD _____	10- 31
MS Laura E Williams	Georgia Inst of Technology , Atlanta , GA Data Simulation Supporting Range Estimating for Research and Sevelopment Alternatives	WL/FIVC- _____	10- 32

SRP Final Report Table of Contents

Author	University/Institution Report Title	Wright Laboratory Directorate	Vol-Page
MR Cornelious W Williams Jr.	University of Cincinnati , Cincinnati , OH Allyl & Propargyl Resins	WL/MLBC	10- 33
MS Melissa R Wilson	University of Missouri - Rolla , Rolla , MO A Study of The Particulate Emissions of A Well-Stirred Reactor	WL/POSC	10- 34
ami Zendah	Wright State University , Dayton , OH Develop an Explosive simulated Testing Apparatus for Impact Physics Research at Wright Laboratory	WL/FIV	10- 35

SRP Final Report Table of Contents

Author	University/Institution Report Title	Wright Laboratory Directorate	Vol-Page
MR David W Fanjoy	Purdue University , West Lafayette , IN Demonstration of Genetic Algorithms for Wngineering Optimization Problems	WL/FIIB _____	10- 11
	Western Michigan University , Kalamazoo , MI Comparison of self-assembled monolayers and chitosan as functional substrates for deposition fo ultr	WL/MLPJ _____	10- 12
MR Carl C Hoff	Wright State University , Dayton , OH Similarity Measures for pattern Recognition	WL/AACA _____	10- 13
MR Adam R Hoffman	Wright State University , Dayton , OH Evaluation and Integratin of Electrodynamic Simulation Packages for Madmel Program	WL/POOX _____	10- 14
MR. George W Jarriel, Jr.	Auburn University , Auburn , AL Exploding Foil Initiator Flyer Velocity Measurement Using VISAR	WL/MNMF _____	10- 15
MR Brett A Jordan	Wright State University , Dayton , OH Capacitor Based DC Backup Power Supply with Integrated Cahrging Circuit	WL/POOC _____	10- 16
MR Edward L Kiely	Ohio State University , Columbus , OH	WL/FIBD _____	10- 17
MS Janae N Lockett	University of Toledo , Toledo , OH A Study of Electronics Design Environments in Terms of Computer aided Design A Psychological Persper	WL/AAST _____	10- 18
MS Stephanie Luetjering	University of Dayton , Dayton , OH Fatigue Crack GrowthBehavior of Ti-22A1-23Nb	WL/MLLN _____	10- 19
MR Alfred L Malone	Auburn University , Auburn , AL Electrical and Mathematical Characterization of th Semiconductor	WL/MNMF _____	10- 20
MR Herbert F Miles II	Tulane University , New Orleans , LA	WL/MLLN _____	10- 21
Dawn H Miller	Georgia Inst of Technology , Atlanta , GA	WL/FIVC _____	10- 22

SRP Final Report Table of Contents

thor	University/Institution Report Title	Arnold Engineering Development Center Directorate	Vol-Page
S Jessica L Thomas	Tennessee Univ Space Institute , Tullahoma , TN Incorporating Condensation into Nasta	AEDC	11- 1
R Derek E Lang	University of Washington , Seattle , WA Hue Analysis Factors For Liquid Crystal Transient Heat Transfer Measurements	USAFA	11 - 2
S Bridget V McGrath	Univ of Colorado at Colorado Springs , Colorado Spring , CO A Setup for Photoassociation of cold, Trapped Cesium Atoms	USAFA	11 - 3
S Donna M Lehman	Univ of Texas Health Science Center , San Antonio , TX Relationship between Growth Hormone and Myelin Basic Protein Expression in Vivo	WHMC	11 - 4

1. INTRODUCTION

The Summer Research Program (SRP), sponsored by the Air Force Office of Scientific Research (AFOSR), offers paid opportunities for university faculty, graduate students, and high school students to conduct research in U.S. Air Force research laboratories nationwide during the summer.

Introduced by AFOSR in 1978, this innovative program is based on the concept of teaming academic researchers with Air Force scientists in the same disciplines using laboratory facilities and equipment not often available at associates' institutions.

The Summer Faculty Research Program (SFRP) is open annually to approximately 150 faculty members with at least two years of teaching and/or research experience in accredited U.S. colleges, universities, or technical institutions. SFRP associates must be either U.S. citizens or permanent residents.

The Graduate Student Research Program (GSRP) is open annually to approximately 100 graduate students holding a bachelor's or a master's degree; GSRP associates must be U.S. citizens enrolled full time at an accredited institution.

The High School Apprentice Program (HSAP) annually selects about 125 high school students located within a twenty mile commuting distance of participating Air Force laboratories.

AFOSR also offers its research associates an opportunity, under the Summer Research Extension Program (SREP), to continue their AFOSR-sponsored research at their home institutions through the award of research grants. In 1994 the maximum amount of each grant was increased from \$20,000 to \$25,000, and the number of AFOSR-sponsored grants decreased from 75 to 60. A separate annual report is compiled on the SREP.

The numbers of projected summer research participants in each of the three categories and SREP "grants" are usually increased through direct sponsorship by participating laboratories.

AFOSR's SRP has well served its objectives of building critical links between Air Force research laboratories and the academic community, opening avenues of communications and forging new research relationships between Air Force and academic technical experts in areas of national interest, and strengthening the nation's efforts to sustain careers in science and engineering. The success of the SRP can be gauged from its growth from inception (see Table 1) and from the favorable responses the 1997 participants expressed in end-of-tour SRP evaluations (Appendix B).

AFOSR contracts for administration of the SRP by civilian contractors. The contract was first awarded to Research & Development Laboratories (RDL) in September 1990. After completion of the

1990 contract, RDL (in 1993) won the recompetition for the basic year and four 1-year options.

2. PARTICIPATION IN THE SUMMER RESEARCH PROGRAM

The SRP began with faculty associates in 1979; graduate students were added in 1982 and high school students in 1986. The following table shows the number of associates in the program each year.

YEAR	SRP Participation, by Year			TOTAL
	SFRP	GSRP	HSAP	
1979	70			70
1980	87			87
1981	87			87
1982	91	17		108
1983	101	53		154
1984	152	84		236
1985	154	92		246
1986	158	100	42	300
1987	159	101	73	333
1988	153	107	101	361
1989	168	102	103	373
1990	165	121	132	418
1991	170	142	132	444
1992	185	121	159	464
1993	187	117	136	440
1994	192	117	133	442
1995	190	115	137	442
1996	188	109	138	435
1997	148	98	140	427

Beginning in 1993, due to budget cuts, some of the laboratories weren't able to afford to fund as many associates as in previous years. Since then, the number of funded positions has remained fairly constant at a slightly lower level.

3. RECRUITING AND SELECTION

The SRP is conducted on a nationally advertised and competitive-selection basis. The advertising for faculty and graduate students consisted primarily of the mailing of 8,000 52-page SRP brochures to chairpersons of departments relevant to AFOSR research and to administrators of grants in accredited universities, colleges, and technical institutions. Historically Black Colleges and Universities (HBCUs) and Minority Institutions (MIs) were included. Brochures also went to all participating USAF laboratories, the previous year's participants, and numerous individual requesters (over 1000 annually).

RDL placed advertisements in the following publications: *Black Issues in Higher Education*, *Winds of Change*, and *IEEE Spectrum*. Because no participants list either *Physics Today* or *Chemical & Engineering News* as being their source of learning about the program for the past several years, advertisements in these magazines were dropped, and the funds were used to cover increases in brochure printing costs.

High school applicants can participate only in laboratories located no more than 20 miles from their residence. Tailored brochures on the HSAP were sent to the head counselors of 180 high schools in the vicinity of participating laboratories, with instructions for publicizing the program in their schools.

High school students selected to serve at Wright Laboratory's Armament Directorate (Eglin Air Force Base, Florida) serve eleven weeks as opposed to the eight weeks normally worked by high school students at all other participating laboratories.

Each SFRP or GSRP applicant is given a first, second, and third choice of laboratory. High school students who have more than one laboratory or directorate near their homes are also given first, second, and third choices.

Laboratories make their selections and prioritize their nominees. AFOSR then determines the number to be funded at each laboratory and approves laboratories' selections.

Subsequently, laboratories use their own funds to sponsor additional candidates. Some selectees do not accept the appointment, so alternate candidates are chosen. This multi-step selection procedure results in some candidates being notified of their acceptance after scheduled deadlines. The total applicants and participants for 1997 are shown in this table.

1997 Applicants and Participants			
PARTICIPANT CATEGORY	TOTAL APPLICANTS	SELECTEES	DECLINING SELECTEES
SFRP	490	188	32
(HBCU/MI)	(0)	(0)	(0)
GSRP	202	98	9
(HBCU/MI)	(0)	(0)	(0)
HSAP	433	140	14
TOTAL	1125	426	55

4. SITE VISITS

During June and July of 1997, representatives of both AFOSR/NI and RDL visited each participating laboratory to provide briefings, answer questions, and resolve problems for both laboratory personnel and participants. The objective was to ensure that the SRP would be as constructive as possible for all participants. Both SRP participants and RDL representatives found these visits beneficial. At many of the laboratories, this was the only opportunity for all participants to meet at one time to share their experiences and exchange ideas.

5. HISTORICALLY BLACK COLLEGES AND UNIVERSITIES AND MINORITY INSTITUTIONS (HBCU/MI)

Before 1993, an RDL program representative visited from seven to ten different HBCU/MI annually to promote interest in the SRP among the faculty and graduate students. These efforts were marginally effective, yielding a doubling of HBCU/MI applicants. In an effort to achieve AFOSR's goal of 10% of all applicants and selectees being HBCU/MI qualified, the RDL team decided to try other avenues of approach to increase the number of qualified applicants. Through the combined efforts of the AFOSR Program Office at Bolling AFB and RDL, two very active minority groups were found, HACU (Hispanic American Colleges and Universities) and AISES (American Indian Science and Engineering Society). RDL is in communication with representatives of each of these organizations on a monthly basis to keep up with their activities and special events. Both organizations have widely-distributed magazines/quarterlies in which RDL placed ads.

Since 1994 the number of both SFRP and GSRP HBCU/MI applicants and participants has increased ten-fold, from about two dozen SFRP applicants and a half dozen selectees to over 100 applicants and two dozen selectees, and a half-dozen GSRP applicants and two or three selectees to 18 applicants and 7 or 8 selectees. Since 1993, the SFRP had a two-fold applicant increase and a two-fold selectee increase. Since 1993, the GSRP had a three-fold applicant increase and a three to four-fold increase in selectees.

In addition to RDL's special recruiting efforts, AFOSR attempts each year to obtain additional funding or use leftover funding from cancellations the past year to fund HBCU/MI associates. This year, 5 HBCU/MI SFRPs declined after they were selected (and there was no one qualified to replace them with). The following table records HBCU/MI participation in this program.

SRP HBCU/MI Participation, By Year				
YEAR	SFRP		GSRP	
	Applicants	Participants	Applicants	Participants
1985	76	23	15	11
1986	70	18	20	10
1987	82	32	32	10
1988	53	17	23	14
1989	39	15	13	4
1990	43	14	17	3
1991	42	13	8	5
1992	70	13	9	5
1993	60	13	6	2
1994	90	16	11	6
1995	90	21	20	8
1996	119	27	18	7

6. SRP FUNDING SOURCES

Funding sources for the 1997 SRP were the AFOSR-provided slots for the basic contract and laboratory funds. Funding sources by category for the 1997 SRP selected participants are shown here.

1997 SRP FUNDING CATEGORY	SFRP	GSRP	HSAP
AFOSR Basic Allocation Funds	141	89	123
USAF Laboratory Funds	48	9	17
HBCU/MI By AFOSR (Using Procured Addn'l Funds)	0	0	N/A
TOTAL	9	98	140

SFRP - 188 were selected, but thirty two canceled too late to be replaced.

GSRP - 98 were selected, but nine canceled too late to be replaced.

HSAP - 140 were selected, but fourteen canceled too late to be replaced.

7. COMPENSATION FOR PARTICIPANTS

Compensation for SRP participants, per five-day work week, is shown in this table.

1997 SRP Associate Compensation

PARTICIPANT CATEGORY	1991	1992	1993	1994	1995	1996	1997
Faculty Members	\$690	\$718	\$740	\$740	\$740	\$770	\$770
Graduate Student (Master's Degree)	\$425	\$442	\$455	\$455	\$455	\$470	\$470
Graduate Student (Bachelor's Degree)	\$365	\$380	\$391	\$391	\$391	\$400	\$400
High School Student (First Year)	\$200	\$200	\$200	\$200	\$200	\$200	\$200
High School Student (Subsequent Years)	\$240	\$240	\$240	\$240	\$240	\$240	\$240

The program also offered associates whose homes were more than 50 miles from the laboratory an expense allowance (seven days per week) of \$50/day for faculty and \$40/day for graduate students. Transportation to the laboratory at the beginning of their tour and back to their home destinations at the end was also reimbursed for these participants. Of the combined SFRP and GSRP associates, 65 % (194 out of 286) claimed travel reimbursements at an average round-trip cost of \$776.

Faculty members were encouraged to visit their laboratories before their summer tour began. All costs of these orientation visits were reimbursed. Forty-three percent (85 out of 188) of faculty associates took orientation trips at an average cost of \$388. By contrast, in 1993, 58 % of SFRP associates took

orientation visits at an average cost of \$685; that was the highest percentage of associates opting to take an orientation trip since RDL has administered the SRP, and the highest average cost of an orientation trip. These 1993 numbers are included to show the fluctuation which can occur in these numbers for planning purposes.

Program participants submitted biweekly vouchers countersigned by their laboratory research focal point, and RDL issued paychecks so as to arrive in associates' hands two weeks later.

This is the second year of using direct deposit for the SFRP and GSRP associates. The process went much more smoothly with respect to obtaining required information from the associates, only 7% of the associates' information needed clarification in order for direct deposit to properly function as opposed to 10% from last year. The remaining associates received their stipend and expense payments via checks sent in the US mail.

HSAP program participants were considered actual RDL employees, and their respective state and federal income tax and Social Security were withheld from their paychecks. By the nature of their independent research, SFRP and GSRP program participants were considered to be consultants or independent contractors. As such, SFRP and GSRP associates were responsible for their own income taxes, Social Security, and insurance.

8. CONTENTS OF THE 1997 REPORT

The complete set of reports for the 1997 SRP includes this program management report (Volume 1) augmented by fifteen volumes of final research reports by the 1997 associates, as indicated below:

1997 SRP Final Report Volume Assignments

LABORATORY	SFRP	GSRP	HSAP
Armstrong	2	7	12
Phillips	3	8	13
Rome	4	9	14
Wright	5A, 5B	10	15
AEDC, ALCs, WHMC	6	11	16

APPENDIX A – PROGRAM STATISTICAL SUMMARY

A. Colleges/Universities Represented

Selected SFRP associates represented 169 different colleges, universities, and institutions.
GSRP associates represented 95 different colleges, universities, and institutions.

B. States Represented

SFRP -Applicants came from 47 states plus Washington D.C. Selectees represent 44 states.

GSRP - Applicants came from 44 states. Selectees represent 32 states.

HSAP - Applicants came from thirteen states. Selectees represent nine states.

Total Number of Participants	
SFRP	189
GSRP	97
HSAP	140
TOTAL	426

Degrees Represented			
	SFRP	GSRP	TOTAL
Doctoral	184	0	184
Master's	2	41	43
Bachelor's	0	56	56
TOTAL	186	97	298

SFRP Academic Titles	
Assistant Professor	64
Associate Professor	70
Professor	40
Instructor	0
Chairman	1
Visiting Professor	1
Visiting Assoc. Prof.	1
Research Associate	9
TOTAL	186

Source of Learning About the SRP		
Category	Applicants	Selectees
Applied/participated in prior years	28%	34%
Colleague familiar with SRP	19%	16%
Brochure mailed to institution	23%	17%
Contact with Air Force laboratory	17%	23%
<i>IEEE Spectrum</i>	2%	1%
<i>BIIHE</i>	1%	1%
Other source	10%	8%
TOTAL	100%	100%

APPENDIX B – SRP EVALUATION RESPONSES

1. OVERVIEW

Evaluations were completed and returned to RDL by four groups at the completion of the SRP. The number of respondents in each group is shown below.

Table B-1. Total SRP Evaluations Received

Evaluation Group	Responses
SFRP & GSRPs	275
HSAPs	113
USAF Laboratory Focal Points	84
USAF Laboratory HSAP Mentors	6

All groups indicate unanimous enthusiasm for the SRP experience.

The summarized recommendations for program improvement from both associates and laboratory personnel are listed below:

- A. Better preparation on the labs' part prior to associates' arrival (i.e., office space, computer assets, clearly defined scope of work).
- B. Faculty Associates suggest higher stipends for SFRP associates.
- C. Both HSAP Air Force laboratory mentors and associates would like the summer tour extended from the current 8 weeks to either 10 or 11 weeks; the groups state it takes 4-6 weeks just to get high school students up-to-speed on what's going on at laboratory. (Note: this same argument was used to raise the faculty and graduate student participation time a few years ago.)

2. 1997 USAF LABORATORY FOCAL POINT (LFP) EVALUATION RESPONSES

The summarized results listed below are from the 84 LFP evaluations received.

1. LFP evaluations received and associate preferences:

Table B-2. Air Force LFP Evaluation Responses (By Type)

Lab	Evals Recv'd	How Many Associates Would You Prefer To Get ?								(% Response)			
		SFRP				GSRP (w/Univ Professor)				GSRP (w/o Univ Professor)			
		0	1	2	3+	0	1	2	3+	0	1	2	3+
AEDC	0	-	-	-	-	-	-	-	-	-	-	-	-
WHMC	0	-	-	-	-	-	-	-	-	-	-	-	-
AL	7	28	28	28	14	54	14	28	0	86	0	14	0
USAF	1	0	100	0	0	100	0	0	0	0	100	0	0
PL	25	40	40	16	4	88	12	0	0	84	12	4	0
RL	5	60	40	0	0	80	10	0	0	100	0	0	0
WL	46	30	43	20	6	78	17	4	0	93	4	2	0
Total	84	32%	50%	13%	5%	80%	11%	6%	0%	73%	23%	4%	0%

LFP Evaluation Summary. The summarized responses, by laboratory, are listed on the following page. LFPs were asked to rate the following questions on a scale from 1 (below average) to 5 (above average).

2. LFPs involved in SRP associate application evaluation process:
 - a. Time available for evaluation of applications:
 - b. Adequacy of applications for selection process:
3. Value of orientation trips:
4. Length of research tour:
5.
 - a. Benefits of associate's work to laboratory:
 - b. Benefits of associate's work to Air Force:
6.
 - a. Enhancement of research qualifications for LFP and staff:
 - b. Enhancement of research qualifications for SFRP associate:
 - c. Enhancement of research qualifications for GSRP associate:
7.
 - a. Enhancement of knowledge for LFP and staff:
 - b. Enhancement of knowledge for SFRP associate:
 - c. Enhancement of knowledge for GSRP associate:
8. Value of Air Force and university links:
9. Potential for future collaboration:
10.
 - a. Your working relationship with SFRP:
 - b. Your working relationship with GSRP:
11. Expenditure of your time worthwhile:

(Continued on next page)

12. Quality of program literature for associate:
13. a. Quality of RDL's communications with you:
b. Quality of RDL's communications with associates:
14. Overall assessment of SRP:

Table B-3. Laboratory Focal Point Responses to above questions

	<i>AEDC</i>	<i>AL</i>	<i>USAFA</i>	<i>PL</i>	<i>RL</i>	<i>WHMC</i>	<i>WL</i>
<i># Evals Recv'd</i>	0	7	1	14	5	0	46
<i>Question #</i>							
2	-	86 %	0 %	88 %	80 %	-	85 %
2a	-	4.3	n/a	3.8	4.0	-	3.6
2b	-	4.0	n/a	3.9	4.5	-	4.1
3	-	4.5	n/a	4.3	4.3	-	3.7
4	-	4.1	4.0	4.1	4.2	-	3.9
5a	-	4.3	5.0	4.3	4.6	-	4.4
5b	-	4.5	n/a	4.2	4.6	-	4.3
6a	-	4.5	5.0	4.0	4.4	-	4.3
6b	-	4.3	n/a	4.1	5.0	-	4.4
6c	-	3.7	5.0	3.5	5.0	-	4.3
7a	-	4.7	5.0	4.0	4.4	-	4.3
7b	-	4.3	n/a	4.2	5.0	-	4.4
7c	-	4.0	5.0	3.9	5.0	-	4.3
8	-	4.6	4.0	4.5	4.6	-	4.3
9	-	4.9	5.0	4.4	4.8	-	4.2
10a	-	5.0	n/a	4.6	4.6	-	4.6
10b	-	4.7	5.0	3.9	5.0	-	4.4
11	-	4.6	5.0	4.4	4.8	-	4.4
12	-	4.0	4.0	4.0	4.2	-	3.8
13a	-	3.2	4.0	3.5	3.8	-	3.4
13b	-	3.4	4.0	3.6	4.5	-	3.6
14	-	4.4	5.0	4.4	4.8	-	4.4

3. 1997 SFRP & GSRP EVALUATION RESPONSES

The summarized results listed below are from the 257 SFRP/GSRP evaluations received.

Associates were asked to rate the following questions on a scale from 1 (below average) to 5 (above average) - by Air Force base results and over-all results of the 1997 evaluations are listed after the questions.

1. The match between the laboratories research and your field:
2. Your working relationship with your LFP:
3. Enhancement of your academic qualifications:
4. Enhancement of your research qualifications:
5. Lab readiness for you: LFP, task, plan:
6. Lab readiness for you: equipment, supplies, facilities:
7. Lab resources:
8. Lab research and administrative support:
9. Adequacy of brochure and associate handbook:
10. RDL communications with you:
11. Overall payment procedures:
12. Overall assessment of the SRP:
13.
 - a. Would you apply again?
 - b. Will you continue this or related research?
14. Was length of your tour satisfactory?
15. Percentage of associates who experienced difficulties in finding housing:
16. Where did you stay during your SRP tour?
 - a. At Home:
 - b. With Friend:
 - c. On Local Economy:
 - d. Base Quarters:
17. Value of orientation visit:
 - a. Essential:
 - b. Convenient:
 - c. Not Worth Cost:
 - d. Not Used:

SFRP and GSRP associate's responses are listed in tabular format on the following page.

Table B-4. 1997 SFRP & GSRP Associate Responses to SRP Evaluation

	Arnold	Brooks	Edwards	Eglin	Griffin	Hanscom	Kelly	Kirtland	Lackland	Robins	Tyndall	WPAFB	average
# res	6	48	6	14	31	19	3	32	1	2	10	85	257
1	4.8	4.4	4.6	4.7	4.4	4.9	4.6	4.6	5.0	5.0	4.0	4.7	4.6
2	5.0	4.6	4.1	4.9	4.7	4.7	5.0	4.7	5.0	5.0	4.6	4.8	4.7
3	4.5	4.4	4.0	4.6	4.3	4.2	4.3	4.4	5.0	5.0	4.5	4.3	4.4
4	4.3	4.5	3.8	4.6	4.4	4.4	4.3	4.6	5.0	4.0	4.4	4.5	4.5
5	4.5	4.3	3.3	4.8	4.4	4.5	4.3	4.2	5.0	5.0	3.9	4.4	4.4
6	4.3	4.3	3.7	4.7	4.4	4.5	4.0	3.8	5.0	5.0	3.8	4.2	4.2
7	4.5	4.4	4.2	4.8	4.5	4.3	4.3	4.1	5.0	5.0	4.3	4.3	4.4
8	4.5	4.6	3.0	4.9	4.4	4.3	4.3	4.5	5.0	5.0	4.7	4.5	4.5
9	4.7	4.5	4.7	4.5	4.3	4.5	4.7	4.3	5.0	5.0	4.1	4.5	4.5
10	4.2	4.4	4.7	4.4	4.1	4.1	4.0	4.2	5.0	4.5	3.6	4.4	4.3
11	3.8	4.1	4.5	4.0	3.9	4.1	4.0	4.0	3.0	4.0	3.7	4.0	4.0
12	5.7	4.7	4.3	4.9	4.5	4.9	4.7	4.6	5.0	4.5	4.6	4.5	4.6
Numbers below are percentages													
13a	83	90	83	93	87	75	100	81	100	100	100	86	87
13b	100	89	83	100	94	98	100	94	100	100	100	94	93
14	83	96	100	90	87	80	100	92	100	100	70	84	88
15	17	6	0	33	20	76	33	25	0	100	20	8	39
16a	-	26	17	9	38	23	33	4	-	-	-	30	
16b	100	33	-	40	-	8	-	-	-	-	36	2	
16c	-	41	83	40	62	69	67	96	100	100	64	68	
16d	-	-	-	-	-	-	-	-	-	-	-	0	
17a	-	33	100	17	50	14	67	39	-	50	40	31	35
17b	-	21	-	17	10	14	-	24	-	50	20	16	16
17c	-	-	-	-	10	7	-	-	-	-	-	2	3
17d	100	46	-	66	30	69	33	37	100	-	40	51	46

4. 1997 USAF LABORATORY HSAP MENTOR EVALUATION RESPONSES

Not enough evaluations received (5 total) from Mentors to do useful summary.

5. 1997 HSAP EVALUATION RESPONSES

The summarized results listed below are from the 113 HSAP evaluations received.

HSAP apprentices were asked to rate the following questions on a scale from 1 (below average) to 5 (above average)

1. Your influence on selection of topic/type of work.
2. Working relationship with mentor, other lab scientists.
3. Enhancement of your academic qualifications.
4. Technically challenging work.
5. Lab readiness for you: mentor, task, work plan, equipment.
6. Influence on your career.
7. Increased interest in math/science.
8. Lab research & administrative support.
9. Adequacy of RDL's Apprentice Handbook and administrative materials.
10. Responsiveness of RDL communications.
11. Overall payment procedures.
12. Overall assessment of SRP value to you.
13. Would you apply again next year? Yes (92 %)
14. Will you pursue future studies related to this research? Yes (68 %)
15. Was Tour length satisfactory? Yes (82 %)

	Arnold	Brooks	Edwards	Eglin	Griffiss	Hanscom	Kirtland	Tyndall	WPAFB	Totals
#	5	19	7	15	13	2	7	5	40	113
resp										
1	2.8	3.3	3.4	3.5	3.4	4.0	3.2	3.6	3.6	3.4
2	4.4	4.6	4.5	4.8	4.6	4.0	4.4	4.0	4.6	4.6
3	4.0	4.2	4.1	4.3	4.5	5.0	4.3	4.6	4.4	4.4
4	3.6	3.9	4.0	4.5	4.2	5.0	4.6	3.8	4.3	4.2
5	4.4	4.1	3.7	4.5	4.1	3.0	3.9	3.6	3.9	4.0
6	3.2	3.6	3.6	4.1	3.8	5.0	3.3	3.8	3.6	3.7
7	2.8	4.1	4.0	3.9	3.9	5.0	3.6	4.0	4.0	3.9
8	3.8	4.1	4.0	4.3	4.0	4.0	4.3	3.8	4.3	4.2
9	4.4	3.6	4.1	4.1	3.5	4.0	3.9	4.0	3.7	3.8
10	4.0	3.8	4.1	3.7	4.1	4.0	3.9	2.4	3.8	3.8
11	4.2	4.2	3.7	3.9	3.8	3.0	3.7	2.6	3.7	3.8
12	4.0	4.5	4.9	4.6	4.6	5.0	4.6	4.2	4.3	4.5
Numbers below are percentages										
13	60%	95%	100%	100%	85%	100%	100%	100%	90%	92%
14	20%	80%	71%	80%	54%	100%	71%	80%	65%	68%
15	100%	70%	71%	100%	100%	50%	86%	60%	80%	82%

Associate did not participate in the program.

A STUDY OF LASER INDUCED PLASMA
DAMAGE OF THIN METAL FOILS

Mark L. Adams
National Science Foundation Fellow
Department of Electrical Engineering

Auburn University
200 Broun Hall
Auburn University, AL 36849

Final Report For:
Summer Graduate Research Program
Wright Laboratory

Sponsored by:
Air Force Office of Scientific Research
Bolling Air Force Base, Washington DC

and

Wright Laboratory

September 1997

A STUDY OF LASER INDUCED PLASMA DAMAGE OF THIN METAL FOILS

Mark L. Adams
National Science Foundation Fellow
Department of Electrical Engineering
Auburn University

Abstract

Various metal foils were subjected to repeated exposure to laser energy and the plasma discharge and damage associated with the exposure was studied. Two types of aluminum foils and gold foil were exposed to a low power, 1061 nm Nd:Glass laser. The foils underwent unconfined ablation and the plasma intensity was recorded using a Silicon PIN detector. The recorded intensity varies directly with the type and surface of the material. After initial exposure, the intensity varied due to material impurities and surface finish.

A STUDY OF LASER INDUCED PLASMA DAMAGE OF THIN METAL FOILS

Mark L. Adams

Introduction

Since the development of the laser, scientists have been studying the effects of exposure of different materials to laser radiation. In the last two decades, with the development of high power lasers, this study has been broadened to include plasma generation by laser ablation. It has been shown that once a material has undergone ablation, the plasma generated induces a shock wave that propagates through the material. This phenomena has been studied both in confined and unconfined environments and has many practical applications. Unfortunately, until recently the sheer size of the laser needed to produce this effect limited its applications. With the advent of smaller, medium to high power lasers the applications of laser ablation and laser produced plasmas are becoming realized. To this end, it has become necessary to understand the material damage caused by repeated laser ablation.

Experimental Methods

I. Laser

The experiments were performed with an Allied Signal AFLL Fire Set System Model 2020L designed and built specifically for Wright Laboratory. The optical energy source for the system is a Q-switched, Nd:Cr:GSGG laser operating at 1061 nm. The efficiency of the laser is approximately twice that of a comparable Nd:YAG laser. The optical energy output from the laser is 120-230 mJ per shot and has an 10 – 22 nsec pulsewidth with a beam diameter of approximately 6 mm. The laser radiation is focused onto the samples with an Oriel 252 mm focal length convergent lens to the desired spot size. The experiments were performed with

typical focal spots of .75 to 1 mm diameter (80 - 90% of full energy), and maximum variations of 25% of the radial intensity distribution were observed. A conservative estimate of the power density obtained is 1.7 GW/cm^2 . The laser setup is shown in Figure 1.

II. Target

The target samples consisted of three types of metal foils of various thickness and composition. A .0254 mm thick 99.45% (metals basis) polished Aluminum foil was tested first and used as the control group throughout the experiment. A .5 mm thick 99.9% (metals basis) Aluminum foil and a .1 mm thick 99.95% (metals basis) polished Gold foil were also tested. The targets were held in place by a quick release spring clamp.

III. Absorption measurements

Absorption measurement of the laser light was easily performed using an Oriel integrating sphere (Figure 2.) The inside surface of the sphere is covered with a highly diffusive white paint. The target is placed at the rear center of the integrating sphere assuring that all the reflected and produced light is collected. The experiments were conducted under normal atmospheric conditions. The light inside the sphere was measured with a Newport battery biased Silicon PIN detector covered with a 1061 nm interference filter. The detector was calibrated using a highly reflective mirror instead of the target. The waveforms were observed on an Hewlett Packard 54542A Oscilloscope.

Experimental Results and Discussion

In the first part of the experiment, each foil was shot with the laser four times in succession. The results for the polished Aluminum foil can be seen in Figures 3-6. The results agreed with the theoretical expectations. The initial pulse had the greatest amount of reflective energy and the

successive shots dropped in intensity. The polished Gold foil had similar characteristics, as can be seen in Figures 7-10, with its initial shot intensity even higher than the polished Aluminum. The other Aluminum sample provided very interesting results. Since the sample was not polished and had a fairly granular surface, the initial shot was substantially lower than its polished counterpart (Figure 11.) Surprisingly, the successive shots were all more intense than the initial shot (Figures 12 – 14.) This phenomenon is a result of the plasma damage. The initial shot occurs on the rough surface of the foil. After the initial shot, the damage area has been made smoother by the laser pulse thus it becomes more reflective.

The rest of the experiment consisted of taking repeated shots on the foils and measuring the peak reflected intensity and observing the damage area. The three foil types were each shot twelve times and the intensity values were recorded. Figure 15 shows the trends of the three foils during the successive shots. As can be seen from the figure, the same phenomenon observed in the first part of the experiment was encountered again. The intensity for the later shots reached an approximate equilibrium value and randomly oscillated around that value. These oscillations are best explained by material impurities. Pictures of the foils after the initial shots are shown in Figures 16 – 18. The plasma damage to the foil is very noticeable even after the first shot. Figures 19 – 21 show the foils after twelve shots. The damage pattern is noticeably more intense, larger in diameter, and more circular. Even after twelve shots even the thinnest of the foils had not been completely penetrated. The effect of the induced pressure wave was also noticeable from the raised singularity on the back of the foil.

Conclusion

Through this research the effects of laser-induced plasmas have been experimentally studied. The results can be applied to low-power laser ablation applications that occur in open-air environment. The results obtained agreed with theoretical expectations with the exception of the unpolished aluminum foil. The author found that the plasma damage smoothed the surface of the foil producing greater reflection during the later shots. Even after multiple repeated shots, the damage inflicted was not enough to completely penetrate the foils. Overall the results show that low-power laser ablation is feasible and the effects of the ablation can be used in practical applications.

Acknowledgements

The author is grateful to United States Air Force Wright Laboratory at Eglin AFB for the use of their facilities and equipment. This work is part of the Air Force Office of Scientific Research Summer Research Program carried out by Research Development Labs. The author would also like to thank Dr. Keith Thomas and LT Jeff McGuirk for their cooperation and support.

Appendix

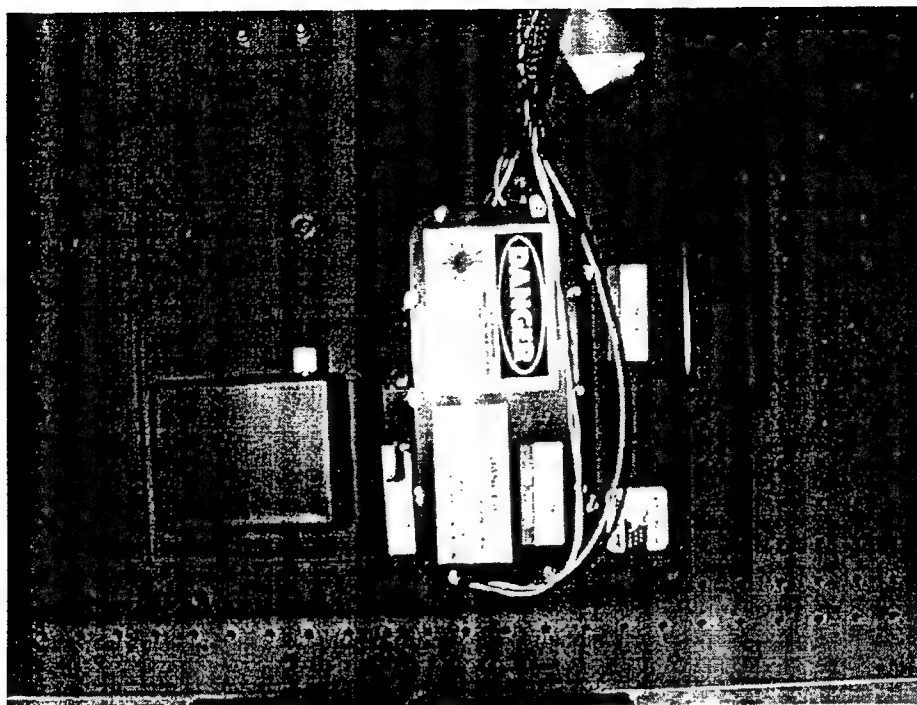


Figure 1.

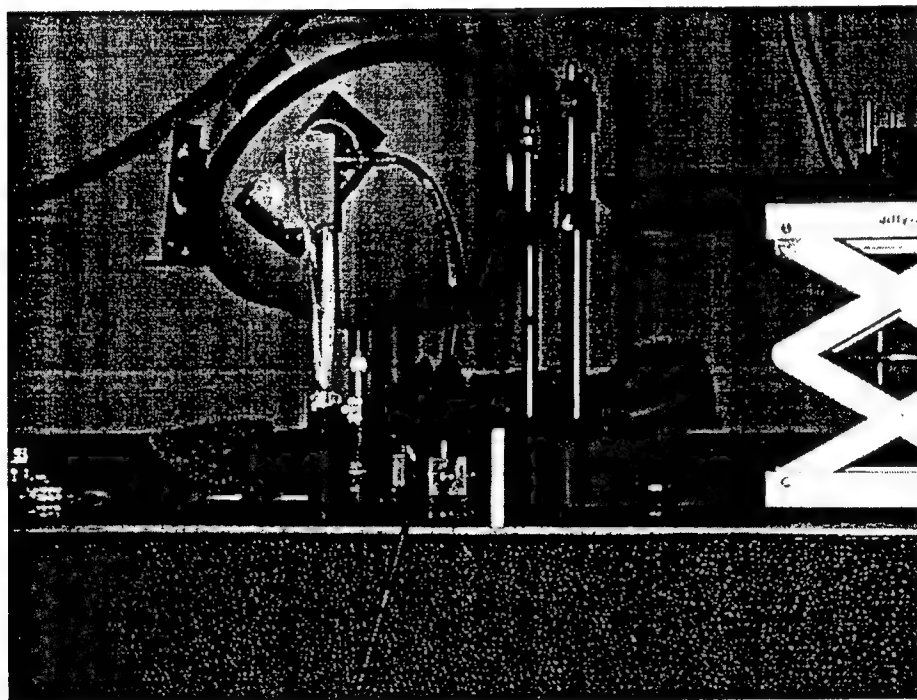


Figure 2.

Polished Aluminum Foil (Initial Shot)

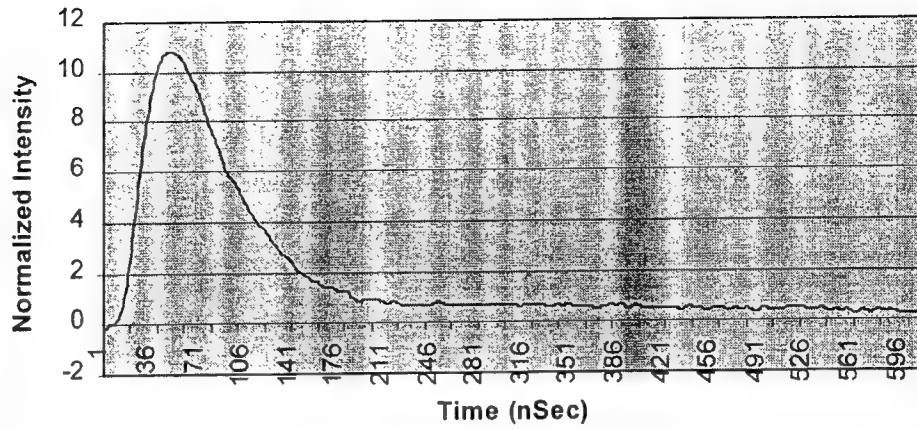


Figure 3.

Polished Aluminum Foil (Second Shot)

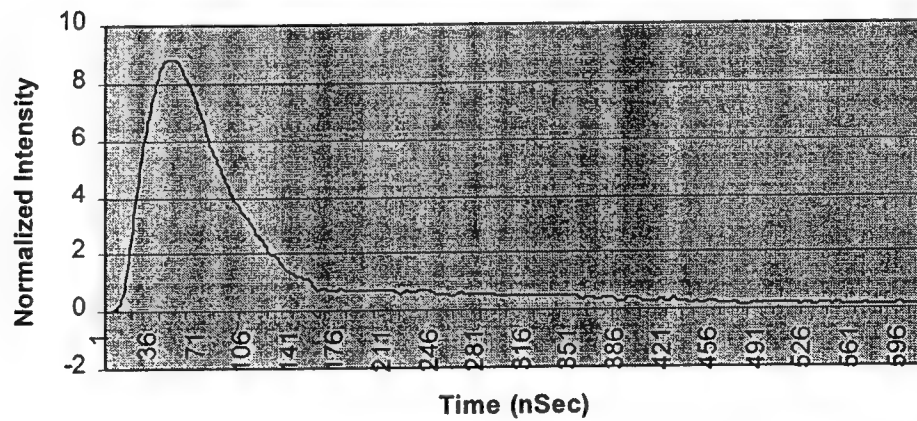


Figure 4.

Polished Aluminum Foil (Third Shot)

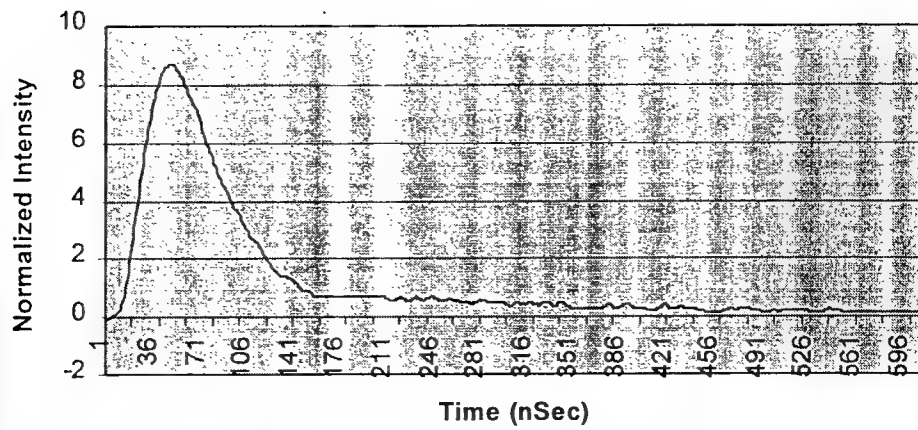


Figure 5.

Polished Aluminum Foil (Fourth Shot)

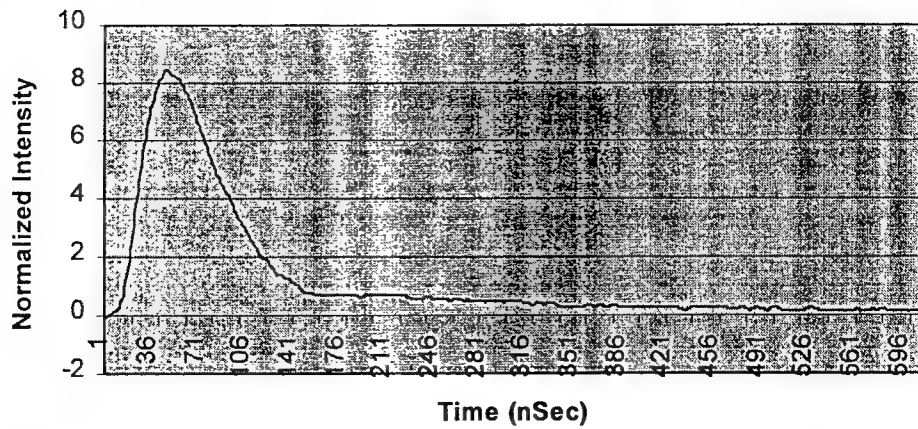


Figure 6.

Gold Foil (Initial Shot)

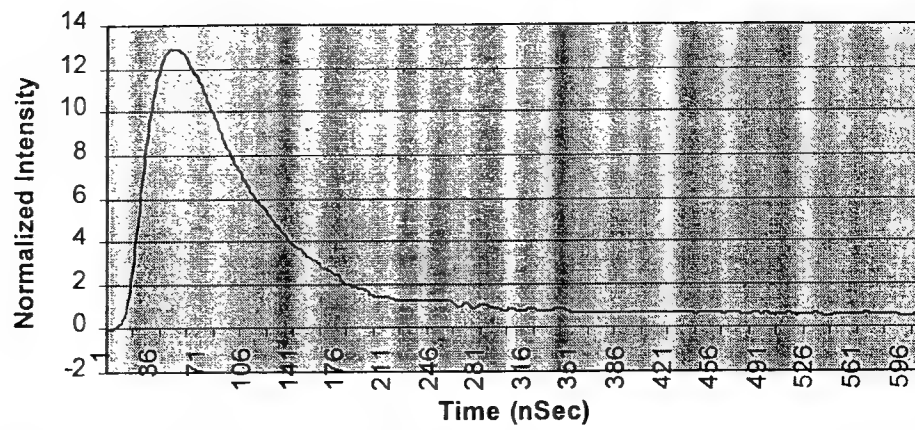


Figure 7.

Gold Foil (Second Shot)

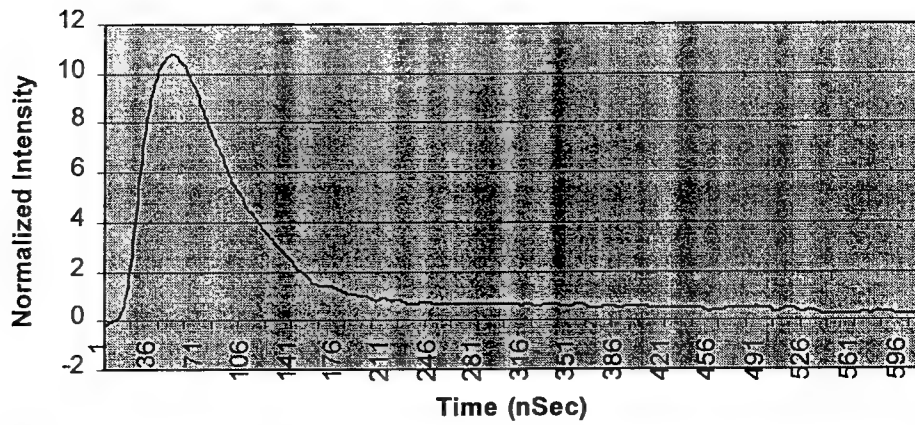


Figure 8.

Gold Foil (Third Shot)

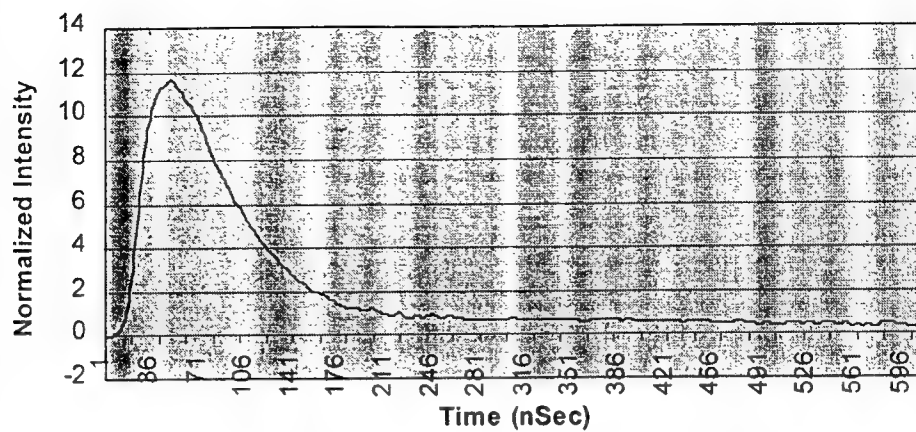


Figure 9.

Gold Foil (Fourth Shot)

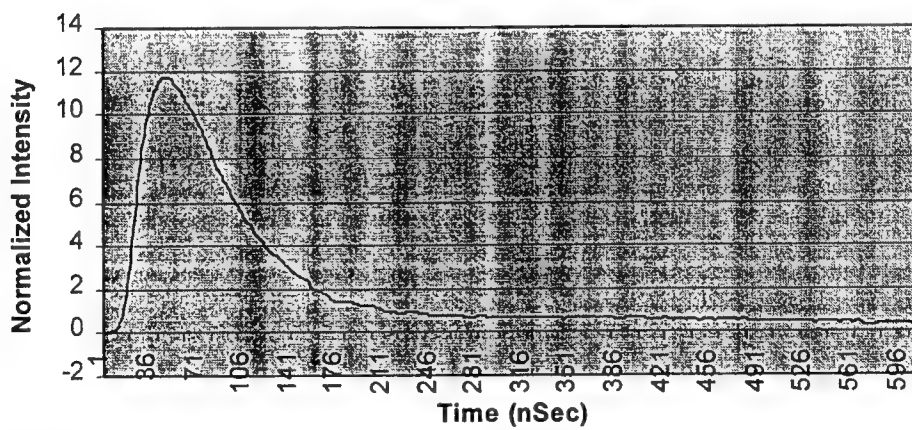


Figure 10.

Aluminum Foil (Initial Shot)

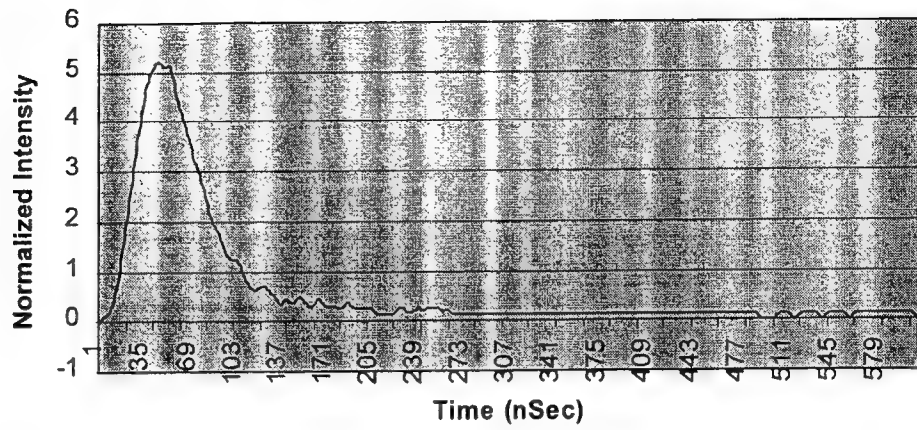


Figure 11.

Aluminum Foil (Second Shot)

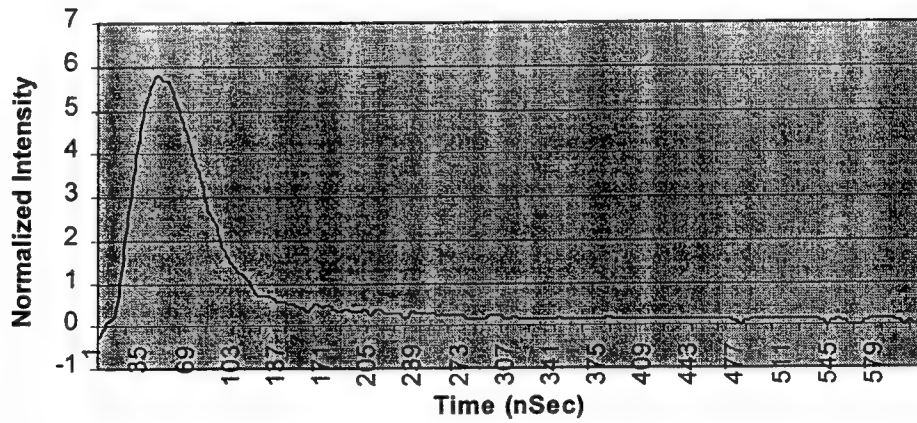


Figure 12.

Aluminum Foil (Third Shot)

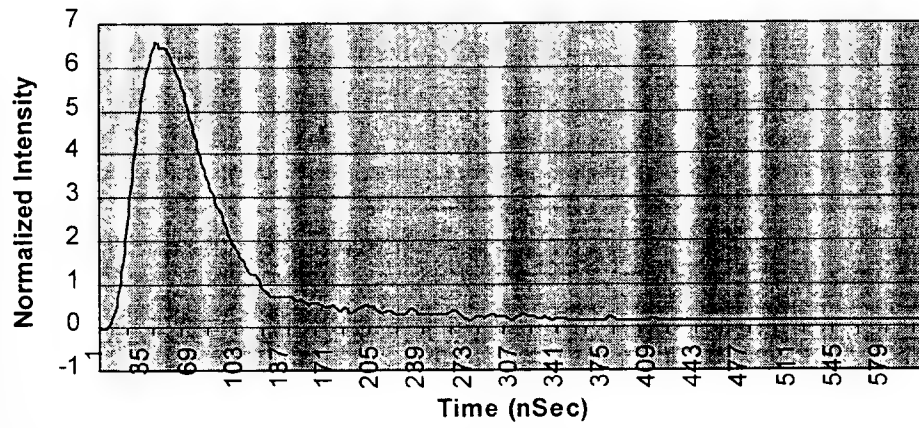


Figure 13.

Aluminum Foil (Fourth Shot)

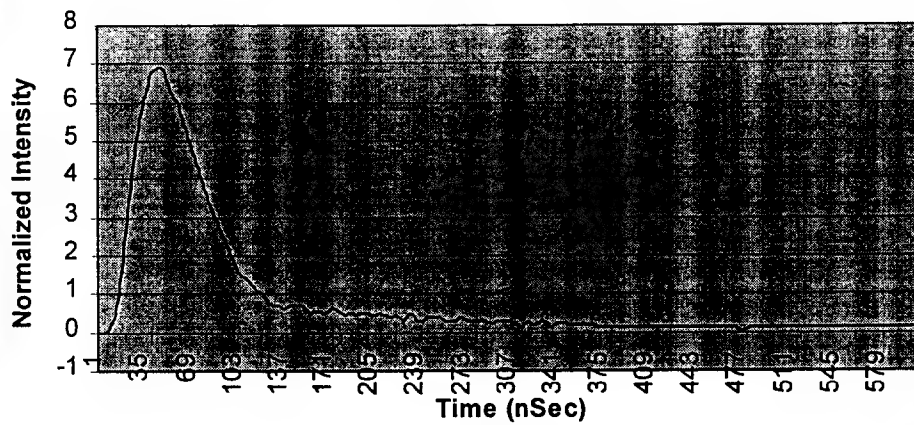


Figure 14.

Recorded Intensity Over Repeated Shots

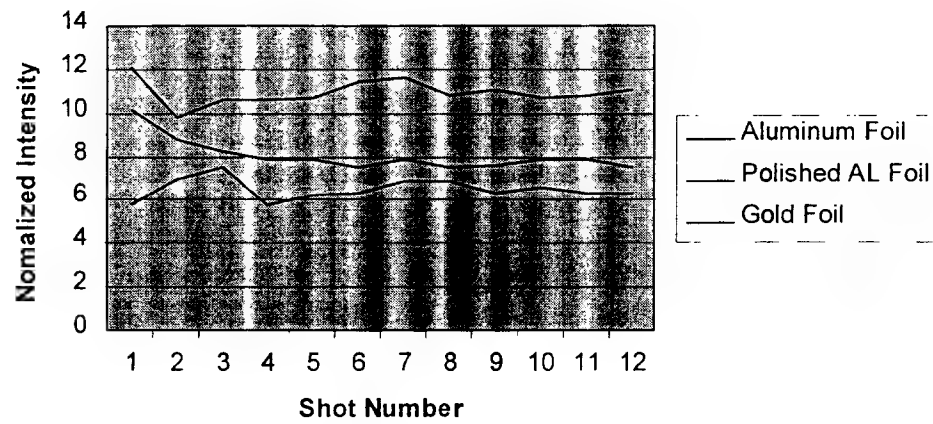


Figure 15.

Polished Aluminum Foil after One Shot

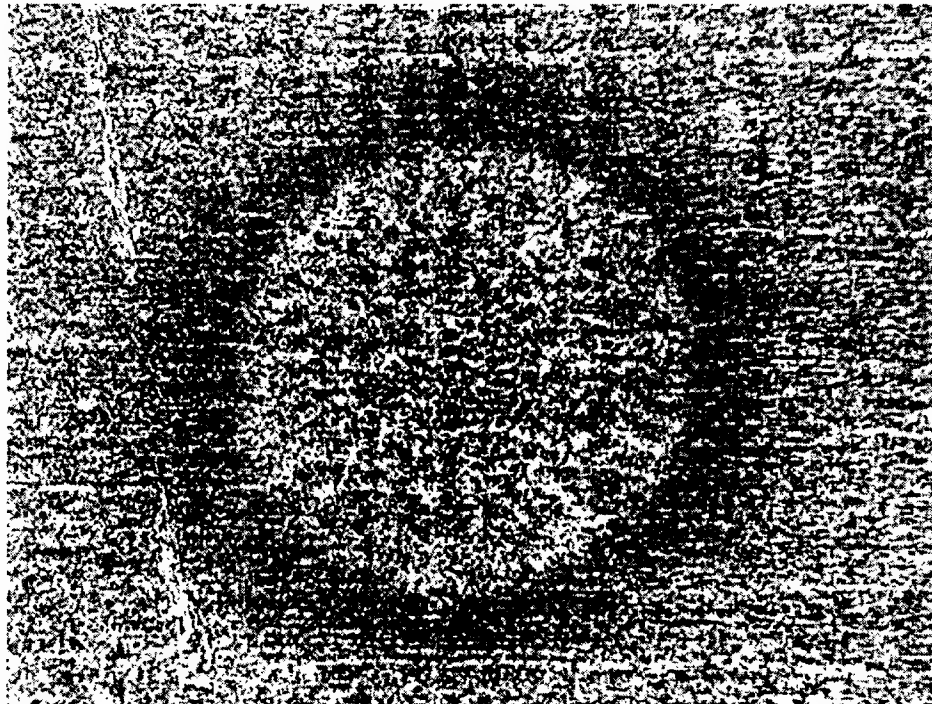


Figure 16.

Aluminum Foil after One Shot

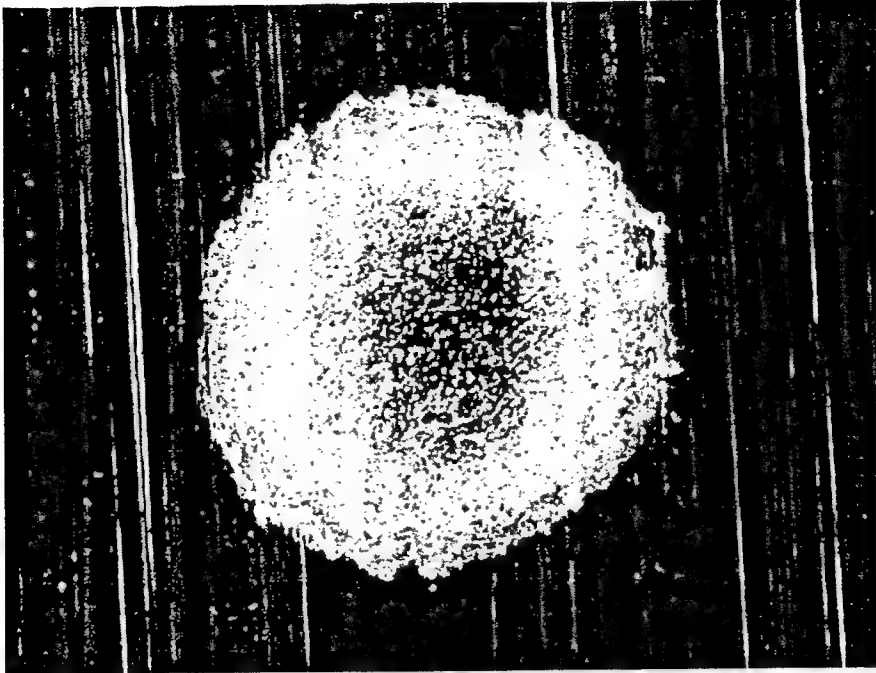


Figure 17.

Gold Foil after One Shot

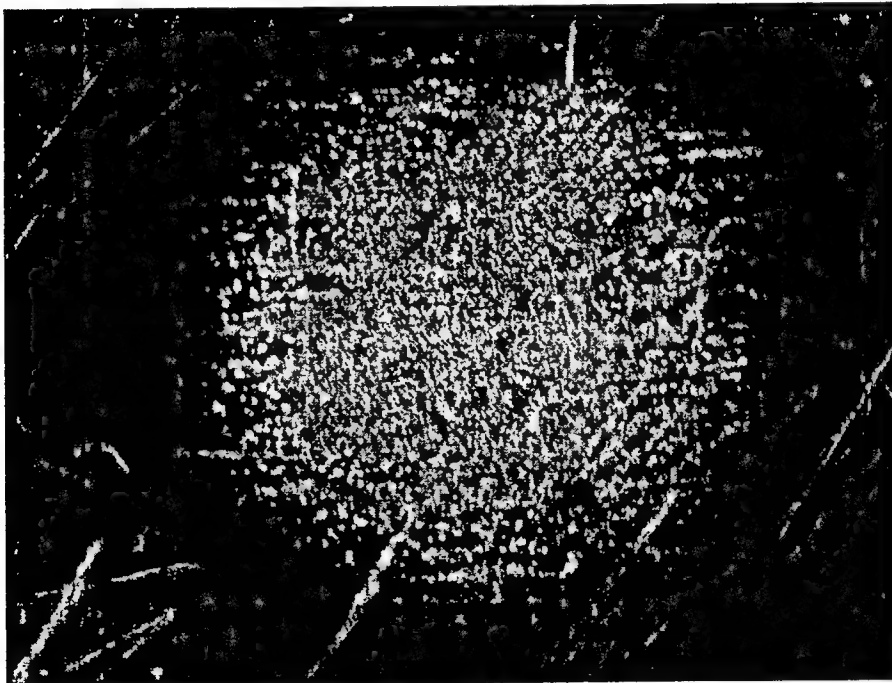


Figure 18.

Polished Aluminum Foil after Twelve Shots

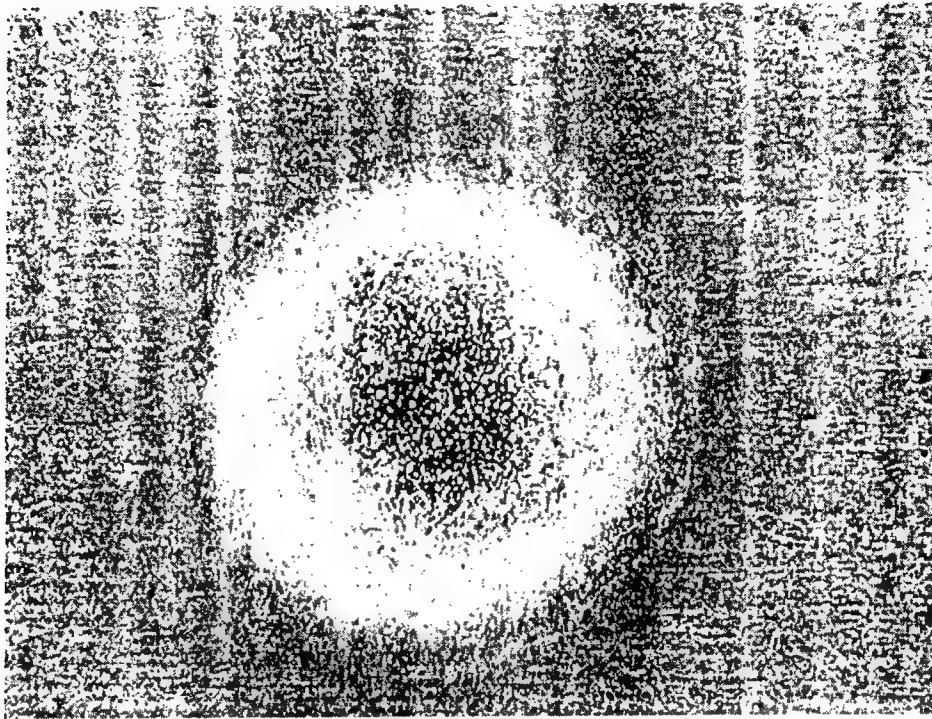


Figure 19.

Aluminum Foil after Twelve Shots

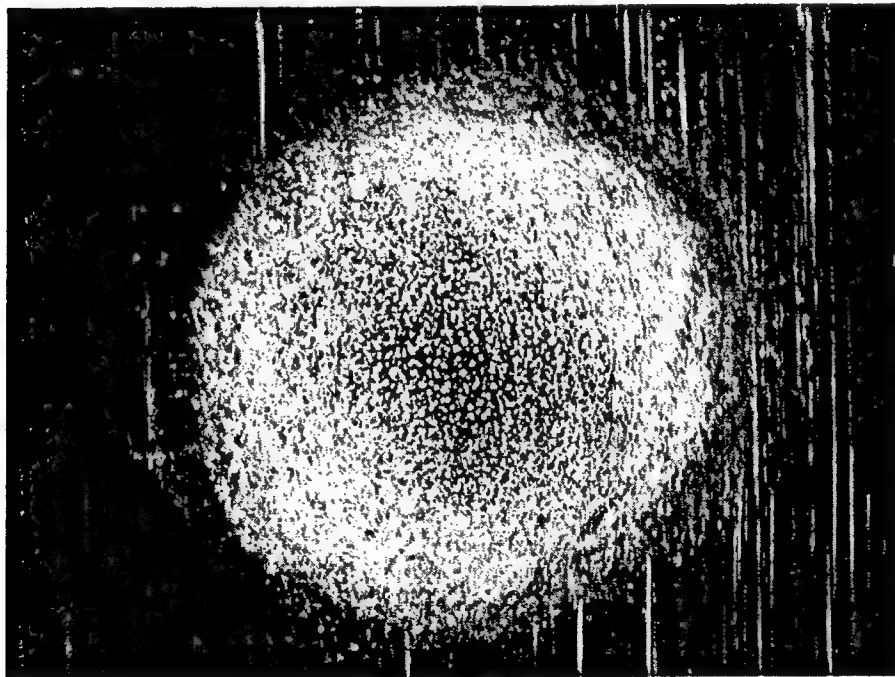


Figure 20.

Gold Foil after Twelve Shots

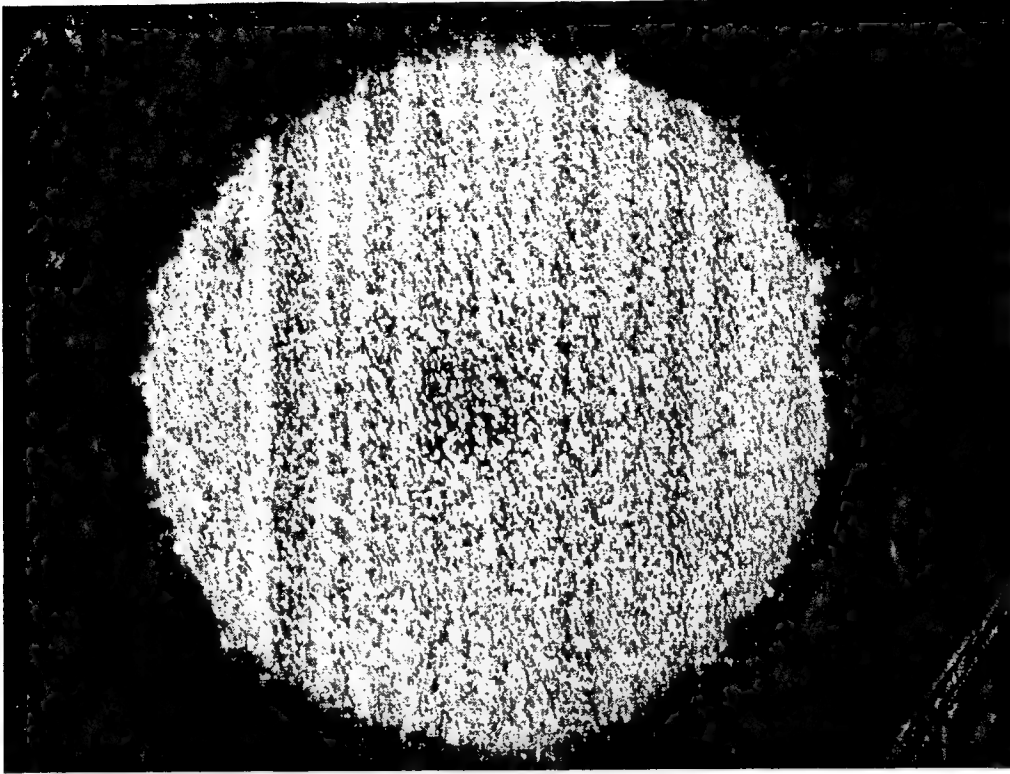


Figure 21.

**CONTRIBUTION OF A SCENE PROJECTOR'S NON-UNIFORMITY TO A
TEST ARTICLE'S OUTPUT IMAGE NON-UIFORMITY**

**T. James Belich
Graduate Student
Department of Physics**

**Bethel College
3900 Bethel Drive
St. Paul, MN 55112**

**Final Report for:
Graduate Student Research Program
Wright Laboratory**

**Sponsored by:
Air Force Office of Scientific Research
Bolling Air Force Base, DC**

And

**Wright Laboratory
Eglin Air Force Base, FL**

August 1997

CONTRIBUTION OF A SCENE PROJECTOR'S NON-UNIFORMITY TO A TEST ARTICLE'S OUTPUT IMAGE NON-UNIFORMITY

Brian P. Beecken, Professor
T. James Belich, Graduated Student
Department of Physics
Bethel College

ABSTRACT

A mathematical model of the contribution of the non-uniformity of a projector array to the non-uniformity of a test article's output image was developed. Using this model the maximum theoretical limit for the output image non-uniformity was determined. The realistic situations likely to be encountered during simulation testing were all found to be significantly below the theoretical maximum. The output image non-uniformity is dependent upon the non-uniformity of the projector array, as well as a weighting factor which results from the contribution of the different emitters upon individual detector elements. It is through this weighting factor that parameters such as the sampling ratio, the fill factor of the detector array, the optical blur of the emitters, and the alignment of the emitters with respect to the detectors influence the non-uniformity. A computer program has been written to numerically approximate the weighting factor for a user defined set of parameters.

CONTRIBUTION OF A SCENE PROJECTOR'S NON-UNIFORMITY TO A TEST ARTICLE'S OUTPUT IMAGE NON-UNIFORMITY

Brian P. Beecken
T. James Belich

Introduction

The mission of the KHILS (Kinetic Kill Vehicle Hardware-In-the-Loop Simulator) facility at Wright Laboratory's Armament Directorate is to test infrared imaging sensors in the lab by projecting simulated IR scenes that subtend the sensor's field of view.[1] The IR projector, an integral component of the simulation testing, is produced under Wright Lab's WISP (Wideband Infrared Scene Projector) program.

The WISP projector consists of an array of emitters at least as large in number as the array of detectors on the sensor's focal plane.[2] Unfortunately, when the emitter array is set to produce a uniform IR scene, there is significant non-uniformity in the array's output.[3] Although this non-uniformity can be corrected to a large extent, it can never be completely eliminated. Thus, the non-uniformity of the projector will exist as an artifact in the test article's output image. This artifact is solely the result of the simulation, and represents a degradation of the actual scene that would be encountered during the sensor's mission.

The goal of this paper is to predict analytically how the non-uniformity of the projector impacts the uniformity of the test article's output image. Such information will be valuable for determining both the realism of the simulation and the non-uniformity correction requirements. The prediction should be as general as possible, without any reference to a particular emitter array or sensor. These components will be changed as program requirements change, but the need to know the projector's impact on the test article's output image uniformity will always be present.

In order to make our prediction as general as possible, a number of parameters will be

required. These parameters are the ratio of the projector's non-uniformity to the detector array's non-uniformity, the linear ratio of the emitters to detectors (i.e., the sampling ratio), the relative size of the optical blur on the detector array, the alignment of the emitters relative to the detectors, and the fill factor of the detector array. These are believed to be the test parameters of primary importance and will be incorporated into the following analysis.

1 Theory

In this section, we will derive the primary statistical equation for predicting the contribution of projector non-uniformity to the output image non-uniformity. First, we will consider the simplest case for which there is so little blur that a one-to-one mapping of emitters to detectors results. Next, this case will be generalized by increasing the ratio of emitters to detectors and allowing one detector to receive the radiation from multiple emitters. There will still be no blurring of the incident radiation, however, so each emitter will still be detected by only one detector. These two cases will be examined first because they set the pattern for the most general case.

The most general situation will be the last case examined in this section. This case will include parameters such as the relative optical blur size (the size of the radiation from one emitter on the detector array measured in detector pitch), the alignment of the emitters relative to the detectors, and the fill factor of the detector array.

1.1 "No Blur" with 1 to 1 Mapping of Emitter to Detector

The output signal v of a detector is often approximated by

$$v = g\eta\Phi + b \quad (1)$$

where g is the detector's conversion gain, η is the detector's quantum efficiency, Φ the average number of incident photons per integration time, and b is the signal offset that

exists even for zero incident photon flux.¹ In this paper, we will only be considering those situations in which non-uniformity noise dominates over the other noise sources that are more apparent at low flux levels. Consequently, the incident flux will be assumed to be large enough that any variation in the offset b can be ignored.²

Each detector on the array produces a signal that differs from the other detectors if either the conversion gain or the quantum efficiency of the detector varies, or if the incident photon flux is different. We are not interested in whether a variation in signal is due to a detector's conversion gain or quantum efficiency. Therefore, these terms will be combined together to represent the detector's sensitivity $g\eta$. The non-uniformity of the detector array can then be conveniently represented as the standard deviation of all the detector sensitivities divided by the average sensitivity, $\frac{\sigma_{g\eta}}{g\eta}$. Similarly, the non-uniformity of the emitter array can be represented by $\frac{\sigma_{\Phi}}{\Phi}$, where Φ is the average emittance across the emitter array and σ_{Φ} is the standard deviation. Because we are discussing the one-to-one mapping case, the non-uniformity of the emittances will be identical to the non-uniformity of the incident flux:

$$\frac{\sigma_{\Phi}}{\Phi} = \frac{\sigma_{\phi}}{\phi}. \quad (2)$$

Eq. (1) is a product of two terms (detector sensitivity and incident flux) that each have an uncertainty. The standard error propagation equation in this situation is

$$\left(\frac{\sigma_v}{v}\right)^2 = \left(\frac{\sigma_{g\eta}}{g\eta}\right)^2 + \left(\frac{\sigma_{\Phi}}{\Phi}\right)^2. \quad (3)$$

Simple algebra puts the equation in a more useful form,

$$\frac{\frac{\sigma_v}{v}}{\frac{\sigma_{g\eta}}{g\eta}} = \sqrt{1 + \left(\frac{\frac{\sigma_{\Phi}}{\Phi}}{\frac{\sigma_{g\eta}}{g\eta}}\right)^2}. \quad (4)$$

This result gives the ratio of the output image non-uniformity to the detector's non-uniformity as a function of the ratio of the projector's non-uniformity to the detector's non-uniformity. It is easily seen, for example, that if the projector has a non-uniformity

¹The output signal v can only be represented by a linear function over a limited region. It is this region, however, for which two point calibration (offset and gain correction) is performed.

²Further work should enable us to remove this limitation so that the non-uniformity's contribution to the total noise could be predicted even when other noise sources are comparable in size.

equal to that of the detector's non-uniformity, then the output image non-uniformity will be increased by a factor of $\sqrt{2}$ over the detector's non-uniformity. As expected, if either the projector or the detector array has significantly larger non-uniformity, it will dominate the output image.

This equation applies in the simplest case where each emitter has an output of ϕ detected by only one detector, and each detector receives the radiation emitted by only one emitter. This simple case will serve as the baseline for further calculations.

1.2 “No Blur” with a Sampling Ratio of n to 1

The *sampling ratio* n is defined as the ratio of emitters to detectors when counted in one dimension. The previous case was restricted to a sampling ratio of one-to-one. Now we will allow for any integer sampling ratio, but we will again restrict ourselves to virtually “no blur.” All radiation emitted by an emitter is still received by one and only one detector (Fig. 1).

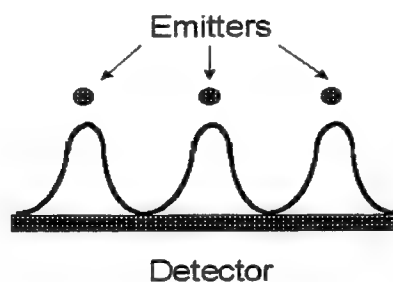


Figure 1: Illustration of a sampling ratio of 3 to 1 with essentially “no blur.”

Now there are several emitters contributing to the signal of one detector. Thus, the Φ in Eq. (1) represents the *total* radiation landing on the detector from all the emitters in its field of view:

$$\Phi = \phi_1 + \phi_2 + \phi_3 + \dots + \phi_n. \quad (5)$$

Each ϕ_i refers to both the radiation received from emitter i as well as the flux produced by emitter i (since all of each emitter's flux lands on one detector). If one assumes that the

sampling ratio is the same in both directions, then there will be n^2 emitters per detector. Each individual emitter's flux ϕ_i can be approximated by the average flux $\bar{\phi}$ of all the emitters. Therefore,

$$\Phi \approx n^2 \bar{\phi}. \quad (6)$$

The goodness of the approximation of each ϕ_i by $\bar{\phi}$ is given by the standard deviation of the emittances in the emitter array σ_ϕ . Thus,

$$\phi_i \approx \bar{\phi} \pm \sigma_\phi \quad (7)$$

The uncertainty of a sum of variables is simply the square root of the sum of the squares of each variable's uncertainty. Since each emittance ϕ_i is approximated in the same way, we have

$$\sigma_\Phi^2 = n^2 \sigma_\phi^2. \quad (8)$$

A combination of Eqs. (6) and (8) can be used to represent the non-uniformity of the flux incident on the detector array,

$$\frac{\sigma_\Phi}{\Phi} = \frac{n \sigma_\phi}{n^2 \bar{\phi}} = \frac{\sigma_\phi}{n \bar{\phi}}. \quad (9)$$

Thus, Eq. (4) becomes

$$\frac{\frac{\sigma_v}{v}}{\frac{\sigma_{g\eta}}{g\eta}} = \sqrt{1 + \left(\frac{\frac{\sigma_\phi}{\bar{\phi}}}{\frac{\sigma_{g\eta}}{g\eta}} \right)^2 \frac{1}{n^2}}. \quad (10)$$

This result is plotted in Fig. 2 for three different sampling ratios. It will turn out that each line in Fig. 2 represents the greatest non-uniformity possible for a particular sampling ratio. Thus, we will refer to these lines as the *no blur limits*.

1.3 The General Case

Up until now, we have assumed that each emitter illuminates only one detector—what we have referred to as the “no blur” case. Now we will allow the image of the emitters on the focal plane array to be blurred out so that each emitter is seen by multiple detectors. Under these circumstances, it is still true that there will be n^2 emitters per detector. Thus, as before,

$$\Phi \approx n^2 \bar{\phi}. \quad (11)$$

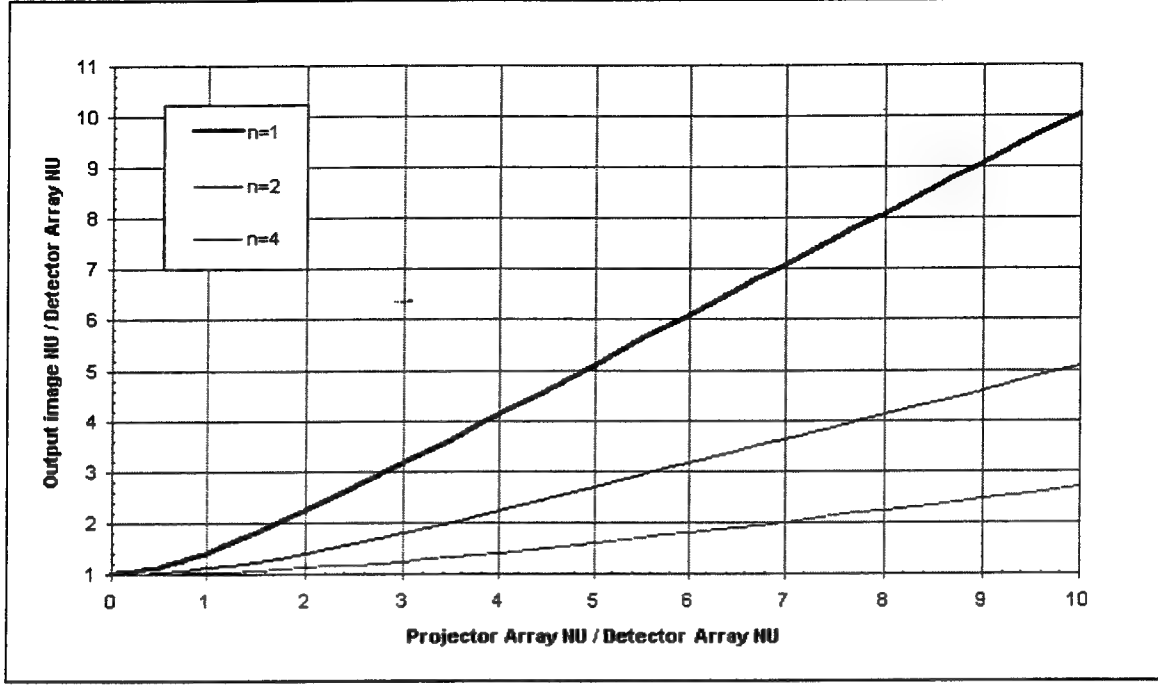


Figure 2: A plot of Eq. (10) for three different sampling ratios. Each line serves as the upper limit of non-uniformity, regardless of blur size.

But Eq. (5) now becomes

$$\Phi = y_1\phi_1 + y_2\phi_2 + y_3\phi_3 + \dots + y_M\phi_M, \quad (12)$$

where y_i is some weighting function that accounts for how much a particular emitter contributes based on its position relative to the detector. Here M is used to represent the total number of emitters seen by one detector. If the blur is large, then M can become quite large. Because of Eq. (11),

$$\sum_{i=1}^M y_i = n^2. \quad (13)$$

It is convenient to normalize this weighting function by defining x_i as $\frac{y_i}{n^2}$. Then, due to normalization,

$$\sum_{i=1}^M x_i = 1. \quad (14)$$

The normalized *weighting function* x_i is simply the geometry dependent fraction of each emitter i 's contribution to the total flux received by the detector. It will be discussed more fully in the next section.

The uncertainties add as the sum of the squares:

$$\begin{aligned}\sigma_{\Phi}^2 &= y_1^2 \sigma_{\phi_1}^2 + y_2^2 \sigma_{\phi_2}^2 + y_3^2 \sigma_{\phi_3}^2 + \dots + y_M^2 \sigma_{\phi_M}^2 \\ &= n^4 \left[x_1^2 \sigma_{\phi_1}^2 + x_2^2 \sigma_{\phi_2}^2 + x_3^2 \sigma_{\phi_3}^2 + \dots + x_M^2 \sigma_{\phi_M}^2 \right].\end{aligned}$$

But all the uncertainties are the same, because they are all represented by the same standard deviation of the emittances across the emitter array. Thus, $\sigma_{\phi_i} = \sigma_{\phi}$, so

$$\sigma_{\Phi}^2 = n^4 \sigma_{\phi}^2 \sum_{i=1}^M x_i^2. \quad (15)$$

Substituting Eq. (11) and Eq. (15) into Eq. (4) we get

$$\frac{\frac{\sigma_v}{\bar{v}}}{\frac{\sigma_{g\eta}}{g\eta}} = \sqrt{1 + \left(\frac{\frac{\sigma_{\phi}}{\bar{\phi}}}{\frac{\sigma_{g\eta}}{g\eta}} \right)^2 \sum_{i=1}^M x_i^2}. \quad (16)$$

This is our *primary equation* which will be used to calculate the non-uniformity of the output image. Parameters such as fill factor, alignment (or registration), and relative optical blur size affect the output's uniformity only through the *weighting factor* $\sum_{i=1}^M x_i^2$. As discussed in the next section, the calculation of this weighting factor is done through numerical approximations.

Before moving on, it is instructive to ensure that our primary equation reduces to Eq. (10) for cases of small blur. When the blur is sufficiently small, $M \rightarrow n^2$ because the detector sees only those emitters whose unblurred images fall directly on top of it. Since each emitter's radiation is received only by one detector, all $x_i \rightarrow \frac{1}{n^2}$. Thus, the weighting factor becomes

$$\sum_{i=1}^{n^2} x_i^2 = n^2 \left(\frac{1}{n^2} \right)^2 = \frac{1}{n^2}, \quad (17)$$

which makes Eq. (16) reduce to Eq. (10) as it should.

2 Determination of the Weighting Function

In the previous section, we derived the primary equation, Eq. (16), that predicts the non-uniformity of the detector's output image. In order to use this equation, however, it is necessary to first calculate the weighting factor, $\sum_{i=1}^M x_i^2$. Unfortunately, the weighting

function x_i cannot be solved analytically. In this section, we will first describe our numerical approach to finding the weighting function. Next we will discuss the calculation of the *relative optical blur size* K , a crucial parameter that must be used in the calculation of the weighting function.

2.1 Numerical Calculation of the Weighting Function

Determining the contribution of each emitter to the total flux received by a given detector is a difficult task because the optical blur is governed by Fraunhofer diffraction. We chose to approximate the distribution of the flux incident on the FPA from a single emitter with a two dimensional Gaussian function. The portion of the emitter's flux which lands on a detector is determined by integrating the two dimensional Gaussian over the detector's area. The fractional contribution of each individual emitter to the total flux incident on a detector is what we have defined as the weighting function x_i .

Because the emitter array is two dimensional, it is necessary to relabel our weighting function as x_{ij} in order to obtain a realistic calculation. Each x_{ij} is then the energy from emitter ij divided by the total flux falling upon the detector. Because the weighting function is normalized, $\sum_i \sum_j x_{ij} = 1$. Although the idea behind this calculation is relatively simple, it becomes difficult in practice for two reasons. First, since we cannot analytically solve the integral of the two dimensional Gaussian over square areas, we approximated it numerically by doing Riemann-like sums. Second, the equation for x_{ij} becomes rather complex once parameters such as fill factor and alignment are taken into account. Our approximation for the weighting function is:

$$x_{ij} \approx \frac{1}{(nA)^2} \sum_{p=-S}^S \sum_{q=-S}^S \frac{\exp \left\{ -\frac{1}{2} \left[\left(\frac{i-T_x-\frac{p}{A}F_x}{0.2616Kn} \right)^2 + \left(\frac{j-T_y-\frac{q}{A}F_y}{0.2616Kn} \right)^2 \right] \right\}}{\sum_{a=-L}^L \sum_{b=-L}^L \exp \left\{ -\frac{1}{2} \left[\left(\frac{a-T_x-\frac{p}{A}F_x}{0.2616Kn} \right)^2 + \left(\frac{b-T_y-\frac{q}{A}F_y}{0.2616Kn} \right)^2 \right] \right\}} \quad (18)$$

where

$$S = \frac{1}{2}(nA - 1) \quad \text{and} \quad L = 0.7848Kn + \frac{n}{2}.$$

The integration of the two dimensional Gaussian is approximated by using a number of "detection points" distributed across the active detector area. The total number of detection points is given by $(nA)^2$, where A^2 is the number of detection points per emitter. The value of the Gaussian at each detection point is multiplied by the fraction $\frac{1}{(nA)^2}$ of the detector's area being represented by the detection point. The sum of these values yields a good approximation of the integral, assuming that a large enough value of A has been chosen. The computer program we developed to calculate x_{ij} will automatically choose an appropriate value for A when given values for the sampling ratio n and the relative optical blur size K . (Determination of K is discussed in the next subsection.) Clearly, a larger A will provide a better approximation, but computer processing time increases rapidly with A .

In order for x_{ij} to be normalized, the denominator of the larger fraction in Eq. (18) must be the sum of the total energy. Therefore, the sum limits $\pm L$ are chosen so that the contribution of the emitters within at least three σ of optical blur from the detector will be counted. Emitters outside this range are assumed to be far enough away from the detector that their impact upon it is negligible. The value of L also determines the number M of weighting functions x_{ij} that must be summed to find the weighting factor in Eq. (16). In terms relevant to this numerical calculation, the weighting factor is now

$$\sum_{i=-L}^L \sum_{j=-L}^L x_{ij}^2. \quad (19)$$

These implications are all incorporated into our computer program which calculates the weighting factor.

In Eq. (18), T_x and T_y account for the alignment of the emitter array relative to the detector array. Each variable represents a translation of the emitter centered over the detector in the x and y directions (measured as a fraction of the emitter spacing).³ Their values may range from 0 to 0.5. The detector's fill factor is accounted for by F_x and F_y ,

³Zero translation is defined as one emitter being centered over each detector element. In our computer program, in an effort to be as user friendly as possible, zero translation is defined as the emitters being symmetrically distributed over the detector. This difference in definitions only occurs when the sampling ratio n is even.

which are the linear fill factors in the x and y directions. Each must be in the range of 0 to 1, where 1 is a 100% linear fill factor.

2.2 Determination of the Relative Optical Blur Size K

Determination of K , the size of the optical blur relative to the detectors on the FPA, is crucial to determining the weighting factor in Eq. (16). In our weighting function, Eq. (18), we have implicitly defined:

$K \equiv$ number of detector pitches in the diameter of a circular blur
containing 83.9% of the radiation.

Now we will derive a means of determining K from the characteristics of the optical system. For a distant point source viewed through a circular aperture, it is well known that the angular diameter (in radians) of the central maximum is given by

$$\theta = \frac{2.44\lambda}{D} \quad (20)$$

where D is the aperture diameter and λ is the wavelength of the incident radiation. When the radiation is focused on the FPA, this equation becomes

$$d = \frac{2.44\lambda}{D} f, \quad (21)$$

where f is the focal length and d is the diameter of the central maximum, which is called the Airy disk. The Airy disk contains 83.9% of the incident radiation.[4] The value for K can be calculated by dividing Eq. (21) by the detector pitch w (the center-to-center detector spacing):

$$K = 2.44 \frac{\lambda f}{Dw}. \quad (22)$$

In Eq. (18) we used a two dimensional Gaussian blur to approximate the actual radiation distribution, and we can now examine how it relates to the actual diffraction pattern. The number of σ that correlates to the energy in the Airy disk can be found by integrating the two dimensional Gaussian. Surprisingly, the integral in two dimensions is not difficult

because the blur is radially symmetric. First, we choose a dimensionless variable r equal to $(x - \mu)/\sigma$. Next, we set the mean μ equal to zero so that r is simply the radius in σ . Then we solve for the value for R , the radius which contains 83.9% of the two dimensional Gaussian:

$$\int_0^R r e^{-\frac{1}{2}r^2} dr = 0.839 \int_0^\infty r e^{-\frac{1}{2}r^2} dr$$

becomes

$$R = 1.911.$$

Consequently, a Gaussian blur will include the same energy as the Airy disk when its diameter is 3.822σ . The σ of the Gaussian is given by

$$\sigma = \frac{K}{3.822} = 0.2616K. \quad (23)$$

This form is found in our weighting function, Eq. (18).

3 Results

Several parameters are required to determine the weighting factor in Eq. (16). Therefore, one simple plot of the primary equation cannot be made. In this section, we will display several plots that are chosen to demonstrate general trends over regions of interest.

Figures (3) and (4) illustrate the output image non-uniformity as a function of the projector non-uniformity for sampling ratios of 1:1 and 4:1. As in Fig. (2), the comparison is done with the projector non-uniformity varying from perfect uniformity to a non-uniformity that is an order of magnitude greater than the detector array's non-uniformity. In these two figures, however, each line represents a different optical blur, unlike Fig. (2), which was for virtually "no blur." Recall that the relative optical blur size K represents the detector pitch per diameter of 83.9% of the blurred radiation. Thus when $K = 1$, one detector gets 83.9% of the radiation from one emitter. Note that the "no blur" limit coincides with the appropriate sampling ratio line in Fig. (2). If the blur is infinite, then each detector sees every emitter and the non-uniformity of the projector array cannot be observed. Consequently, large K values cause the lines to move toward

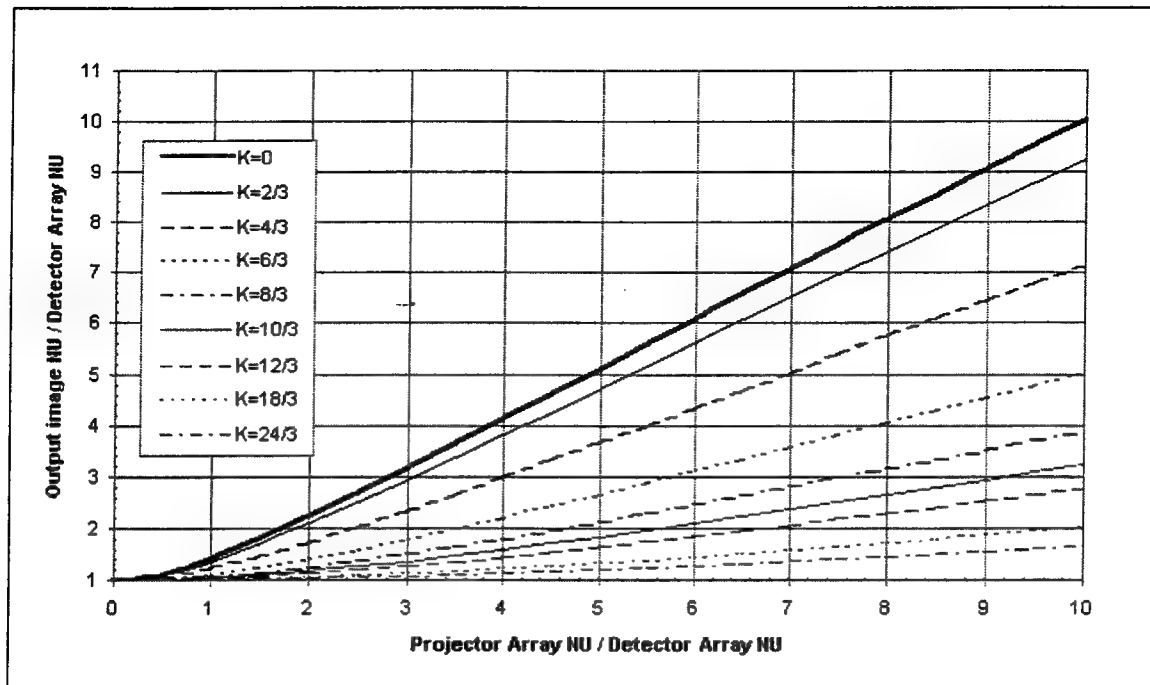


Figure 3: Output image NU vs. projector NU for different relative optical blur sizes K . Sampling ratio is 1:1, fill factor is 100%, and each emitter is centered over one detector.

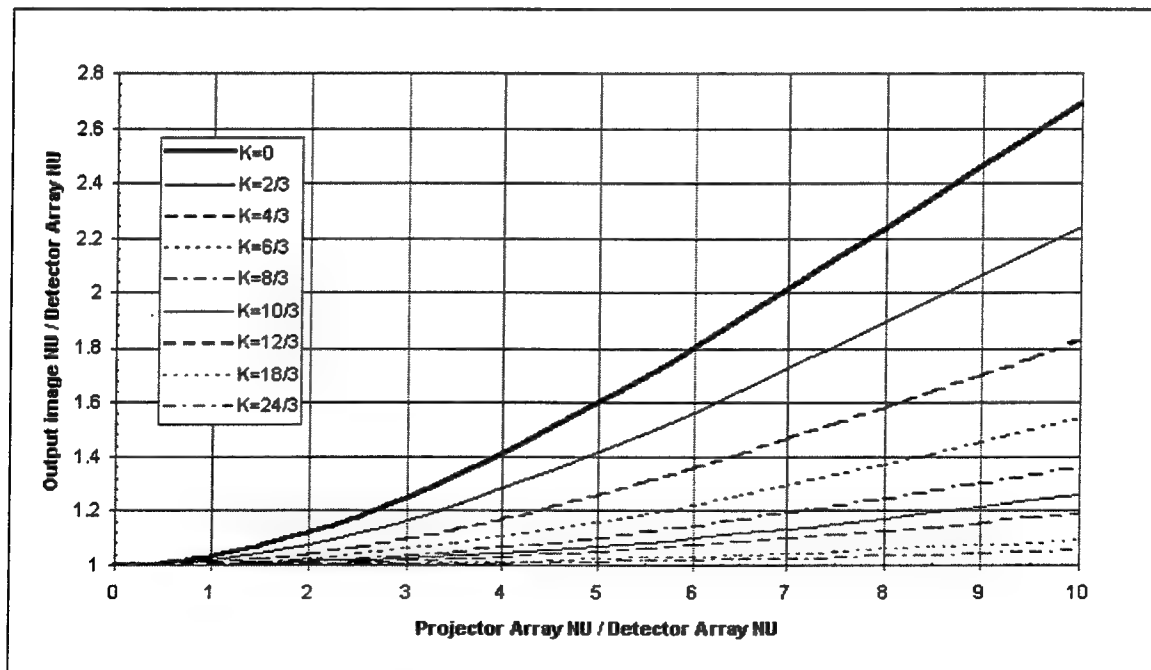


Figure 4: Output NU vs. projector NU for different relative optical blur sizes K . Sampling ratio is 4:1, fill factor is 100%, and emitters are symmetrically centered over detectors.

the horizontal axis where the output image non-uniformity is entirely due to the detector array's non-uniformity.

In order to display the effect of the detector array's fill factor, we chose the particular case of a projector non-uniformity five times greater than the detector array's non-uniformity. Then we plotted the non-uniformity of the output image resulting from different fill factors (in terms of detector area) as a function of the relative optical blur size K . The results are shown in Fig. (5) for a sampling ratio of 1:1 and in Fig. (6) for a sampling ratio of 4:1. Clearly, fill factor makes a difference if it changes significantly, but the more important parameter is the blur size.

As a side point, note that in Fig. (6) the no blur limit of Fig. (2) appears to be violated. The output image non-uniformity in Fig. (6) is as high as 170% above the detector array non-uniformity, whereas the no blur limit for this case should be a 60% increase according to Fig. (2). The apparent discrepancy occurs only when there is virtually no blur and a sampling ratio greater than 1:1. Very small fill factors cause the emittance of some emitters to effectively drop off the edge of the detector's active area. The result is essentially a smaller sampling ratio and a higher no blur limit.

Two more plots, Figs. (7) and (8), were also made with the output image non-uniformity as a function of optical blur, only this time the alignment of the arrays was varied by as much as half an emitter spacing. (Further translations would be the mirror images of lesser translations.) Apparently, alignment makes relatively little difference when there is 100% fill factor, especially if there is a large sampling ratio. To check this, Fig. (9) was done with only 64% fill factor at different alignments. As might be expected, the lower fill factors made a greater difference than the effects of alignment.

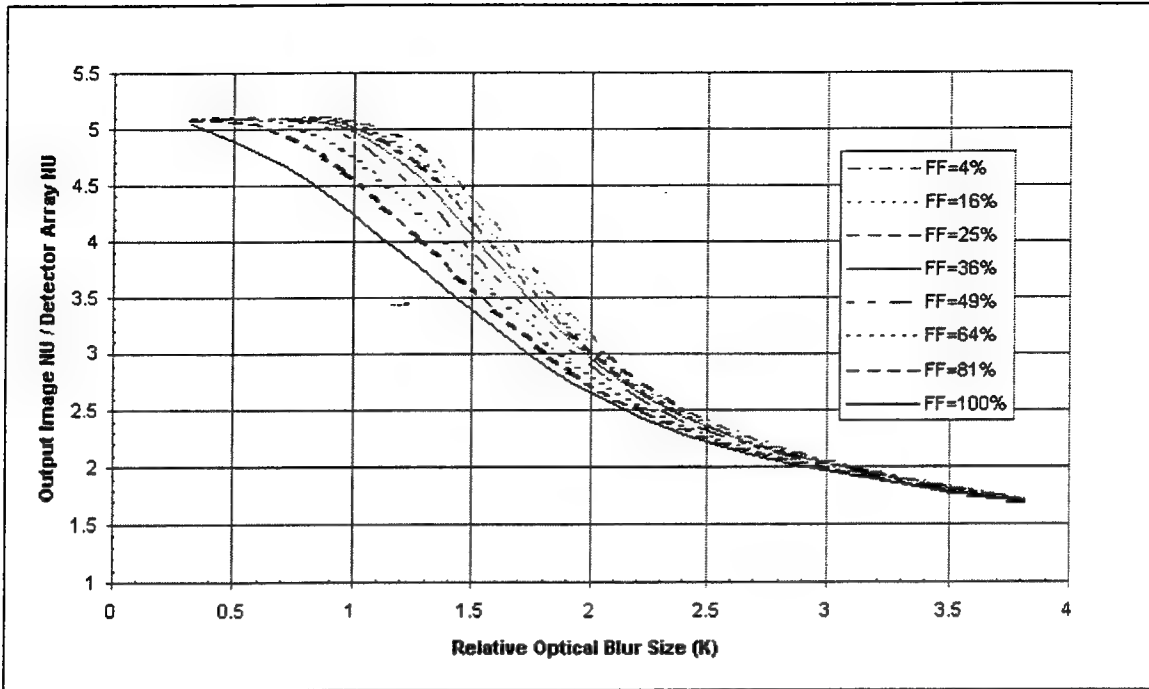


Figure 5: Output image NU vs. relative optical blur size for different fill factors. Sampling ratio is 1:1, projector NU/detector NU is 5, and each emitter is centered over one detector.

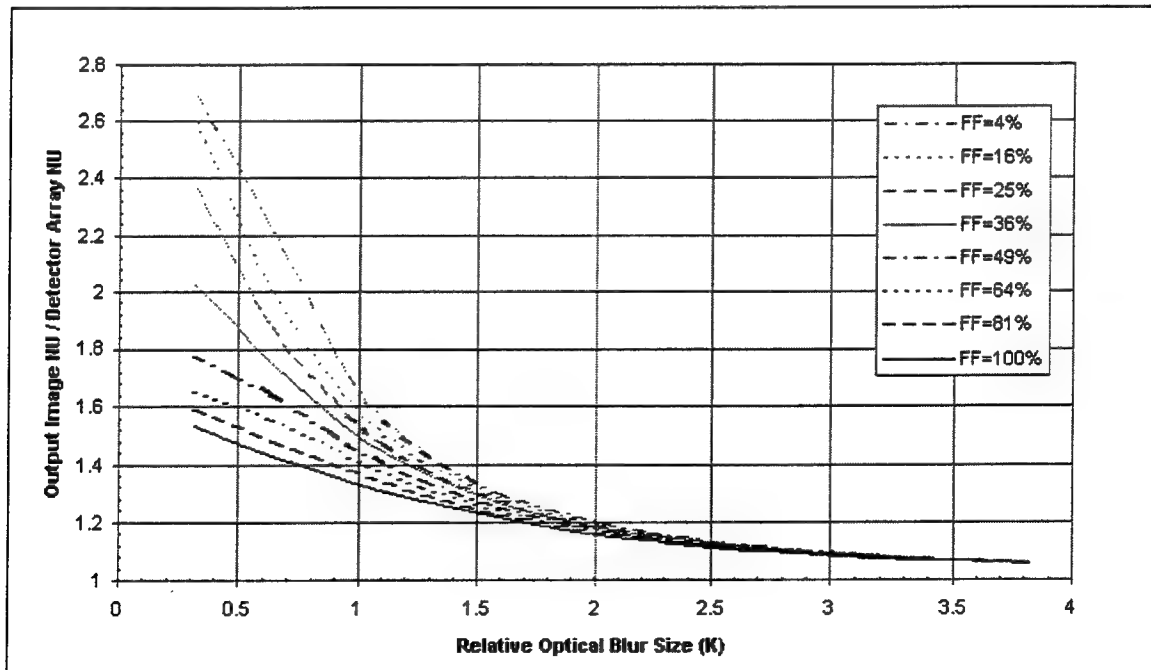


Figure 6: Output NU vs. relative optical blur size for different fill factors. Sampling ratio 4:1, projector NU/detector NU is 5, and emitters symmetrically centered over detectors.

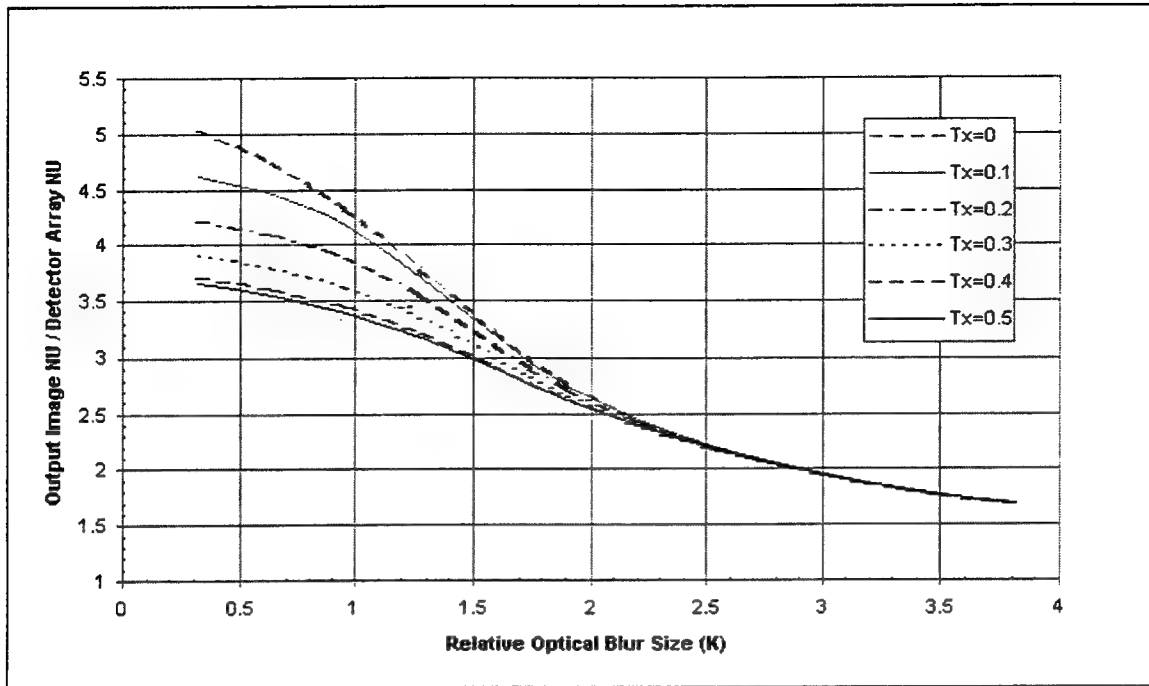


Figure 7: Output image NU vs. relative optical blur size for different alignments. Sampling ratio is 1:1, projector NU/detector NU is 5, and fill factor is 100%.

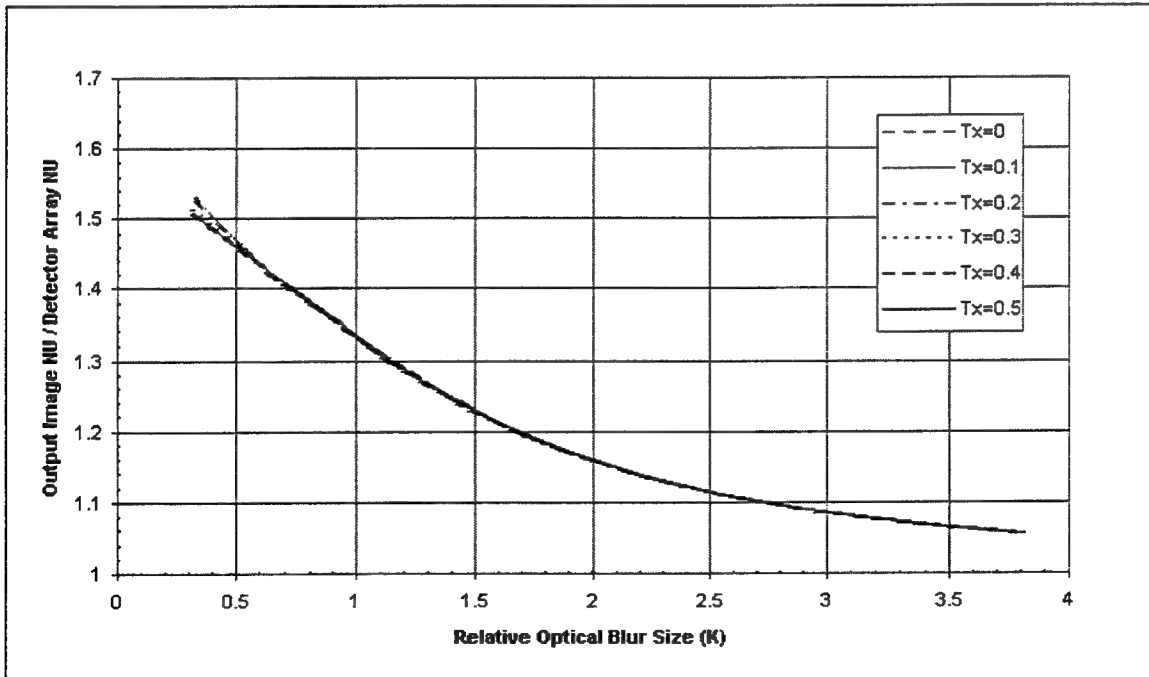


Figure 8: Output image NU vs. relative optical blur size for different alignments. Sampling ratio is 4:1, projector NU/detector NU is 5, and fill factor is 100%.

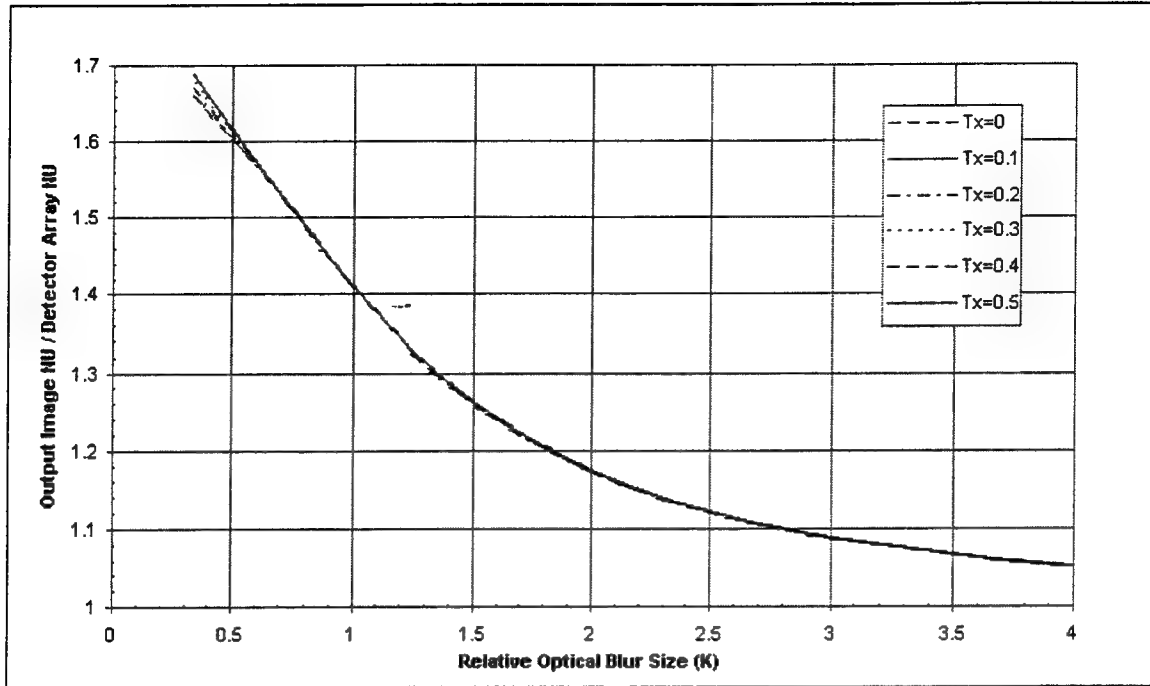


Figure 9: Output image NU vs. relative optical blur size for different alignments. Sampling ratio is 4:1, projector NU/detector NU is 5, and fill factor is 64%.

Conclusion

We have derived an equation (16) that predicts analytically how the non-uniformity of the projector will impact the uniformity of the output image. In order to be applicable to the widest range of possible systems, the equation is written in terms of the ratio of the projector's non-uniformity to the detector array's non-uniformity. The most significant parameter in determining the output image non-uniformity is the sampling ratio (linear number of emitters per detector), which sets an upper limit on the output non-uniformity, as given in Eq. (10). This upper limit decreases dramatically with an increase in sampling ratio n . Other parameters, such as relative optical blur size, fill factor of the detector array, and alignment of the emitters relative to the detectors (also called registration), have a lesser impact on the output image uniformity. In order to account for these parameters, it was necessary to develop a weighting function that determines the contribution of each emitter to the flux incident on a particular detector. The necessary integrals could not

be done analytically, so a computer program was written to obtain approximate values for the necessary weighting function.

The most important of the lesser parameters is the relative optical blur size. As intuition would suggest, the larger the optical blur, the smaller the output image non-uniformity. The reason is simply that as the blur increases each detector "sees" more emitters and so the differences between the emitters tend to balance out. The effect is quite dramatic for large blur, as illustrated in Figs. (3-4), but large blur also has a negative impact on things such as resolution. Fill factor and alignment have relatively little impact, especially as the blur is increased, as shown in Figs. (5-9). As can be seen from these figures, if the blur is large enough so that more than one detector is needed to collect 83.9% of one emitter's radiation ($K > 1$), then fill factor and alignment make relatively small differences in the output image uniformity.

This effort has provided a statistical model which predicts the impact of a projector's non-uniformity on output image uniformity. The contribution of the sampling ratio, the relative optical blur size, the alignment of emitters with the detectors, and the fill factor of the detector array can all be quantitatively predicted. It is clear from this work that the best way to reduce output non-uniformity, other than improving the uniformity of the projector, is to increase the sampling ratio.

Despite the progress that has been made, there are several more factors that should be considered. Spatial droop (also called busbar robbing) occurs when bright images are being projected by the emitter array.[5] Another issue is the accuracy of the measurement of the projector array's non-uniformity. The accuracy can be compromised both by measurement limitations and by temporal changes.

One important restriction to the model developed in this paper is the requirement that the sampling ratio n always be an integer. It is easy to show that a non-integer sampling ratio will cause a regular pattern of non-uniformity even for a perfectly uniform emitter array and a detector array with 100% fill factor. Intuitively, the amplitude of this pattern will decrease as the relative optical blur is increased. This non-uniformity is different in nature from the non-uniformity discussed in this paper and should be explored in depth.

4 Acknowledgments

The authors are grateful for many productive conversations with Lawrence Jones, Walt Krawczyk, and Eric Olson of Science Applications International Corp. and Dave Flynn and Steve Marlow of SeeTec. We also appreciate the support of WISP program manager Robert Stockbridge and KHILS program manager Lee Murrer, both of WL/MNGI.

This work was performed at the Armament Directorate, Wright Laboratory, Eglin AFB, and was funded by summer research fellowships provided by the Air Force Office of Scientific Research, Bolling AFB.

References

1. D.L. Garbo, E.M. Olson, C.F. Coker, and D.R. Crow, "Real-time Three Dimensional Infrared Scene Generation Utilizing Commercially Available Hardware," The 10th Annual International Aerospace Symposium, April 1996.
2. L.E. Jones, R.G. Stockbridge, A.R. Andrew, W.L. Herald, and A.W. Guertin, "Characterization Measurements of the Wideband Infrared Scene Projector Resistor Array (Part II)," presented at SPIE, Orlando, Florida, April 1997.
3. L.E. Jones, E.M. Olson, R.L. Murrer, and A.R. Andrew, "A Simplified Method for the Implementation of Nonuniformity Correction on a Resistor Array Infrared Scene Projector," presented at SPIE, Orlando, Florida, May 1997.
4. W.L. Wolfe and G.J. Zissis, Eds., *The Infrared Handbook*, prepared by the Infrared Information Analysis Center, Ann Arbor, MI, pg. 8-28. (1989)
5. A.P. Pritchard, M.A. Venables, and D.W. Gough, "Output accuracy and resolution limitations in resistor array infra-red scene projection systems," *Proceedings of SPIE*, vol. 2742, p. 15.

VISUALIZATION AND TWO-COLOR DIGITAL PIV MEASUREMENTS IN CIRCULAR AND SQUARE COAXIAL NOZZLES

**Jason W. Bitting
Dr. Dimitris Nikitopoulos
Department of Mechanical Engineering**

**Louisiana State University
2508 CEBA
Baton Rouge, LA 70803**

with

**Dr. Sivaram Gogineni
Innovative Scientific Solutions, Inc.
WPAFB**

**Final Report for:
Graduate Student Research Program
Wright Laboratory**

**Sponsored by:
Air Force Office of Scientific Research
Bolling Air Force Base, Washington D.C.**

and

**Wright Laboratory
Wright-Patterson Air Force Base, Dayton OH**

and

NASA EPSCoR Program and the LA BoR LEQSF

August 1997

VISUALIZATION AND TWO-COLOR DIGITAL PIV MEASUREMENTS IN CIRCULAR AND SQUARE COAXIAL NOZZLES

Jason W. Bitting
Dr. Dimitris Nikitopoulos
Department of Mechanical Engineering
Louisiana State University

Abstract

The results of Laser-Sheet Visualizations carried out in cold air flows generated by coaxial, non-circular jets are presented. Various geometry combinations employing square, triangular, lobed, and circular nozzles have been examined. The flows are at modestly high Reynolds numbers between 14,000 and 29,000. The inner-to-outer jet velocity ratio λ^{-1} varies from 0.15 to 0.22 to 0.3. The visualizations were carried out on vertical planes and cross-stream (horizontal) planes, using a pulsed laser sheet and seeding the air flow with TiCl_4 . Images were recorded with a high-resolution (3000x2000 pixels) CCD array camera. Time-averaged visualizations were used to qualitatively assess shear layer growth in the near field of the jets. Comparisons between the circular and non-circular jet configurations indicated considerable mixing enhancement when non-circular nozzles were used. The visualizations revealed interesting interactions between the inner and outer non-circular shear layers in the near field. The interaction regions of inner and outer jet shear layers are characterized by more "wispy," stretched-out structures, or bulges in the shear layer, as seen in the cross-stream planes, than those observed in the regions where such interaction is absent. The presence of large-scale periodic structures is evident near the origin of the shear layers, although not as clear as in lower Reynolds number flows. Internal unmixed regions diminished with decreasing velocity ratio and at the low velocity ratios strong evidence of unsteady re-circulation and back-flow was observed at the end of the core of the inner jet manifested by oscillating mushroom vortex pairs. Two-color digital PIV measurements were made on the centerplane of the circular and square jets at a Reynolds Number of 19000 for the coflow air and a jet velocity ratio of 0.3. A time increment of 20 μsec was used between the green and red laser pulse to provide sufficient resolution of the velocity vectors. Scans across the square jet were made with the DPIV system. Aluminum oxide was used as the seeding particles for the DPIV images.

VISUALIZATION AND TWO-COLOR DIGITAL PIV MEASUREMENTS IN CIRCULAR AND SQUARE COAXIAL NOZZLES

Jason W. Bitting

1.1 Introduction

Coaxial nozzles are an integral part of many engineering systems where mixing of streams of different fluids is required. They are used to provide the mixing between fuel and oxidizer in combustors of propulsion systems and power producing gas turbine systems as well as waste combustion and incineration systems. A properly designed nozzle will efficiently mix the air and fuel while providing the best overall combustion parameters. Much research has been performed aimed at increasing the overall efficiency of the gas turbine combustion systems, reduce harmful emissions, and reduce the overall system size. Control of coaxial nozzles used in combustors, either passively or actively, is the interest of current research. The present work is related to the application of passive forcing by employing non-circular coaxial nozzles. Single non-circular nozzles have been shown to have better mixing characteristics than their axisymmetric counterparts. Therefore, combinations of such nozzles into coaxial configurations is promising. This report presents a summary of flow visualization and DPIV measurement results from non-circular coaxial nozzles for the first time.

1.2 Background

1.2.1 Coaxial Nozzles

Many studies have been done on single planar circular jets. These jet configurations are well understood and pose little difficulty to current numerical simulations available to design engineers. Of more importance are coaxial circular jets which have complex vortices produced as the jet develops and the shear layers interact. The vortices help produce the necessary large-scale mixing and small scale enhancement which are both needed for efficient combustion of a fuel. Work done by Ko (1976, 1978) provides information about the mean velocity and turbulence fields of coaxial jets with different inner to annular air velocity ratios, λ^{-1} . More recent studies on coaxial jets have shown that the development of large-scale coherent structures down stream from the exit depends on the exit shear layer thickness and other initial conditions. A flow visualization study by Dahm (1992) nicely shows the large-scale vortical structures and their interactions for various λ^{-1} . Higher entrainment rates of surrounding air are obtained for certain velocity ratios, λ^{-1} , so that the conditions may be optimized to give the best fuel/air mixing for combustion.

Tang (1993) has performed further research on the coaxial jet for the case where $\lambda^{-1}=0.3$. Again, the initial region of the jet plays an important role in the downstream formation of large scale structures. There were also important processes which developed through the interaction of vortices manifesting in incomplete coalescence and amalgamation processes by the vortices.

1.2.2 Swirl Flow Nozzles

1.2.2 Swirl Flow Nozzles

In practical applications swirl is added to the flow through the nozzle in order to stabilize the flame in the combustor. A review of swirl flow in combustion by Lilley (1977) shows that the swirl has the benefits of modifying the jet growth rate while increasing the entrainment rate. The flame size, shape, and stability also are modified and enhanced through the use of swirl flows. Panda (1994) also show that the use of swirl leads to reduction in the growth of unstable disturbances which would tend to destabilize the combustion flame. A coaxial jet with swirl flow is also examined by Ben-Yeoshua (1993) with flow visualization showing the complexities of the flow. In this study of non-circular coaxial nozzles, we will not introduce swirl (that is something to do in the future) so we will not elaborate on the relevant background.

1.2.3 Nonconventional Jets

Of current interest are nonconventional jets and their unique characteristics of vortex formation by self-induction, higher entrainment rates, and passive control of the jet flow. Four configurations have been researched to date for a single jet: 1) Rectangular/Square, 2) Triangular, 3) Elliptic, 4) Crown-Shaped and Nonplanar Exit.

The rectangular and square nozzles produce non-circular vortex rings at the exit which then deform and lead to a switching of the jet axis. The axis switching is due largely to the self-induction produced by the sharp corners of the nozzle and depends on the initial velocity profile characteristics. Early studies by Sforza (1966), Trentacoste (1976), and duPlessis (1974) showed the axis switching by the square jets but no insight was given to the underlying fundamental behavior of the square jet vortical interactions. Quinn (1988) showed that for a square jet of the same hydraulic diameter as a circular jet, the square jet had a faster spreading rate at similar distances from the jet exit as compared to the circular jet. A detailed numerical simulation followed by experimental investigation illustrated that the axis switching is due to self-induction governed by the Biot-Savart Law with hairpin vortices developing along the diagonals of the square jets (Grinstein 1991). A phenomenon of off center velocity peaks has also been observed by Quinn (1992) for a square slot orifice exit. A further study by Grinstein (1995) on reactive square jets showed higher entrainment rates where the vortices roll up in the flow field.

The triangular jet has also been investigated by Schadow (1988). The flow results were different for triangular orifice exits or pipe/nozzle emphasizing the importance of initial conditions. A numerical and experimental study by Koshigoe (1988) explained the differences and formulated conditions for which axis switching occurs. An enhancement in the fine scale mixing and combustion stability in the corner regions of the triangular jet were verified by Schadow (1990). Large scale mixing was accomplished on the flat sides with reduced pressure oscillations as compared to the circular jet. Fuel injection in the corners of the jet produced the best combustion results for the triangular jet.

Elliptic jets have also been studied, and have exhibited the same axis switching and self-induction as found in triangular and rectangular jets. Gutmark (1986) produced flow visualization of the elliptic jet with axis switching, resulting in entrainment rate of 8 times higher than a circular jet (see also Koshigoe, 1988).

As passive control devices, nonconventional nozzles such as a stepped shape or crown shape exit geometry have been studied. Wlezein (1986) showed that a stepped circular nozzle and a circular nozzle with a slanted exit

the angle cut, the jet could be passively controlled. A crown-shaped nozzle produces similar effects since the shear layers differ in thickness at the bottom of the crown as compared to the point of the crown. Different entrainment rates were shown by Longmire (1992) to depend upon the azimuthal location relative to the peaks of the crown. The vortices exited in a square shape with a secondary *X* or cross pattern evident in the flow structure of vortices.

2 Experimental Setup and Method

A circular coaxial nozzle with an inner diameter of 0.6 inches and an outer diameter of 1.5 inches was used as the baseline nozzle for the flow study. With the above dimensions, the hydraulic diameter of the inner jet and outer jet is 0.6 inches and 0.75 inches respectively. For the other nozzles, such as the square geometry, the hydraulic diameters are the same as for the circular jet so that the velocities would not have to be scaled to compare the jet flows between the circular jet and the other jet geometries. A top view of the circular and square nozzles is shown in Figure 1, followed by a picture of the jet facility in Figure 2. The orientation of the inner square jet can be changed with respect to the outer square jet to give a centerline offset of 22.5° or 45° .

The air flow through the outer nozzle was varied between the following Reynolds numbers based on previous work for coaxial nozzles by Ko. The mass averaged velocity at the exit of the jet is given in parenthesis.

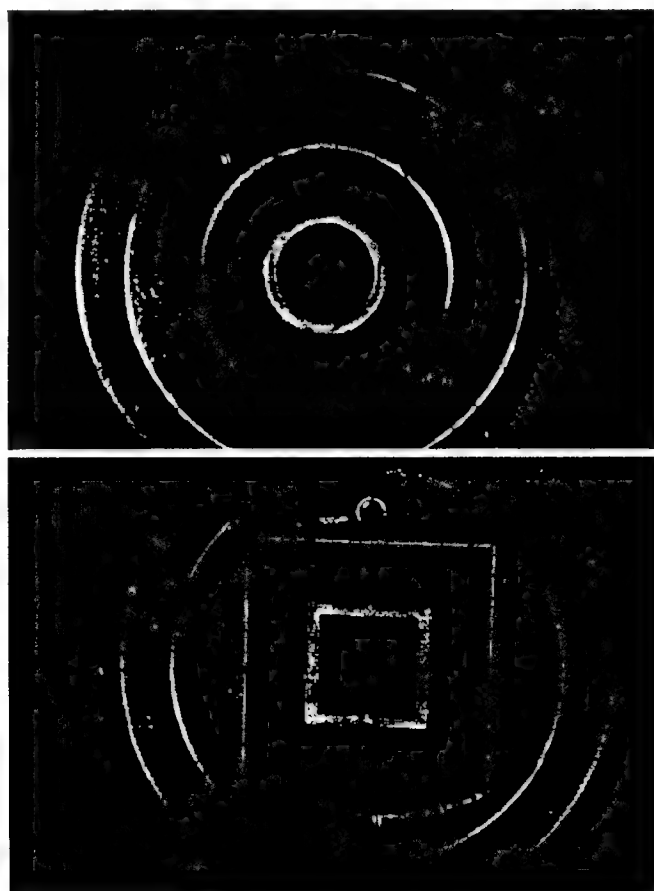


Figure 1
Circular and Square Coaxial Nozzles

$Re_o=14000(11 \text{ m/sec})$
 $Re_o=19000(14.8 \text{ m/sec})$
 $Re_o=24000(18.7 \text{ m/sec})$
 $Re_o=29000(22.5 \text{ m/sec})$

The velocity ratios for the inner jet were varied between 0.15, 0.22, and 0.3 for each of the above Reynolds numbers.

Flow visualization on the air flow was performed using $TiCl_4$ as seed in the dry coflow air, with water vapor in the inner jet air flow. Instantaneous and time averaged cuts were made with a laser sheet from a YAG laser pulsing at 10 Hz. Figure 3 shows the laser sheet location for the vertical cuts for several different geometries of the nozzles. A Kodak CCD camera captured the images with the shutter open for 2 seconds for the time averaged images. Horizontal cross flow cuts were made at heights of 1", 1.5", and 3" above the exit of the jet for the circular and square jet configurations. These heights correspond to distances of 2/3, 1, and 2 outer jet diameters or 1.67, 2.5, and 5 inner jet diameters from the nozzle exit.



Figure 2
Jet Facility

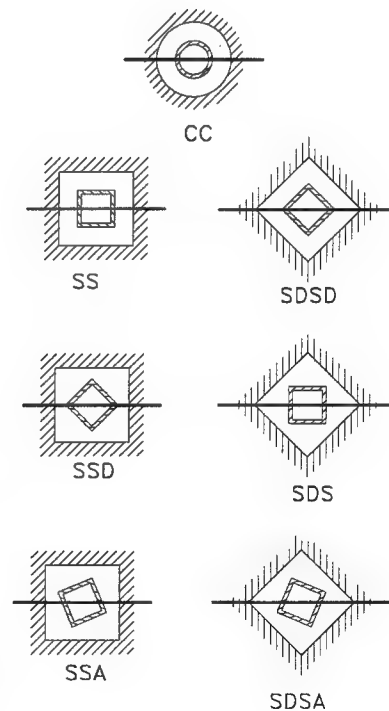


Figure 3
Laser Sheet Cuts

3 Flow Visualization

The flow visualization shown in figures 4 through 12 use TiCl_4 as the seed with aluminum oxide (Al_2O_3) particles of $d=5\mu\text{m}$ being used as the seed in figures 13 through 17.

The flow visualization shown in this report is only a brief presentation of the work done at WPAFB, but a large volume of images was obtained for the various configurations. The conditions tested will be outlined here, but will not be further discussed beyond what is included in the figures in this report.

Smoke visualization was done on the nozzles for all of the combinations of the square and circular coaxial jets for all of the flow conditions. Scans across the jet were also made with the smoke visualization. The inner jet only was seeded with Al_2O_3 particles for the square and circular jets for all of the flow conditions. The coflow dry air was seeded with TiCl_4 with moist air in the jet flow to do visualizations for all of the configurations at $\text{Re}_0=19000$ and $\lambda=0.3$. The square and circular coaxial nozzles were seeded with TiCl_4 in the coflow air with moist air in the jet flow for all of the flow conditions and combinations. Scans across the square jet were made for selected velocity conditions. The seeding was switched to TiCl_4 in the jet flow with moist air in the coflow for the square and circular coaxial nozzles with $\text{Re}_0=19000$ and a jet flow ratio of $\lambda=0.3$ and 0.22 .

Both jets were seeded with Al_2O_3 particles for the DPIV measurements. All configurations were tested at the condition of $\text{Re}_0=19000$ and $\lambda=0.3$. More time was spent on taking data for the square coaxial jet with the sides parallel and the circular jet to make mean-flow data comparisons along the centerline of both configurations. Other DPIV images for the square jet were made for the remaining velocity conditions, with seeding both air flows, the jet flow only, the coflow only, and in some cases the ambient air.

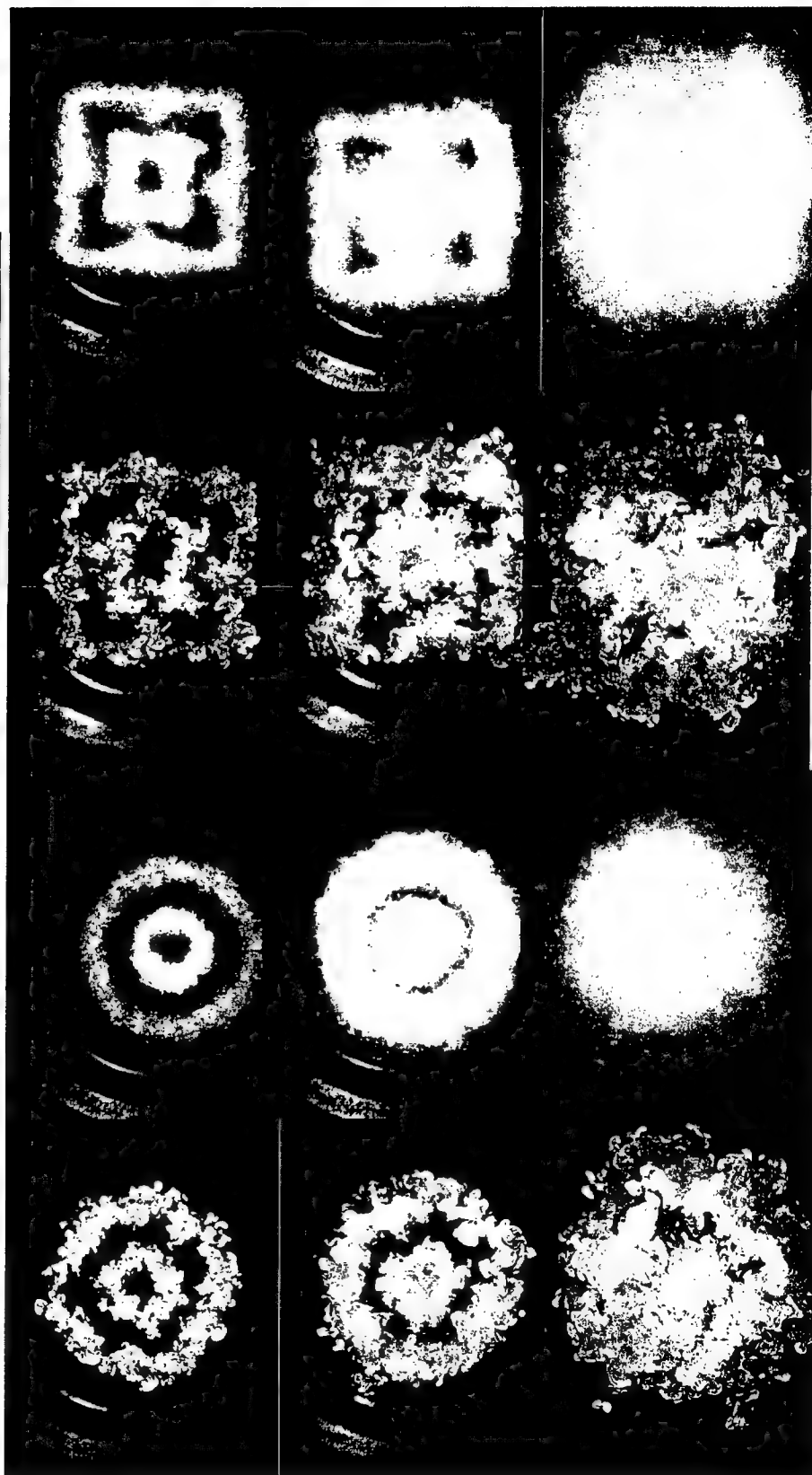
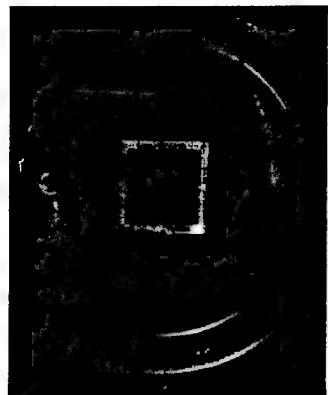


Figure 4 $Re_0=19000$ $\lambda=0.3$ $z/d_0=2/3, 1, 2$

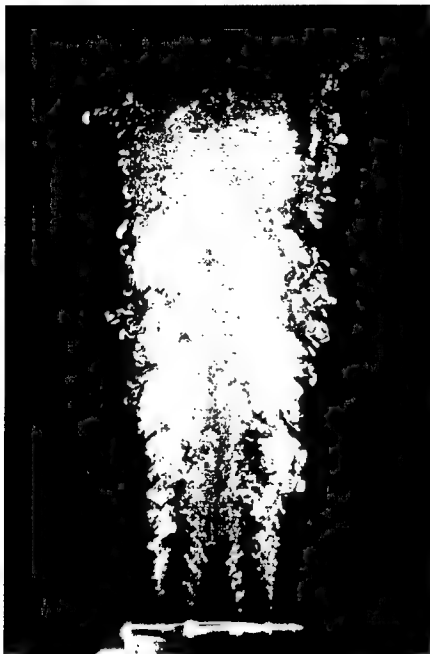


Figure 5
Circular Coaxial Jet
 $Re_0=29000$ $\lambda=0.3$



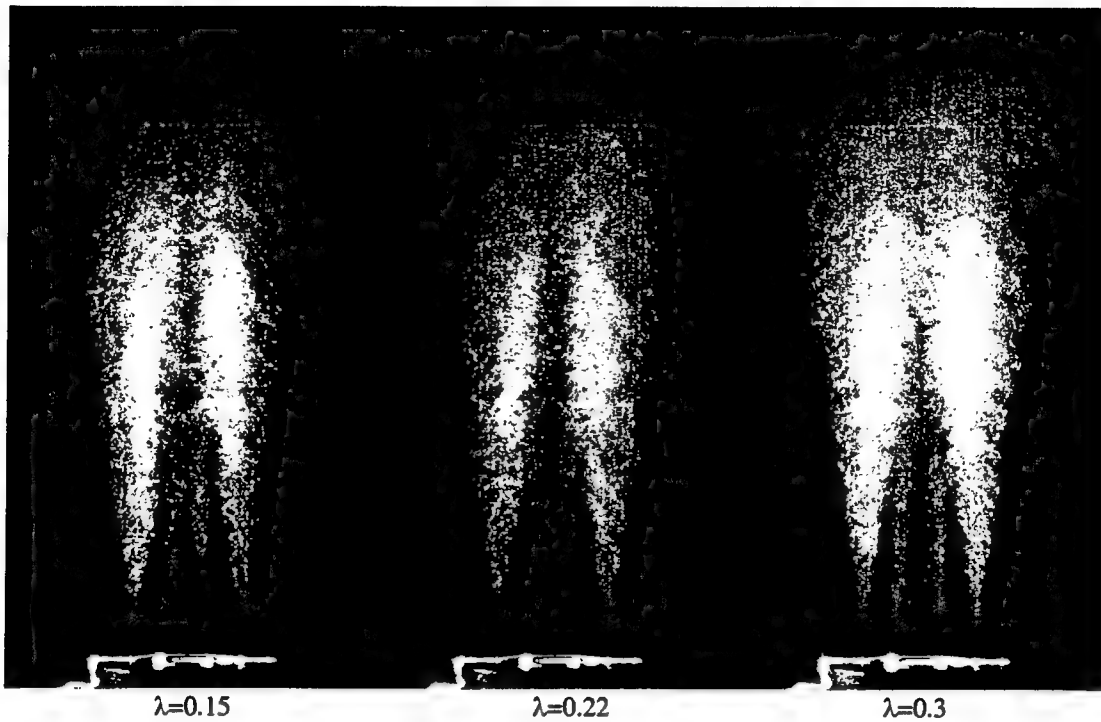
Figure 6
Square Coaxial Jet
 $Re_0=29000$ $\lambda=0.3$



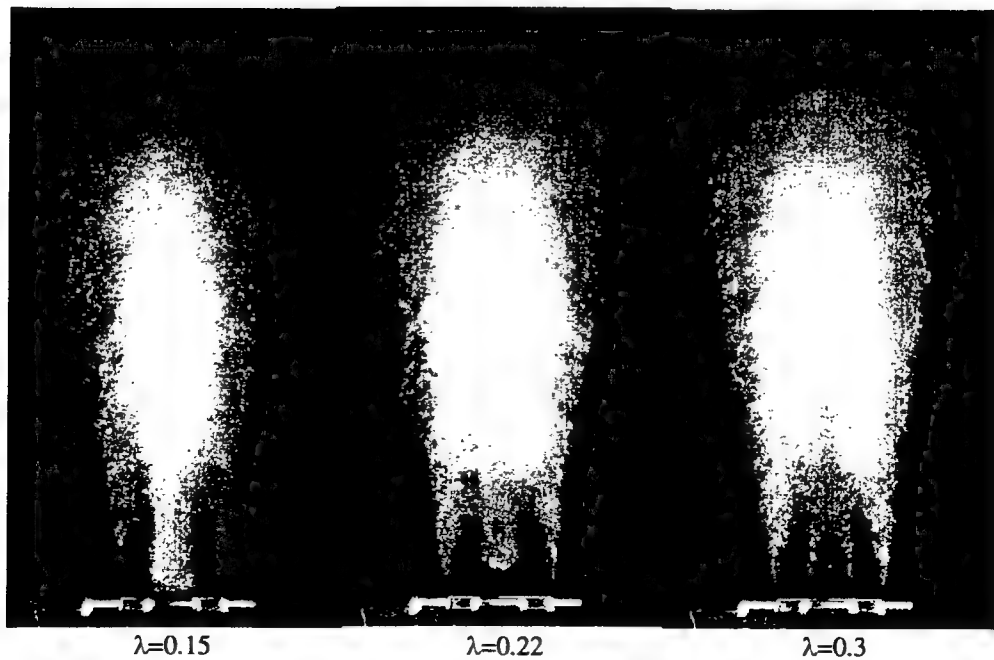
Figure 7
Circular Coaxial Jet
 $Re_0=19000$ $\lambda=0.3$



Figure 8
Square Coaxial Jet
 $Re_0=19000$ $\lambda=0.3$



$\lambda=0.15$ $\lambda=0.22$ $\lambda=0.3$
Figure 9
 Circular Coaxial Jet
 $Re_0=29000$



$\lambda=0.15$ $\lambda=0.22$ $\lambda=0.3$
Figure 10
 Square Coaxial Jet
 $Re_0=29000$

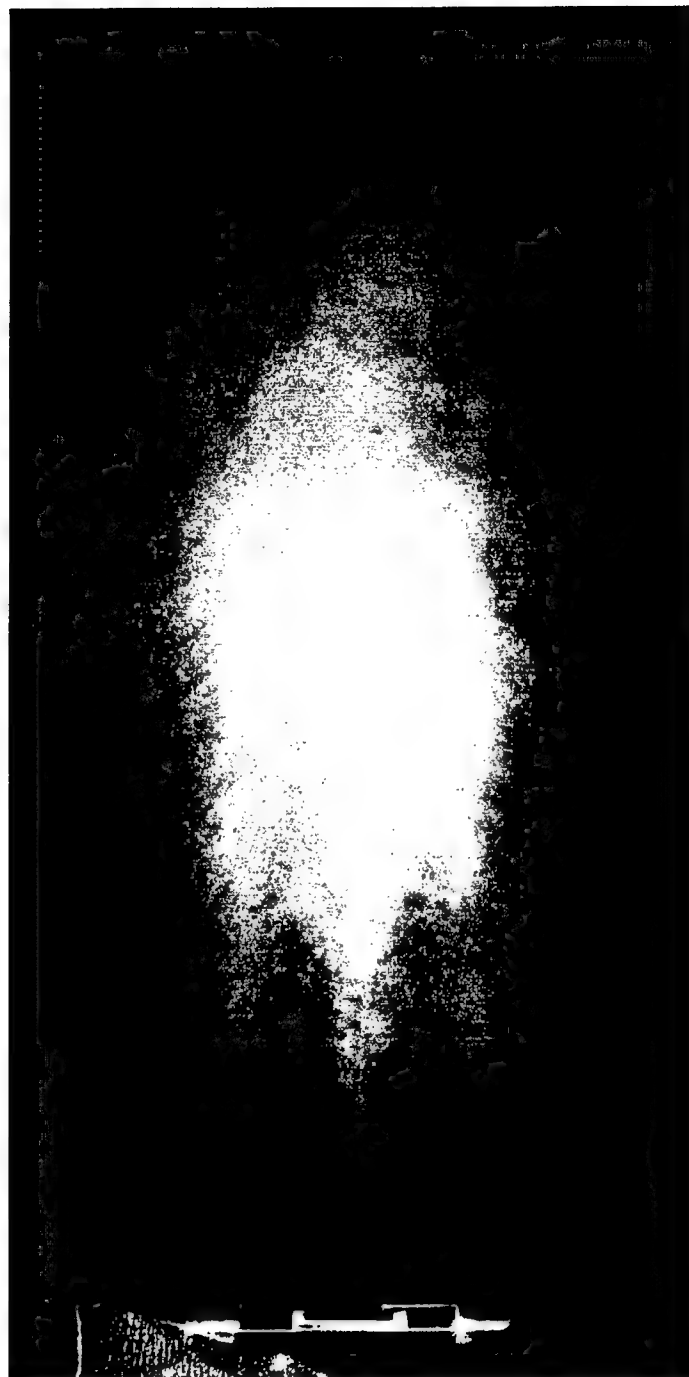
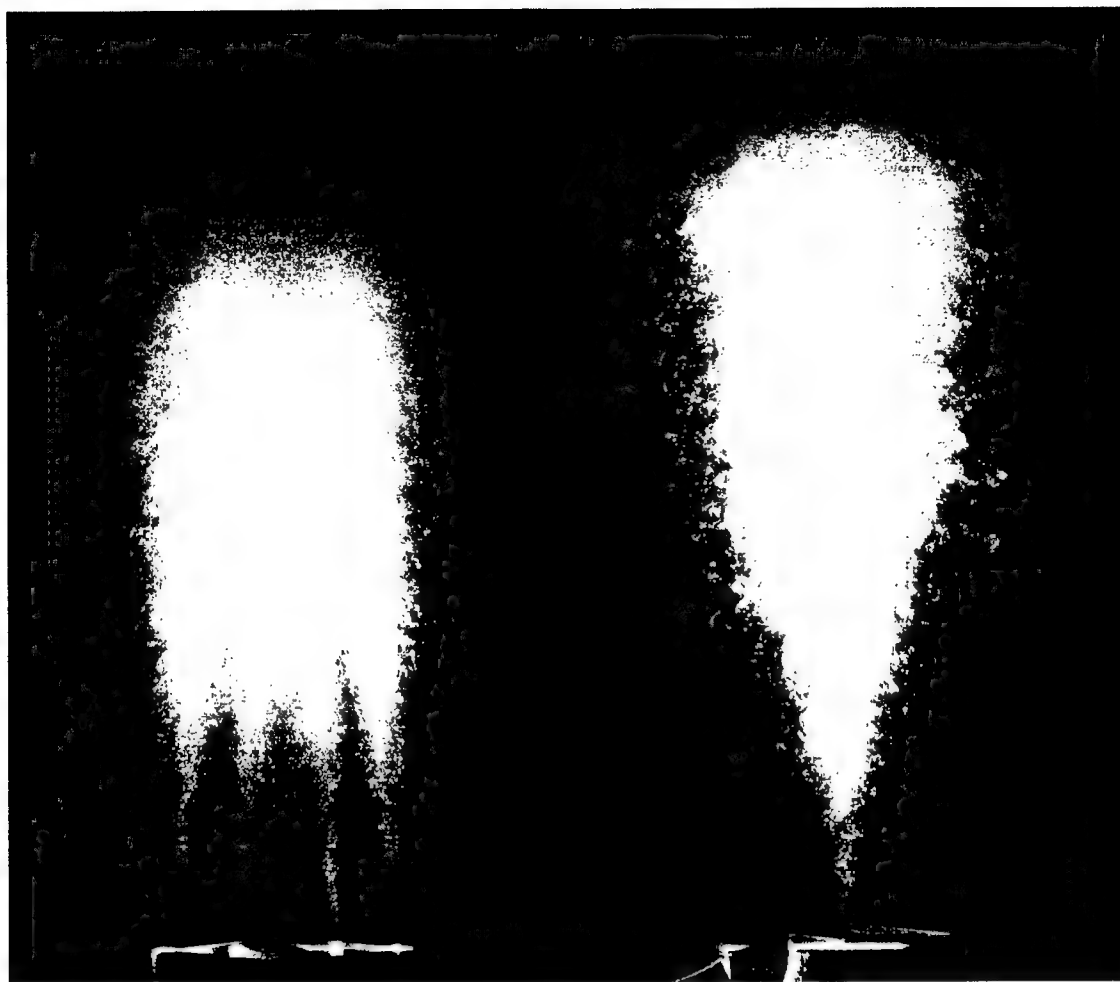


Figure 11
Square Coaxial Jet
 $Re_0=29000$ $\lambda=0.3$
 $Y=13.97\text{mm}$



$\theta=45^\circ$

$\theta=45^\circ, r=26.9\text{mm}$

Figure 12
Square Coaxial Jet
 $Re_0=29000 \quad \lambda=0.3$

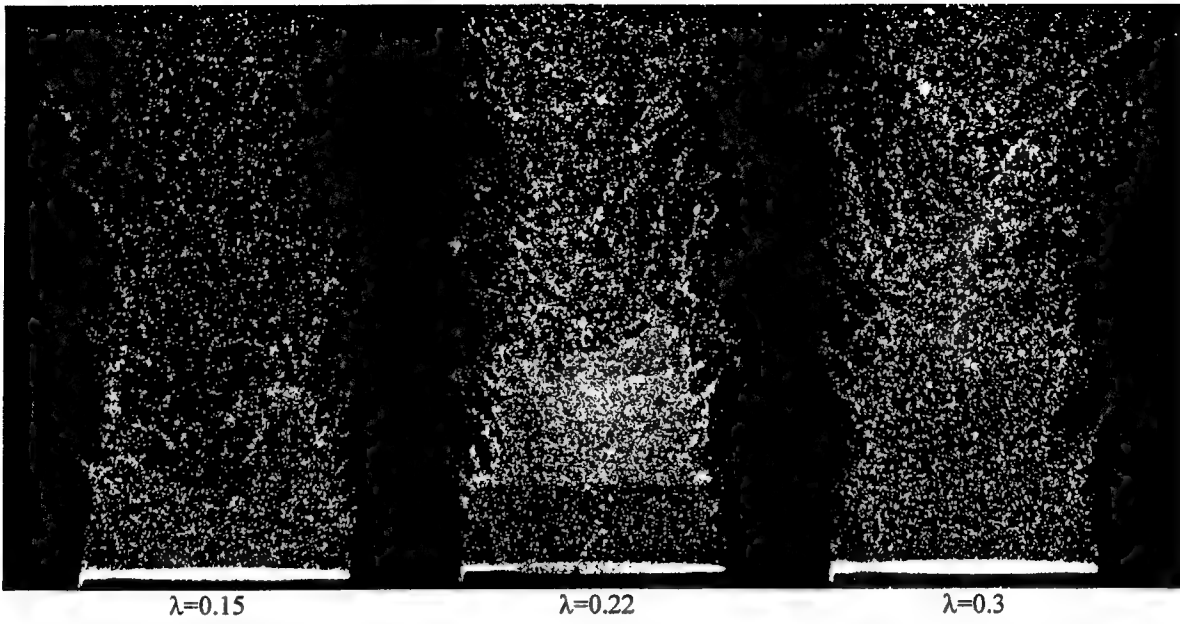


Figure 13
Circular Coaxial Jet
 $Re_0=29000$

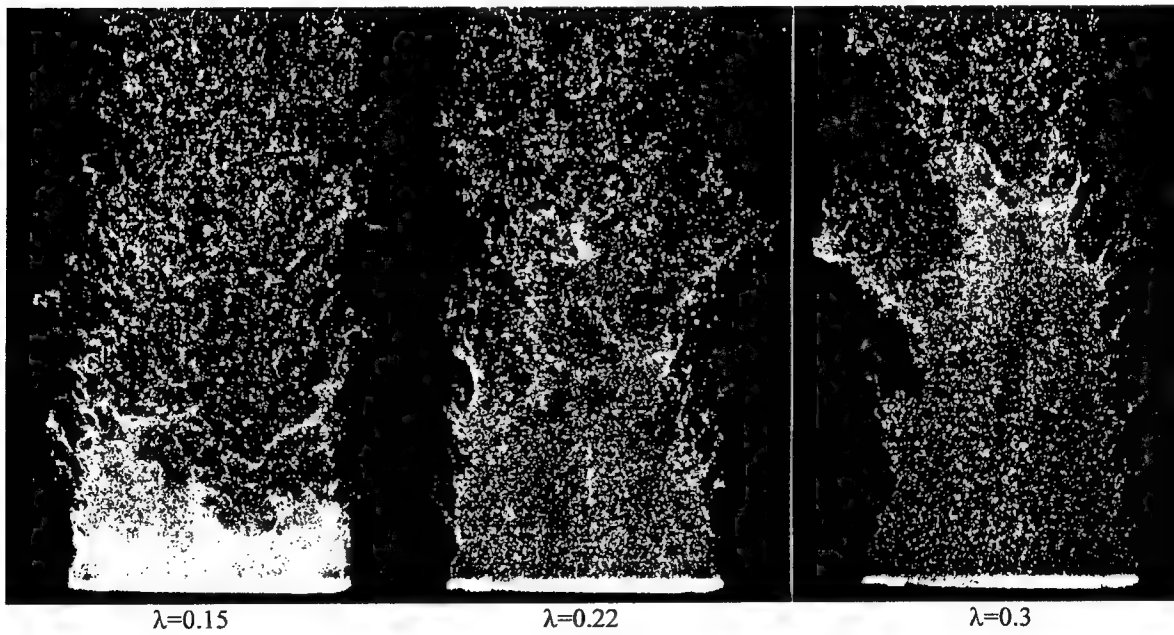


Figure 14
Square Coaxial Jet
 $Re_0=29000$

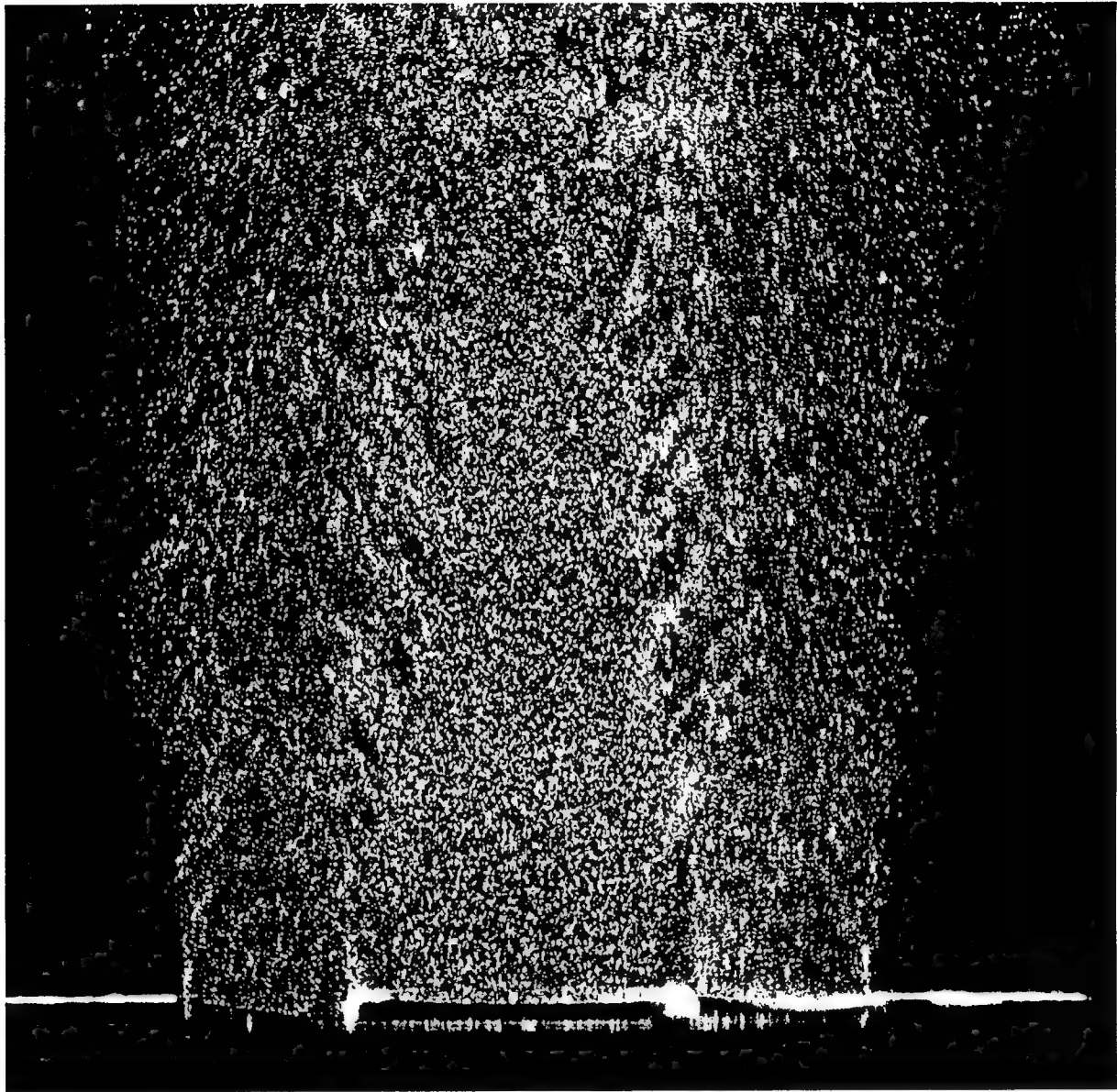


Figure 15
Circular Coaxial Jet
 $Re_0=19000$ $\lambda=0.3$

Coaxial Circular Jet
 $Re=19000$
Velocity Ratio $\lambda=0.3$
Centerline Profile

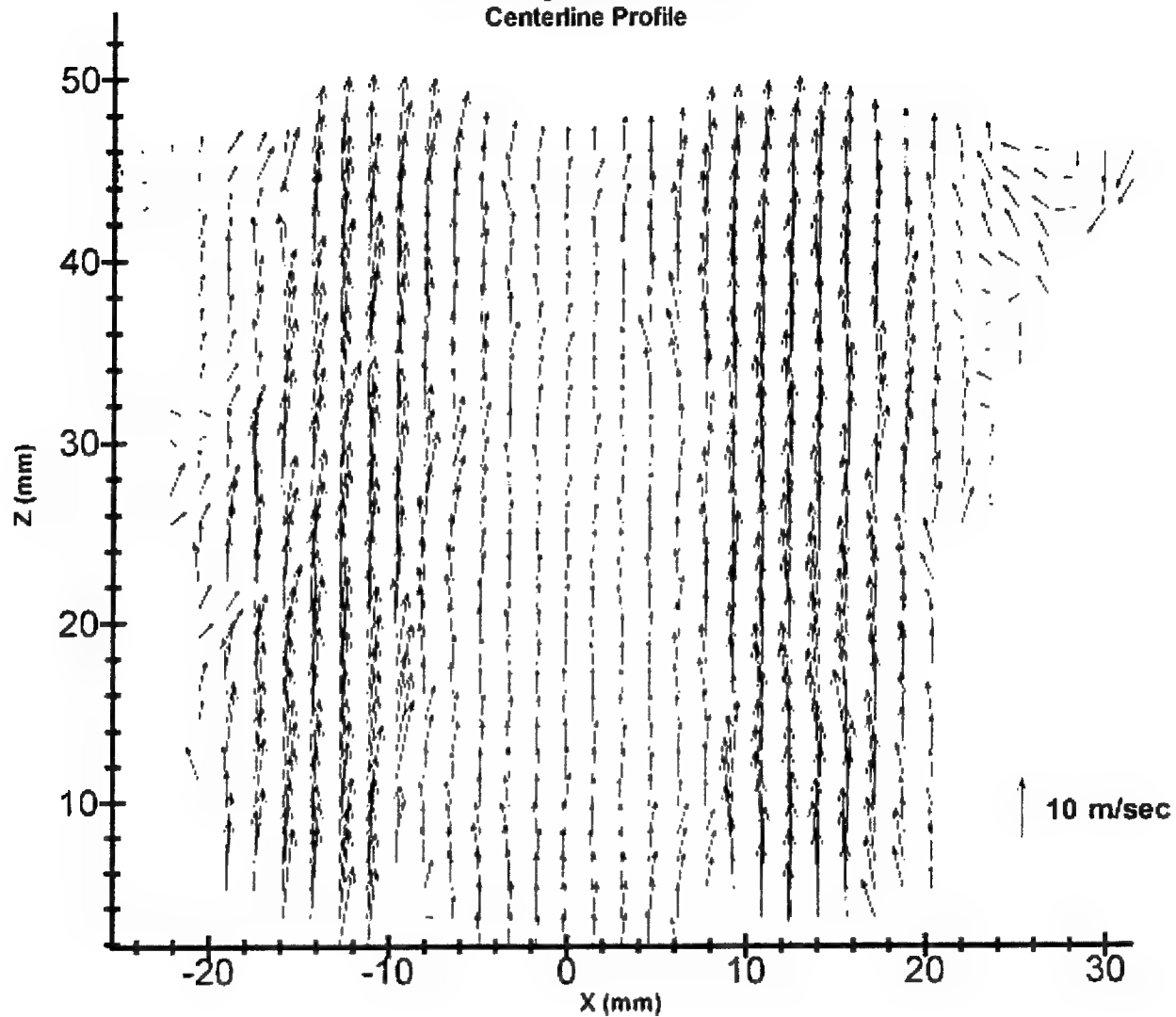


Figure 16
PIV Data

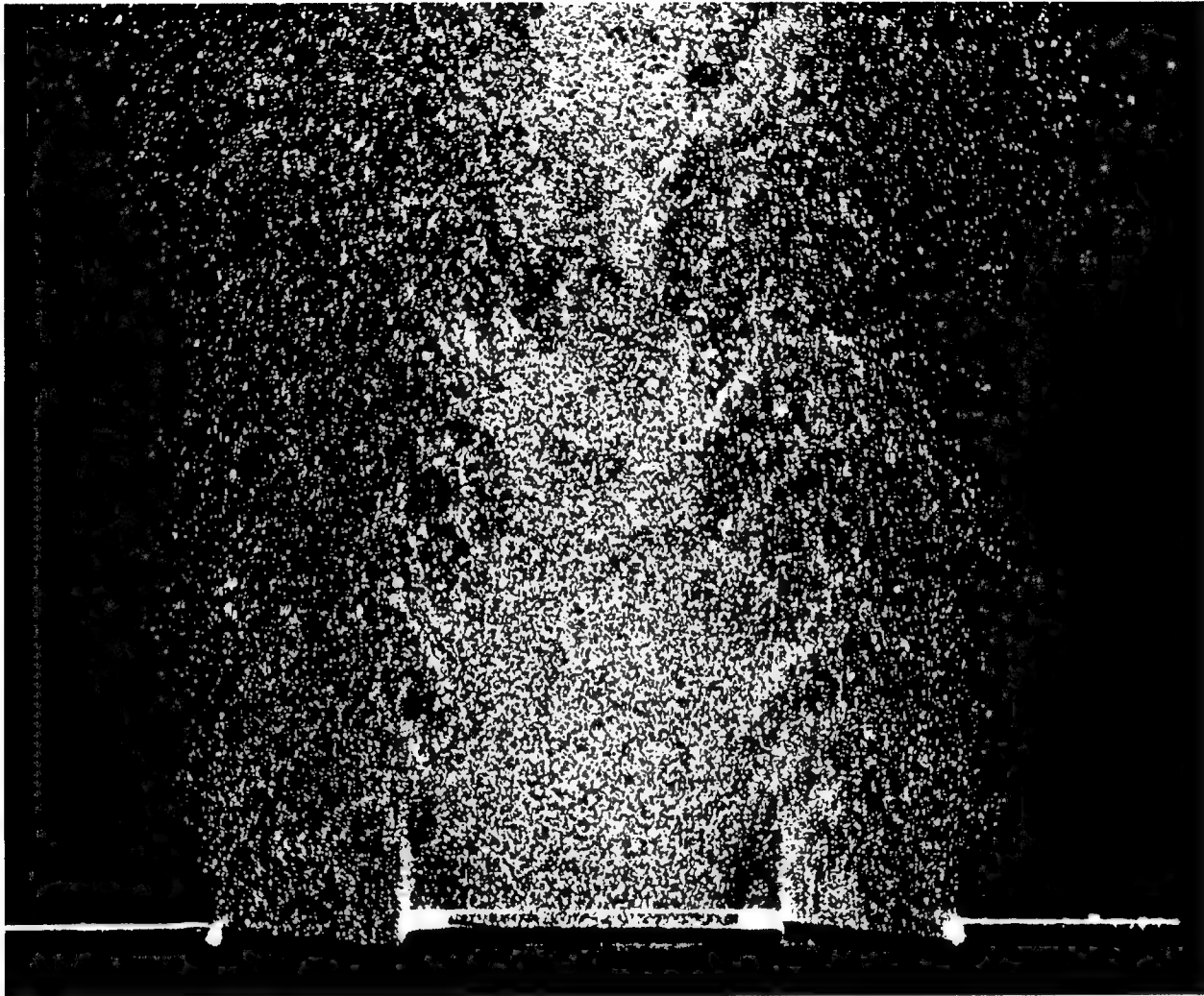


Figure 17
Square Coaxial Jet
 $Re_0=19000$ $\lambda=0.3$

Square Coaxial Jet
Re=19000
Velocity Ratio $\lambda=0.3$
Centerline Profile

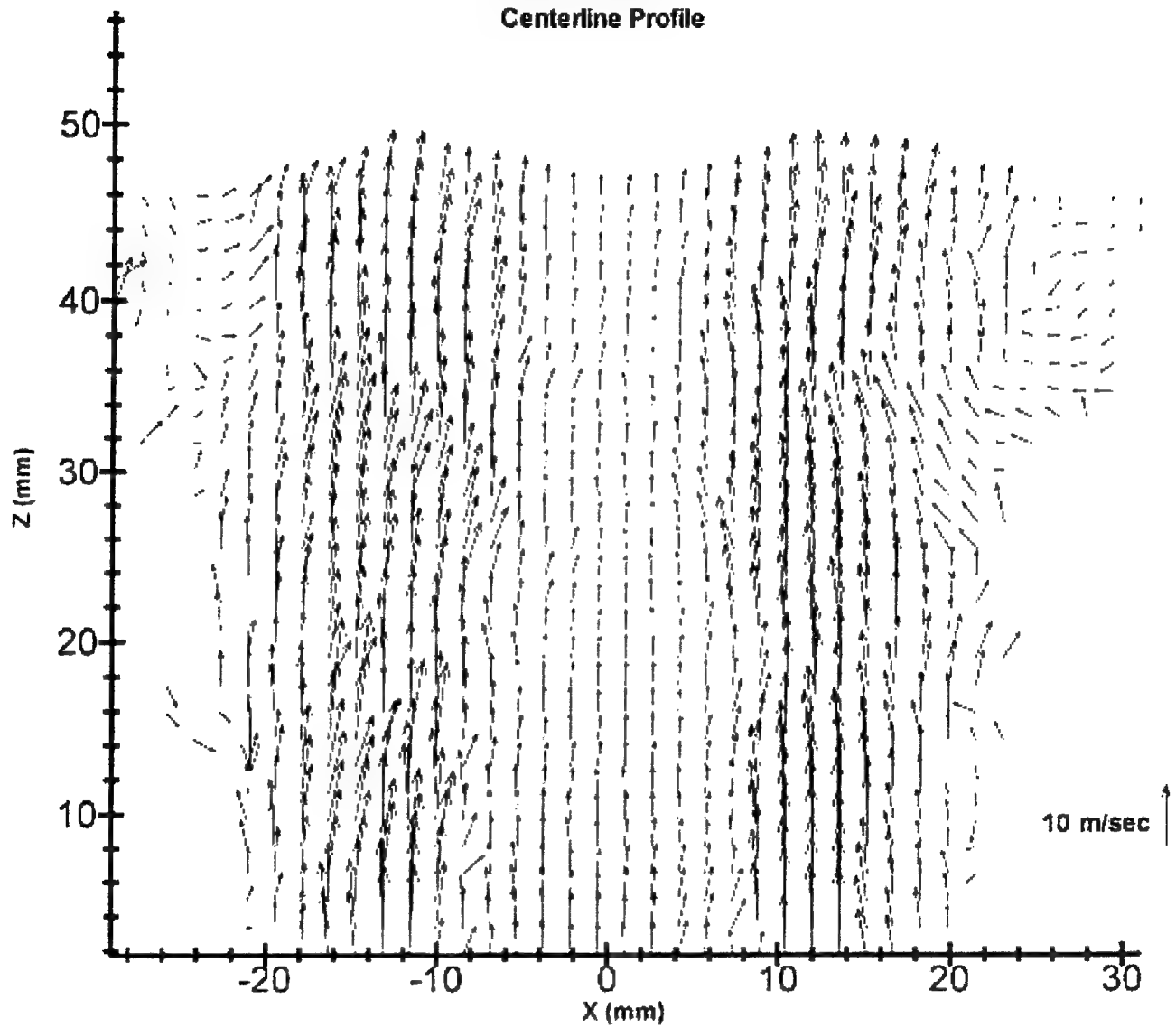


Figure 18
PIV Data

4 Some Conclusions

From the images shown in the previous figures, several interesting features should be recognized and noted. In the horizontal cuts in Figure 4, the shear layer of the square jet has developed a bulge in the sides near the center of each side. The bulge is an indication of greater interaction between the jet shear layers on the flat sides. Although axis switching is a phenomenon observed in single square jets, no conclusion about the presence of axis switching in the square coaxial jet can be made at this time. Supplemental hot-wire measurements will focus on quantifying the presence of axis switching in the coaxial square jet. The bulge mentioned above is clearly shown in the time averaged vertical cut in Figure 6, as the shear layer of the outer jet grows more rapidly toward the central jet for the square coaxial nozzles as compared to the circular jet which is shown in Figure 5. There is also an increased growth of the shear layer for the square jet at the interface between the coflow air and the ambient air, as indicated by a smaller slope at the edge of the jet in the time averaged image in Figure 6. The circular jet in Figure 5 shows a steeper slope at the edge of the jet shear layer with the ambient air. A close-up image of the circular and square coaxial jet is shown in Figure 7 and 8. These figures clearly show the increased growth of the outer shear layer inward toward the inner jet for the square nozzle in the time averaged image. In the instantaneous image in Figure 7, a mushroom vortex is ejecting from the outer shear layer into the ambient air. These vortex bursts were observed sporadically throughout all of the TiCl_4 flow visualizations due to the highly turbulent and three-dimensionality of the air flows.

Comparisons of the velocity ratio effect on the jet flow are shown in Figures 9 and 10. The lower the velocity ratio of the inner jet, the shorter the potential core region of the inner jet. A strong recirculating region at the exit of the inner jet was observed for the case of $\lambda=0.15$ in both the square and circular jets. Again, increased jet spread is shown in Figure 10 for the square coaxial jet as compared to circular jet. Figure 11 shows a cut at 0.55" from the centerline of the square coaxial jet, or approximately half way between the inner and outer jet walls. The middle structure in the air flow is part of the bulge as seen in the outer shear layer of the square jet in Figure 4. Figure 12 is a cut across the diagonal of the square jet next to an image taken at the closest corner of the outer jet in the same orientation. Also note the higher frequency of "burst" occurrence in the corner image.

The potential core region of the inner jet is very distinguishable as seen by the aluminum oxide seed in Figure 13 and 14. The lowest velocity ratio shows the smallest potential core in both the square and circular jet. With both jets seeded, PIV images for the circular and square coaxial jets along the centerline were taken and the results are shown in Figures 16 and 18. The PIV images are still being reduced to obtain velocity information, and therefore will not be discussed further.

In summary, the square coaxial jet provided increased spreading in the shear layers as compared to the spreading observed in the circular coaxial jet for the same flow conditions. A wealth of other useful information is contained in the visualization and PIV images obtained. Analysis of these images as well as supplementary hot-wire measurements are ongoing and are expected to lead to more definite conclusions.

For further information on the other coaxial jet configurations, with more quantitative data from the PIV images, contact Dr. Dimitri Nikitopoulos at Louisiana State University, 2508 CEBA, Baton Rouge, LA 70803, e-mail address meniki@imr00.me.lsu.edu. The information will be incorporated into the thesis written by Jason W. Bitting at LSU as part of the Master's Degree program in Mechanical Engineering.

Acknowledgements

The work done at WPAFB would not be possible without the extensive help of Sivaram Gogineni of Innovative Scientific Solutions, Incorporated, along with Larry Goss, Ben Sarka, Darryl Trump, and many others at ISSI. The guidance and support by Dr. Mel Roquemore was also very helpful and inspirational in completing the work at WPAFB.

References

- Ko, N.W.M., and Kwan, A.S.H. (1976) "The Initail Region of Subsonic Coaxial Jets," *Journal of Fluid Mechanics*, Vol. 73, pp. 305-332.
- Dahm, W.J.A., Frieler, C.E., and Tryggvason, G. (1992) "Vortex Structure and Dynamics in the Near Field of a Coaxial Jet," *Journal of Fluid Mechanics*, Vol. 241, pp. 371-402.
- Tang, D.K., and Ko, N.W.M. (1993) "Coherent Structure Interactions in Excited Coaxial Jet of Mean Velocity Ratio of 0.3," *AIAA Journal*, Vol. 31, No. 8, pp. 1521-1524.
- Lilley, D.G. (1977) "Swirl Flows in Combustion: A Review," *AIAA Journal*, Vol. 15, pp. 1063-1078.
- Panda, J., and McLaughlin, D.K. (1994) "Experiments on the Instabilities of a Swirling Jet," *Physics of Fluids*, Vol. 6, No. 1, pp. 263-276.
- Ben-Yeoshua, Moshe (1993) "Coaxial Jets with Swirl," M.S. Thesis, Department of Aerospace and Mechanical Engineering, The Universtiy of Arizona.
- Sforza, P.M., Steiger, M.H., and Trentacoste, N. (1966) "Studies on Three-Dimensional Viscous Jets," *AIAA Journal*, Vol. 4, No. 5, pp. 800-806.
- Trentacoste, N. and Sforza, P. (1967) "Further Experimental Results for Three-Dimensional Free Jets," *AIAA Journal*, Vol. 5, No. 5, pp. 885-891.
- duPlessis, M.P., Wang, R.L., and Kahawita, R. (1974) "Investigation of the Near-Region of a Square Jet," *Transactions of the ASME, Journal of Fluids Engineering*, September 1974, pp. 247-251.
- Quinn, W.R. (1992) "Streamwise Evolution of a Square Jet Cross Section," *AIAA Journal*, Vol. 30, No. 12, pp. 2852-2857.
- Grinstein, F. F., E. Gutmark, and T. Parr, (1995) "Near Field Dynamics of Subsonic Free Square Jets. A Computational and Experimental Study," *Physics of Fluids*, Vol. 7, No. 6, pp. 1483-1497.
- Schadow, K.C., Gutmark, E., Parr, D.M., and Wilson, K.J. (1988) "Selective Control of Flow Coherence in Triangular Jets," *Experiments in Fluids*, Vol. 6, pp. 129-135.
- Koshigoe, S., Gutmark, E., Schadow, K.C., and Tubis, A. (1988) "Wave Structures in Jets of Arbitrary Shape. III. Triangular Jets," *Physics of Fluids*, Vol. 31, No. 6, pp. 1410-1419.
- Schadow, K.C., Gutmark, E., Wilson, K.J. and Smith, R.A. (1990) "Noncircular Inlet Duct Cross-Section to Reduce Combustion Instabilities," *Combustion Science and Technology*, Vol. 73, pp. 537-553.
- Gutmark, E. and Ho, C. (1986) "Visualization of a Forced Elliptic Jet," *AIAA Journal*, Vol. 24, No. 4, pp. 684-685.
- Wlezien, R.W. and Kibens, V. (1986) "Passive Control of Jets with Indeterminate Origins," *AIAA Journal*, Vol. 24, No. 8, pp. 1263-1270.
- Longmire, E.K., Eaton, J.K., and Elkins, C.J. (1992) "Control of Jet Structure by Crown-Shaped Nozzles," *AIAA Journal*, Vol. 30, No. 2, pp. 505-512.

SYNTHESIS OF A NOVEL SECOND ORDER NONLINEAR OPTICAL POLYMER

Lawrence L. Brott (97-0330)

Graduate Student

Department of Materials Science and Engineering

497 Rhodes Hall

University of Cincinnati

OH 45221-0012

Final Report for:

Graduate Student Research Program

WL/MLBP

Wright Patterson AFB

Sponsored by:

Air Force Office of Scientific Research

Bolling Air Force Base

Washington DC

September 1997

SYNTHESIS OF A NOVEL SECOND ORDER NONLINEAR OPTICAL POLYMER

Lawrence L. Brott

**Department of Materials Science and Engineering
University of Cincinnati**

ABSTRACT

Synthesis of second order nonlinear optical (NLO) polymers represents an exciting field with the resulting chromophore containing materials being used in such devices as frequency doublers or electro-optical computers. In this research, a novel NLO monomer is developed by incorporating a fluorene molecule in its backbone with amine and benzothiazole end groups that act as electron donating and withdrawing groups, respectively. Ethyl chains are attached to the C-9 carbon on the fluorene backbone to aid in the polymer's overall solubility. Different reaction conditions for polymerization are also examined.

SYNTHESIS OF A NOVEL SECOND ORDER NONLINEAR OPTICAL POLYMER

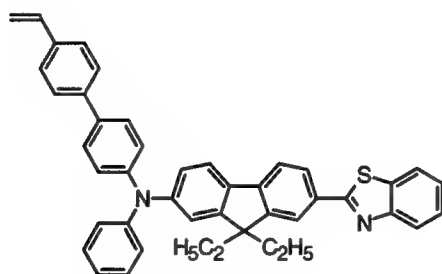
Lawrence L. Brott

Department of Materials Science and Engineering

University of Cincinnati

INTRODUCTION

Interest in second order nonlinear optical (NLO) polymers has increased dramatically in the past few years as potential applications (for example, frequency doublers, optical switches, or electro-optical computers) begin to be realized [1, 2]. Second order NLO compounds have multiple double bonds between electron donor and acceptor groups. Present polymers however still lack the nonlinearity and stability that are necessary for them to be used commercially. The objective of this research is to synthesize a new fluorene-containing compound for a monomer (**1**) and then polymerize it for the use by the U.S. Air Force that will optimize nonlinearity while remaining thermally and structurally stable.



1

Fig. 1

Fluorene-containing monomer.

RESULTS AND DISCUSSION

The monomer synthesis required six separate reactions, which began with two required to attach a benzothiazole unit to a dibromofluorene. The first step converted one brominated end of the fluorene to an aldehyde and then reacted the product **2** with 2-aminothiophenol to produce compound **3** (see figure 2).

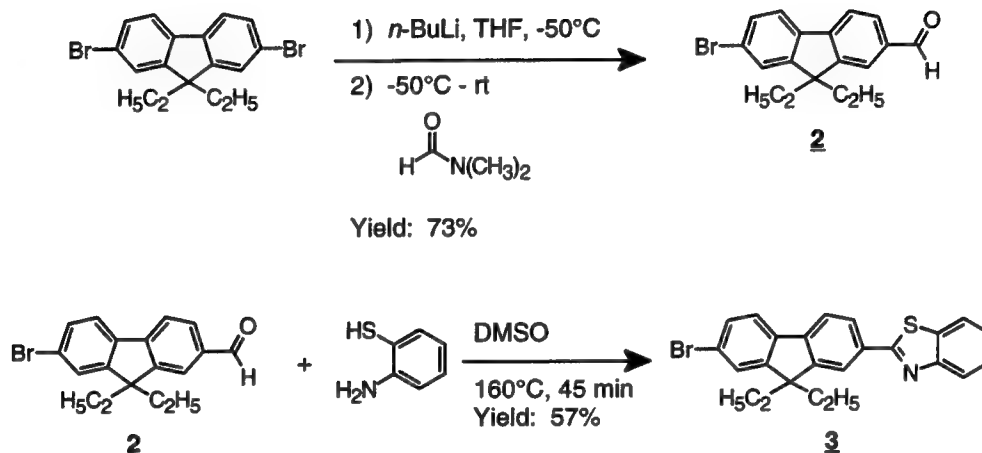


Fig. 2

Two steps for the benzothiazole synthesis.

The next reaction involved an Uhlmann coupling in which acetanilide was coupled with compound **3** in the presence of copper and base (see figure 3). Without purification, the product was reduced with KOH to produce the desired compound **5**. It was realized that the product could be recrystallized from either heptane or 1-propanol.

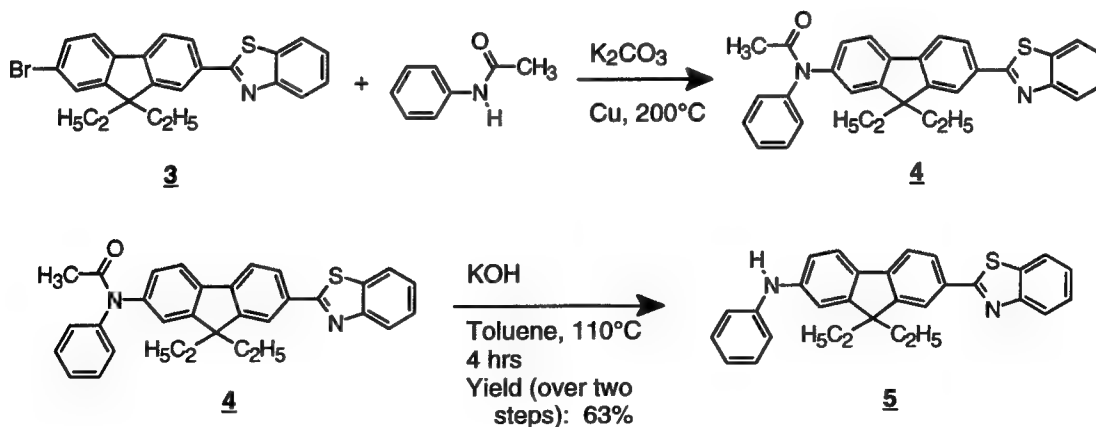


Fig. 3

Uhlmann coupling.

At this point any spacer group could be attached to the chromophore. It was decided that since thermal stability was important to this project, phenyl rings would be used. Two phenyl rings would be used with the expectation that this distance would allow enough room for the monomer to polymerize while not crowding the chromophore side groups during any subsequent poling processes. As a result, a second Uhlmann reaction was performed between compound **5** and 4-bromo-4'-iodobiphenyl. With this reaction, the phase transfer catalyst tris[2-(2-methoxyethoxy)ethyl]amine (TDA-1) was used (see figure 4).

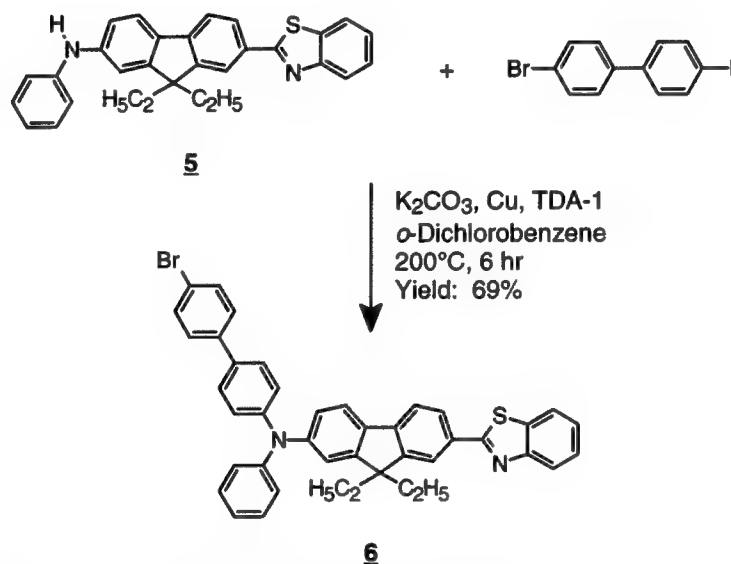


Fig. 4 Second Uhlmann coupling.

The final step involved coupling tributyl(vinyl)tin with compound **6** to produce the desired monomer (see figure 5) [3]. During the workup and purification of the monomer, it was necessary to not heat any solutions with the monomer over 50 °C or expose the solid to excessive light. The product was purified by column chromatography and then twice by recrystallization.

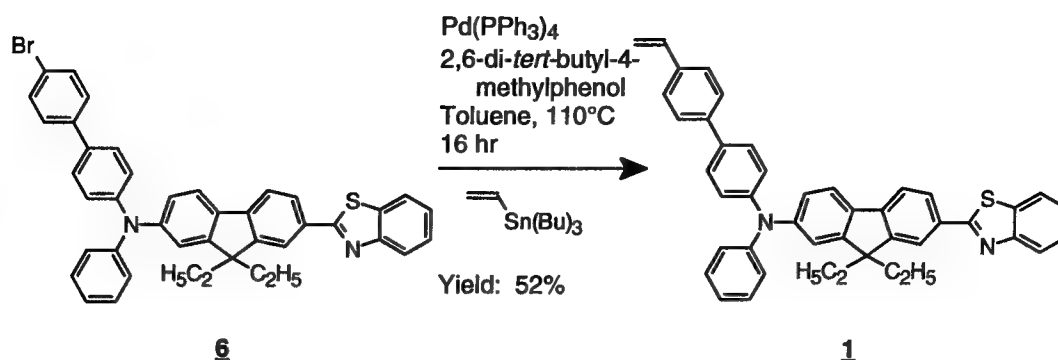


Fig. 5 Final step in the monomer **1** synthesis.

Different polymerization schemes were attempted, which are summarized in table 1. Initially the polymerization was done with AIBN in CCl_4 . When this did not yield a high molecular weight polymer, a new reaction was attempted simply by heating the monomer neat at 200°C. While this appeared to work, the magnetic stir bar stopped too soon and again high molecular weight polymer was not realized. Heating the monomer in tributylamine with mechanical stirring also did not work. Decahydronaphthalene (decalin) worked better and different concentrations and reaction times were tried. However, high molecular weight polymer still has not been achieved.

Sample	Initiator	Solvent	$\frac{\text{Wgt. of Monomer}}{\text{Wgt. of Solvent}}$	Time (hr)	Temp (°C)
1	AIBN	CCl_4	0.10	24	76
2	--	--	--	0.25	200
3	--	Tributyl-amine	1.00	24	200
4	--	Decalin	1.00	1	195
5	--	Decalin	0.25	24	195
6	--	Decalin	1.00	3	195
7	--	Decalin	1.00	24	195

Table 1 Different polymerization conditions.

CONCLUDING REMARKS

The synthetic methods to yield a novel second order NLO monomer containing a fluorene group has been successfully developed. The synthesis, purification and characterization of this

compound will be carried out. The author will continue this successful investigation on NLO materials and second order NLO measurements of this material will be carried out in the coming months.

EXPERIMENTAL DETAILS

Compound 2

2,7-Dibromo-9,9-diethyl-9*H*-fluorene [10.00 g, 26.31 mmol] and THF [57 mL, dried over sodium and freshly distilled] were added to an oven dried three-necked round-bottom flask equipped with a magnetic stir bar, thermometer, nitrogen inlet, and an addition funnel filled with *n*-butyllithium [17.26 mL of a 1.6M solution in hexane, 27.62 mmol]. The fluorene solution was cooled in a dry ice/acetone bath and the butyllithium was slowly added as to not raise the temperature above -50 °C. The resulting dark brown solution had no crystals and was allowed to stir for 0.5 hours after the addition of the butyllithium was complete.

The empty addition funnel was exchanged for a second one which was filled with DMF [3.5 mL, 68.40 mmol] and THF [5.5 mL, freshly distilled]. The DMF solution was slowly added so that the temperature never rose above -50 °C. The dark brown solution was then allowed to return to room temperature and stirred another 16 hours.

A dilute acidic solution [1 mL HCl in 9 mL H₂O] was added and stirred 0.5 hours. Toluene [60 mL] was then added and the layers separated. The organic layer was washed with equal parts water, a slightly basic solution (NaHCO₃), and twice more with water. The organic layer was dried with anhydrous MgSO₄, filtered and concentrated to yield a yellow solid. The solid was stirred with hexane and filtered again to afford the product in 73.33% yield.

Compound 3

To a 50 mL three-necked round bottom flask equipped with a short distillation apparatus and a thermometer, compound 2 [6.00 g, 18.22 mmol], DMSO [9 mL, dried overnight over 4Å sieves] and 2-aminothiophenol [2.05 mL, 19.14 mmol] were added. The mixture was magnetically stirred under air and heated in an oil bath. At around 60 °C, the starting materials went into solution and at 125 °C the reaction bubbled. The reaction was heated at 160 °C for 45 minutes. After being cooled to room temperature, the mixture was then poured into water in a blender. The resulting solid was puréed to produce a gray solid. The solid was recrystallized from ethanol to produce white crystals in 56.69% yield.

Compound 4

Compound 3 [56.49 g, 130.04 mmol], acetanilide [87.89 g, 650.22 mmol], potassium carbonate [53.92 g, 390.13 mmol] and copper [8.26 g, 129.98 mmol] were added to a single-necked round-bottom flask equipped with a short distillation apparatus. The mixture was magnetically stirred under nitrogen and heated to 200 °C in an oil bath for 16 hours. When the mixture had cooled, water and toluene were added and vigorously stirred for 1 hour. The copper was filtered off and the organic layer was washed twice more with water, dried with anhydrous MgSO₄, filtered and concentrated. The product 4 was left unpurified.

Compound 5

Unpurified compound 4 from the previous experiment [130.04 mmol], KOH [14.59 g, 260.08 mmol, finely powdered] and toluene [200 mL] were added to a single-necked round-bottom flask equipped with a magnetic stirrer and condenser. The solution was refluxed for 4 hours under nitrogen. When the solution had cooled, the organic layer was washed five times with equal parts water, dried with anhydrous MgSO₄, filtered and concentrated to produce a solid. The product was refluxed in methanol for an hour before filtering. The solid was then recrystallized from heptane to afford a yellow solid in 63.30% (over two steps) yield. The product can also be recrystallized from 1-propanol.

Compound 6

Compound 5 [10.00 g, 25.09 mmol], 4-bromo-4'-iodobiphenyl [13.51 g, 37.64 mmol], K₂CO₃ [13.87 g, 50.20 mmol], tris[2-(2-methoxyethoxy)ethyl]amine (TDA-1) [0.80 mL, 2.51 mmol] and *o*-dichlorobenzene [45 mL] were added to a single-necked round-bottom flask equipped with a short distillation apparatus. The mixture was heated under nitrogen at 180 °C for 6 hours, being careful that not too much solvent distilled over. When the reaction had cooled, water [200 mL] and toluene [200 mL] were added and vigorously stirred for an hour. The copper was filtered off and the organic layer was washed twice more with water, dried with anhydrous MgSO₄, filtered, and the solvents distilled off under reduced pressure to produce an oil. The product was stirred with methanol to produce a solid which was filtered and dried. The solid could either be purified by recrystallization from 1-propanol (preferred) or heptane with enough toluene to get the solids into solution. The yellow crystals were afforded in 69.35%.

Compound 1

Compound 6 [8.80 g, 12.99 mmol], tributyl(vinyl)tin [4.14 mL, 14.16 mmol], Pd(PPh₃)₄ [0.30 g, 0.26 mmol], toluene [45 mL, distilled and degassed for 15 minutes with nitrogen] and a few crystals of 2,6-di-*tert*-butyl-4-methylphenol were added to a single-necked round-bottom flask equipped with a condenser. The solution was refluxed for 16 hours under nitrogen. After cooling, a concentrated KF solution was added and stirred for an hour. The organic layer was washed twice more with water, dried with anhydrous MgOS₄, filtered and concentrated. The product was purified by column chromatography using silica gel and a 8/92 ethyl acetate/hexane mixture as eluent. After passing through the column, care must be given not to heat the product over 50 °C or to expose it to excessive light. The monomer was then recrystallized in either 1-propanol or a heptane/toluene mixture to afford yellow crystals in 51.85% yield.

Polymerization

Monomer 1 [0.25 g, 0.40 mmol] and decalin [0.25 g] were added to a 5 mL three-necked round-bottom flask equipped with a condenser, mechanical stirrer and a stopper. The reaction chamber was purged ten times via a Firestone valve by alternating a vacuum and nitrogen. The mixture was heated in an oil bath that was at 195 °C for 3 hours under nitrogen. Upon cooling, the polymer solidified. The solid was redissolved in methylene chloride and precipitated into methanol. The polymer was then filtered and dried.

ACKNOWLEDGMENTS

It is a pleasure to thank the individuals who have made the research visit to WL/MLBP both a fruitful and pleasurable experience. In particular, thanks go to Mr. Bruce Reinhardt, Dr. Bob Evers, Ms. Lisa Denny, Ms. Marilyn Unroe, Ms. Ann G. Dillard, Bob Haaga and Dr. Ram Kannan for all their help and kind hospitality.

BIBLIOGRAPHY

1. Prasad, P.N.; Williams, D.J., *Introduction to Nonlinear Optical Effects in Molecules and Polymers*, Wiley-Interscience, New York, 1991.
2. Allen, S. *New Scientist*, **1989**, 1, 59-63.
3. McKean, D.R.; Parrinello, G.; Renaldo, A.F.; Stille, J.K. *Journal of Organic Chemistry*, **1987**, 52, 422-424.

AN EXPERIMENTAL AND COMPUTATIONAL ANALYSIS OF THE UNSTEADY BLADE ROW
POTENTIAL INTERACTION IN A TRANSONIC COMPRESSION STAGE

Danielle E. Brown
Graduate Student

J. Mitch Wolff
Assistant Professor

Department of Mechanical and Materials Engineering

Wright State University
3640 Colonel Glenn Highway
Dayton, OH 45435-0001
Ph: (937) 775-5040
Fax: (937) 775-5009

Final Report for:
Summer Faculty Research Program
Summer Graduate Student Research Program
Wright Laboratory

Sponsored by:
Air Force Office of Scientific Research
Bolling Air Force Base, DC

and

Wright-Patterson Air Force Base, Dayton, OH

September 1997

AN EXPERIMENTAL AND COMPUTATIONAL ANALYSIS OF THE UNSTEADY BLADE ROW POTENTIAL INTERACTION IN A TRANSONIC COMPRESSION STAGE

Danielle E. Brown
Graduate Student

J. Mitch Wolff
Assistant Professor

Department of Mechanical and Materials Engineering
Wright State University

Abstract

A computational and experimental investigation is performed to investigate the unsteady upstream traveling forcing function from a high speed, highly loaded compression rotor. The IGV unsteady surface pressures are experimentally measured for a near-stall transonic operating point to determine the forcing function. The data is analyzed in both the time and frequency domain based on the blade pass frequency. The experimental configuration is computationally modeled with a nonlinear unsteady viscous vane/blade interaction 2D code for comparisons with the experimental data in both the time and frequency domain.

Significant upstream traveling pressure effects were both measured and predicted. A detached bow shock is caused by the increased back pressure consistent with a near stall operating point. The bow shock is shown to impact the IGV blades. Its strongest effect is at the trailing edge of the IGV's with a 3.4 psia fluctuation. The nonlinear viscous unsteady vane/blade interaction computational analysis showed excellent agreement with the experimental results in both the time and frequency domain. Significant higher harmonic content was evident near the trailing edge of the IGV's. This is important, in light of recent trends toward use of linearized Euler and Navier-Stokes models for turbomachinery designs. The results of this research indicate the importance of higher harmonics, therefore extreme caution should be taken when designing transonic compression stages with linearized methods.

AN EXPERIMENTAL AND COMPUTATIONAL ANALYSIS OF THE UNSTEADY BLADE ROW POTENTIAL INTERACTION IN A TRANSONIC COMPRESSION STAGE

Danielle E. Brown
J. Mitch Wolff

Introduction

Gas turbines are a vital energy source for both military and industrial applications with recent research focusing on identifying high cycle fatigue unsteady flow mechanisms. There is a constant need for an improved understanding of the flow physics through the various components. This greater understanding leads to the ability of manufacturers to achieve higher levels of performance and a more efficient system. As technology increases, there are continually increasing demands on gas turbine engines involving greater durability, reduced noise levels, reduced size and greater thrust. A jet engine consists of several distinct components; the inlet, compressor, combustor, turbine, and exit nozzle. A considerable portion of the recent research involves the unsteady interaction between adjacent blade rows in both the compressor and turbine sections.

The two principle types of blade row interaction are usually referred to as wake and potential flow interactions.¹ Wake interaction is the effect upon the flow through a downstream blade row of the vortical and entropic wakes shed by one or more upstream rows. Potential flow interaction results from the variations in the velocity potential or pressure fields associated with the blades of a neighboring row and their effect upon the blades of a given row moving at a different rotational speed. This type of interaction is of serious concern when the axial spacing between adjacent blade rows is small or the flow Mach number is high.

Recently, computational work has been initiated to develop nonlinear, time-accurate, inviscid (Euler) and viscous (Navier-Stokes) solution techniques for unsteady flows through isolated and aerodynamically coupled blade rows (see Verdon, 1992 for a review). For coupled systems of rotating and

stationary blade rows, the relative motions between adjacent rows give rise to unsteady aerodynamic excitations which can initiate blade vibrations, generate discrete-tone noise, and degrade aerodynamic efficiency. Two categories of numerical procedures have recently been developed for determining the effects of relative motion between adjacent blade rows. In the first category of numerical procedures, incoming wakes are specified at the inlet of isolated blade rows.² In these methods, the wakes are usually assumed to be parallel with uniform pressure and prescribed total enthalpy and/or velocity variations. In the second category of numerical analyses, both blade rows are modeled and the relative position of one blade row is varied to simulate blade motion.^{3,4,5}

Some joint computational and experimental investigations have been made into vane/blade interactions. These investigations have been primarily on turbine configurations, with the experimental data acquired in generally two different types of experimental rigs. First, large scale turbine rigs are used to simplify the experimental investigation. The large scale of the rig is a distinct advantage because it permits the use of extensive instrumentation on both the stationary and rotating blades. The large scale also has the advantage of giving Reynolds numbers which are typical of high pressure turbines at nominal model running conditions⁶, but it can not simulate transonic flow phenomena. Full-scale transonic turbines are being tested using blow down or shock tube facilities.⁷ These facilities are beneficial for testing actual hardware components with research issues being miniature measurement techniques and short test duration times.

In summary, little research has been directed at vane/blade interaction in a compressor section. Thus, relatively little is known about the unsteady IGV/blade interactions which occur within a compression system. Since these unsteady aerodynamic interactions can lead to high vibratory stresses, models must be developed to analyze vane/blade interaction. In addition, relevant experiments are needed to assess the validity of these models and direct future research efforts.

The objective of this research is to investigate and quantify the fundamental vane/blade interaction phenomena relevant to the upstream potential forcing function of a downstream rotor in a compression system. This is accomplished by performing a series of experiments in the Compressor Aero Research Lab

(CARL), a high speed, highly loaded compression stage facility. IGV unsteady surface pressures are experimentally determined for a near-stall transonic operating point. The data is analyzed in both the time and frequency domain based on the blade pass frequency. In addition, a two dimensional nonlinear viscous unsteady multi-blade row computational (CFD) analysis is compared with the experimental data in both the time and frequency domain.

Compressor Aero Research Laboratory (CARL)

The Compressor Aero Research Lab facility at Wright Patterson Air Force Base's Wright Laboratory is a full scale, high speed, highly loaded compression stage. The single stage compressor facility consists of an open or closed loop (currently open) tunnel system with an upstream venturi flow meter to measure the mass flow rate. The test compressor is driven by a 2,000 hp electric motor with a variable speed range of 6,000 to 21,500 rpm.

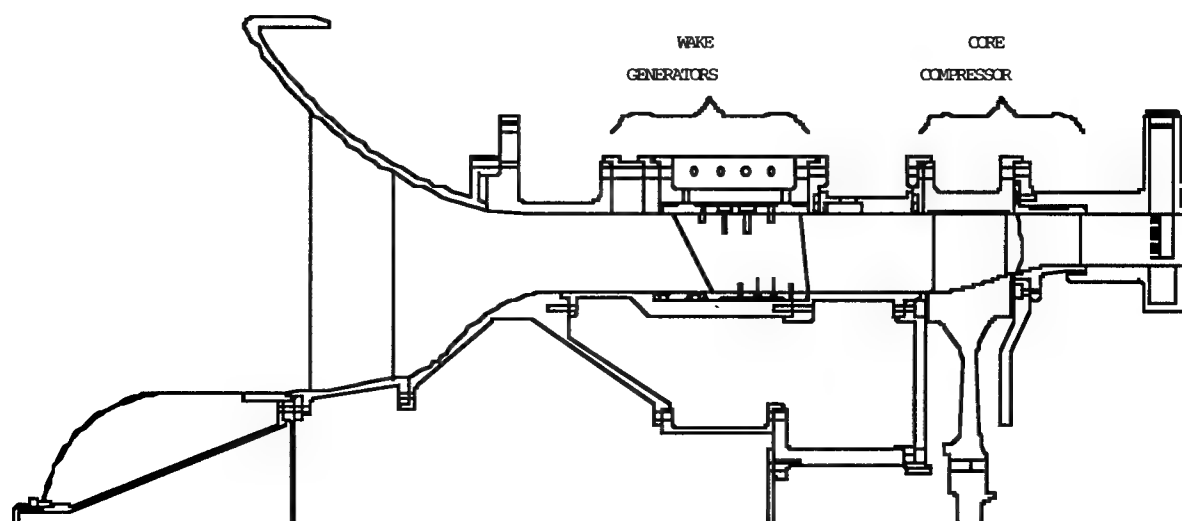


Figure 1. Schematic of SMI Compressor Rig.

The research compressor, Figure 1, was designed by CARL personnel and manufactured by Pratt & Whitney Aircraft Engines. The primary intent for this research compressor is for a Stage Matching Investigation (SMI), characterizing overall compressor performance. Therefore, a single stage core compressor consisting of a rotor and stator with 33 and 49 airfoil blades respectively is used. The outer

diameter for both the rotor and stator is 19 inches. The SMI's core compressor design results in a transonic rotor.

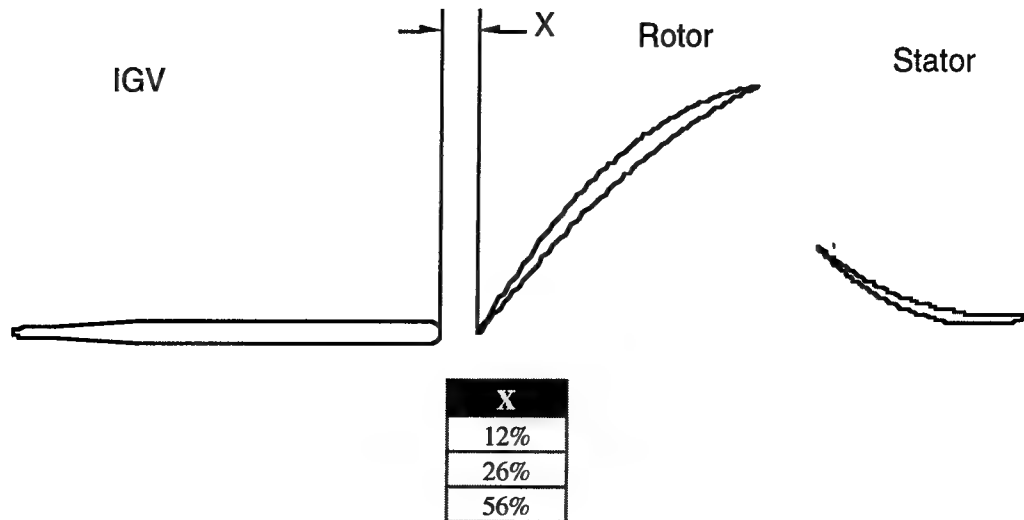


Figure 2. Flow path through SMI Compressor Rig

To study the effect of different upstream stages, an IGV assembly is placed upstream of the rotor section. The IGV's were designed by Pratt and Whitney with the purpose of creating a propagating wake consistent with a modern technology, highly loaded, low aspect ratio stage, therefore they are sometimes referred to as Wake Generators. This term along with Inlet Guide Vanes (IGV) will be used interchangeably. The wake generators do not turn the flow as would a normal IGV assembly. They have a constant solidity (spacing to chord ratio) along the span and have no aerodynamic loading in order to achieve a uniform two dimensional wake. With this design, several ways are utilized to modify the wake profile generated. First, the number of IGV blades in the upstream passage can be varied. A split ring assembly is used for installation and three different numbers of IGV blades can be utilized 12, 24, and 40. It is also possible to vary the axial spacing between the IGV's and the rotor, Figure 2. Three different spacings are possible 12%, 26%, and 56% of the rotor chord from the IGV trailing edge to the rotor leading edge. In this research, only the 24 IGV and 26% spacing data set has been examined.

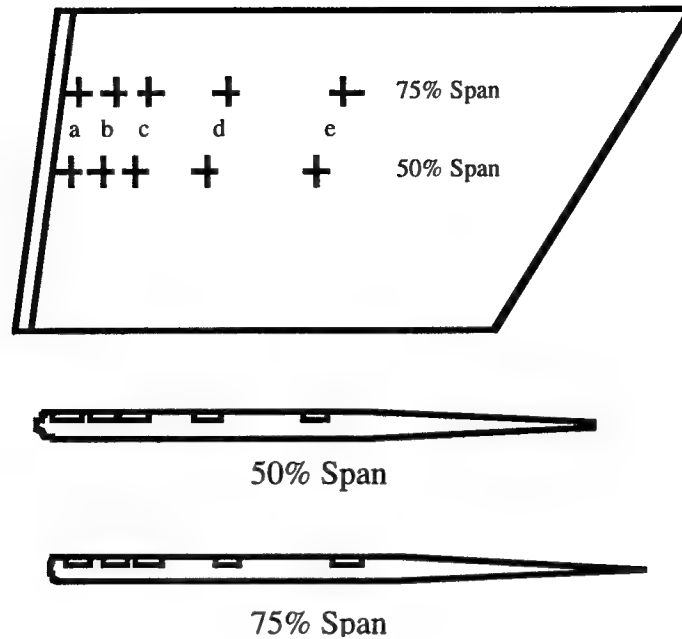


Figure 3. Transducer Locations on IGV

IGV Surface Pressure Instrumentation

The wake generators are instrumented with miniature Kulite pressure transducers. Figure 3 shows the locations of these pressure transducers. Two different blades are instrumented with 10 pressure transducers each. To investigate three dimensional effects, two different spanwise locations are instrumented, 50% and 75% as shown. The blade surface is machined to allow the pressure transducers to be mounted flush. To protect the pressure sensor, a thin layer of RTV was placed over the diaphragm. Grooves for the lead wires are also machined to ensure no disturbance to the flow. The lead wires are bundled and fed out of the casing.

Two adjacent wake generators are instrumented giving data for one flow passage. Surface pressure data is collected for only the 24 wake generator case. Flow periodicity is assumed with one blades data phase shifted to the other blade for analysis purposes.

LQ-125 miniature pressure transducers from Kulite are used for the surface pressure measurements. The pressure transducers are manufactured directly on the blades using chip on technology. The pressure sensing element is 0.060 inches in diameter. It has an internally compensated temperature range of 30 to 130°F. The natural frequency of the pressure transducer is 300 kHz, giving a usable frequency range of 60

kHz. During initial testing, it was discovered that one pressure transducer was bad so the experimental data could not be collected at the 75% span 50% chord location.

Calibration of the transducers for sensitivity and offset was achieved in the following manner. Before installation of the instrumented wake generator, the transducers were subjected to variable pressures at a nominal temperature of 70°F and an elevated temperature of 110°F. The results of this study indicated for this range of temperature transducer sensitivity was 0.01% per degree F. However, offset was influenced by temperature variation and the magnitude of the shift varied from a high of 0.017 psia/degree F to a low of 0.001 psia/degree F.

Based on this bench calibration, no special procedures were established to control sensitivity with inlet air temperature shifts. However, to control transducer offset variation, the transducers' amplifiers were re-balanced at atmospheric conditions for any inlet temperature shift of 3°F or greater.

From these procedures, offset and precision errors were established as ± 0.06 psi and ± 0.04 psi, respectively. In addition, a zero response data set was recorded. The data was then processed in the same manner as the actual test data. Therefore, this signal is representative of the actual static pressure uncertainty due to noise influences. The measured random uncertainty was a ± 0.1 psia fluctuation in static pressure. This value includes precision error due to random noise and temperature changes.

Computational Analysis

In 1992, a nonlinear unsteady Euler/Navier-Stokes vane blade interaction model, VBI 2D, was developed by Rao et al⁸ for turbine configurations. This analysis models the relative motion of adjacent blade rows by allowing one row to move with respect to the other. The VBI code is utilized for the IGV/rotor interaction in the compression stage by modeling both the IGV and rotor. A brief overview of the VBI code will now be given.

Grid Generation

Two separate grids are generated using VGRID, an H and O grid for each blade row. The two grids are then embedded to form a composite grid by a chimera scheme called PEGSUS.⁹ PEGSUS creates the appropriate hole boundaries and interpolation stencils involved in the communication of embedded grids.

The embedding process eliminates problems with cell skewness near the leading and trailing edges of the airfoils. The transition from the inflow and outflow boundaries to the airfoil leading and trailing edges causes this problem. The PEGSUS results are read directly into the VBI code.

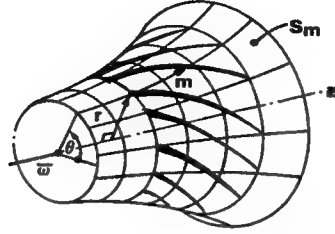


Figure 6. Coordinate system used in VBI formulation

Numerical Method

The VBI code solves the Euler/Navier Stokes equations using an explicit runge kutta scheme in quasi-three-dimensional space. Figure 6 represents the coordinate system used in the formulation.⁸ The Baldwin-Lomax¹⁰ model for turbulence and transition is utilized within the code. The governing equations for flow on a blade-to-blade surface of revolution will now be given:⁵

$$\frac{\partial Q}{\partial t} + \frac{\partial E}{\partial m} + \frac{\partial F}{\partial \theta} = H \quad (1)$$

where:

$$Q = rb \begin{bmatrix} \rho \\ \rho u \\ \rho v \\ \rho e \end{bmatrix}$$

$$F = b \begin{bmatrix} \rho v \\ \rho uv \\ \rho v^2 + p \\ v(\rho e + p) \end{bmatrix}$$

$$F_v = \frac{b}{Re} \begin{bmatrix} 0 \\ \sigma_{12} \\ \sigma_{22} \\ F_4 \end{bmatrix}$$

$$H = H_i - H_v + \frac{\partial E_v}{\partial m} + \frac{\partial F_v}{\partial \theta}$$

$$E = rb \begin{bmatrix} \rho u \\ \rho u^2 + p \\ \rho uv \\ u(\rho e + p) \end{bmatrix}$$

$$E_v = \frac{rb}{Re} \begin{bmatrix} 0 \\ \sigma_{11} \\ \sigma_{12} \\ E_4 \end{bmatrix}$$

$$H_i = rb \begin{bmatrix} 0 \\ \left(\rho v^2 + p \right) \frac{1}{r} \frac{dr}{dm} + p \frac{1}{b} \frac{db}{dm} \\ -\rho uv \frac{1}{r} \frac{dr}{dm} \\ 0 \end{bmatrix}$$

$$H_v = \frac{rb}{Re} \begin{bmatrix} 0 & & \\ \sigma_{22} \frac{1}{r} \frac{dr}{dm} + \sigma_{33} \frac{1}{b} \frac{db}{dm} & & \\ -\sigma_{12} \frac{1}{r} \frac{dr}{dm} & & \\ 0 & & \end{bmatrix}$$

The following equations represent the energy components

$$e = \frac{p}{\rho(\gamma-1)} + \frac{1}{2}(u^2 + v^2) \quad (2)$$

$$E_4 = u\sigma_{11} + v\sigma_{12} + \frac{1}{\gamma-1} \frac{\mu}{Pr} \frac{\partial a^2}{\partial n} \quad (3)$$

$$F_4 = u\sigma_{12} + v\sigma_{22} + \frac{1}{\gamma-1} \frac{\mu}{Pr} \frac{1}{r} \frac{\partial a^2}{\partial \theta} \quad (4)$$

where E_4 and F_4 are the viscous terms from the energy equation. It is now necessary to represent the shear stress equations:

$$\sigma_{11} = 2\mu \frac{\partial u}{\partial n} + \lambda \nabla \cdot V \quad (5)$$

$$\sigma_{12} = \mu \left(\frac{\partial v}{\partial m} - \frac{v}{r} \frac{dr}{dm} + \frac{1}{r} \frac{\partial u}{\partial \theta} \right) \quad (6)$$

$$\sigma_{22} = 2\mu \left(\frac{1}{r} \frac{\partial v}{\partial \theta} + \frac{u}{r} \frac{dr}{dm} \right) + \lambda \nabla \cdot V \quad (7)$$

$$\sigma_{33} = 2\mu \frac{u}{b} \frac{db}{dm} + \lambda \nabla \cdot V \quad (8)$$

For this analysis, it is assumed that Stokes' hypothesis is true. For turbulent results, the viscosity is represented in an appropriate form. The laminar and turbulent viscosity's are accounted for with the turbulent viscosity found from the Baldwin-Lomax eddy-viscosity model.

Frequency Analysis

A fast fourier transform algorithm (FFT) was added to the VBI source code to allow frequency comparisons to be made between the experimental and computational results, as suggested by Probasco et al⁹. The fundamental use of FFT algorithms are for computing the discrete Fourier transforms of sequences. The FFT algorithm utilized in this source code was developed with the help of an existing algorithm by Pickering.¹⁰ The algorithm is based on blade pass frequency and calculates the first five harmonics of both the magnitude and phase of the unsteady delta pressure for each chord location along the entire surface of the IGV blade. A frequency analysis is required for any forced response analysis, because it is the unsteady pressure phase response which determines the flutter stability of the cascade. The addition of a frequency

capability makes the VBI code a more useful tool in high cycle fatigue analysis. Originally the code only calculated unsteady envelopes (i.e., maximum and minimum unsteady distributions).

Results

The results discussion is divided into two sections, experimental and computational. A series of experiments were performed in the Compressor Aero Research Lab SMI compression stage to investigate the IGV unsteady surface pressure response due to the upstream traveling potential field generated by the downstream rotor. A computational study was then completed utilizing the VBI code with comparisons made to the experimental data.

Experimental Data Reduction

The experimental data was recorded on a 28 channel analog tape recorder with a flat response up to 80kHz. The data was digitized off-line at an effective sample rate of 500 kHz. Anti-aliasing was achieved using a Precision Filters TD6B Linear Phase Time Delay Filter. A cutoff frequency of 132 kHz was used for the data reduction. This gives a 1% attenuation of the signal at 77 kHz. The blade pass frequency is 7.8 kHz. Therefore, the first 11 blade pass harmonics are resolved without aliasing. Data was digitized for a time record of 68 milliseconds, which gives approximately 16 rotor revolutions. Ensemble averaging was performed on the data in order to average out any inconsistencies that may exist from one rotor blade to the next. The ensemble averaging was accomplished based on the rotor blade pass frequency, since the rotor has 33 blades, about 520 records were ensemble averaged.

Computational Analysis Parameters

Four thousand time steps were used per rotor blade pass with a time step of approximately 2.9×10^{-8} seconds being used. Figure 7 represents a pressure time history for one node of the flow field. A total of 37 rotor blade passes were analyzed to reach a nearly periodic solution as shown in Figure 7. There appears to be a possible low frequency rotating stall cell present in the computational solution. This is not seen in the experimental data, but the experimental results are obtained with a downstream stator section included, while the computational analysis did not model the downstream stator blade row. The consequences of this difference will be discussed later when the computational Mach number contours are presented. For the

quasi-three-dimensional effects, a 20% streamtube contraction through the rotor is input into the VBI code to take care of the spanwise direction component of the three dimensional analysis. Finally, an algebraic turbulence model is utilized to model viscous effects in the computational results presented.

Discussion of Results

A comparison of computational results and experimental data will be shown. The operating point used for this comparison is 105% corrected speed and a near stall throttle setting on the performance curve. This operating point is shown in Figure 8. The inlet guide vane assembly can be located either 12%, 26% or 56% of rotor chord away from the rotor leading edge and with either 12, 24, or 40 vanes. The data and results discussed here are for the 26% rotor chord spacing and 24 vane configuration. The computational results shown are the last two blade passes of thirty-seven.

Figure 9 represents the computational Mach contour lines for six rotor blades and four inlet guide vanes. For this operating point, a bow shock at the leading edge of the rotor is known to exist. The high back pressure needed to operate at this low of a flow rate forces the bow shock upstream of the rotor leading edge. In the computational analysis, the bow shock is clearly evident in the plot and can be seen to progress upstream. The upstream shock interaction causes a significant unsteady pressure force on the IGV blades which is not considered in typical turbomachinery compressor designs. The separation near the trailing edge can be accounted in two manners. First, the downstream stator stage is not modeled, therefore, the exit pressure for the rotor is not known. A rise in the exit pressure would provide a more favorable pressure gradient for the flow removing the trailing edge separation. Secondly, the computational analysis is 2-D. The streamtube contraction method of modeling the 3-D flow within the actual rig may not include all the flow physics to keep the flow attached. Finally, the primary interest of this research is the upstream traveling potential blade row effect. So, a separated flow region at the trailing edge of the rotor is not of major importance to the upstream solution.

Figure 10 represents a comparison of the unsteady normalized difference (upper surface - lower surface) pressure for the computational and experimental results at the 50%, 70%, 83%, 89%, and 95% chord locations on the Inlet Guide Vanes. This figure will be discussed from the trailing edge forward, since

the strongest interaction is at the trailing edge. At the 95% chord location, there is excellent agreement between the experimental and computational blade pass response. The upstream traveling bow shock is the dominating feature of both the experimental and computational response. The computational analysis models the nonlinear shock interaction extremely well in both magnitude and phase. For the 89% chord location, the shock structure is less evident but is still the dominating phenomenon. The computational analysis slightly over predicts the unsteady magnitude response with the phase in excellent agreement. At 83%, the shock structure has disappeared. The computational analysis again over predicts the unsteady magnitude response with an excellent phase agreement. The general character of the unsteady response at the 70% chord location is modeled by the computational analysis. The magnitude and phase are in reasonable agreement with experimental data, but the shape of the response is slightly off. Finally, at the 50% chord location, the magnitude is modeled adequately, but the phase is about 180° off.

It is evident in Figure 10 the effect of moving farther away from the rotor has on the unsteady response. At the 50% chord location the unsteady pressure response is about 1/4th of the response at the trailing edge. At the trailing edge, the net pressure fluctuation acting on the IGV blades is 3.4 psia. The unsteady response at the trailing edge is dominated by the rotor bow shock which is traveling upstream. It is encouraging for the turbomachinery designer, the agreement found between the experimental and computational results. These results definitely increase the designer's confidence in the computational design tools available.

Figure 11 represents a comparison of the magnitudes of the first five harmonics for the computational results and experimental data versus chord position. The first harmonic computational results are generally lower than the experimental results. The computational results show a very high response at the 98% chord location. Since there was not any instrumentation at this location, it is unknown if this response is actual. The second harmonic response in general has much better agreement with the experimental results. It is important to note the magnitude of the 2nd harmonic response near the trailing edge. At the 98% chord position, the 2nd harmonic response is greater than the 1st. If the shock wave is hitting the IGV at the 98% chord location, then this kind of behavior would be expected. The 3rd through

5th harmonic response show negligible response except at the trailing edge. Again, this is consistent with a shock interaction at the trailing edge.

These results have significant implications for turbomachinery design models. For transonic compressor design the shock interaction upstream of the rotor is significant. By the nature of this shock wave, the interaction is highly nonlinear. Therefore, to properly model a transonic compressor design a nonlinear analysis is required. Current trends in turbomachinery design systems is toward linearized methods, either linearized Euler or Navier-Stokes models. These linearized methods are quite computationally efficient, but they only consider the 1st harmonic response. As the above results show, the designer should be extremely cautious about using linearized design tools for transonic compressor designs.

Conclusions

A computational and experimental investigation was performed to investigate the unsteady upstream traveling forcing function from a high speed, highly loaded compression rotor. The IGV unsteady surface pressures were experimentally measured for a near-stall transonic operating point to determine the forcing function. The data was analyzed in both the time and frequency domain based on the blade pass frequency. The experimental configuration was computationally modeled with a nonlinear unsteady viscous vane/blade interaction 2D code for comparisons with the experimental data in both the time and frequency domain.

Significant upstream traveling pressure effects were both measured and predicted. A detached bow shock is caused by the increased back pressure consistent with a near stall operating point. The bow shock is shown to impact the IGV blades. Its strongest effect is at the trailing edge of the IGV's with a 3.4 psia fluctuation. The nonlinear viscous vane/blade interaction computational analysis showed excellent agreement with the experimental results in both the time and frequency domain. Significant higher harmonic content was evident near the trailing edge of the IGV's. This is important, in light, of recent trends toward use of linearized Euler and Navier-Stokes models for turbomachinery designs. The results of this research indicate the importance of higher harmonic, therefore extreme caution should be taken when designing transonic compression stages with linearized methods.

Acknowledgments

The authors would like to thank all of the personnel at CARL. In particular, Dr. Randy Chriss and Dr. Bill Copenhaver for help in analyzing the experimental data. Also, Dr. Rolf Sondergaard and Charles Stevens from WL/POTT are thanked for help with the computational results. In addition, the authors would like to acknowledge the support of Doug Probasco, a Wright State University Master's student, who was instrumental in the successful completion of this research. Finally, this work was supported in part by a grant of HPC time from the DoD HPC Center, MSRC at Wright Patterson Air Force Base through the use of the HPC07 and CFS01 machines.

References

¹Verdon, Joseph M, "Unsteady Aerodynamic Methods for Turbomachinery Aeroelastic and Aeroacoustic Applications," *AIAA Paper No. 92-0011*, 1992.

²Suddhoo, A., Giles, M.B., and Stow, P, "Simulation of Inviscid Blade Row Interaction Using a Linear and a Non-Linear Method," *AIAA Paper No. 91-7049*, 1991.

³Giles, M.B., "Stator/Rotor Interaction a Transonic Turbine," *AIAA Paper No. 88-3093*, 1988.

⁴Rai, Man Mohan, "Three-Dimensional Navier-Stokes Simulations of Turbine Rotor-Stator Interaction; Part I-Methodology," *Journal of Propulsion*, Vol. 5, No. 3, 1989, pp. 305-311.

⁵Rao, K.V., and Delaney, R., "Investigation of Unsteady Flow Through Transonic Turbine Stage; Part 1: Analysis," *AIAA Paper No. 90-2408*, 1990.

⁶Dring, R.P., Joslyn, H.D., Hardin, L.W., and Wagner, J.H., "Turbine Rotor-Stator Interaction," *Journal of Engineering for Power*, Vol. 104, 1982, pp. 729-742.

⁷Dunn, M.G., Bennett, W.A., Delaney, R.A., and Rao, K.V., "Investigation of Unsteady Flow Through a Transonic Turbine Stage: Data/Prediction Comparison for Time-Averaged and Phase-Resolved Pressure Data," *Journal of Turbomachinery*, Vol. 114, 1992, pp. 91-99.

⁸Rao, K.V., Delaney, R.A., and Topp, D.A., "Turbine Vane-Blade Interaction," *Interim Report WL-TR-92-2002*, 1992.

⁹Probasco, D.P., Wolff, J.M., Copenhaver, W.W., and Chriss, R.M., "Unsteady Blade Row potential Interaction in a Compression Stage," *AIAA Paper No. 97-3285*, 1997.

¹⁰Pickering, M., "An Introduction to Fast Fourier Transform Methods for Partial Differential Equations, with Applications," 1943, pp 163.

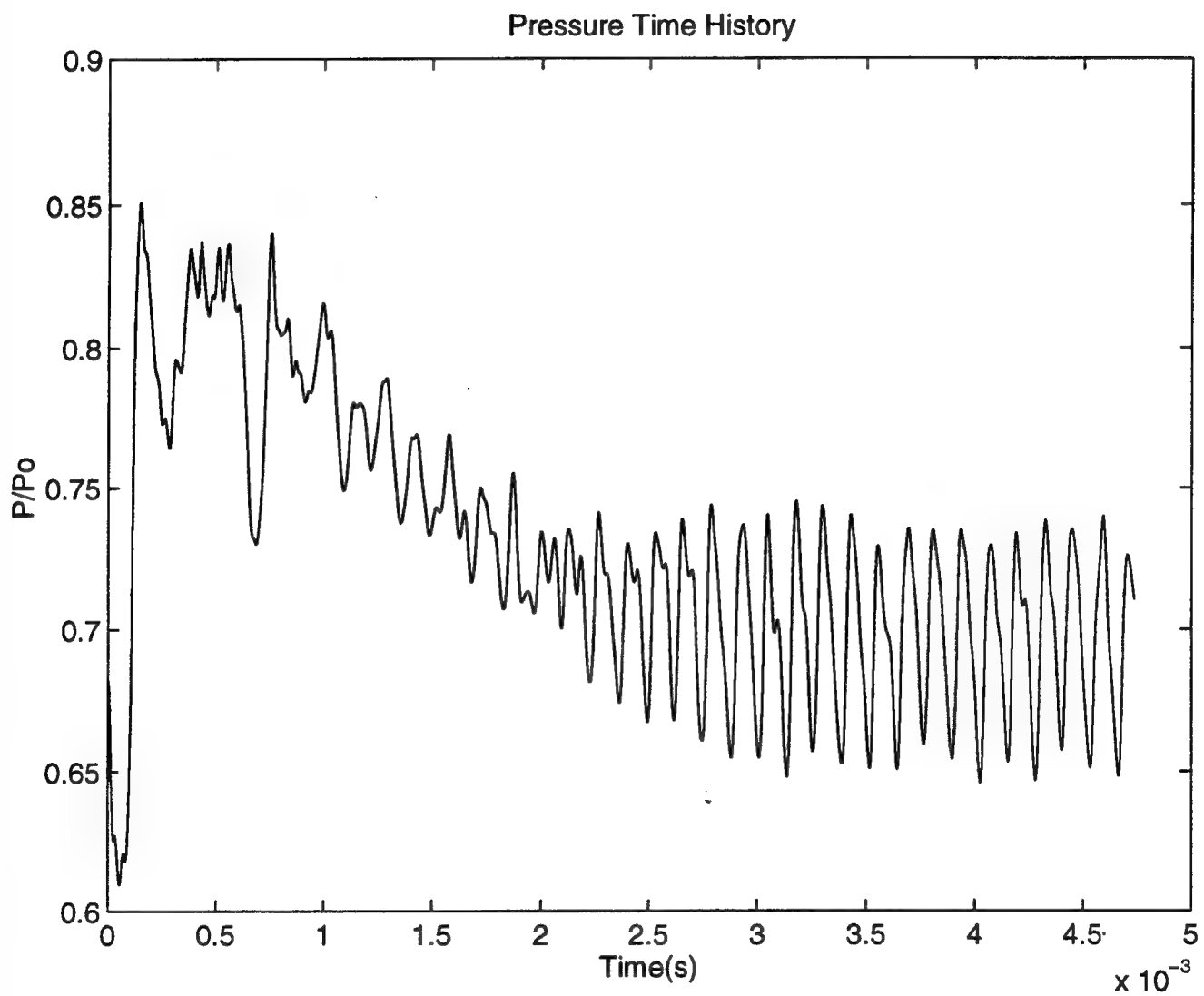


Figure 7. Pressure Time History

Compressor Performance Map

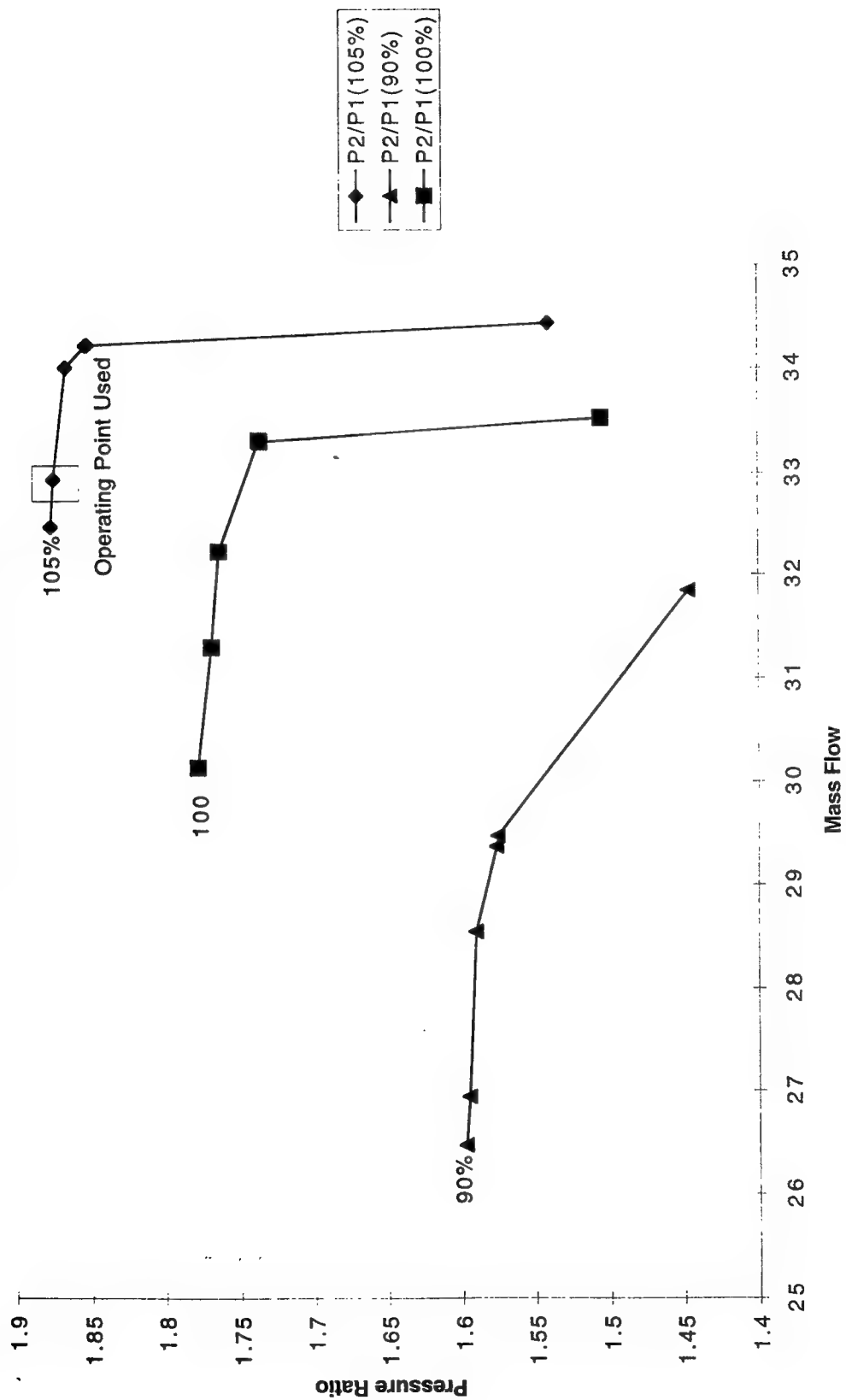


Figure 8. Compressor Performance Map SMI Rotor

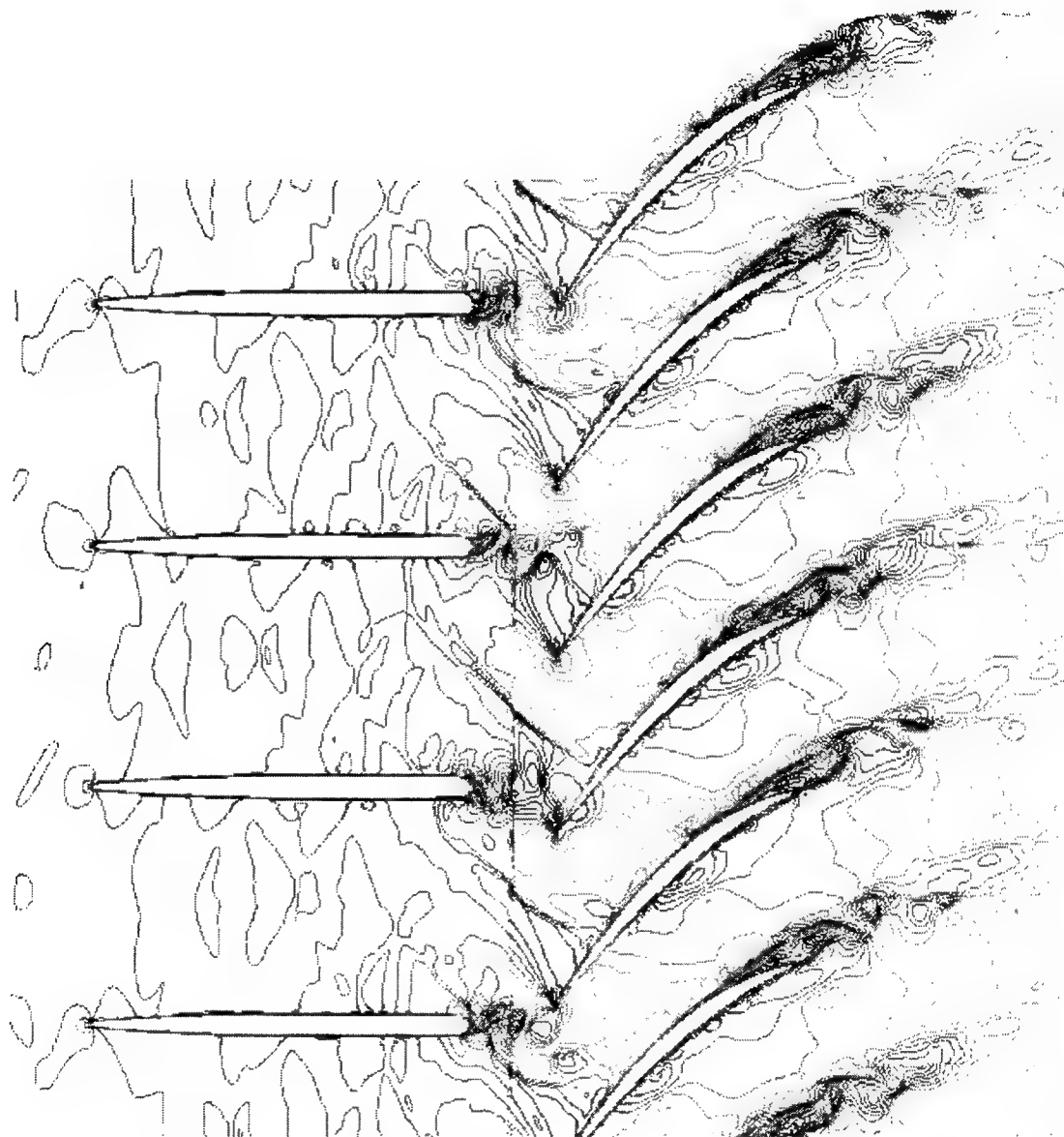


Figure 9. Snap Shot of Mach Number Contours

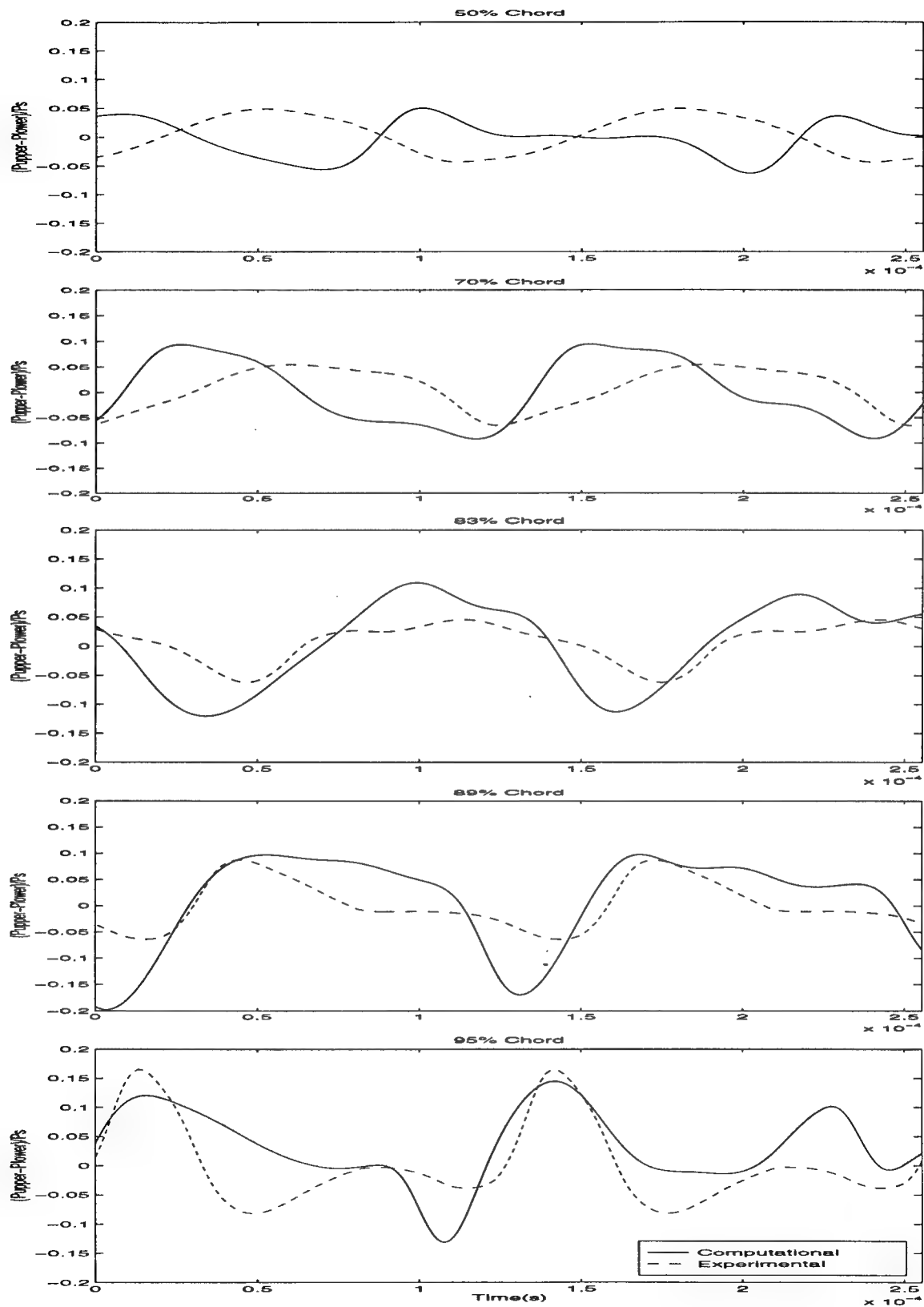


Figure 10. Unsteady Delta Pressure Comparison for 5 Chordwise Locations

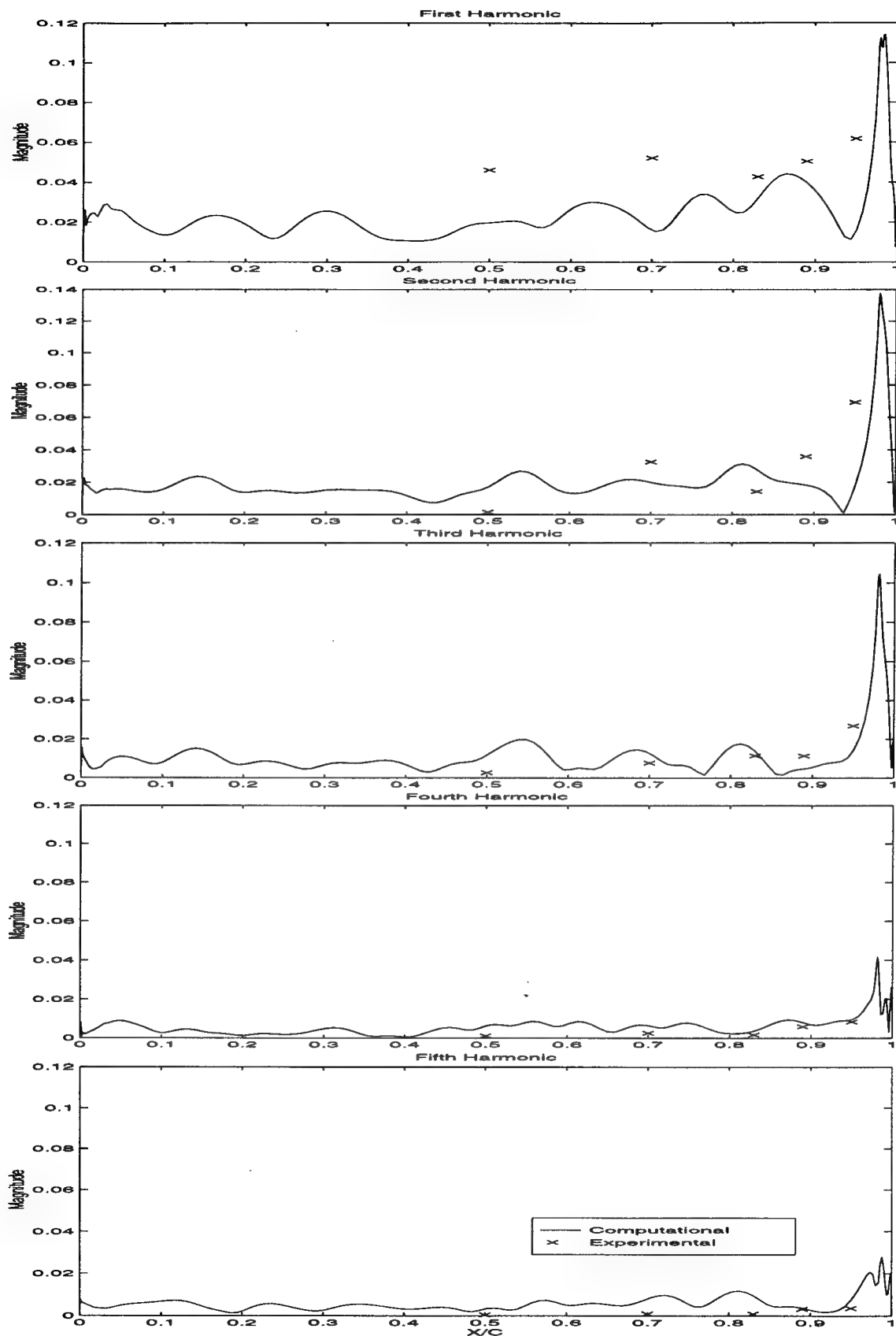


Figure 11. Unsteady Delta Pressure Magnitude Harmonic Response

THE SYNTHESIS OF A PROTECTED CARBOXYLIC
ACID DERIVATIVE FOR ATTACHMENT TO C₆₀

Angela M. (Manders) Cannon
Graduate Assistant
Department of Chemistry

Pennsylvania State University
152 Davey Laboratory
University Park, PA 16802

Final Report for:
Graduate Student Research Program
Wright Laboratory

Sponsored by:
Air Force Office of Scientific Research
Bolling Air Force Base, Washington DC

and

Wright Laboratory

September 1997

THE SYNTHESIS OF A PROTECTED CARBOXYLIC ACID DERIVATIVE FOR ATTACHMENT TO C₆₀

Angela M. (Manders) Cannon
Graduate Assistant
Department of Chemistry
Pennsylvania State University

Abstract

Three steps (Scheme 1) in a literature synthesis of a carboxylated C₆₀ derivative were completed. These three steps yielded the precursor protected carboxylic acid derivative which will be added to the C₆₀ and subsequently deprotected (Scheme 2) for further study as an optical limiting chromophore. The first step involves a condensation reaction between a hydrazide and an aldehyde to form a hydrazone. This product which contains a carboxylic acid is chlorinated to the acid chloride. In the final step, two reactions occur in the same pot. The acid chloride is protected using an ester linkage and the hydrazone is deprotected forming a diazide. The synthesis sounds straight-forward but proved to be troublesome.

THE SYNTHESIS OF A PROTECTED CARBOXYLIC ACID DERIVATIVE FOR ATTACHMENT TO C₆₀

Angela M. (Manders) Cannon

Introduction

Laser radiation can readily damage sensors and detectors on electronic equipment used in Air Force systems. The over all purpose of this research is to identify organic materials that can be used to make an optical switch. The optical switch is placed in the optical system at the focus of the laser beam. Laser energy that is focused into the optical switch is absorbed, reducing the throughput energy of the laser to a level that is not damaging to the sensor or detector. This behavior is called optical limiting.

Many criteria must be met for a material to be suitable for this application. They include: broad band absorption, robust resistance to photodegradation, acceptable solubility, low optical limiting threshold and high damage threshold. The problems that can arise in a single material may limit it's performance in any one of these areas. There are several mechanisms that describe the optical limiting performance in terms of the electronic activity that occurs within the laser pulse of typically nano seconds time frame. Many of these mechanisms involve the excitation of an electron/s from it's ground state. Each material must be evaluated by its mechanism and the longevity of it's ability to maintain absorption before chemical breakdown or the return of electrons to the ground state. These electronic interactions determine the suitability of materials for each application.

Work within the Laser Harden Materials Branch on this project has identified porphyrins and C₆₀ as excellent materials for an optical switch. The mechanism involved excites an electron from the ground state to the 1st excited singlet state and then it is transferred via inter system crossing to the 1st triplet state. The concept being investigated involves using a bichromaphore to enhance the filling of this triplet state on the porphyrin. We are attempting to use C₆₀ to pump electrons from the ground state to the

1st excited singlet state. These electrons could potentially transfer to the 1st triplet state of the porphyrin via a bridging connector from the C_{60} . The focus of this research is to synthesize the C_{60} bridging link portion of the final bichromophore.

Discussion

Although, the task at hand may seem straight-forward. In reality, there are many problems to overcome. The synthetic chemistry involved in preparing both C_{60} derivatives and porphyrins is intensive, especially when trying to limit functionality of either to one site. This is due to the fact that C_{60} and porphyrins are highly symmetrical. Even if one obtains a mixture which includes the monofunctionalized derivative, separation is quite difficult and very few analytical techniques, if any, can distinguish the difference between pure monofunctionalized material and an average of a mixture of non-, mono-, and di- functionalized material. If one is capable of synthesizing and purifying each of the desired C_{60} and porphyrin derivatives, one is still left with questions of can the chemistry to connect the derivatives be accomplished and will the bridge connecting them be short enough to allow electron transfer and long enough not to permit steric hindrance.

One must always think ahead in the procedure to ensure that the sequence of chemistry will not lead to a step which produce undesired side reactions. This is especially true in the synthesis of C_{60} derivatives. Fullerenes are unique in their chemistry. In some senses, they behave like aromatic compounds and in others, like most unsaturated double bonds. Therefore, monofunctionalization becomes particularly difficult. In this research, we attempted to follow a literature procedure on the monocarboxylation of C_{60} .^{1,2} As will be shown, following a literature procedure is not always effortless.

Experimental (Scheme 1)

Preparation of the Acid Sulfonylhydrazone (1). - Place 15.00 g (0.1630 moles) of commercial (Aldrich) glyoxylic acid monohydrate, 30.33 g (0.1630 moles) of commercial (Aldrich) *p*-toluenesulfonyl hydrazide, and approximately 40 g anhydrous sodium sulfate (Aldrich) as a drying agent into a 1 liter erlenmeyer. Add 500 - 600 ml of anhydrous ether and stir. Reaction mixture is a milky white for about first 0.5 hour and then turns a clear pale yellow, except for Na_2SO_4 . After approximately 3.5 hours, allow Na_2SO_4 to settle and decant off ether into a flask containing molecular sieves. As the reaction becomes complete and the ether is dried, the product will begin to crystallize out. In this case, the reaction was stirred over the molecular sieves for the weekend. The ether was decanted off and fresh ether was used to redissolve most of the product that had precipitated with the sieves. The solution was placed in the freezer for recrystallization. The product was filtered out of the ether covering the funnel with foil as not to let water condense into the product, 19.85 g of dry product with a melting point of 152 - 154 degrees. Later, another 9.35 g of product was recrystallized from the remainder of crude product. The theoretical yield would be 39.31 g (0.1630 moles). A total of 29.20 g (0.1210 moles) was recovered, a 74% yield.

Preparation of the Acid Chloride Sulfonylhydrazone (2). - A suspension of 7.19 g (0.02980 moles) of **1** in a mixture of 100 ml benzene and 9.26 g (0.07948 moles) of thionyl chloride was refluxed with stirring until the mixture attained a distinct yellow color (not golden) and only a small amount of suspended insoluble material remained. The mixture was cooled and filtered through a magnesium sulfate to give a clear light yellow solution which was rotary evaporated dry. The residual solid was powdered and placed on a vacuum filter where it was washed with a few ml (3 - 5) of benzene to remove most of the colored impurities. Careful, not to expose to air too much. The remaining solid was dissolve in a minimum quantity of benzene (20 - 30 ml), diluted with petroleum ether (5 - 10 ml), and allowed to recrystallized. Note petroleum ether was added until the solution became

slightly cloudy and would not swirl away. Crystals formed from the solution setting on the bench top capped. The crystals were filtered and dried. The melting point was 105 - 110 degrees and yielded 5.38 g (0.02072 moles). Theoretical yield would be 7.74 g (0.02980 moles) and a 69.5 % yield was obtained.

Preparation of (Ethoxycarbonyl)methyl Diazoacetate (3). - A solution of 3.16 g (0.01211 moles) of **2** was made in 50 ml dichloromethane. Under nitrogen, 1.72 ml (1.89 g, 0.01817 moles) of ethyl glycolate was added. After dropwise addition of 4.22 ml (3.07 g, 0.03029 moles) of triethylamine over 5 minutes, the mixture generated a white gas, rapidly became red and was stirred for 3 hours. The solution was washed with 50 ml each 0.1M HCl, saturated aqueous sodium bicarbonate, and saturated aqueous sodium chloride. The organic layer was dried over magnesium sulfate and evaporated. Column chromatography was run on the crude product using silica gel and a 4:1 mixture of hexane and ethyl acetate. The R_f of the product is 0.41 in this medium and seen under a UV lamp. The combined product of four of these reactions was distilled under vacuum and yielded g.

Discussion

This synthetic endeavor was trouble plagued from the very beginning. We attempted to follow the literature procedure referenced by Diedrich.^{1,2} This procedure synthesized the acid hydrazone in aqueous acid. Our two attempts at this procedure yielded two different products, melting points 60-63 degrees and 75-77 degrees, neither of which was the desired product. Even after a week of refluxing, no product crystallized out as described in the procedure. A literature search yielded two articles^{3,4} on condensation of a hydrazide with an aldehyde or ketone in anhydrous ethanol. All attempts of the reaction on the 1 g of aldehyde scale yielded decently pure product with a melting point of 151-154 degrees. However, once the reaction was scaled up to 5-15 g aldehyde the product became impossible to purify from the reactants. A closer look at the reaction revealed that since our aldehyde came as a monohydrate, the reaction

produced water, and reversed with access water. The problem of obtaining pure product could be solved by successful removal of water from the reaction. This did not prove possible with ethanol. We attempted using ether as a solvent. The reaction was attempted on a 1 g scale in a test-tube over sodium sulfate. The reactants dissolved yielding a clear pale yellow solution which within a few minutes became cloudy. The desired product was only slightly soluble in ether. Fortunately, the large scale reaction takes significantly longer to reach completion. The reaction could therefore be stirred over sodium sulfate for hours without product precipitating out. We would then decant the reaction mixture off the sodium sulfate onto molecular sieves which a much easier to separate from the product.

Some keys to the synthesis of the acid chloride hydrazone were learned. Do not let the reaction mixture turn to a golden yellow. Filtering the reaction mixture through magnesium sulfate gave a better yield. This might have been due to mastering the procedure but it was more than a 15% difference. Do not attempt to wash away all the colored impurities. These impurities do not effect the melting point of the product.

The synthesis of (ethoxycarbonyl)methyl diazoacetate has a very low yield. It is believed that this could be improved. However, further literature research needs to be done to understand the reaction mechanisms and what type of yield one should expect.

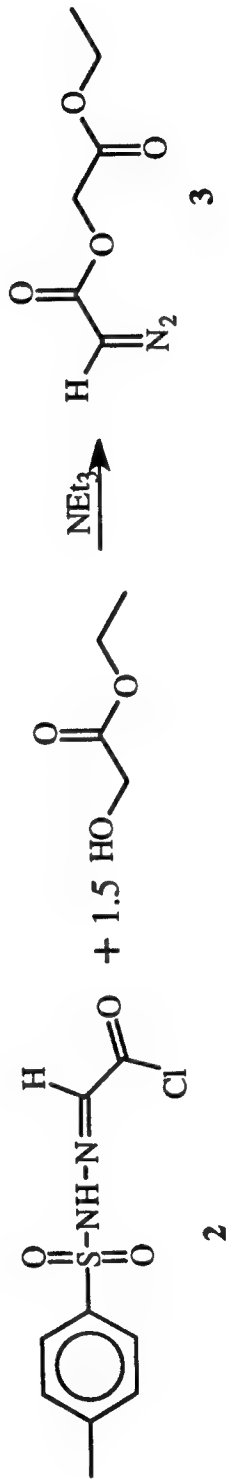
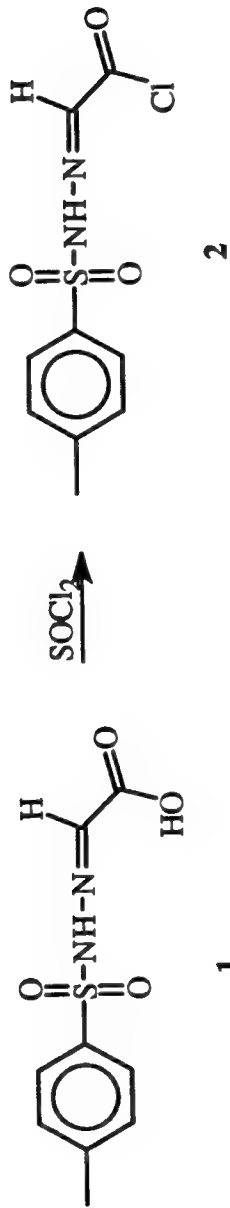
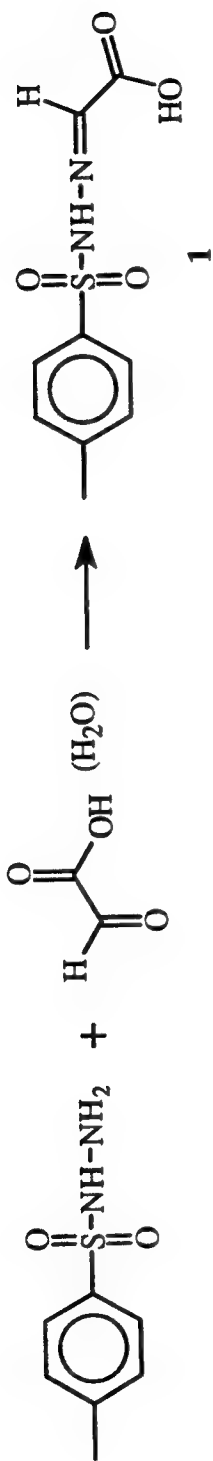
Conclusion

This paper was focused to be thorough with what has been learned throughout this research. One hopes that this may allow those who continue on with the project to more thoroughly understand the problems and avoid them, saving precious time. Fortunately, one usually learns the most from the difficulties they encounter.

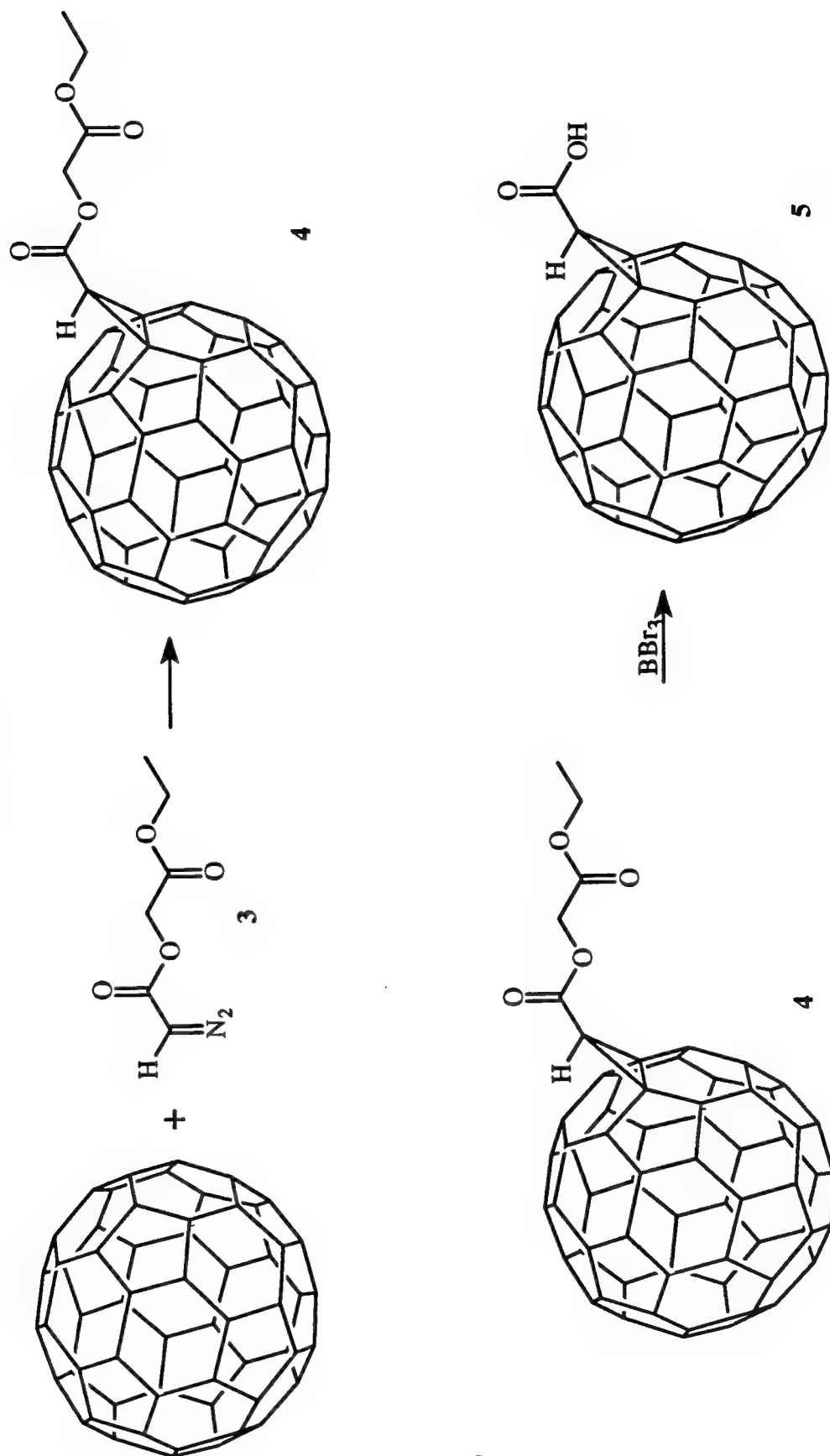
References

- [1] Isaacs, Lyle; and Diederich, Francois; *Helvetica Chimica Acta*, **1993**, 76, 2454 - 2464.
- [2] House, Herbert H.; and Blankley, C. John; *The Journal of Organic Chemistry*, **1968**, 33, 53 - 60.
- [3] Hutchins, Robert O.; Milewski, Cynthia A.; and Maryanoff, Bruce E.; *The Journal of the American Chemical Society*, **1973**, 95, 3662 - 3668.
- [4] Hutchins, Robert O.; Kacher, Mark; and Rua, Louis; *The Journal of Organic Chemistry*, **1975**, 40, 923 - 926.

Scheme 1



Scheme 2



VISION ALGORITHMS FOR MILITARY IMAGE PROCESSING

**Chuck C. Conklin
Graduate Student
Department of Electrical Engineering**

**Florida State University
2525 Pottsdammer St.
Tallahassee, FL 32304**

**Final Report for:
Graduate Student Research Program
Wright Laboratory**

**Sponsored by;
Air Force Office of Scientific Research
Bolling Air Force Base, DC**

and

**Wright Laboratory
Eglin Air Force Base, FL**

July 1997

VISION ALGORITHMS FOR MILITARY IMAGE PROCESSING

Charles C. Conklin
Graduate Student
Department of Electrical Engineering
Florida State University

ABSTRACT

Two vision-inspired algorithms were written to decode the wavelength and intensity maps of images. One uses a two-layer detector approach, while the other attempts to simulate a two-layer detector using a checkerboard configuration. To test these innovative detector concepts, an algorithm had to initially encode the wavelength and intensity maps of the images. Experimental results indicate that the vision algorithm, which uses two layers of detectors, would decode the simulated images exactly. On the other hand, the checkerboard pattern vision algorithm, which uses one layer of detectors, showed only minimal degradation with the test images. However, the checkerboard layout may have unique benefits such as a built-in edge detection system.

INTRODUCTION

The vision algorithms use two image matrices to encode an image. The first matrix is a wavelength map, where the pixels are representing the colors present in the image. The second matrix is an intensity map, representing the intensity of all the objects in the viewing area. In the intensity map, all of the pixels are represented by a grayscale, where 0 represents the darkest intensity, and 255 represents the brightest intensity.

The first step is to generate the Photon Absorption Curves corresponding to both medium and large cone detectors in the human eye. Using Matlab, a Gaussian curve is generated using a vector length of 401 and a variance of 40. The curve is then normalized to have a maximum peak of one. A second Gaussian curve is then generated, by taking a copy of the first curve and shifting it to the right by 15 units. The two Gaussian curves are then overlapped together, forming both a medium and large cone absorption curve. The curves are then reduced from a vector length of 401 to a vector length of 331, which are representing the responsivity values (M, L) between the wavelengths (λ) of 385nm to 715nm. These curves are selected to closely resemble measured photon absorption data of the M and L cones². Two monotonic ratio curves are generated for decoding interpolations;

$$\text{Ratio (M / L)} = \ln (\text{medium cone responsivity} / \text{large cone responsivity})$$

$$\text{Ratio (L / M)} = \ln (\text{large cone responsivity} / \text{medium cone responsivity})$$

NOTE: The Photon Absorption Curves can be seen in the appendix (figure 1).

The second step is to simulate two encoded images, which will represent what will be seen by the medium and large cone detectors. Two matrices are initially generated to simulate both the wavelength and intensity maps of the different objects. The wavelength map is interpolated with the given photon absorption curves, to generate both a medium and large cone responsivity matrices. The intensity map (I)

is convoluted with a Gaussian filter to simulate the Point Spread Function. Then the responsivity matrices (M, L) and the filtered intensity map (I) are then multiplied together, using matrix array multiplication, producing an encoding of the wavelength and intensity maps for both the medium and large cone detectors.

MI = encoding of medium cone responsivity matrix with the intensity map.

LI = encoding of large cone responsivity matrix with the intensity map.

The third step is to be able to decode both the wavelength and intensity maps back out of the encoded matrices MI and LI. If the MI matrix is divided by the LI matrix (MI / LI), the intensity values (I) will cancel out, leaving a ratio of medium to large responsivity values (M / L). The (M / L) matrix can then be interpolated with the ratio curves to get the wavelength (λ) and responsivity values (M and L). Then the intensity values (I) can be calculated by taking the encoded images (MI or LI) and dividing them by the interpolated responsivity values (M, L). The simulated process can be seen in the appendix (figure 2a and 2b, page 11).

$$\text{Intensity (I)} = \text{MI} / \text{M} \quad \text{or} \quad \text{Intensity (I)} = \text{LI} / \text{L}$$

NOTE: Interpolation uses the Photon Absorption Curves, which can be seen in the appendix (figure 1, page 10).

EXPERIMENTS AND RESULTS

A hexagonal filter using a two layer detector

In the experiment a hollow square shaped object was used to simulate a target. As expected, the wavelength (in nm) map (λ) and intensity (in mV/pixel) map (I) calculated back exactly what was originally encoded in.

Filename: Vision3.m Ratio Method (1) Gaussian Variance (.2)

LAM1 = [λ (background) = 460nm & λ (object) = 650nm]

INT1 = [I(background) = 30 mV/pixel & I(object) = 90 mV/pixel]

A checkerboard detector concept

The detector array will be laid out in a checkerboard fashion, representing medium and large cone detectors. The Photon Absorption Curves are used to help encode, as well as decode the mosaic (checkerboard) image. The pixel location of the matrix, the cone type from the checkerboard array, and the wavelength can be used to interpolate a monotonic ratio value. Then each identical array of both the monotonic ratio matrix and the filtered intensity matrix can be multiplied together, forming an encoded mosaic image.

The next step is to be able to completely decode the mosaic image. First each pixel will be averaged with the neighboring pixels. Then each average valued pixel will be interpolated with the

monotonic ratio curve to decode an approximate wavelength matrix. The same average value pixel will then be interpolated to decode a responsivity matrix. The encoded mosaic image can then be divided, using matrix array division, with the responsivity matrix. This result will be an approximation of the filtered intensity map. The simulated process can be seen in the appendix (figure 3a and 3b, page 11).

The same hollow square shaped object in the previous experiment is used to simulate checkerboard vision algorithm.

Filename: Vision1.m Ratio Method (2) Gaussian Variance (.2)

LAM1 = [λ (background) = 460nm & λ (object) = 650nm]

INT1 = [I(background) = 30 mV/pixel & I(object) = 90 mV/pixel]

The input and output wavelength and intensity maps decoded results having a slight error.

LAM2 = [λ (background) = 464.575nm & λ (object) = 649.389nm]

INT2 = [I(background) = 25.084 mV/pixel & I(object) = 88.471 mV/pixel]

The spiked edges occur because the monotonic ratio curve was initially an approximation. The calculated ratios use all the medium cones as the same responsivity value, and all large cones as the same responsivity value. When the decoding occurs, an averaging ratio takes place. This average ratio can have a different ratio than the ratio produced from the Photon Absorption Curves, especially if the averaging takes place at the edge of an object. When either the medium or large cones are different, for an example at an edge of an object, the ratio values will sometimes be outside the Photon Absorption Curves. This means the values, when interpolated, sometimes approach zero or infinity. When the values are outside the limits of the curves, a default is applied. This default forces the value to be at the end points of the curves (still causing the spiked edges to occur). See appendix (figure 5, bottom, page 12).

When looking at the INT2 map the spikes are not symmetric, they are very large on the right side of the image. This is due to the shape of the hexagonal array used in the rectangular coordinates. This can be seen in the appendix (figure 5 top and bottom, page 12). To determine that this theory is true, the shape of the array will be symmetrically laid out. This will be seen in the symmetrical filter experiment.

The wavelengths and intensities would not decode the exact values that are encoded. One possibility is that the interpolations had a rounding error. A second possibility is that the interpolations during the decoding process, uses two different monotonic ratio curves (M and L curves). This could possibly carry small errors during the averaging process, which could lead to larger errors in the interpolation during the decoding process. A third possibility of generating errors could be that a linear interpolation is taking place on a nonlinear system (a restriction imposed by Matlab, surely the most easily controlled of the three possibilities).

The monotonic curves are developed using a ratio between the M and L responsivity curves. The values of these curves are stored in vectors, which can then be used to interpolate between two known

points. It turns out, that the ratio of two lines is only linear if both lines intersect at the origin. This is where the greatest error is occurring. See proof in appendix (figure 6, page 13).

A more precise interpolation algorithm

The checkerboard concept is tested using the same object. The difference is using a more precise interpolating algorithm, which is developed in the program 'vision2.m'.

Filename: Vision2.m Ratio Method (2) Gaussian Variance (.2)

LAM1 = [λ (background) = 460nm & λ (object) = 650nm]

INT1 = [I(background) = 30 mV/pixel & I(object) = 90 mV/pixel]

The same edge effects occurred (which was expected), but the routine decoded back exactly the values that were encoded (figure 7, page 14 & figure 8, page 15). This experiment shows how important it is to use a precise interpolation. In order to do a precise interpolation, more sample points are needed. When many sample points are used, the time it takes to find the interpolation points takes longer. One method to optimize the points of interpolation is to use a *binary search*⁶, which must be used on a monotonic curve. This minimizes the number of comparisons it takes to find the two points to interpolate. In this algorithm, a value is being searched for within a vector of 331 elements. This could take a maximum of 330 comparisons. By using the binary search, the maximum number of searches per pixel is;

$$N = \log_2(331) = 8.37 \Rightarrow 9 \text{ maximum searches / pixel}$$

Using a symmetrical filter

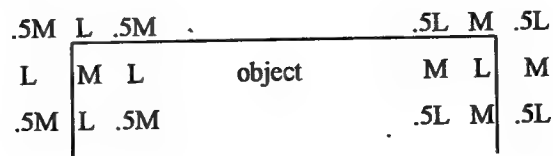
The medium and large cones will be reconstructed in a symmetrical model. This layout will be tried on the same hollow squared object. This can be seen in the appendix (figure 9, top, page 16)

Filename: Vision2.m Ratio Method (5) Gaussian Variance (.2)

LAM1 = [λ (background) = 460nm & λ (object) = 650nm]

INT1 = [I(background) = 30 mV/pixel & I(object) = 90 mV/pixel]

All the edges around the hollow squared object are the same height. The only spiked edges that are a little larger are the corners. The corners are affected more than the sides alone, because there are two edges that are affected, as shown below.



This experiment shows that the symmetry that is used, when averaging the cones for decoding, plays a factor in the edges that are generated around the objects. This edge effect can possibly be useful in outlining objects. It is also possible that the edge effect could distort too much of an image, making it impossible to determine where or what the objects viewed are.

Edge effect analysis

Next, to further confirm the edge effect theory, this experiment will use a vertical ratio of M/L. This half of the experiment is trying to see if only the horizontal edges will appear, similar to using a horizontal edge Sobel operator. The second part of this experiment will use a horizontal ratio of M/L. This half of the experiment is trying to see if only the vertical edges will appear, similar to using a vertical edge Sobel operator.

Filename: Vision2.m Ratio Method (1) Gaussian Variance (.2)

and

Filename: Vision2.m Ratio Method (7) Gaussian Variance (.2)

LAM1 = [λ (background) = 460nm & λ (object) = 650nm]

INT1 = [I(background) = 30 mV/pixel & I(object) = 30 mV/pixel]

Both the vertical and horizontal edges appeared. This can be seen in the appendix (figure 10, bottom, page 17). It is possible that the edge effect will not always appear. If the wavelength or intensity of two neighboring objects is very close, the difference in the edges may not cause a large spike to occur. In this case, edge detection would not be dependable. The next experiment will test this theory to see if it is valid.

Dependability of the edge effect

This experiment is testing to see if it is possible that the edge effect will not work. This test will have the intensities of both the background and object the same. The wavelengths will slightly vary.

Filename: Vision2.m Ratio Method (1) Gaussian Variance (.2)

LAM1 = [λ (background) = 525nm & λ (object) = 575nm]

INT1 = [I(background) = 30 mV/pixel & I(object) = 30 mV/pixel]

In this experiment the horizontal edges in the intensity map are slightly visible. This can be seen in the appendix (figure 11, bottom, page 18).

This experiment shows that it is possible that the edges can not always be relied upon. In this example, it is possible that the intensity of the edges could blend in with other parts of the image. It should be said that, "the edge detection can be an enhanced feature when possible, but can not always be relied upon."

2-D chirp signal using 2 layer detector array

This experiment is testing a chirp signal, where the wavelength map is represented by a horizontal chirp signal, and the intensity map is represented by a vertical chirp signal.

Filename: Vision3.m Ratio Method (1) Gaussian Variance (.2)

$$\text{LAM1}(i,j) = 550 + 150 * (\sin(2 * \pi * j / (50 - (j/4))))$$

$$\text{INT1}(i,j) = 95 + 90 * (\sin(2 * \pi * i / (50 - (i/4))))$$

The wavelength and intensity maps decoded the exact signal that was encoded. It will be challenging to test this chirp signal with the vision2.m algorithm, which averages with the nearest neighbors in decoding. This test will be performed in the next experiment.

2-D chirp signal using a 1 layer detector array

This experiment is testing the chirp signal that was used in 2-D chirp signal using a 2 layer detector array. The difference will be that the checkerboard algorithm will be used to encode and decode the mosaic image.

Filename: Vision2.m Ratio Method (6) Gaussian Variance (.2)

$$\text{LAM1}(i,j) = 550 + 150 * (\sin(2 * \pi * j / (50 - (j/4))))$$

$$\text{INT1}(i,j) = 95 + 90 * (\sin(2 * \pi * i / (50 - (i/4))))$$

When the vertical chirp is encoded with the horizontal chirp, mostly all the combinations of low and high frequencies will be observed. This will provide a challenge for the vision2.m program and the edge distortions that occur when using the algorithm.

Both vertical and horizontal edge distortions appeared (figure 12, bottom, page 19). They appeared strongly in the valleys of the chirp signals. This edge distortion was strongly expected to be a problem with the mosaic chirp signal. The stronger distortions occur where the high frequencies valleys are. This could be due to small ratio values, which occur in the valleys, whereas larger ratio values occur on the hills of the chirp signal. This theory will be tested in the next experiment.

Local gradient ratio distortion

In this experiment the wavelength map will be constant and the intensity map will use a chirp signal. A vertical M/L filter will be tested across the intensity map. Then a horizontal M/L filter will be tested with the intensity map.

When the ratio filter is parallel to the chirp signal, the distortions appear. This is due to the fact that the filter is moving across the changing values of the chirp. When the ratio filter is orthogonal to the chirp signal, there is no distortion, since there are no changes in the signal.

Due to the algorithm being used, distortion is dependent on how close values are to the zero reference plane. For example, if $M = 4$ and $L = 5$ from a reference point, then the ratio of $M/L = 4/5 = 0.8$;

$$\text{Distortion Ratio} = 1 - 0.8 = 0.2$$

If the signal is shifted 20 units from the same reference point, so that $M = 24$ and $L = 25$, still a difference of 1 unit, then the ratio of $M/L = 24/25 = 0.96$;

$$\text{Distortion Ratio} = 1 - 0.96 = 0.04$$

This example can be seen in the appendix (figure 4, bottom, page 2), where the signal was at 3, 15, and 50 units from the same reference point.

CONCLUSION

A two-layer detector decodes the exact wavelength and intensity maps of an ideal image. For these ideal images, a single checkerboard detector can also retrieve both wavelength and intensity information, with only minor degradation. This degradation can be minimized using more precise interpolation routines. In any case, when using the checkerboard detector, edge distortions occur, that can possibly be beneficial as an edge detector. This edge detection will not be completely reliable on low contrast monochromatic images. As the chirp test indicates, the checkerboard detector distorts images more in rapidly changing visual environments. However, some compensations can be made merely by varying baselines in the checkerboard algorithm.

FUTURE DIRECTIONS

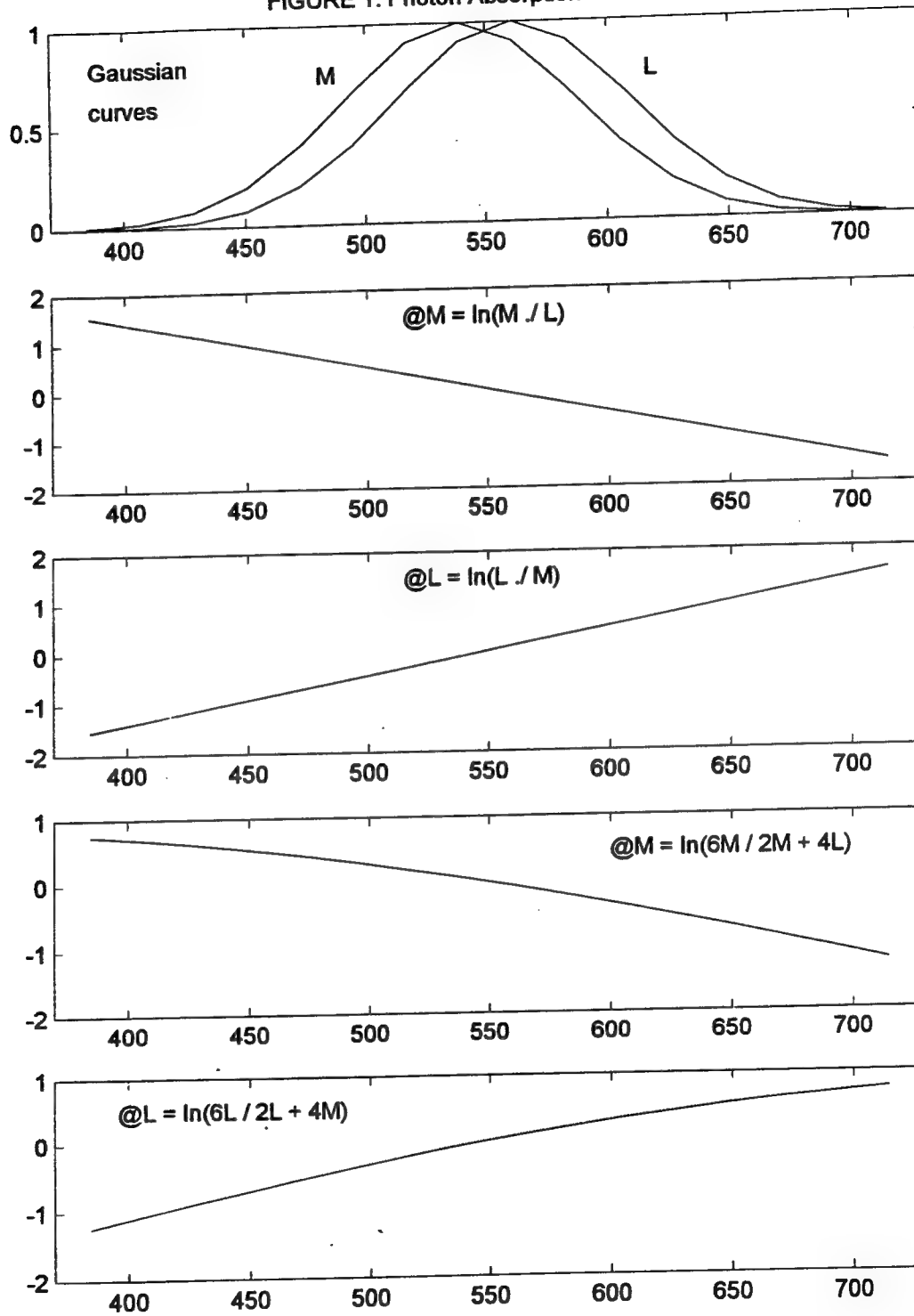
The tests performed in these experiments used ideal models. It would be interesting to know how these algorithms perform on real imagery.

- 1) Will the edge distortions, in the checkerboard algorithm, dominate in an image with many edges?
- 2) Will the edge distortions, in the checkerboard algorithm, dominate in a noisy image?
- 3) Using an actual sensor, will edge distortions occur using the two-layer detector algorithm, since individual detectors may have varying tolerances (mismatches)?
- 4) The vision algorithms for the checkerboard and 2 layer detectors have been looked at for optimization. Many changes have been made to these programs to save time. There are probably other shortcuts or algorithm techniques that could speed up the algorithm process. Looking into program optimizations?

REFERENCES

1. Brooks, Geoffrey W. "Modeling Retinal Processing Using Wavelet Theory," Ph.D. Thesis, Florida State University, 1996.
2. De Valois, R. L., & De Valois, K. K., Spatial Vision, Oxford University Press, New York, NY 1988.
3. Dowling, John E., The Retina: An Approachable Part of the Brain, Harvard University Press, Cambridge, Massachusetts, 1987.
4. Marr, David, Vision, W. H. Freeman and Company, New York, 1982.
5. MATLAB®, for MATrix LABoratory, is a product of *The Mathworks, Inc.*, 21 Elliot St., S. Natick, MA. 01760.
6. Sedgewick, Robert Algorithms, 2nd ed., Addison-Wesley, New York, 1988.

FIGURE 1: Photon Absorption Curves



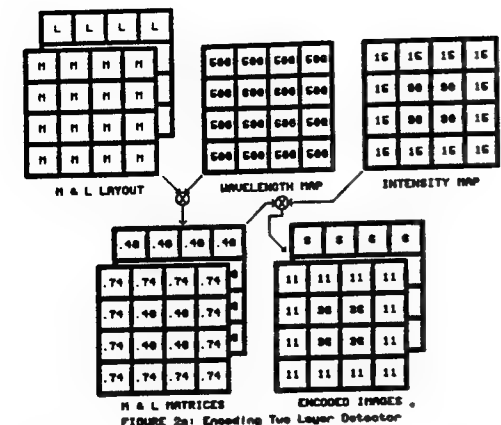


FIGURE 2a: Encoding Two Layer Detector

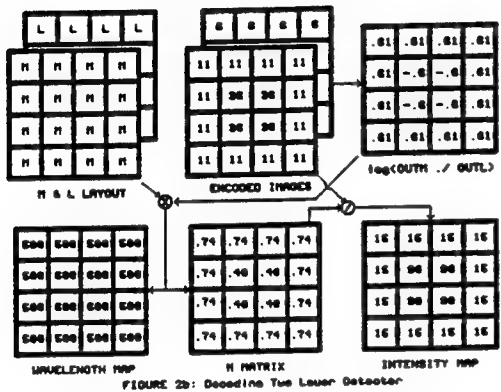


FIGURE 2b: Decoding Two Layer Detector

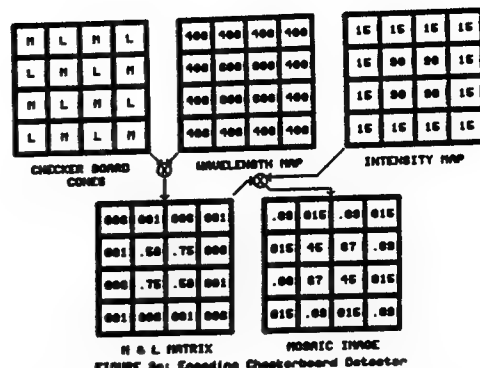


FIGURE 3a: Encoding Checkerboard Detector

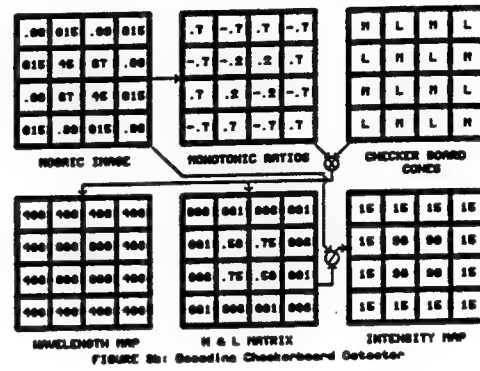


FIGURE 3b: Decoding Checkerboard Detector

Figure 2: Two-Layer Detector

Figure 3: Checkerboard Detector

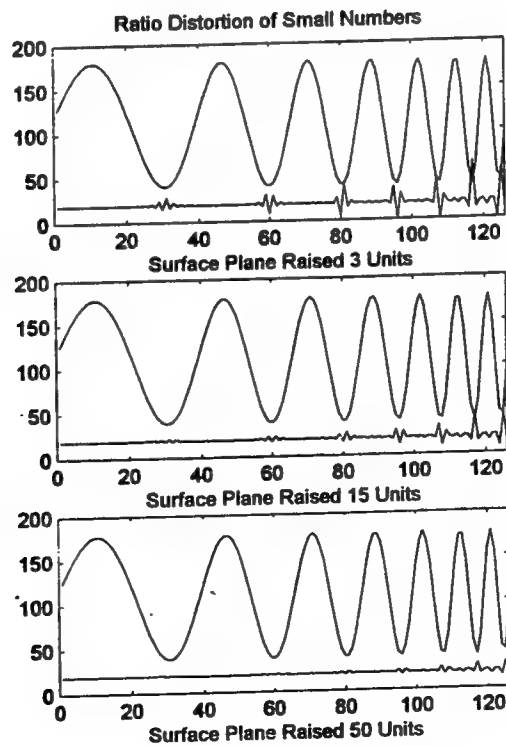
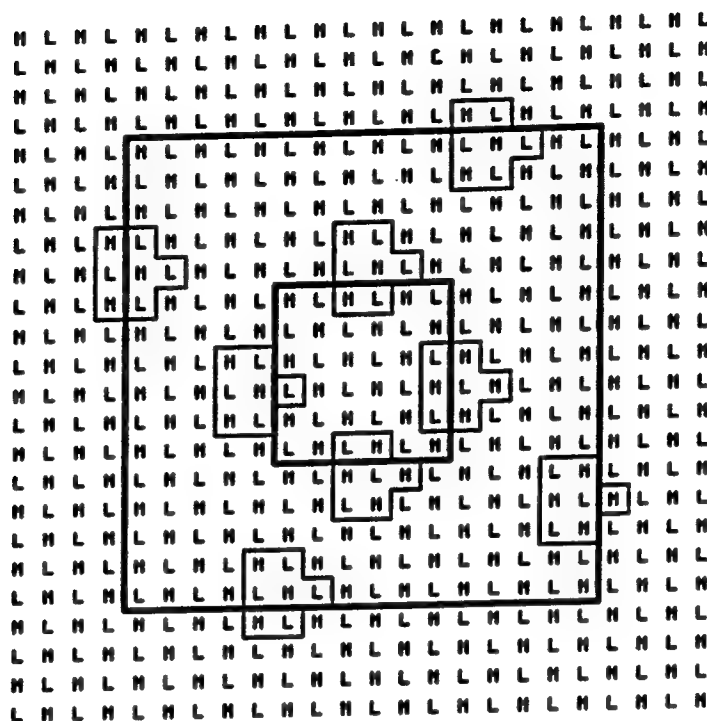
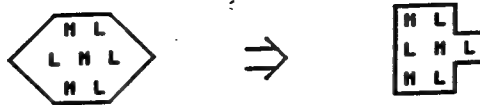
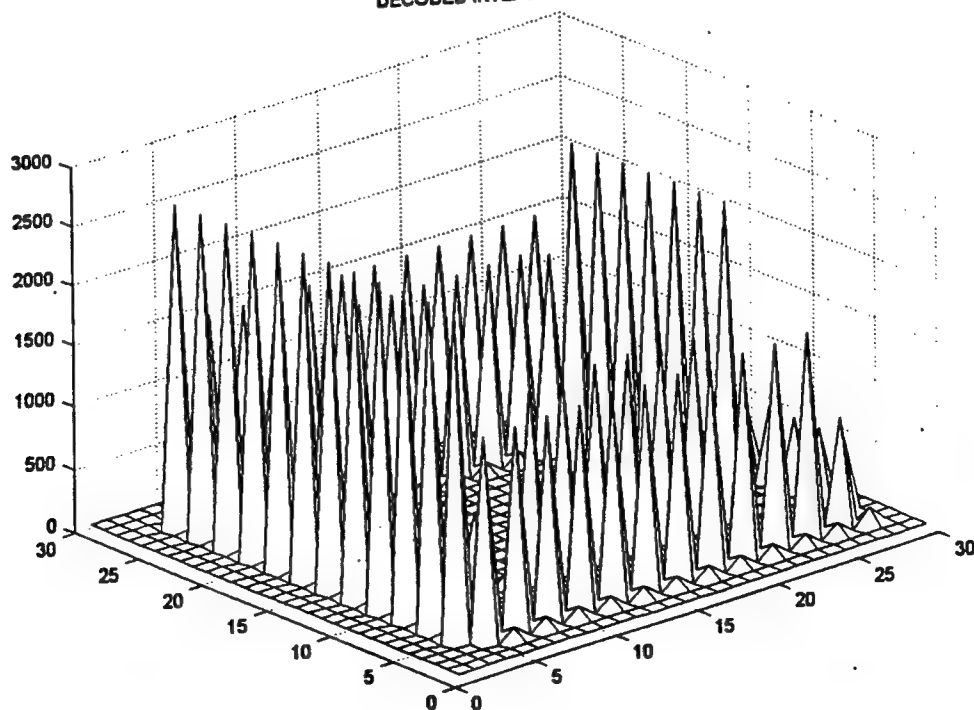


Figure 4: Ratio Distortion of Small Numbers



DECODED INTENSITY MAP



PROOF

Let M and L be two distinct monotone linear relations, with x their independent variable.

i.e. M can be represented by $M(x) = m_1x + b_1$ and likewise L by $L(x) = m_2x + b_2$. Further suppose $M(0)$ and $L(0)$ are not zero, i.e. b_1 and b_2 are not zero. Now, let R be their ratio (point wise) i.e. $R = M / L$ and R can be represented by $R(x) = M(x) / L(x) = (m_1x + b_1) / (m_2x + b_2)$. Now, we want to show that R is not a linear relation. To this end, let us assume R is linear and proceed to a contradiction.

First note that, if R is linear, $R(x)$ has a non-zero constant slope, m_0 (m_0 is defined and not zero since both $M(x)$ and $L(x)$ are linear monotone relations.)

Now, recall that $R'(x)$ is the slope of $R(x)$. By our assumption then $R'(x)$ is a non-zero constant. However, $R(x) = M(x) / L(x) = (m_1x + b_1) / (m_2x + b_2)$ and, as such,

$$\begin{aligned} R'(x) &= [(m_2x + b_2) m_1 - (m_1x + b_1) m_2] / (m_2x + b_2)^2 \\ &= (m_1 b_2 - m_2 b_1) / (m_2x + b_2)^2 \end{aligned}$$

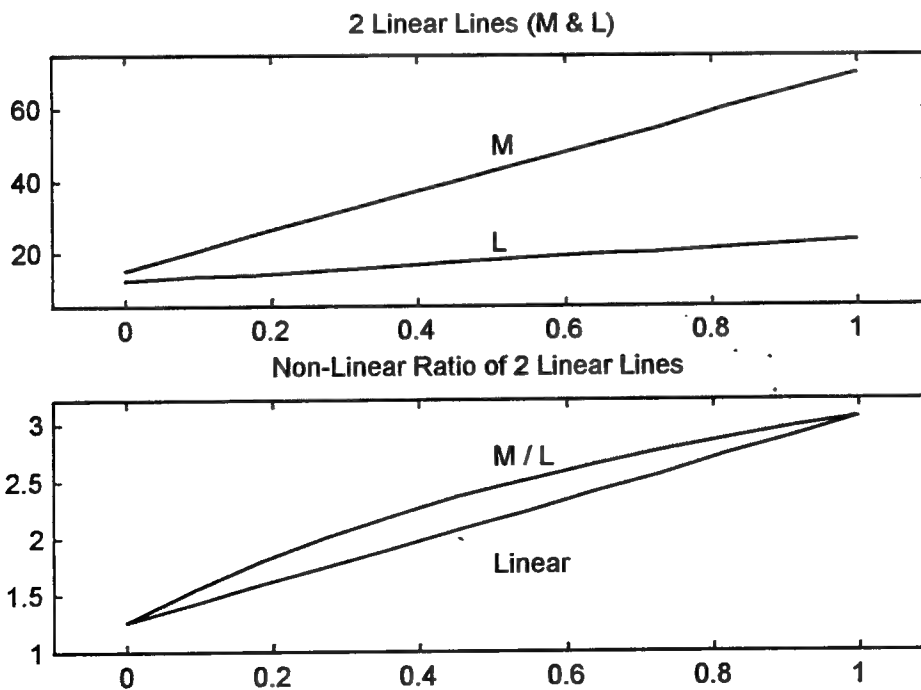
now if this is a constant our choice x is immaterial, so

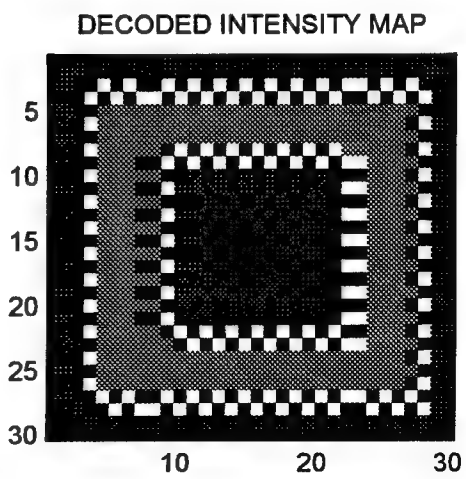
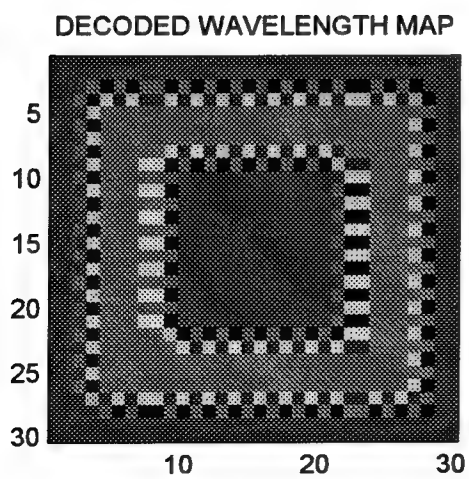
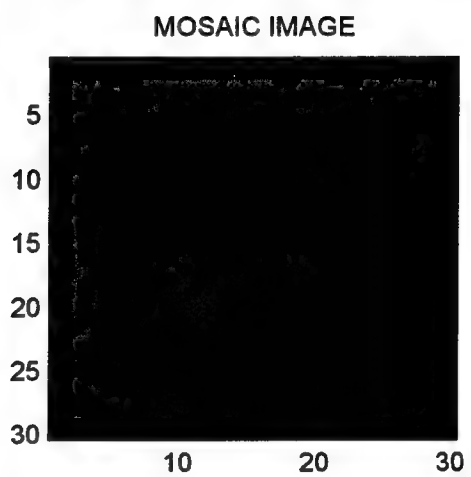
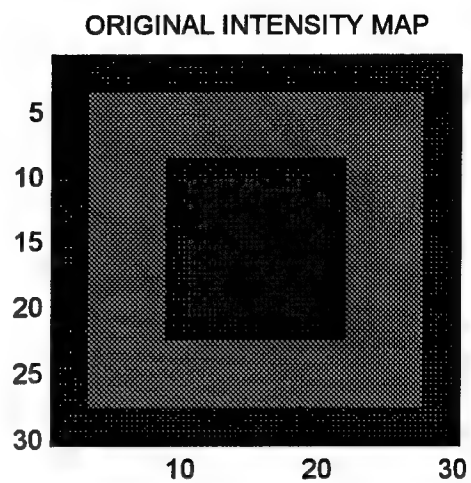
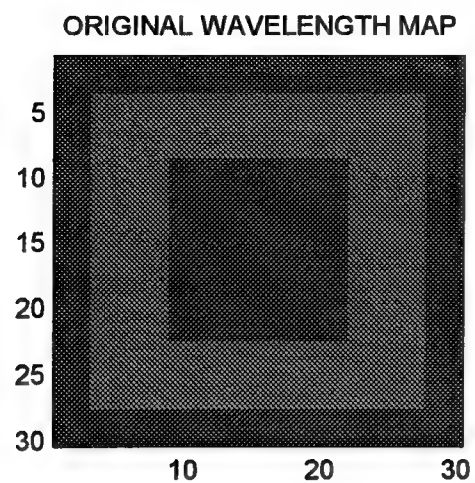
$$\begin{aligned} [(m_1 b_2 - m_2 b_1) / (m_2x + b_2)^2]_{x=1} &= [(m_1 b_2 - m_2 b_1) / (m_2x + b_2)^2]_{x=-1} \\ (-m_2 + b_2)^2 &= (m_2 + b_2)^2 \\ m_2^2 - 2 m_2 b_2 + b_2^2 &= m_2^2 + 2 m_2 b_2 + b_2^2 \\ - 2 m_2 b_2 &= 2 m_2 b_2 \end{aligned}$$

recall M and L are monotone and the slopes are not zero

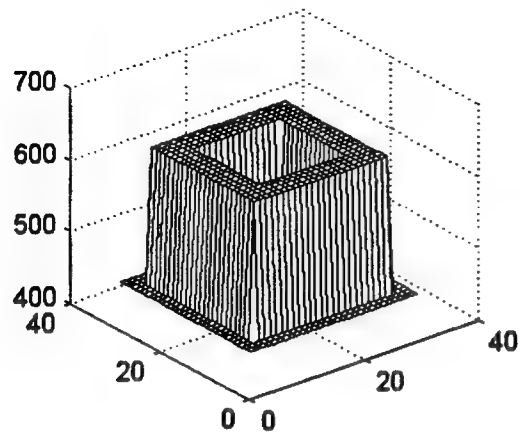
$$- b_2 = b_2 \rightarrow b_2 = 0$$

A symmetric argument, interchanging m_1 with m_2 and b_1 with b_2 shows $b_1 = 0$.

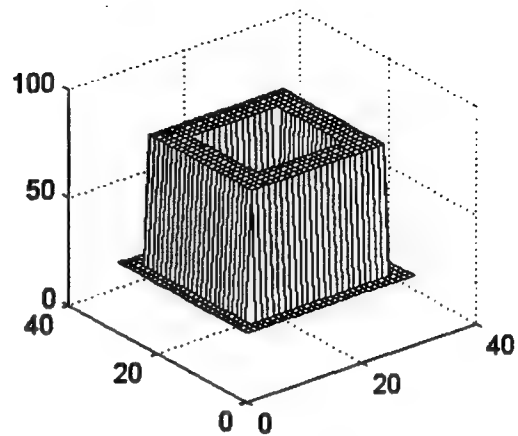




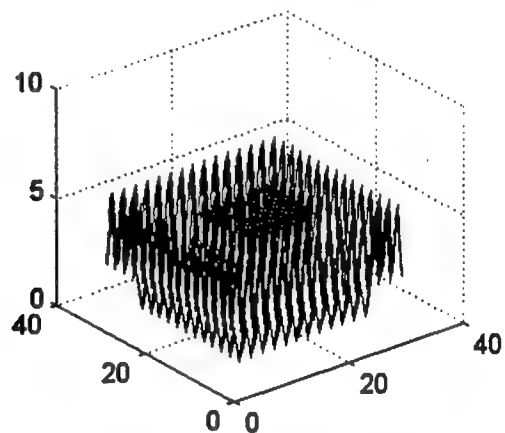
ORIGINAL WAVELENGTH MAP



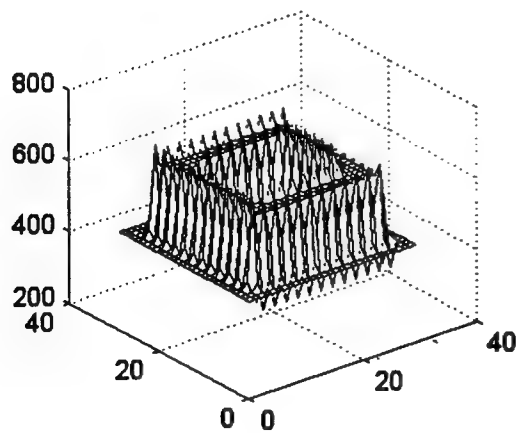
ORIGINAL INTENSITY MAP



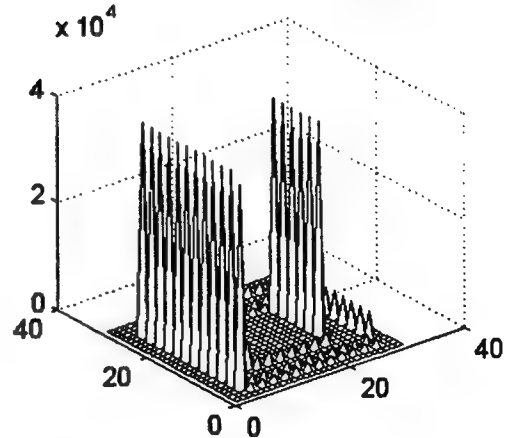
MOSAIC IMAGE



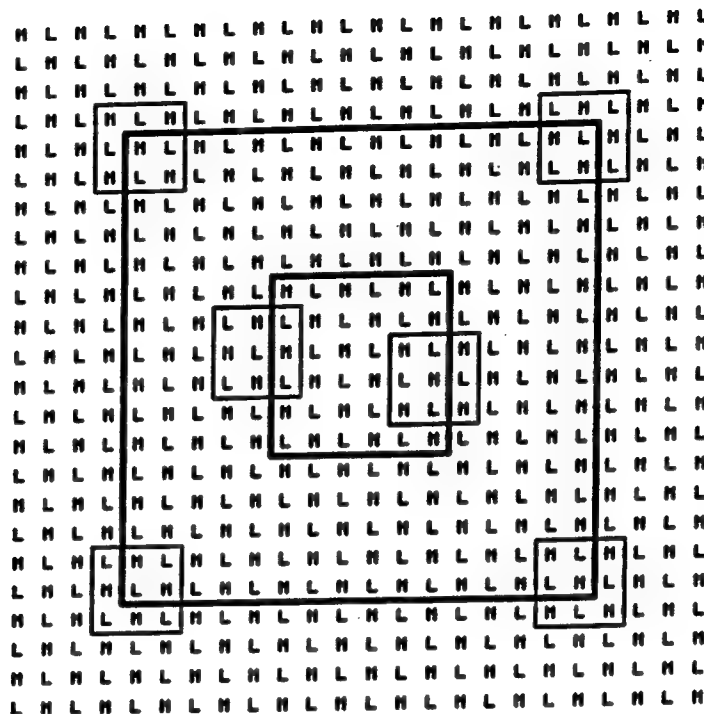
DECODED WAVELENGTH MAP



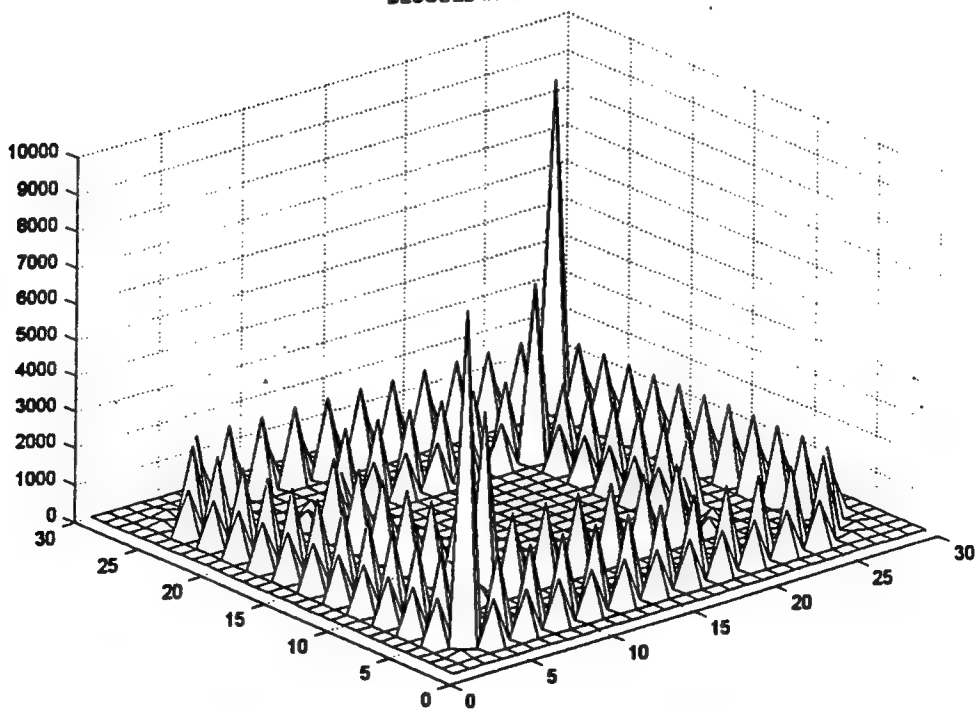
DECODED INTENSITY MAP



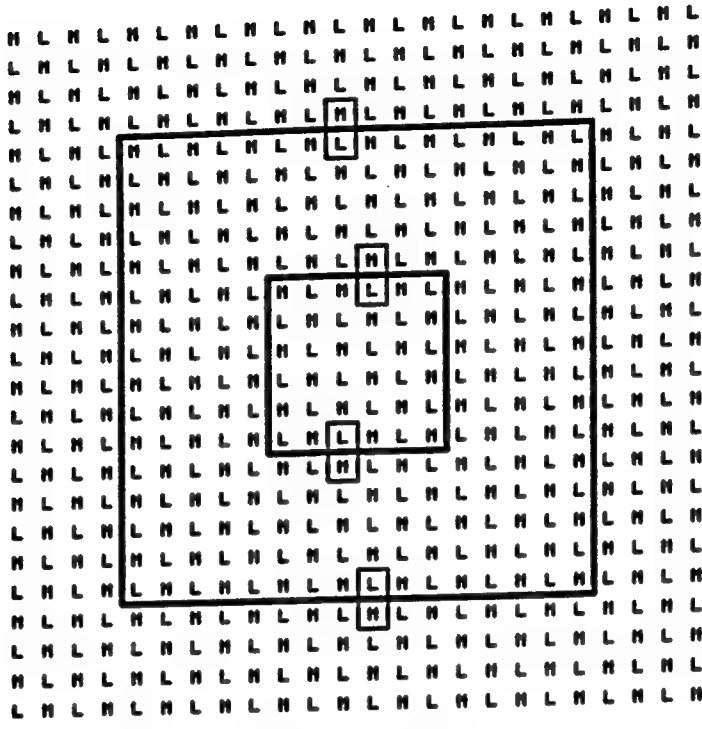
.5M	L	.5M
L	M	L
.5M	L	.5M



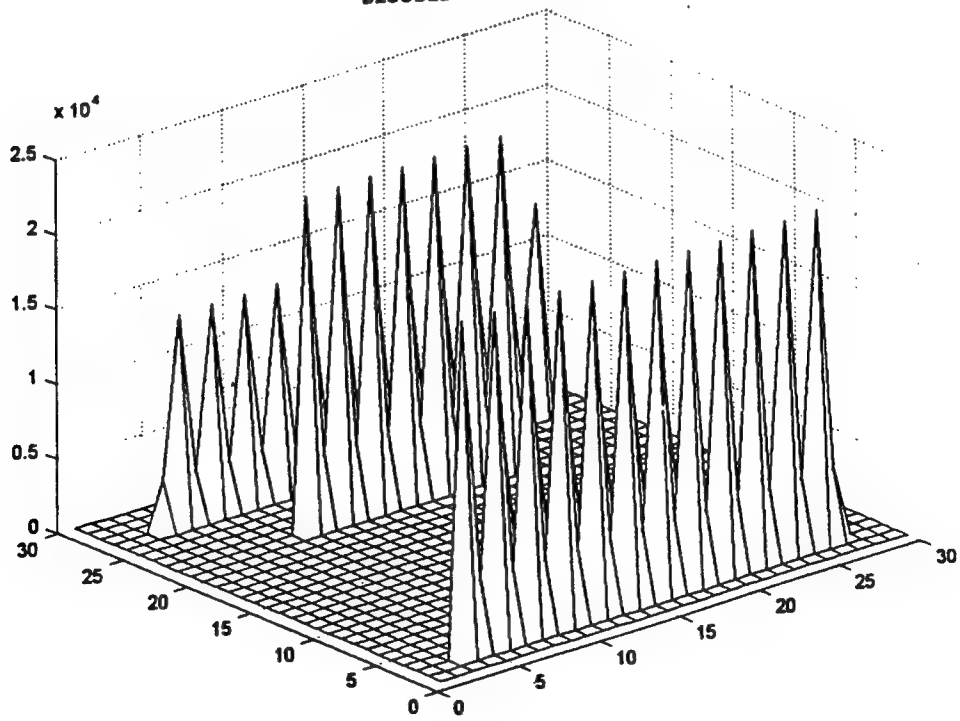
DECODED INTENSITY MAP



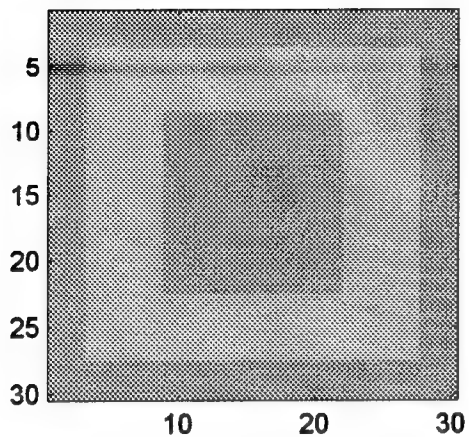
H
L
 H L



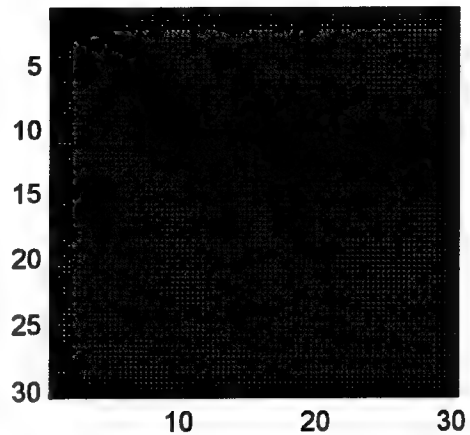
DECODED INTENSITY MAP



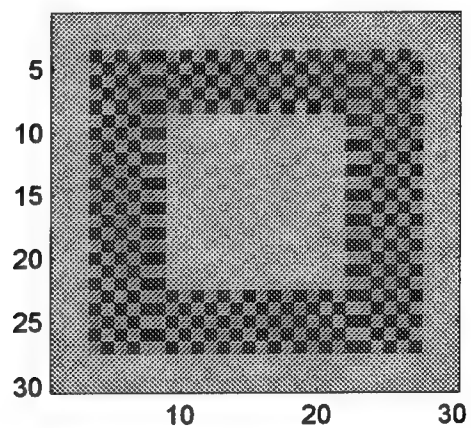
ORIGINAL WAVELENGTH MAP



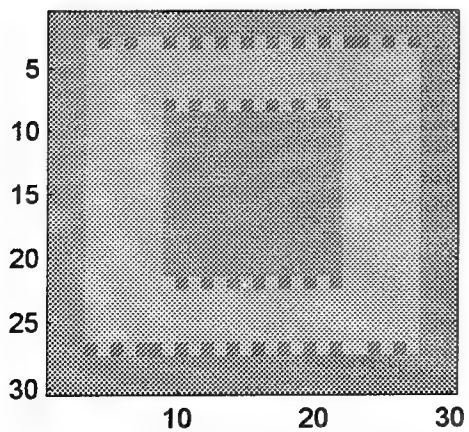
ORIGINAL INTENSITY MAP



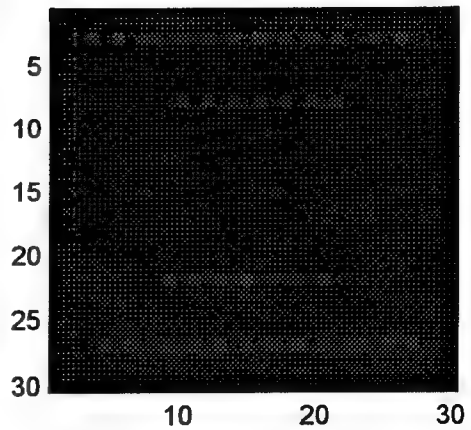
MOSAIC IMAGE

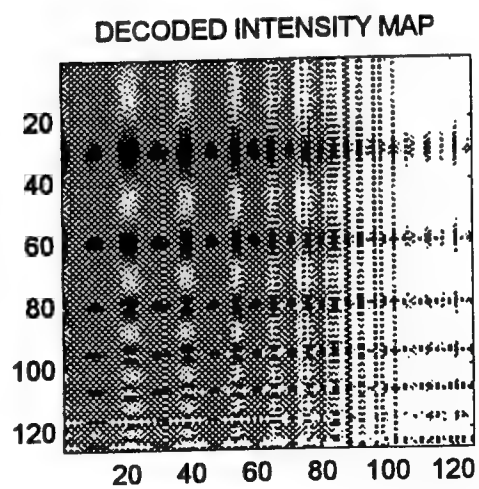
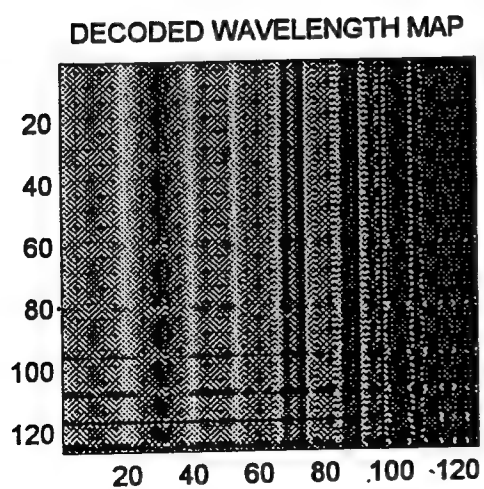
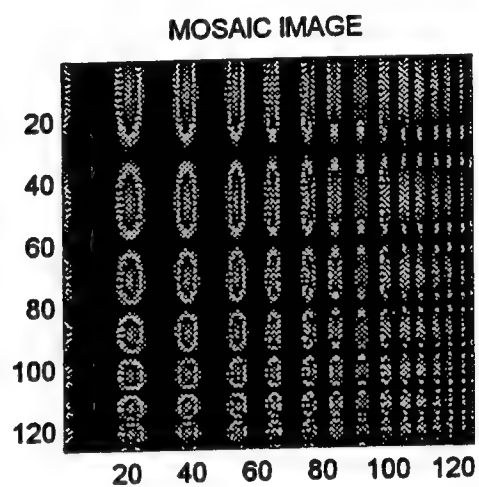
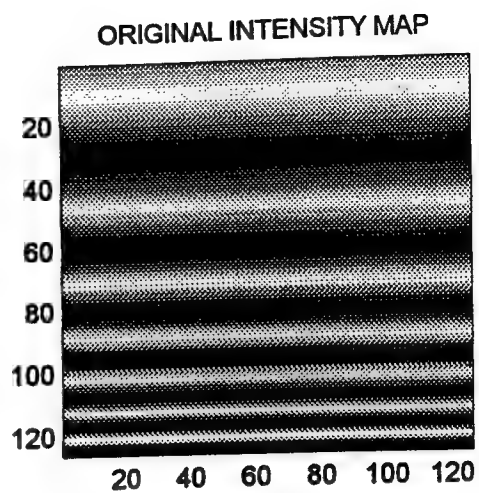
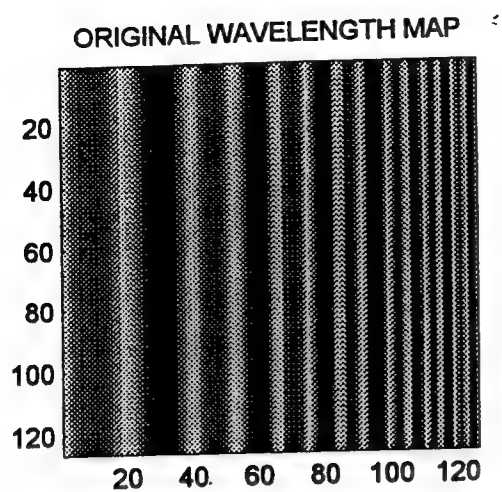


DECODED WAVELENGTH MAP



DECODED INTENSITY MAP





Associate did not participate in program.

**Investigation of Conductive Cladding Layers for Improved Poling in
Non-Linear Optical Polymer Waveguides**

**James P. Drummond
Ph.D. Graduate Student
Department of Materials Science and Engineering**

**The University of Cincinnati
PO Box 210012
Cincinnati, OH 45221-0012**

**Final Report for:
Graduate Student Research Program
Wright Laboratory**

**Sponsored by:
Air Force Office of Scientific Research
Bolling Air Force Base, DC
and
Wright Laboratory
Wright-Patterson AFB, OH**

September, 1997

Investigation of Conductive Cladding Layers for Improved Poling in Non-Linear Optical Polymer Waveguides

James P. Drummond
Ph.D. Graduate Student
Department of Materials Science and Engineering
University of Cincinnati

Abstract

The use of conductive layers to improve poling in non-linear optical waveguides was investigated. Research was centered on conductive layers formed from the conducting polymer poly (ethylene dioxythiophene) (PEDOT), and its blends. Preliminary investigations of other materials are also included. Thin films of these materials were produced by spin casting from solution and were then evaluated for their conductive, thermal and optical properties. These films were subsequently used to produce waveguides and simple Electro-Optic (EO) devices. Results indicate that these conductive layers performed well in EO devices, acting as buffer layers and providing improvements in poling. The conductive layers were also found to exhibit qualities necessary for construction of optical waveguides. Processing and Characterization techniques are presented for the materials investigated, and construction of devices is described.

Investigation of Conductive Cladding Layers for Improved Poling in Non-Linear Optical Polymer Waveguides

James P. Drummond

Introduction

In the past decade, the growing demand for dense communication networks, and the ever-increasing desire for rapid data transfer has bolstered the development of optical communications. Optical systems have provided the advantage of greater bandwidth and immunity to electro-magnetic interference or cross talk.¹ The wide spread acceptance of optics in communications and their gradual integration into computing has lead to the need for new optical materials and device structures. Currently, optical communications networks are based on glass fiber with active components designed in Lithium Niobate (LiNbO_3).⁽²⁻⁴⁾ These inorganic based systems have supported the development of the technology, but with these advancements comes the need for materials having greater capabilities. A search for new materials for use in these areas has led to the investigation of polymeric materials. In active components and for integrated technology, polymers promise many advantages over the current inorganic-based materials. Polymers permit relatively easy fabrication techniques, allow integration with conventional silicon based electronics and produce components which are less brittle.^{5,6} Polymers developed for use in active components have also been found to exhibit fast response times, and large Electro-Optic (EO) coefficients.^{7,8}

While this seems to make polymers ideal for optical applications, polymers also have their problems. One of the major problems seen in these materials is that in order to attain large EO coefficients the materials must be poled to produce a non-centrosymmetric structure. Poling refers to the use of an electric field to induce molecular alignment.^{7,9} Achieving the most efficient poling turns out to be

a difficult task that is affected by many material and physical properties. In general poling of a single layer polymer film is relatively simple. In order to produce devices from this polymer film however, a waveguide structure must be developed. This waveguide structure adds two cladding layers, one on either side of the guiding layer, making poling a more difficult task. If common highly resistive cladding layers such as SiO_2 are used, the voltages needed to pole the structure could easily reach well into the kilovolt range. These dangerous poling voltages can, however, be avoided through the use of conductive layers for the claddings of the polymer waveguide. Using cladding layers with lower resistance than that of the guiding layer would in effect drop the majority of the voltage across just the guiding layer. Development of this type of cladding layers has not been previously seen to any large extent. Previous research by S. Ermer et al demonstrated the use of an Acrylate cladding layer in polyimide systems.¹⁰ The success of the system presented was primarily based on the decrease in the resistance of the acrylate at temperature near its glass transition (T_g). The acrylate was found to work for this polyimide system, however, little has been done to find cladding layers which exhibit conductivity below T_g as well as at high temperatures. These proposed cladding layers could be used with a wide range of polymer guiding layers. With the successful development of these layers safe poling voltages could be used to produce efficiently poled non-linear optical polymer waveguides.

Experimental

Work was initiated by first finding promising materials to begin testing for use as cladding layers. The assumption was made that materials could be found having the conductive, thermal, and optical properties needed to produce these cladding layers. Procedures were designed to test materials for each of these

properties. The majority of the testing done was centered on poly (ethylene dioxythiophene) (PEDOT), and blends of this material with other polymers. Descriptions of this and other materials investigated will be discussed later. The polymers, once found, were then tested to determine their usefulness for this application. Experiments performed included testing these materials for their optical, thermal, and conductive properties. Data from these experiments were used to analyze how these materials would perform in poled waveguide devices.

Testing of the materials for their optical properties was an important component of the work done. In order to be used as cladding layers for waveguiding, absorption in these materials had to be relatively low. Determining the absorption of the materials was accomplished using a Cary Spectrophotometer. The percent transmission was measured over a range from 300nm to 1600nm. Analysis of the absorption seen in these spectra allowed materials to be chosen that had good optical transmission near the wavelength used in waveguiding.

Optical characterization continued with attempts to waveguide in samples containing these conductive cladding layers. Using an end fire coupled waveguide setup assembled for this project, analysis of materials for their waveguiding and optical loss characteristics was performed.

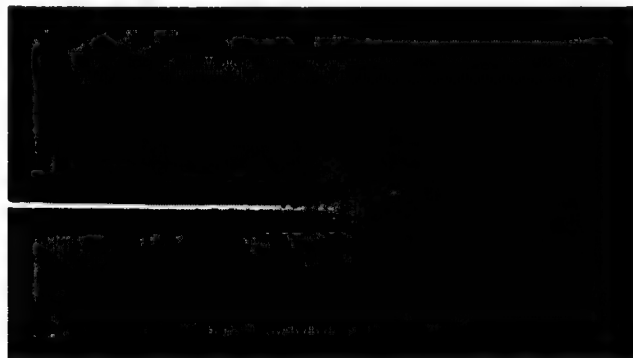


Figure 1: Outscattered light from poly (vinylchloride) waveguide

The system used included a 630nm HeNe laser, which was focused onto the cleaved edge of a polymer waveguide by a 5X-microscope objective. The propagation losses along the waveguide were then analyzed using a video capture method. The guide was observed by a Hamamatsu C2741 video camera from

which an image (Fig. 1) was captured and processed into a bitmap file using Adobe Premiere and Photoshop. This file was then analyzed for the reduction in outscattered light intensity along the streak. To determine the effect, which the cladding layers had on the propagation loss of a waveguide, a material with a consistent and easily measured optical loss first had to be found. Several materials were investigated. Materials such as poly (methyl methacrylate) (PMMA), poly (carbonate) (PC) and poly (styrene)(PS) all produced good quality waveguides, but had very low losses, and did not provide easily measured loss values. Other materials were found with suitable loss values such as poly (vinyl chloride)(PVC), poly (2-Acrylamido-2-methyl-1-propane sulfonic acid) (PAMPS), poly (phenylene oxide)(PPO) and poly (vinyl carbazole)(PVK). Of these, PVC was found to produce the highest quality films and provide reproducible loss values. PVC was therefore chosen to be the guiding layer for testing of cladding layers. A typical loss value for PVC can be seen in Figure 2.

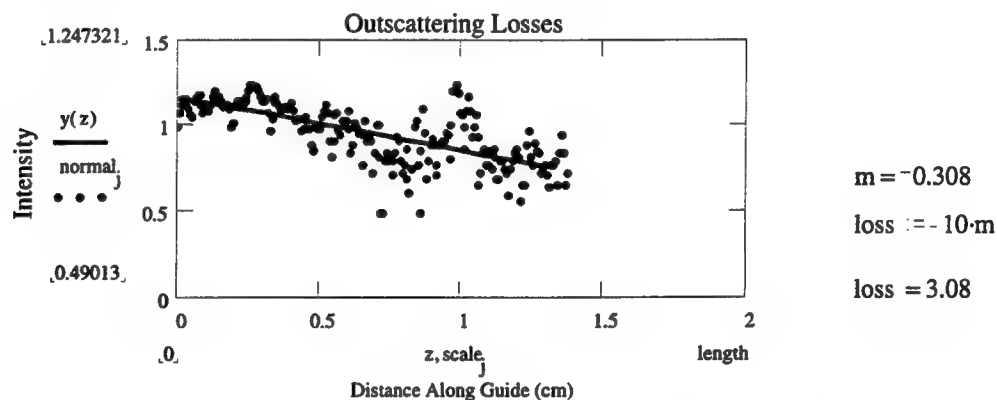


Figure 2: Optical Loss Measurement for PVC Waveguide with 630nm LASER.

In evaluating the conductive materials as cladding layers, the ability of the cladding to restrict the light to the guiding layer without increasing the loss or absorbance was to be determined. To test the capabilities of these cladding layers, two-layer waveguide structures were built. These waveguides had various conductive cladding layers combined with the guiding layers described above. It was found that the most important property in these evaluations was the index of refraction of the materials. In most cases the refractive index determined the

guiding properties of these structures. The refractive index of a waveguide was generally obtained through the use of a Metricon 210 prism coupler. The Metricon is a basic prism coupler, having a 630nm laser which is coupled into the sample by a prism having a refractive index of $n = 1.8$. The guides produce reflections, which vary corresponding to guided and non-guided modes. These reflections are monitored by a photo diode and this modal data is analyzed with respect to the angle of the incident laser beam. This analysis is used to obtain precise refractive index measurements for both multilayer, and single layer films.

The conductivity of the materials was investigated using a two-probe system enclosed in an inert nitrogen atmosphere. Tests were done to determine the conductivity of the materials with respect to voltage applied, and also with respect to temperature. This data was used to compare the prospective cladding materials to common guiding layers. The conductivity of these materials relative to the common guiding materials proved to be the dominating factor in choosing materials. Since only relative conductivity was necessary, absolute conductivity measurements were not pursued in these studies. Simple surface conductivity measurements were made using "per square" notation. The voltage for these measurements was supplied by a Bertan high voltage source. It was applied across 5mm square samples of the polymer thin films. The current in the samples was monitored and these values were recorded. Computer control was used to vary the temperature of the sample as well as the voltage applied to the sample. The results from this testing were used as a basis for choosing materials having the desired electrical properties for cladding layers.

The conductive materials were finally tested for their use in poling of EO polymers. These experiments required the construction of four-layered test structures. The samples constructed consisted of two electrodes, a conductive layer and the electro-optic layer, which was to be poled. The general design of these structures can be seen in figure 3. They were fabricated by first spincoating

the conductive polymer onto patterned indium tin oxide (ITO) glass, then adding a layer of EO polymer, and finally evaporating gold electrodes onto the top of the

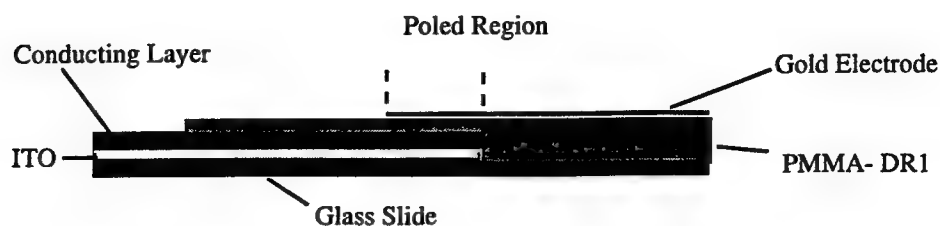


Figure 3: Test structure for use in measuring Electro-Optic Coefficients

structure. The samples were tested using a simple ellipsometric method, based on a measurement developed by Teng and Mann. In this method EO values are measured by monitoring the change in the polarization state of an incident light beam as it passes through the sample film, and is then reflected back to a photodetector.¹¹ The intensity values measured at the photo diode are analyzed by a Stanford Research 530 lock-in. This data is then processed using IGOR Pro technical software to calculate EO values in pm/V. The design of the experimental setup allowed measurement and monitoring of most of the important experimental variables throughout the poling process. This led to a better understanding of the poling kinetics of the system and tighter control over poling parameters. With this in-situ poling setup, more can be learned about the properties of the system during poling, such as chromophore mobility, glass transition temperature and dielectric properties.

Results and Discussion

Initial research was performed on a conducting polymer supplied by the Bayer Corporation. The polymer poly (ethylene dioxythiophene) (PEDOT) is transparent blue in color and comes in a poly (styrene sulfonic acid)/water solution. This material was tested in its pure form, as well as in blends with other

polymers. Preliminary testing of PEDOT/PSS found that films could be produced from the solution as obtained, however, film thickness was low ($\sim 0.3\mu\text{m}$). Analysis of the transmission spectra of these films also indicated that in this form, they had only 70-80 % transmission. This level of absorbance would probably lead to large losses in any attempt to waveguide. This indicated that blending of this material with another polymer might be necessary to improve thickness and transparency. Testing however continued in order to determine the other abilities of these PEDOT films. Conductivity testing on these samples proved promising having a value of resistance of approximately $5 \times 10^5 \Omega$. The conductivity also seemed to be very stable with both increased temperature and voltage. Attempts were also made to produce EO devices and waveguide structures out of these films. During this time it was determined that the PEDOT polymer films were slightly soluble in many common organic solvents. This made it difficult to produce any two layered structures. It was found that spinning a polymer such as PMMA on top of the PEDOT layer would cause the entire two layered film to become conductive. This phenomenon was believed to be due to the diffusion of the polythiophene into the PMMA layer. This prevented poling of the EO devices using pure PEDOT conductive layers and also discouraged any hope of waveguiding in these structures. These two layer PEDOT/PMMA films, however, have been investigated as another method of producing thicker more transparent conducting films.

The investigation above lead to the idea of blending the PEDOT material with another polymer. In order to accomplish this task, the solubility properties of the PEDOT material were first investigated. It was found that although the polymer was slightly miscible in many solvents, it could not be completely dissolved in any of the solvents investigated other than water. This narrowed the possible blending polymers to those that were water-soluble. Several polymers

were investigated for these blends. Poly (2-Acrylamido-2-methyl-1-propane sulfonic acid) (PAMPS), poly (vinyl acetate) (PVAc), poly (vinyl alcohol)(PVAI), poly (acrylamide) (PACY) and poly (methacrylic acid)(PMA) were all chosen as possible blending agents. It was determined that the PEDOT/PVAI films were most promising. The solutions produced from this blend were clear blue in color, and were miscible at any ratio of the two solutions. Solutions of PVAI were first made by dissolution of the PVAI in water with heat and stirring. The PEDOT/PSS solution was then added to create the desired blend. Solutions of PVAI in water were 7wt% and 10wt%. To these solutions, various loading percentages of PEDOT solution were added. The solutions made ranged from 1wt% up to 60wt% PEDOT in PVAI. Films were then produced by spin casting at 1000 rpm under a heat lamp. The films produced were on average 1.5 μm thick for 7% PVAI solutions and 2 μm thick for 10% PVAI solutions. Films spun at 1000rpm were uniform and transparent. The transmission spectra for the various PEDOT loaded

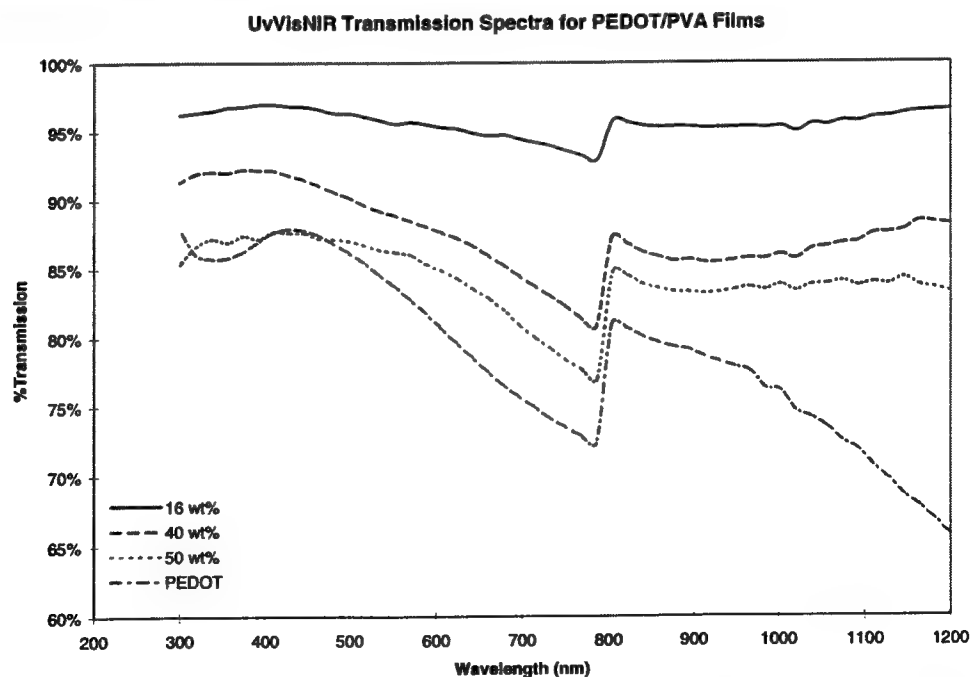


Figure 4: UVVis Data for PEDOT/PVAI Blends with Increasing PEDOT Doping.

films were analyzed and as expected, there was a gradual increase in absorption as doping levels were increased (Fig. 4).

It was also interesting to observe that a similar trend occurred in the conductivity of the films. As doping levels were increased, the conductivity also began to increase. This indicated that the PEDOT polymer must retain conductive pathways even at low doping levels. This is opposed to what is seen in some doped polymers where a threshold doping level is required to achieve conductivity and below this threshold little conduction is observed. The conductivity of pure PVAI was first tested, and then films with increased PEDOT doping were measured. These measurements can be seen in Figure 5.

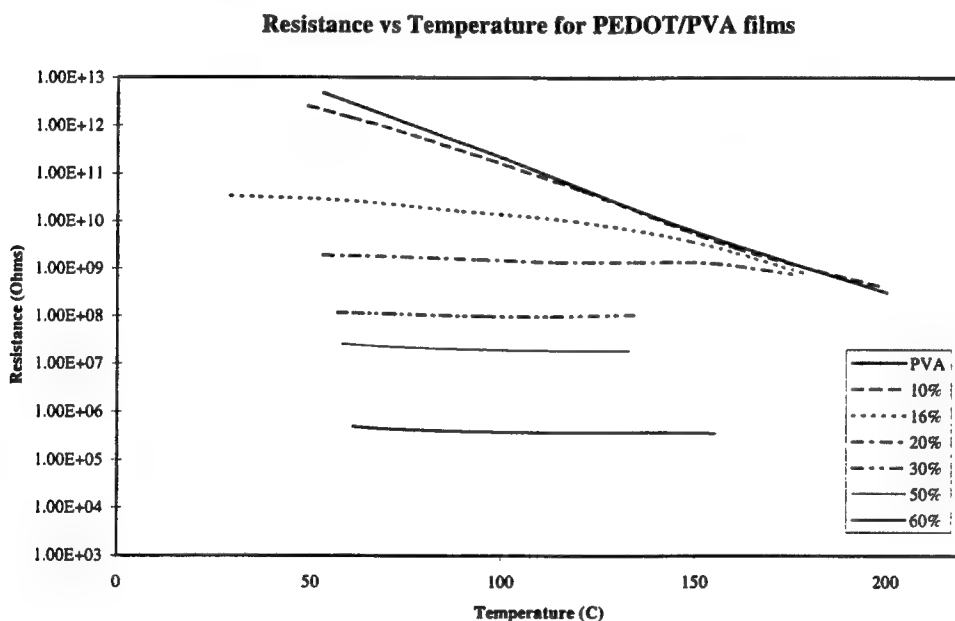


Figure 5: Resistance Measurements for PEDOT/PVAI Blends Having Increasing PEDOT Doping.

The conductivity of highly doped PEDOT/PVAI blends was relatively constant with temperature, and well above that of the pure PVAI sample. Testing samples with very low doping levels showed that although they had relatively constant conductivity at low temperatures, at higher temperatures their

conductivity followed that of pure PVAI. This indicated that even in samples having low doping levels, the low temperature conductivity of the PVAI could be enhanced. This would improve the poling of EO samples at low temperatures, and retain more of the EO value during the cooling process. A comparison of the conductivity of these films to that of a common guiding layers showed that at all temperatures between 50 and 180°C, these PEDOT/PVAI films have lower resistance, and are predicted to perform well as conductive layers for the poling of EO devices.

Poling with the PEDOT/PVAI conducting layers was accomplished using the EO test structure mentioned earlier. A standard electroactive layer was chosen for these studies. Due to its widespread use PMMA doped with Disperse Red 1 (DR1) was used as the active layer in these devices. A solution of 10% PMMA in cyclopentanone doped with 10% DR1 was used to create the thin films needed. This solution was spun at 600 rpm and produced excellent films of approximately 1.5 μ m thickness. Initially, simple single layer DR1 samples were made on ITO glass with evaporated gold top electrodes. The area for poling in these devices was determined by the coincident areas of the lower patterned ITO electrode and the gold top electrodes. These samples were used to develop a standard with which to compare the poling data from the devices made with conducting polymer layers. A substantial base of data was gathered on these systems prior to testing samples with the conducting polymer. In producing the devices with conductive layers, PEDOT/PVAI films were first deposited onto the patterned ITO glass, then the active layer was spun onto this lower layer. No dispersion of the PEDOT into the PMMA layer was observed in these systems. It was assumed that the PVAI host polymer sufficiently isolated the PEDOT so that it did not encounter the solvent, and therefore did not dissolve when the top layer was deposited. The devices made were then tested to determine if the active layer could be poled through the

conductive layers. Successful poling of PMMA/DR1 films was accomplished using PEDOT/PVAI films as buffer layers. This indicated that the conductive layers were successful in transferring the DC voltage to create a potential drop across the non-conductive guiding layer. This allowed efficient poling of the guiding layer to be achieved as if contacts were placed directly on the poled film. Another added benefit of these conducting layers was that they seemed to act as buffer layers to prevent the voltage from shorting through the polymer films. It was also seen that even when obvious shorts or sparks developed, the sample did not immediately fail as is often the case with single layered EO samples. These conductive polymers acted as an isolation layer between the EO polymer and the ITO surface, which is often rough and has been known to cause shorting. A large number of tests were performed on this system, and the results showed that EO values obtained from these devices were comparable and on average slightly higher than those achieved by direct poling of PMMA/DR1 films under similar conditions. Because these samples had the added benefit of withstanding higher voltages before breakdown, larger EO coefficients were achieved. The enhancement of the EO value was perhaps the greatest benefit of the incorporation of these conductive layers.

These PEDOT/PVAI layers were also tested on a second active layer to determine if the advantages seen in the PMMA/DR1 system would be seen in various systems. This second set of samples was based on DR1 incorporated into a new matrix polymer, poly (vinyl carbazole) (PVK). Samples were made from solutions of 5wt% PVK in 1,2 Dichloroethane loaded with 10 % DR1. These samples were poled at much higher temperatures and retained much of this poling even at these high temperatures. Significant values of EO coefficient were seen at temperatures up to 160°C. These PVK/DR1 films were therefore shown to be a very stable system for the DR1 chromophore, having moderate to high temperature

capabilities. This allowed testing of the polymer cladding layers in much different set of conditions. As in the PMMA/DR1 system, the PVK/DR1 samples were made as both single layer structures and multi-layer structures with conductive buffer layers. Studies of the PVK/DR1 samples showed that this system had some inherent differences from the PMMA/DR1 system. The EO values obtained for the PVK system were initially somewhat smaller than those seen in PMMA. These values, however, showed lower relaxation over long periods of time. In PMMA systems, relaxation of the EO coefficient with time is a major problem. The differences seen in the PVK/DR1 system can be attributed to the higher T_g of the material and resulting lower chromophore mobility. The testing of this system with the conductive layers had similar results as those seen in the PMMA/DR1 system. Samples attained higher EO values on average, and higher ultimate EO values could be achieved due to the protection provided by the conductive buffer layer. This experiment showed that conductive layers could be effective in devices having different active layers.

Next the PEDOT/PVAI films were investigated for use as cladding layers for waveguiding. The first sample tested consisted of the guiding layer (PVC) deposited on a cladding layer of 10% PEDOT in PVAI. The UVVis spectrum of this cladding layer indicated that the film had between 95% and 100% transparency. The quality of the films spun on SiO_2 , however, was not very high. The films were non-uniform and contained some defects. Attempts at guiding in this first sample were unsuccessful. This result could have been due to trouble coupling into the film or the poor quality of the cladding layer, but was most likely due to a refractive index mismatch. In a waveguide structure, the index of the guide layer must be higher than that of the cladding to obtain the total internal reflection needed for propagation.¹² The refractive index of the cladding layer in this sample was yet to be determined and might have been larger than that of PVC

($n = 1.54$). Although a pure PVAI film has an index of 1.51, the PEDOT doping level could change the refractive index of the blend. This most likely caused the light to couple out of the PVC guiding layer into the cladding layer, resulting in absorption and thus no propagation.

A second sample was constructed consisting of a PVK guiding layer spun onto a 25wt% PEDOT in PVAI cladding layer. This sample exhibited guiding in the PVK top layer and displayed lower than expected losses. The guiding, however, did not form a defined streak. This was possibly due to the poor quality of the cladding surface. In this sample, the refractive index of the PVK film ($n = 1.68$) was much larger than that of PVC, increasing the confinement of the light and increasing its potential for guiding. Examination of this waveguide using the Metricon prism coupler defined the thickness and refractive index of each layer. The refractive index of this 25wt% PEDOT/PVAI film was determined to be $n = 1.58$. These results can be seen in Figure 6.

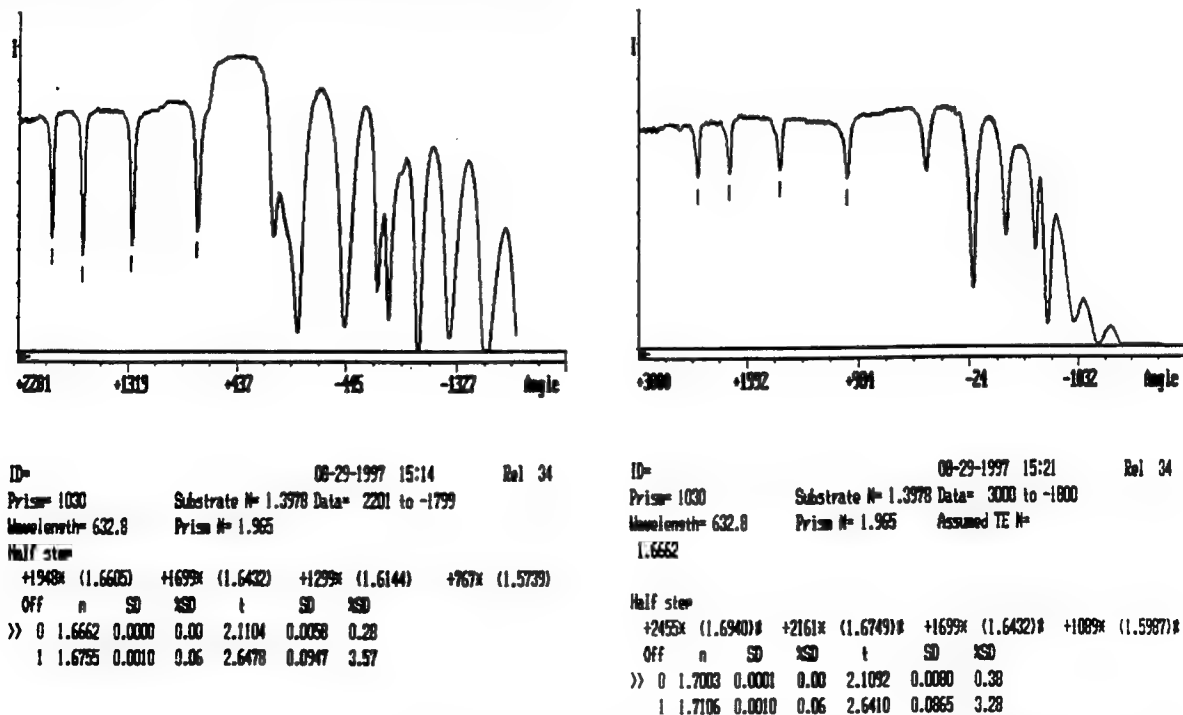


Figure 6: a) TE and b) TM graphs of Dark Line Reflection from Metricon Prism Coupler for Two-Layered Waveguide. Refractive Index (n) and Thickness (t) measurements are displayed.

The change in index of refraction with doping level of these PEDOT/PVAI films was also investigated. PEDOT/PVAI films were made with various levels of PEDOT. The Metricon prism coupler was used to determine the refractive index of these samples. The values were seen to increase incrementally with increased doping level of the PEDOT in the PVAI solution. This information made it possible to choose a guiding layer with the correct refractive index to optimize guiding in these systems. The construction of future guides can therefore be modeled more exactly.

The guiding exhibited in the PVK sample above and the benefits seen in poling demonstrate the potential of using PEDOT/PVAI conductive layers in the constructing of poled waveguide devices.

Investigation of other polymers for use in conductive cladding layers was also initiated. Near the end of this research project, poly (aniline) materials were obtained from the Monsanto Corporation. Due to limited time and continued work on the PEDOT systems, only preliminary testing was accomplished. The materials received were two solutions based on the emeraldine base form of poly (aniline). The first material received was a xylenes soluble version of the polymer. This polymer was referred to as PANDA. The solution formed excellent, uniform, thick films as received. These films, however were very dark in color, and were susceptible to many solvents. Conductivity measurements on these films showed excellent conductivity. Resistance values as low as $8 \times 10^3 \Omega/$ were obtained for these films. This level of conduction indicated that blending of this polymer could yield promising conductive properties. The miscibility of the PANDA material with other solvents also allows blending with a large variety of polymers.

The second material received was a water-soluble version of poly (aniline). This was referred to as PANA. This material, as delivered, was a 10wt % solution of poly (aniline) and Poly (styrenesulfonate) in water. The solution was similar to

the PEDOT solution tested previously in that it only produced very thin films. These films are light green in color and had conductivity that was slightly lower than that of the PANDA materials. Blends of this material were readily made with the variety of polymers tested for the PEDOT system (PMA, PACY, PAMPS, PVAI). The blends made with PANA all produced good quality films. The solubility of the PANA material allowed some solutions in methanol as well as water. The blends created from PAMPS/PANA were investigated to the greatest extent. These films were spun out of methanol allowing much greater film quality than films spun from water. The films produced were blue-green in color, and had a high level of conductivity.

The higher conductivity and the more versatile processing capabilities of these poly (aniline) materials offer many benefits over the PEDOT systems tested previously. Continued testing of these materials should result in further enhancement in the area of conductive cladding layers for optical waveguides.

Conclusion

Through the use of the inherently conductive polymer poly (ethylene dioxythiophene), blended polymer films have been developed for use in conductive cladding layers. Conductivity of these films has been shown to increase linearly with conductive polymer doping level. The conductive properties of these films made them useful as buffer layers in the poling of non-linear optical polymers. Metricon measurements showed that a gradual increase in refractive index was seen with increased doping. The optical properties allowed the films to perform as successful cladding layers for simple planar waveguides. Through continued design this system and investigation of other promising systems, the development of optical devices with conductive cladding layers should be attainable.

References

1. A.Nahata, D. Auston, C. Wu and J.T. Yardley, "Generation of terahertz radiation from a poled polymer" *Appl. Phys. Lett.* **67**,1358 (1995)
2. M. Abe, T. Kitagawa, K. Hattori, A. Himeno and Y. Ohmori, "Electro-optic switch constructed with a poled silica based waveguide on a Si substrate" *Electronics Lett.* **32**, 893 (1996)
3. M.Yamada, N. Nada, M. Saitoh and K. Watanabe, "First-order quasi-phase matched LiNbO₃ waveguide periodically poled by applying an external field for efficient blue second-harmonic generation" *Appl. Phys. Lett.* **62**, 435 (1992)
4. R. Dagani, "Devices based on electro-optic polymers begin to enter marketplace" *Chem. & Eng. News.* p.22, March 4, 1996
5. D. Gerold, R. Chen, W.A. Farone and D. Pelka, "Poled electro-optic photolime gel polymer doped with chlorophenol red and bromomethyl blue chromophores" *Appl. Phys. Lett.* **66**, 2631 (1995)
6. J.S. Cites, P. Ashley, R. Leavitt, "Integration of nonlinear optical polymer waveguides with InGaAs p-i-n photodiodes" *Appl. Phys. Lett.* **68**, 1452 (1996)
7. P.C. Ray and P.K. Das, "Influence of poling methods on the orientational dynamics of 2-methyl-4-nitro-aniline in poly (methyl methacrylate) studied by second harmonic generation" *Euro. Polym. Journal.* **32**, 51 (1996)
8. D. Chen, et al, "Demonstration of 110 Ghz electro-optic polymer modulators" *Appl. Phys. Lett.* **70**, 3335 (1997)
9. R.H. Page et al, " Electrochromic and optical waveguide studies of corona-poled electro-optic polymer films" *Journ. Opt. Soc. Am. B.* **7**, 1239 (1990)
10. S. Ermer et al, "DCM-polyimide system for triple-stack poled polymer electro-optic devices" *Appl. Phys. Lett.* **61**, 2272 (1992)
11. C.C. Teng, and H.T. Man, "Simple reflection technique for measuring the electro-optic coefficient of poled polymers" *Appl. Phys. Lett.* **56**, 1734 (1990)
12. E.D. Jungbluth, "Optical waveguides advance to meet fiberoptic demands" *Laser Focus World*, p.99, Apr. 1994)

**COMPUTER SIMULATION OF FIRE SUPPRESSION
IN AIRCRAFT ENGINE NACELLES**

**Gary Dulaney
Graduate Student
Department of Mechanical Engineering**

**Brown University
184 Hope St.
Providence, RI 02912**

**Final Report for:
Graduate Student Research Program
Wright Laboratory**

**Sponsored by:
Air Force Office of Scientific Research
Bolling Air Force Base, DC**

and

Wright Laboratory

August 1997

COMPUTER SIMULATION OF FIRE SUPPRESSION
IN AIRCRAFT ENGINE NACELLES

Gary Dulaney
Graduate Student
Department of Mechanical Engineering
Brown University

Abstract

Computer modeling of aircraft engine nacelle fire suppression experiments was performed. This is a continuation of a project begun by Applied Research Associates, Inc. A finite difference program is being utilized to replicate tests conducted using the Aircraft Engine Nacelle Fire Test Simulator. Both the meshed configuration of the engine nacelle and processing parameters used to identify all conditions of the experiments were analyzed and evaluated. Where appropriate, corrections were made to the existing model with the goal being to idealize the physical experiments. Future work with this project will hopefully allow for experiments to be conducted using the computer simulation.

Introduction

This report will focus on the efforts to utilize a fluid dynamics-based computer program to simulate the effects of fire suppression techniques in aircraft engine nacelles (AEN).¹ This work will, in part, be used to supplement the National Halon Replacement Program for Aviation (NHRPA), a major project conducted by the Air Force, Army, Navy, and Federal Aviation Administration. This program stemmed from the federal ban of the production of halon due to its depletion of the ozone layer. Because halon-based extinguishing agents are the basis of many fire protection systems on air vehicles, a suitable replacement is needed. The computer program used to model the AEN will be described, along with the various steps taken to set up the model, problems encountered along the way, and future recommendations for the continuation of this part of the program. However, before the project is detailed and explained, a brief summary is necessary to better understand the scope of what was accomplished during the tour.

History

The first task under the NHRPA involved identifying a short-term replacement agent for halon which met certain pre-defined criteria, including fire suppression capability and impact on the environment. The replacement agent eventually chosen was HFC-125. HFC-125, or pentafluoroethane ($\text{CHF}_2\text{-CF}_3$), is a hydrogenated haloethane widely used in refrigeration applications. It was chosen due to its fire suppression effectiveness and minimal harmful interactions with aircraft materials, people, and the environment. The next step taken made use of Design of Experiments (DOX) methods to plan tests and analyze data in such a manner as to limit the required number of tests to a minimum.² The tests were conducted using the Aircraft Engine Nacelle Fire Test Simulator (AENFTS), a template nacelle designed to simulate in-flight conditions for a variety of different aircraft (Figure 1). The AENFTS is located at the Air Force Research Laboratory at Wright-Patterson AFB. The size of the inner core used for this exercise is 36" in diameter and the outer core is 47" in diameter. Fully annular airflow is blown through the nacelle and a fuel spray is directed into the nacelle a set distance downstream from the airflow. Once the fuel is ignited (via a propane/air mixture and spark ignition), the agent is discharged into the nacelle upstream of the fuel point source. Pressure and temperature recordings are measured at various locations throughout the nacelle as the agent is extinguishing the fire. There also exists a 'hot spot', a portion of the inner core

¹ A nacelle is the area between the body of an aircraft and the shell of the aircraft engine.

² Design of Experiments is a powerful technique utilized to obtain the maximum amount of data with the minimum number of trials.

covering a 100° arc and which is 30" long. It is electrically heated and serves as a source of reignition of the flame after it is extinguished. Figure 2 shows a cross-sectional view of the AENFTS.

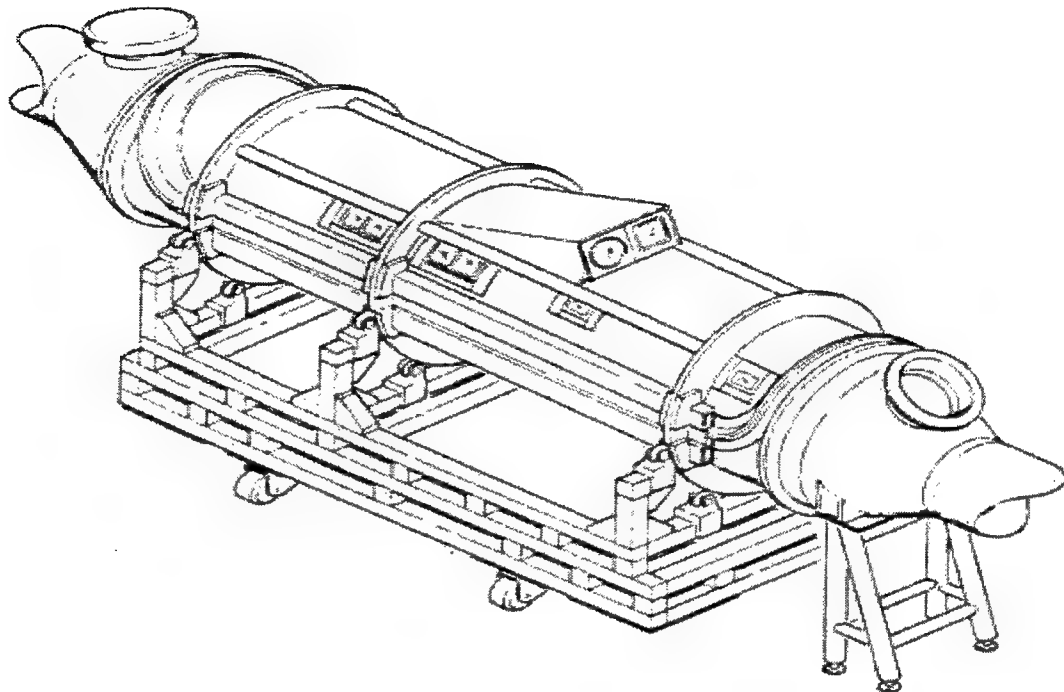


Figure 1. Aircraft Engine Nacelle Fire Test Simulator

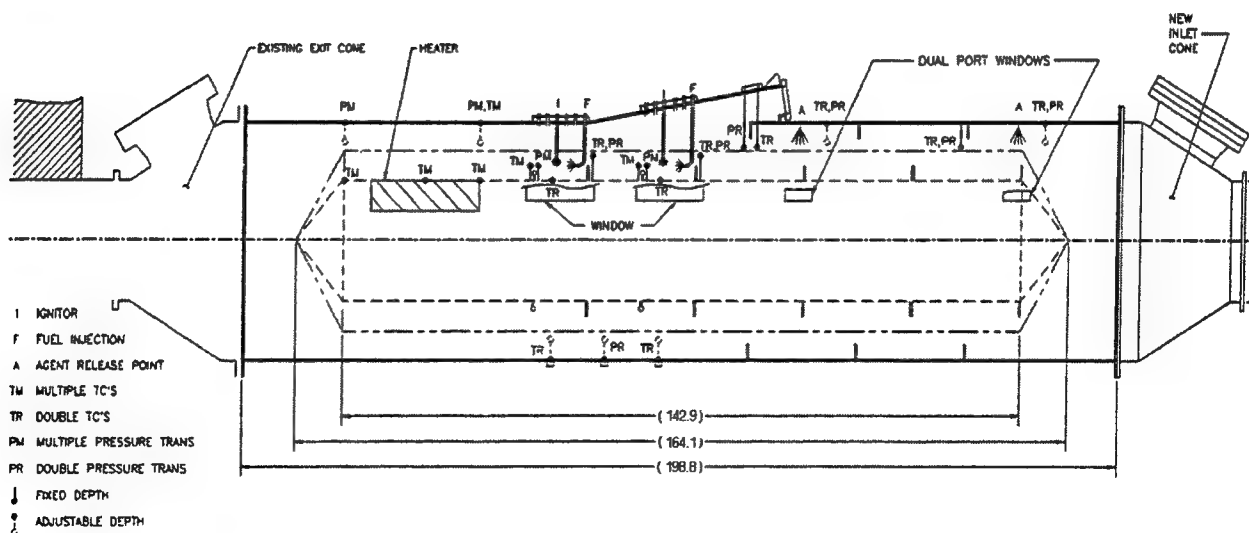


Figure 2. Cross-sectional view of the AENFTS (lengths in inches)

Extensive testing and the use of DOX methods enabled fire protection experts in the Survivability and Safety Branch of Wright Laboratory's Flight Dynamics Directorate (WL/FIVS) to produce empirical-based equations which could be used to solve for the amount of agent needed to suppress fires in engine nacelles. The final aspect of the program is to develop database and computer-simulation capabilities to compare results obtained in experimental tests. A database was desired as a means of archiving test data generated by WL/FIVS. A computer-based system with the capability of simulating fire suppression events in aircraft engine nacelles was also desired by WL/FIVS as an analytic tool to complement and compare against the experimental fire research. This portion of the program was begun by Applied Research Associates, Inc. (ARA).³

In setting out to develop a computer-based system to meet the needs of WL/FIVS, several requirements were established which had to be met. After evaluating a few choices, KIVA-3, a government-owned code, was chosen as the most qualified program to handle all the variables involved in the experiments. KIVA-3 is able to solve the unsteady equations of motion for turbulent flow based on the Arbitrary Lagrangian-Eulerian Finite Volume Method. Although intended to be mainly used for internal combustion problems, ARA was confident sufficient adaptations could be made to handle all the parameters involved. Due to time constraints, these adaptations made to the code have not been optimized for engine nacelle environments and so further work on the code is necessary before simulations can be produced. The code also requires a separate grid generation program to develop the computational mesh. Output from the processing can then be exported to Tecplot for graphing and animation purposes.⁴

This project deals with the work which was not able to be completed by ARA. It focuses on two major areas: the meshed configuration of the engine nacelle and the parameters necessary for the proper processing of the model. The main focus of this portion of the project concerns how the agent is distributed throughout the engine nacelle once it is discharged from its canister. The final goal is to calculate the amount of agent in certain areas inside the nacelle over a certain period of time and to make comparisons between these simulations and experimental tests already conducted. This work will hopefully be the basis for a future computer simulation project which will investigate the combustion of the fuel and the interaction with HFC-125.

³ J. C. Moore, G. K. Fenton, and S. R. Whitehouse. *The WL/FIVS Halon Replacement Database Archive and Interface with 3D Finite Difference AEN Modeling Support*. Applied Research Associates, Inc. March 1997.

⁴ KIVA-3 does contain post-processing capabilities; however, it is very limited. Post-processing of the data using Tecplot provides a better graphical representation of the model.

Methodology

Mesh Modification

ARA supplied a generic mesh of the engine nacelle; however, some alterations were necessary. Since ARA had designed a foundation from which engine nacelles could then be created, modification of the mesh is rather straightforward once the user understands how the grid generation program works. The basic idea behind it is to build stacks of cells like floors of a building. These stacks, or 'levels', are then sub-divided into three zones: Zone 1 is the area between the inner core of the AEN and clutter on the inner core; Zone 3 is the area between the outer core of the AEN and clutter on the outer core; and Zone 2 is the area between Zones 1 and 3.⁵ Located in the engine nacelle are two types of clutter: circumferential and longitudinal. Circumferential clutter exists on both the inner and outer cores of the nacelle, extending from the respective core one inch and possessing a width of 0.25". There are three pieces of clutter on the outer core and seven pieces on the inner core. Longitudinal clutter runs in the direction of the airflow. Its length is approximately 69" and its width is 0.25". There are two pieces of longitudinal clutter, symmetrically located 45° away from the fuel source.

To create the three-dimensional mesh, a block is defined for each zone in each level (14) by designating its eight corner vertices. The grid generator then rotates these blocks 360° as well as dividing them further into the specified number of cells in each direction. Next, each of the block faces must be defined as solid, fluid, inflow, or outflow boundaries. Finally, patching of the blocks to its respective neighbors completes the mesh. Appendix A explains the terms found in *iprep*, the file used for creating the mesh. To represent the circumferential clutter, which in the engine nacelle are radial pieces of stainless steel, adjacent zones between which the clutter are located are assigned z-coordinate values one centimeter in difference (where normally the values would be identical to create a continuum). These cells are also not patched together, resulting in a solid boundary and thus idealizing the clutter in the nacelle. Attempting to place the longitudinal clutter in the mesh proved to be too difficult and time-consuming. Defining it in the same manner as the circumferential clutter is not possible because each of the zones is rotated 360°, which would result in 23 pieces of longitudinal clutter (since there are 24 radial zones). The only viable option seems to be defining each of the radial cells one at a time. For those cells which are adjacent to the longitudinal clutter, the clutter would be built in the same manner as the circumferential clutter. This would be an enormous time-consuming effort not only because each of the cells would have to be input one at a time (meaning the x- and y-values would all have to be calculated and input into *iprep*) but also

⁵ This clutter is a representation of such things as wires, hoses, and supporting which are found in operational engine nacelles.

because each of these cells would require its own individual patching terms (whereas now the grid generation program assumes all the radial cells are patched in the same manner).

As stated previously, corrections to the mesh created by ARA were necessary to idealize the AENFTS. First, it was discovered that the values input into the code for the radii of the nacelle were, in fact, those for the diameter of the nacelle. All the values had to be reduced in half. Second, a better distribution of the cells throughout the nacelle was needed to obtain more accurate results. The initial mesh contained more cells towards the upstream end of the nacelle, but more emphasis is placed on the downstream end where the fire is situated. Also, most of the pressure and temperature transducers were located downstream. Thus, output from the KIVA-3 processor should be more highly concentrated at this portion of the engine nacelle.

Another desired modification to the mesh dealt with the maximum number of allowable cells which the code can handle, currently set at 50,000. Taking into account the volume of the flow area of the AENFTS, each cell would, at best, occupy an average of 5.63 cubic inches. A greater mesh density is desired so each cell will occupy a smaller average volume, making the solution more accurate. This modification was eventually discarded after it was discovered increasing the number of cells in the mesh requires a significant amount of disk space. Unfortunately, enough was not available at this time for use in creating a more dense mesh.

The mesh designed by ARA was defined so a fuel point source would exist and the agent inlet port would be described by an additional block, patched onto an existing block of the engine nacelle. Preliminary work with this mesh resulted in the program exiting prematurely due to various sorts of errors. The consensus from ARA at the time was the stress values for the agent mesh block were severely affecting the time step relating to the stress terms, leading to the main time step becoming too small. It was felt this was occurring because there was too great a transition in mesh density from the agent port to the nacelle itself (the nacelle cells were much bigger than those of the agent inlet port). However, a reduction of the nacelle cell size was accomplished by doubling the number of allowable cells and running the program for a very short time, but the same errors continued to occur.⁶ Therefore, it was felt a different approach was necessary to complete any simulations with the hope of extracting useful data.

An alternative approach to model the agent discharge into the AEN was to define the agent spray as a point source. There are a few drawbacks to this method, however. First, it will not be possible to model the combustion because the point source is no longer the fuel but rather the agent. Because only one type of point source is allowed to be defined for each given mesh, spark ignition of the fuel cannot occur.

⁶ Doubling the allowable number of cells was accomplished in this case because the program ran for only a short period of time; longer runs would not have been accomplished due to the lack of disk space discussed earlier.

This is not a concern for this project because agent concentration is the main focus, but a future project, which will examine the combustion of the fuel and the dispersion of the agent, centers around the program handling the fuel combustion. It was thus agreed that after successful completion of this project using an agent point source, the original method, that of adding the agent inlet port as a separate block, would once again become the main focus, time permitting.⁷

Figure 3 shows the meshed configuration of the AEN. It is a view from *k3post*, the post-processing utility for KIVA-3. The left side of the diagram is the upstream portion (inflow) and the right side of the diagram represents the downstream end (outflow). The darker circles located throughout the nacelle are the clutter.

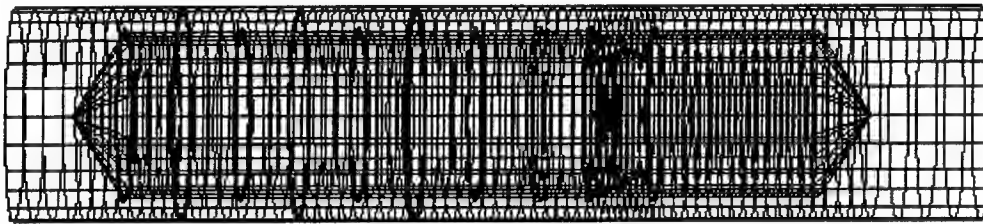


Figure 3. Meshed configuration of aircraft engine nacelle (from *k3post*)

Processing Parameters

Now that the mesh has been created, the next step involves defining all the parameters needed to run the model; that is, such things as boundary conditions, initial conditions, agent point source terms, and various other values. All these are found in a file named *itape*, which KIVA-3 uses to run the processor. Appendix B lists the terms found in *itape* along with their respective definitions; Appendix C lists the values used for each of the terms in our current model.

Most of the values in *itape* will not be changed because they correspond to internal combustion problems or should be the same as the default values already set. The user is allowed to set such things as the initial time step for the program (where a smaller time step results in more accuracy, but also demands more disk space and time to run the problem), how often output is printed to an output file (where a smaller problem time interval results in more data output, but which also requires more disk space), or whether a tape dump should be read first. A tape dump is a very powerful tool because it allows the user to run an initial program beforehand to achieve steady-state conditions in a particular system; then, the user simply has to direct KIVA-3 to read the dump file and use it before it runs the actual

⁷ Unfortunately, my tour ended before work on the original mesh configuration could be resumed.

model. It is powerful because it results in a substantial amount of time and disk space saved since each separate case can use the tape dump (which simply brings the system to steady-state) without having to separately run a new one each time.

Initial conditions can also be adjusted for a particular case. Changing the values for the various temperatures associated with the problem (initial air temp., nacelle wall temp., incoming airflow temp., and agent temp.) can be performed quickly. Initial composition of the amount of each species in the nacelle must then be input. Defining the parameters for complete representation of the agent point source is also accomplished in *itape*. This includes number of nozzle(s), origin, profile (type, size, and mass flow rate of spray), orientation, and composition.

The inflow parameters for the engine nacelle must also be defined. From *tape17* (which KIVA-3 builds after it reads and processes *iprep*), all the inflow cells are flagged and so the inflow (injector) parameters are directed at these cells. These parameters include composition of the species entering the nacelle and velocity of the inflow. Finally, since the current model will not be concerned with any type of chemical reactions, the reaction terms must be turned off. Obviously, this simplifies the problem greatly.

HFC-125 Discharge

Idealizing the agent discharge into the engine nacelle as a point source did not prove to be a simple task. First, the coordinates assigned as the origin of the point source were not the same as those which were being seen in the graphical output. One possible explanation for this is the existence of clutter, which seemed to disrupt the location of the point source during processing. The output was showing the point source located next to the first downstream clutter after the assigned values. This problem was eventually overcome by placing the point source slightly in from the outer core (where in actuality the agent is discharged directly from the outer core).

For this model, the point source is supposed to disperse 454 grams of agent over one second in a continuous flow.⁸ Thus, a square wave injection pulse is used. Some uncertainties of the spray include total number of spray parcels injected, sauter mean radius of the droplets at the injector, and velocity at the injector. These values were set after researching other problems and performing mathematical calculations on known values for this system. Another major problem with the point source addition was the composition of the spray. KIVA-3 requires definition of the spray among a choice of various

⁸ The agent mass flow rate in the AENFTS actually decreases because the tube also contains pressurized nitrogen behind the agent which is used to force the agent into the nacelle rapidly. As the amount of agent in the tube decreases, the composition of the flow into the nacelle becomes a mixture of both HFC-125 and nitrogen.

substances it contains in a 'fuel library'.⁹ Because HFC-125 is not among the choices of fuels in the library, two options were available: use a fuel already found in the library to serve as a substitute, or add HFC-125 to the library.

As for choosing a substitute fuel from among only a few choices, two major factors which had to be considered were molecular weight and chemical state. HFC-125 exists normally in a gaseous state, and so the fuel chosen should also possess this characteristic. However, the program contains a fault which renders use of a normally gaseous compound inoperable. The reason for this is not clear. The library is set up such that if a compound is normally gaseous, the only properties which need to be input are the molecular weight, critical temperature, and an enthalpy table for temperatures ranging from 0-5000 Kelvin. A flag is also present indicating in which state the compound normally exists, and if the flag indicates a liquid state, several more parameters must be set. For some reason, if the program encounters a compound whose flag designates it as a gas, it terminates immediately.

The creator of the program, Anthony Amsden, was eventually consulted to discuss this problem. He stated that there indeed was some sort of problem with the code such that use of a normally gaseous compound as a point source was a difficult task. He also mentioned that work on the problem was underway but he had no guarantee as to the date when the problem would be resolved. Until then, he stated discharge of the agent could be accomplished via a separate inflow port. As mentioned earlier, though, this approach has also had problems which have not been overcome as of yet. Due to this, the compound chosen for preliminary testing was n-octane (C₈H₁₈) because its molecular weight is very similar to that of HFC-125.

Using C₈H₁₈ as the fuel did not solve all the agent flow problems, though. Output from KIVA-3 lists the mass of each species as a vapor mass. Thus, because C₈H₁₈ is normally a liquid compound, only a fraction of the desired amount of 454 grams was actually being listed in the output. Several attempts were made to increase the amount of vapor mass in the nacelle. Among these included lowering the critical temperature and increasing the vapor pressure in the 'fuel library'. After some progress increasing the amount of vapor mass inside the nacelle was made, it was decided to add HFC-125 to the 'fuel library'.

Attempting to add HFC-125 to the library involved careful consideration of all the parameters in the subroutine. Because the program is set up such that adding a new fuel to the library is a somewhat difficult task, isooctane (2,2,4-trimethylpentane) was replaced by HFC-125 so only the corresponding values needed to be changed. These included molecular weight, critical temperature, heat of formation, and a table of enthalpies. To force the program to treat the compound as a gas, the vapor pressure values were set so all the agent dispersed into the nacelle was instantly vaporized. This increase in vapor

⁹ KIVA-3 calls FUELIB, a subroutine in the program, for all the required characteristics of the designated fuel to be used.

pressure, however, resulted in an early termination of the program. Another attempt called for an increase in fuel temperature, which directly leads to an increase in vapor pressure in a more natural manner. This approach did lend to an increased amount of vapor mass in the nacelle; however, it also resulted in the program terminating prematurely.

Processing and Output

Once the *itape* file terms have been described, processing can begin. First, a tape dump should be made to create airflow through the nacelle. This tape dump will then be called upon when the actual *itape* file containing the agent point source terms are used. The reason for this was mentioned earlier: when changes are desired, the processing can begin after steady-state conditions have already been met. For the *itape* file used to reach these steady-state conditions, all that needs to be done is to set the point source velocity to zero. The processor should then run until steady flow is achieved.¹⁰

Finally, KIVA-3 should run utilizing the working *itape* file. The program prompts the user for the amount of time to work on the program. It should be noted that the time input will probably not equal actual time elapsed due to the size of the problem. As a general rule of thumb, the amount of time input should be about half what the user desires. Regarding the TWFILM term in *itape*, which relates to the problem time interval between outputs, the user should simply experiment with it in order to determine the ideal value to use.

Although no reliable output has been gained using HFC-125 as the fuel, modeling of the AENFTS using an alternative fuel has been accomplished to show the system does have potential. Utilizing methanol as the fuel and keeping all the other *itape* parameters identical, the model was able to run for a few seconds in real-time. Figures 4a-d show graphical output from this model. All the figures have been sliced so visual interpretation is made easier. Figure 4a simply shows steady-state airflow of 1.2 m/s flowing through the nacelle. Figure 4b shows a vector representation of the point source velocity immediately after its initial discharge. Figure 4c is a contour plot of the agent 0.552s into the simulation, and Figure 4d is a contour and vector plot 1.053s into the simulation.

¹⁰ For this simulation, a tape dump has not yet been created because time was devoted to working on other parts of the project.

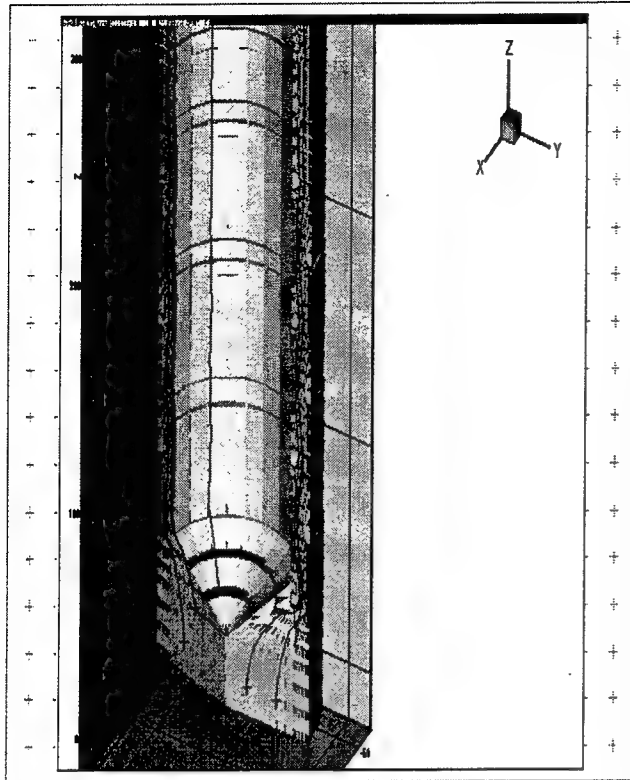


Figure 4a. Steady-state airflow through AENFTS

This graph displays a vector representation of the airflow through the AENFTS, with no agent flow. Also included are a few streamlines to better aid visualization of the figure. The *itape* file used for this particular model will also serve as the one used to create the tape dump.

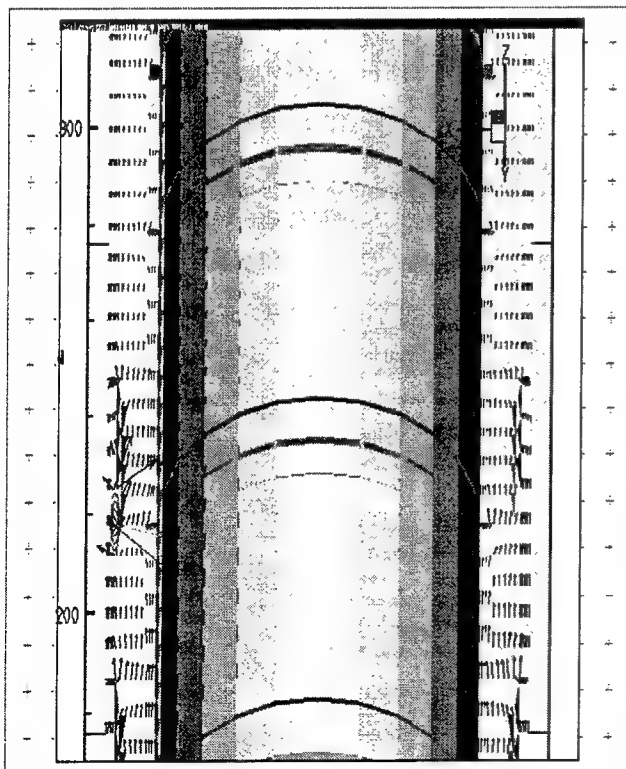


Figure 4b. HFC-125 discharge into AENFTS.

This graph focuses on the vector representation of the agent discharge into the engine nacelle. The discharge is shown on the left side of the figure, represented by the arrows pointing inward. As assigned, the discharge is directed perpendicular to the airflow and at the desired location.

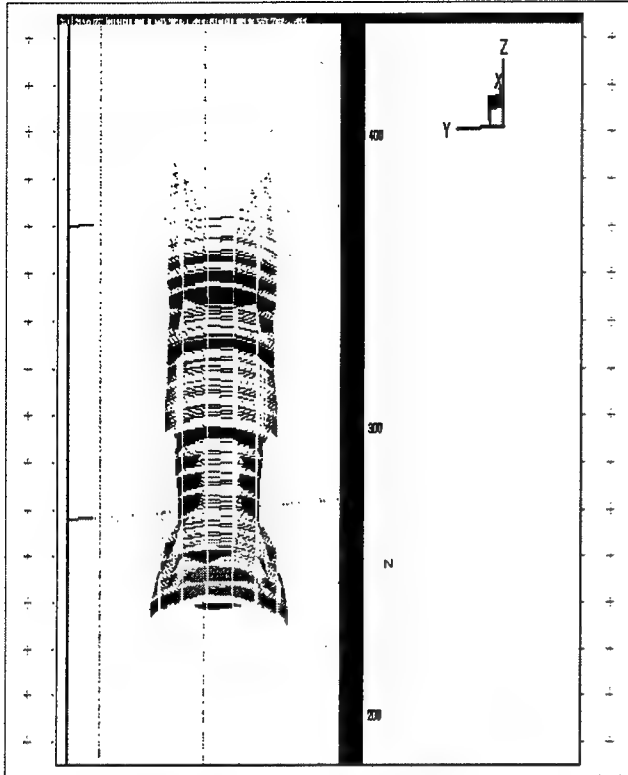


Figure 4c. Methanol contour at $t = 0.552s$

This figure shows a contour plot of the methanol distribution after 0.552s. At this point, the spray is about halfway through its duration. The origin of the spray source occurs towards the bottom of the contours, indicating the flow of the agent eventually begins to flow downstream once it loses enough energy to be carried away by the airflow.

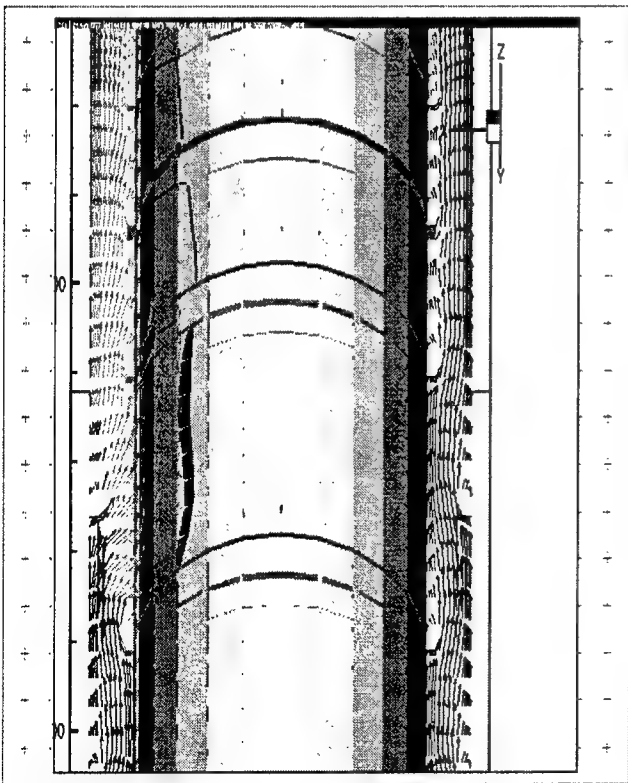


Figure 4d. Methanol distribution after 1.053s

This graph is both a vector and contour representation of the airflow and agent. At this point, the agent point source has just completed its spray duration and so there appears no large vectors around the point source origin.

Conclusions

This model still requires a fair amount of work before reliable output is obtained. Obviously, the 'fuel library' and manner in which the program handles fuel-related parameters needs some fine-tuning. Once the program can handle gases as point sources, modeling of this problem will be virtually complete. Utilization of a more powerful grid generator would also be very beneficial in representing the full geometry of the AENFTS. A greater mesh density could then be placed near the agent port and in areas of concern to WL/FIVS, and longitudinal clutter could be input into the system.

Acknowledgments

There are two people who I would like to thank for their support and guidance. My focal point, Lt. James Tucker, continuously offered advice and suggestions whenever I had problems with the model. He also provided me with a tremendous amount of written publications about the AENFTS in order to help me better understand what exactly I was attempting to model. Dr. James Moore, Senior Research Scientist at ARA, is the contractor who was first hired by WL/FIVS to model the AEN experiments. He taught me the 'basics' about using KIVA-3 and Tecplot, and was always willing to answer my questions when I e-mailed him. His help was extremely useful and much needed. Thank you both.

Appendix A

iprep Setup

To characterize the mesh, KIVA-3 reads *iprep*. This file is essentially divided into two parts: block and patch definition.

Block Designation

Line 1: NX, NY, NZ, NBO, NTYPE, NREGK3

Line 2: XC1, XC2, XC3, ... , XC8

Line 3: YC1, YC2, YC3, ... , YC8

Line 4: ZC1, ZC2, ZC3, ... , ZC8

Line 5: FACEL, FACER, FACEF, FACED, FACEB, FACET

where

NX,NY,NZ => # of fluid zones in respective direction (# of cells in corresponding block)

NBO => # of points in an optional table of coordinates (0)

NTYPE => specifies block type (4)

NREGK3 => region identifier for idreg (1)

FACEL,-R,-F,-D,-B,-T => BC for the six bounding faces (left, right, front, derriere, bottom, top)

Possible values are:

10, moving; **20**, solid; **30**, axis; **40**, fluid; **50**, front periodic boundary(FACEF only); **60**, derriere periodic boundary(FACED only); **70**, specified inflow; **80**, continuative outflow; **90**, pressure inflow; and **100**, pressure outflow.

Ex:

8	24	3	0	4	1		
48.26	48.26	.5	.5	48.26	48.26	.5	.5
0.0	0.0	0.0	0.0	0.0	0.0	0.0	0.0
0.0	0.0	0.0	0.0	30.3	30.3	30.3	30.3
20	20	40	40	70	20		

Note that all the values for Line 3 are zero. This must be done so that the grid generator recognizes the mesh is to be rotated the desired amount of degrees.

Patching

Line 1: NPATCH => # of block patching commands

Remaining lines: NBLK1, NFACE, NBLK2, INDEX1, INDEX2, ICOOR

"Patch face NFACE of block NBLK1 onto the opposite face of block NBLK2, starting at logical vertices (INDEX1, INDEX2) of block NBLK2, and using the coordinates from block ICOOR."

Ex:

11 6 14 1 1 11

Appendix B

itape Setup

——Normal lettering indicates values should remain as is——

——*Italicized lettering indicates values will largely remain the same with some exceptions*——

——**Bolt lettering indicates values will change depending on current conditions**——

——Underlined lettering indicates values which should change once reactions are involved——

<i>irest</i>	<i>restart flag, where 0 = no restart, >0 = dump number to restart from. read in subr. begin, used in main driver</i>
<i>lwall</i>	<i>+1 = law-of-the-wall bdry. layer; 0 = freeslip; -1 = no slip</i>
<i>lpr</i>	<i>long print control: 1 = write on fiche, 0 = emit entirely</i>
<i>irez</i>	<i>rezone flag: 0 = eulerian, 1 = lagrangian, 2 or greater for some specified continuous rezone such as engine</i>
<i>ncfilm</i>	<i>cycle interval between film outputs</i>
<i>ncap8</i>	<i>cycle interval between restart dumps on file tape8</i>
<i>nclast</i>	<i>cycle number when calculation is terminated</i>
<i>cafilm</i>	<i>crank angle interval between film outputs</i>
<i>cafin</i>	<i>crank angle when calculation is terminated</i>
<i>angmom</i>	<i>= 1.0 for angular momentum conservation in momfx (cyl=1.0)</i>
<i>pgssw</i>	<i>= 1.0 to employ pressure gradient scaling, = 0.0 to disable note: setup turns pgs off if pressure boundaries present</i>
<i>sampl</i>	<i>= 1.0 to create file (tfile) for cpu-usage sampling with tally post-processor, = 0.0 for no sampling; warning: there is an appreciable overhead for sampling</i>
dti	initial time step dt supplied in input data file
<i>dtmxca</i>	<i>maximum number of crank angle degrees pre time step; use a large value if you don't want it as an upper limit on dt</i>
<i>dtmax</i>	<i>maximum dt allowed during entire calculation</i>
<i>tlimd</i>	<i>=1.0 forces a restart-dump exit before job time limit, = 0.0 for no restart dump</i>
twfilm	problem time interval between film outputs
twfin	problem time when calculation is terminated
<i>fchsp</i>	<i>time step factor for kinetic reactions and spray evaporation: if tchem (q.v.) > fchsp, dt is reduced by the factor fchsp/tchem; similarly, if tevap (q.v.) > fchsp, dt is reduced by the factor fchsp/tevap</i>
<i>bore</i>	<i>diameter of cylinder</i>
<i>stroke</i>	<i>piston travel from BDC to TDC</i>
<i>squish</i>	<i>clearance between cylinder head & piston top at TDC</i>
<i>rpm</i>	<i>crankshaft rpm (set to zero to stop piston)</i>
<i>atdc</i>	<i>crank angle after TDC at time t = 0.0</i>
<i>datdct</i>	<i>crank angle difference for optional upper piston, + or - e.g., if upper piston reaches its TDC 15 degrees before lower piston, the datdct = -15.0</i>
<i>conrod</i>	<i>connecting rod length, measured from its centerline on the crankshaft to wrist-pin centerline</i>
<i>swirl</i>	<i>initial swirl ratio, = air rpm/crankshaft rpm, positive = clockwise, negative = counterclockwise</i>

swipro	dimensionless constant that determines profile of initial swirl velocity, between 0.0 (wheel flow) and 3.83 (zero at wall). typical value is 3.11
thsect	= 360.0 if full-circle cylinder, =180.0 if half-circle cylinder with symmetry boundary, = 0.5 for 2-d sector mesh, or even fraction of 360.0 for 3-d sector. see also:
sector	= 1.0 for 2-d or 3-d sector mesh with periodic boundaries, = 0.0 otherwise
epsy	allowed relative error in implicit solution of mass diffusion, typically 1.0e-3
epsv	allowed relative error in implicit solution of momentum diffusion, typically 1.0e-3
epsp	allowed relative error in pressure iteration, typically between 1.0e-4 and 1.0e-8
epst	allowed relative error in implicit solution of heat diffusion, typically 1.0e-3
epsk	allowed relative error in implicit solution of tke diffusion, typically 1.0e-3
epse	allowed relative error in implicit solution of epsilon diffusion, typically 1.0e-3
gx	body acceleration in x-direction, + or -
gy	body acceleration in y-direction, + or -
gz	body acceleration in z-direction, + or -
tcylwl	cylinder wall or liner temperature (kelvins). this is also the temp. used for l,r,f,d walls in 3-d cartesian meshes
thead	cylinder head temperature (top boundary of mesh)
tpistn	piston face temperature (and bottom of 3-d cartesian mesh)
tvalve	exhaust valve temperature (not automatically implemented)
tempi	initial cell temperature
pardon	= 1.0 for partial donor-cell fluxing (see also a0, b0), or = 0.0 for quasi-2nd-order upwind fluxing in general, qsou is preferable, but use pdc when speed is more important than accuracy, or when cell Reynolds numbers are < 2.0 see p. 49 of la-11560-ms for more information.
a0,b0	advective flux controls: (effective only when pardon = 1.0). limiting cases:
0, 0	centered (unstable if no viscosity)
1, 0	full donor cell
0, 1	interpolated donor cell (use this with sgs turbulence)
anc4	4th-order node coupler coefficient, between 0 and 0.05
adia	= 0.0 for fixed-temperature walls, = 1.0 for adiabatic walls
anu0	viscosity ratio $\mu/\rho\nu$; should be 0 when sgs or k-e used
visrat	ratio of lambda to mu viscosity, = -2/3 for zero bulk visc
tcut	<u>if cell temp. is lt.tcut, bypass kinetic reaction calc.</u>
tcute	<u>similar cutoff, relating to equilibrium chemistry calc.</u>
epschm	allowed relative error in chemeq iteration, typically 0.02
omgchm	overrelaxation factor in chemeq iteration, typically 1.0
tkei	initial turbulence kinetic energy density (cm/sec)**2.0 in an i.c. engine, we specify tkei as some percentage of the kinetic energy based on the mean piston speed. here, piston speed is stroke over half the period. for non-engine applications, an appropriate tkei is typically 10% of the mean flow kinetic energy
tkesw	= 1.0 if turbulence is on, = 0.0 if off
sgsl	sgs length scale, typically 4 to 5 dz. if sgsl = 0.0, the model reduces to k-epsilon
uniscal	if > 0.0, its value is used as a uniform length scale when initializing eps in the setup. if uniscal = 0.0, initial eps will instead be proportional to distance to the nearest solid wall. the code automatically ensures that the initial length scale is .le. sgsl when sgs is used.
airmu1,airmu2	molecular viscosity of ambient medium is given by $\text{airmu1}*\text{temp}^{1.5}/(\text{temp}+\text{airmu2})$
airla1,airla2	molecular heat conduction coefficient of ambient medium is $\text{airla1}*\text{temp}^{1.5}/(\text{temp}+\text{airla2})$
prl	prandtl no. in the laminar fluid; stde. value for air = 0.74
rpr	reciprocal turbulent prandtl number, $k/(c \text{ sub } p * \mu)$
rprq	rpr for tke diffusion in subroutine drdke, exdif, resk

rpre rpr for eps diffusion in subroutine drdke, exdif, rese
 rsc reciprocal schmidt number, $ro \cdot d / \mu$, for mass diffusion
 xignit reciprocal time constant for ignition energy addition to spark cell(s), at end of
 subroutine chem. set xignit = 0.0 to deactivate ignition option.
 t1ign time to initiate ignition spark
 tdign duration of ignition spark, in seconds
 ca1ign crank angle at TDC to initiate spark ignition, used only if t1ign is less than zero
 cadign duration of ignition spark, in crank angle degrees
 xignl(1), xignr(1), yignf(1), yignd(1), zignb(1), zignt(1): ignition region; may be single cell or a block
 of cells.
 xignl(2), xignr(2), yignf(2), yignd(2), zignb(2), zignt(2): 2nd (dual) ignition region (optional)
 kwikey = 1 to use fast equilibrium chemistry routine chmqgm for 6 built-in reactions; = 0 to use
 slower but general routine chemeq instead. note that chmqgm requires the presence of
 carbon and hydrogen.
 numnoz **number of injector nozzles**
 numvel **number of entries in optional injection velocity table**
 injdist 1 = inject size distribution about smr(i), 0 = inject one size only, smr(i), which is
 interpreted as the nozzle radius
 kolide **+1 turns on droplet collision calculation, 0 bypasses it ((If gas used, set to 0))**
 t1inj **time to initiate droplet injection**
 tdinj **duration of injection pulse, in seconds**
 ca1inj crank angle at TDC to initiate droplet injection, used only if t1inj is less than zero
 cadinj duration of injection pulse, in crank angle degrees
 tspmas **spray mass to be injected, in grams, where: if continuous spray (pulse = 0.0),**
 tspmas is mass injected per unit time; if pulsed spray (pulse.ge.1.0), tspmas is the
 total spray mass to be injected.
 pulse **0.0 = continuous spray injection, 1.0 = half-sine wave injection pulse, 2.0 = square**
 wave injection pulse, 3.0 = pulse defined by injection velocity table velinj().
 tnparc **number of spray parcels to be injected, where: if continuous spray (pulse = 0.0),**
 tnparc is the number of parcels per unit time. if pulsed spray (pulse.ge.1.0), tnparc
 is the total number of parcels to be injected, typically around 2000-5000 if 3-d, or
 500-1000 if 2-d.
 tpi **inflow temperature of fuel droplets (kelvins)**
 turb = 1.0 to include turbulent velocities for droplets
 breakup = 1.0 turns on droplet breakup model, 0.0 bypasses it
 evapp **= 1.0 turns on droplet evaporation, 0.0 bypasses it ((If gas used, set to 0))**
 drnoz() radius of injector nozzle from (x0,y0), in cm
 dznoz() z coord. of fuel injector, in cm
 dthnoz() azimuthal angle of injector nozzle, in degrees, from the j=1 plane, measured
 counterclockwise
 tiltxy() rotation angle of injector in x-y plane, in degrees, where 0.0 points towards the 3:00
 position (j = 1 line), and the angle increases counterclockwise from there
 tiltxz() inclination angle of injector in x-z plane, in degrees, where 0.0 points straight down, >0
 points in the +x direction, <0 points in the -x direction
 cone() fuel injector spray mean cone angle for hollow cone sprays, in degrees; for solid cone
 sprays, input cone = dcone (see below)
 dcone() injection liquid jet thickness, in degrees.
 anoz() area of injector nozzle
 smr() *sauter mean radius of the droplets at injector in cgs; as 1 micron = .0001 cm, 10 microns*
 would be input as 1.e-3 if injdist = 0, smr() --->is<--- the nozzle radius

amp() initial amplitude of droplet oscillation at injector, based on weber number estimate; applicable only if breakup model is turned on

velinj() **velocity at injector, in cm/sec. for a continuous spray or a simple pulse (pulse < 3.0), a single value of velinj is supplied, for the general case (pulse = 3.0), velinj is a table of values that change with time in whatever name the user desires. before using these values, KIVA-3 adjusts them if necessary to ensure that the correct fuel mass (tspmas) will be injected.**

total **fuel mass (tspmas) will be injected.**

nsp **number of species, indexed isp = 1,nsp**

idsp(isp) *species chemical formula, used as identifier and label*

rhoi(isp) *initial density of species isp*

mw(isp) *molecular weight of species isp. mw for specified fuel is set automatically in subroutine fuel.*

htform(isp) *heat of formation of species isp at zero degrees Kelvin, in kcal/mole. htform of specified fuel is set automatically in subroutine fuel.*

nrk **number of kinetic chemical reactions, indexed ir = 1,nrk**

cf(ir) forward pre-exponential factor, afr, for reaction ir

ef(ir) forward activation temp., e+, for reaction ir

zetaf(ir) forward temp. exponent, zetafr, for reaction ir

cb(ir) backward pre-exponential factor, abr, for reaction ir

eb(ir) backward activation temp., e+, for reaction ir

zetab(ir) backward temp. exponent, zetaabr, for reaction ir

am(isp,ir) stoichiometric coeff. of species isp on the left side of kinetic reaction ir

bm(isp,ir) stoichiometric coeff. of species isp on the right side of kinetic reaction ir

ae(isp,ir) exponent of species isp concentration in the forward rate of kinetic reaction ir

be(isp,ir) exponent of species isp concentration in the backward rate of kinetic reaction ir

nre **number of equilibrium reactions, indexed ire = 1, nre note: if kwiqeq = 1, rinput does not even read the nre line or any data-sets for as,bs,cs,ds,es,an, or bn**

as(ire), bs(ire), cs(ire), ds(ire), es(ire): coefficients ar,br,cr,dr,er in functional form of equilibrium constant

an(isp,ire) stoichiometric coeff. of species isp on the left side of equilibrium reaction ire

bn(isp,ire) stoichiometric coeff. of species isp on the right side of equilibrium reaction ire

distamb (applies only to outflow boundaries): if distamb.gt.0.0, the ambient pressure is imposed a distance distamb beyond the boundary, instead of right on it. the purpose is to enable the boundary to absorb acoustic waves, reducing any tendency they may have to be reflected back in. if used, distamb is a typical mesh dimension, e.g. the width.

pamb ambient pressure, used for an open boundary; see distamb

tkeamb ambient tke at an open boundary

sclamb ambient scl at an open boundary, = cmueps*tkeamb**1.5/eps

spdamb(isp) ambient species densities at an open boundary

velin **magnitude of velocity at a specified inflow boundary**

reedin 1.0 prohibits flow reversal at an inflow pressure bdry, 0.0 allows flow to reverse and exit the system

reedout 1.0 prohibits flow reversal at an outflow pressure bdry, 0.0 allows flow to reverse and reenter the system

numppcc number of entries for:

capcc() crank angle corresponding to:

pcc() crankcase pressure, in dynes, from experimental data

numppex number of entries for:

capex() crank angle corresponding to:

pex() exhaust port pressure, in dynes, from experimental data

spdin0(isp) species densities of fluid entering thru inflow bdry.

Appendix C

itape Values (MAKE SURE TO UPDATE VALUES)

irest	1	thsect	360.0	pri	0.74	dthnoz()	0.0
lwall	-1	sector	0.0	rpr	1.11	tiltxy()	0.0
lpr	0	eps[y,v,t,k,e]	1.0e-3	rprq	1.0	tiltbz()	-90.0
irez	0	epsp	1.0e-4	rpre	0.769	cone()	dcone
ncfilm	9999	g[x,y,z]	0.0	rsc	1.11	dcone()	110.0
nctap8	100	tcylwl	234.0	xignit	0.0	anoz()	6.54
nclast	9999	thead	234.0	t1ign	2e10	smr()	5.0e-4
cafilm	9999	tpistn	234.0	tdign	0.1	amp()	0.0
cafin	9999	tvalve	234.0	ca[1,d]ign	99e9	velinj()	1000
angmom	1.0	tempi	234.0	(xyz)ign.	0	nsp	3
pgssw	1.0	pardon	0.0	kwikeq	0	rhoi(hfc125)	0.0
sampl	0.0	a0	1	numnoz	1	rhoi(o2)	2.91e-4
dti	2.5e-3	b0	0	numvel	1	rhoi(n2)	1.01e-3
dtmxca	9.99e9	anc4	0.05	injdist	1	mw(o2)	32.00
dtmax	0.5	adia	0.0	kolide	1	mw(n2)	28.016
tlimd	1.0	anu0	0.0	t1inj	0.0	htform(o2,n2)	0.0
twfilm	5.0e-2	visrat	-2/3	tdinj	1.0	nrk	0
twfin	5.0	tcut(e)	800.0	ca1inj	9999	nre	0
fchsp	0.25	epschm	0.02	cadinj	9999	distamb	2.0
bore	9.843	omgchm	1.0	tspmas	454.0	pamb	1.01e6
stroke	8.25	tkei	0.1	pulse	2.0	tkeamb	3600
squish	1.5	tkesw	1.0	tnparc	4000	sclamb	1.0
rpm	0.0	sgsl	0.0	tpi	234.0	spdam0(din_1)	0.0
atdc	-180.0	uniscal	0.0	turb	1.0	spdam1(din_2)	2.91e-4
datdct	0.0	airmu1	1.457e-5	breakup	1.0	spdam2(din_3)	1.01e-3
conrod	16.269	airmu2	110.0	evapp	1.0	velin	120
swirl	0.0	airla1	252.0	drnoz()	59.0	reedin	0.0
swipro	3.11	airla2	200.0	dznoz()	181.0	reedout	1.0

Appendix C

itape Values

irest	1	thsect	360.0	prl	0.74	dthnoz()	0.0
lwall	-1	sector	0.0	rpr	1.11	tilbxy()	0.0
lpr	0	eps[y,v,t,k,e]	1.0e-3	rprq	1.0	tilbzx()	-90.0
irez	0	epsp	1.0e-4	rpre	0.769	cone()	dcone
ncfilm	9999	g[x,y,z]	0.0	rsc	1.11	dcone()	110.0
nctap8	100	tcylwl	234.0	xignit	0.0	anoz()	6.54
nclast	9999	thead	234.0	t1ign	2e10	smr()	5.0e-4
cafilm	9999	tpistn	234.0	tdign	0.1	amp()	0.0
cafin	9999	tvalve	234.0	ca[1,d]ign	99e9	velinj()	1000
angmom	1.0	tempi	234.0	(xyz)ign.	0	nsp	3
pgssw	1.0	pardon	0.0	kwikeq	0	rhoi(hfc125)	0.0
sampl	0.0	a0	1	numnoz	1	rhoi(o2)	2.91e-4
dti	2.5e-3	b0	0	numvel	1	rhoi(n2)	1.01e-3
dtmxca	9.99e9	anc4	0.05	injdist	1	mw(o2)	32.00
dtmax	0.5	adia	0.0	kolide	1	mw(n2)	28.016
tlimd	1.0	anu0	0.0	t1inj	0.0	htform(o2,n2)	0.0
twfilm	5.0e-2	visrat	-2/3	tdinj	1.0	nrk	0
twfin	5.0	tcut(e)	800.0	ca1inj	9999	nre	0
fchsp	0.25	epschm	0.02	cadinj	9999	distamb	2.0
bore	9.843	omgchm	1.0	tspmas	454.0	pamb	1.01e6
stroke	8.25	tkei	0.1	pulse	2.0	tkeamb	3600
squish	1.5	tkesw	1.0	tnparc	4000	sclamb	1.0
rpm	0.0	sgsl	0.0	tpi	234.0	spdam0(din_1)	0.0
atdc	-180.0	uniscal	0.0	turb	1.0	spdam1(din_2)	2.91e-4
datdct	0.0	airmu1	1.457e-5	breakup	1.0	spdam2(din_3)	1.01e-3
conrod	16.269	airmu2	110.0	evapp	1.0	velin	120
swirl	0.0	airla1	252.0	drnoz()	59.0	reedin	0.0
swipro	3.11	airla2	200.0	dznoz()	181.0	reedout	1.0

Demonstration of Genetic Algorithms for Engineering Optimization Problems

**David W. Fanjoy
Research Assistant
Department of Aeronautical and Astronautical Engineering**

**Purdue University
1282 Grissom Hall
West Lafayette, IN 47906-1282**

**Final Report For:
Graduate Summer Research Program
Wright Laboratory**

**Sponsored by:
Air Force Office of Scientific Research
Bolling AFB, Washington, DC
and Wright Laboratory**

August 1997

Demonstration of Genetic Algorithms for Engineering Optimization Problems

David W. Fanjoy
Research Assistant
Department of Aeronautical and Astronautical Engineering
Purdue University

Abstract

This research program focused on the application of Genetic Algorithms to engineering problems. A series of studies was conducted over the duration of the research period to investigate the effectiveness of a GA in different types of problems. Initially, the GA was tested against published benchmark data. It was shown that the GA can obtain the same results as traditional gradient-based methods, but at a much higher computational cost. The GA was then used to solve a three-dimensional aerodynamics problem using QUADPAN (a linear panel method used for computing maneuver loads), and then to solve a series of truss optimization problems with ANALYZE (an in-house structural analysis code). The truss problems highlighted the versatility of GA techniques by demonstrating multi-objective optimization, the use of discrete variables, and the ability to find solutions to problems that are difficult for traditional optimization techniques.

Demonstration of Genetic Algorithms for Engineering Optimization Problems

David W. Fanjoy

Introduction

A Genetic Algorithm (GA) is a probabilistically guided search technique based on the concept of Darwinian natural selection.¹ When used for optimization, a GA differs from traditional methods in several important ways: no initial design is needed, no gradients are required, and the design variables need not be real numbers. Since a GA is more computationally intensive than gradient-based methods, a need for one or more of the above advantages should exist to justify the use of a GA.

The GA works by coding the variables that describe a design into a binary string called a "chromosome," following the analogy of evolution in nature. The GA begins its search from a population of individuals, each with its own chromosome. Each individual is then evaluated, and a tournament begins, providing the "survival of the fittest" feature of the GA. The better individuals survive to become parents. These parents are randomly chosen for crossover, the "mating" operation in which two offspring chromosomes are created from a combination of the parents' chromosomes. Finally, a mutation operator is applied to the offspring, which very infrequently mutates chromosomes in order to encourage a wider exploration of the design space. A new population is formed from the offspring individuals, and the process repeats until some pre-determined stopping criterion has been met.

Because of the random factor in a GA, a search is not guaranteed to reach the global optimum. Similarly, the solution it reaches can not be proved to be an optimum at all (the Kuhn-Tucker conditions may not be checked). However, if the GA is set up correctly, the chances of reaching the global optimum are quite high. Since the GA starts from a population of points, a GA is less likely than a gradient method to become stuck at a local optimum.

The research described in this report was intended to help validate the use of a GA for engineering problems. The GA was first tested against some standard benchmark cases to show its relative performance. Then the GA was used on two more complex problems, aerodynamic planform optimization via QUADPAN, and ten bar truss optimization with ANALYZE.

Methodology

The Genetic Algorithm used for this report was written in FORTRAN 90 by the author based on previous studies done on GA methodology. Basic structuring for the program was adapted from the methodology described by Goldberg,¹ with modifications to the genetic operators as noted below. The program revolves around the three primary genetic operators: selection, crossover, and mutation.

Selection

One of the most common selection methods for Genetic Algorithms is the "roulette wheel" method. In this method, each member of the population is assigned a slot on a virtual roulette wheel with size proportional to its fitness. The roulette wheel is "spun" one time for each member in the new population, and the appropriate individual is selected to be a parent. The sizing of the roulette wheel slots makes it more likely that a more fit individual will be chosen. A downfall to this method is that it can lead to premature convergence. For example, if one individual in the initial population is ten times better than the next best, the next population could well contain only copies of that individual.

Several other methods for selection have been investigated, and for this study a tournament selection routine without replacement was used for comparing individuals. At random, two individuals are chosen from the population. The one with the best fitness is placed into the parent pool, and the other is not used. When the whole population has been considered in this manner, the parent pool is exactly half full. At this point, the process is repeated to fill the other half of the parent pool. As a consequence of this method, the best individual in the population will be included in the parent pool exactly twice, the worst will be excluded, and each other individual can appear in the parent pool between zero and two times.

Crossover

The first GAs used a model of crossover that closely mimics that found in nature. For this "single point" crossover method, two offspring are generated from two parents, and one crossover location is chosen at random along the string. The first offspring receives bits from the first parent up to this point, and receives bits from the remaining parent after this point. The other offspring receives all remaining bits, so that the two offspring are complements of each other. The drawback to this method is that it tends to encourage the development of known "good" designs, and discourage further exploration of the design space.

For this study, a uniform crossover was used. This method is also very common, and has the advantage of searching more of the design space by providing higher mixing. Similarly to single point crossover, two parents are used to obtain two offspring. However, uniform crossover randomly decides at each bit location whether the first offspring should receive the corresponding bit from the first or the second parent. The second offspring receives the other bit. A uniform crossover operator applied to two parents produces two complementary offspring.

Mutation

Like other genetic operators, mutation is modeled after natural phenomenon. On occasion, an offspring can have a chromosome that contains elements not found in either parent. These mutations are infrequent, seemingly random changes to the chromosome. In the GA, a mutation operator is applied to each new chromosome. There is a small percentage chance that each bit will switch to its complement.

Mutation is included in the GA to help prevent any difficulties that could arise from random chance. If, for example, an initial random population contained members with the same first bit, mutation would allow the

GA to also consider individuals with a different first bit. Mutation also aids in the exploration of the design space, but it occurs infrequently enough so as not to be a primary method for exploration.

The mutation rate for this study was set according to published guidelines for uniform crossover GA methods.² The formula is based on population size and chromosome length, and is given by:

$$P_{mut} = \frac{l+1}{2N_{pop}l} \quad (1)$$

Benchmark problems for the GA

Genetic algorithms are not optimization methods, rather they provide an environment in which optimization occurs. As a result, a GA cannot be guaranteed to find the correct answer. Therefore, it seems worthwhile that a GA be tested with common benchmarks to demonstrate its ability to perform comparably with other methods. The benchmark problems demonstrated in this section do not take advantage of the features of a GA; it would always be more efficient to solve this type of problem with other methods. The purpose of this demonstration is to show that the GA can obtain results similar to those found by more traditional methods.

Test Problem #1

This problem has a linear objective function in two variables and three constraints (one of which is non-linear).³ For the problem statement, the variables are not bounded. However, bounds must be placed on the variables for the GA, and so relatively wide bounds (0 ± 5.0). The problem is stated as follows, with the objective of minimizing the function F subject to the constraints g_i which must be non-positive.

$$F = 10x_1 + x_2 \quad (2)$$

$$g_1 = -2x_1 + x_2 + 1 \quad (3)$$

$$g_2 = -x_1 + 2x_2 - 1 \quad (4)$$

$$g_3 = x_1^2 - 2x_1 - 2x_2 + 1 \quad (5)$$

Problem 1 is a very straightforward problem. A simple linear external penalty was used, with 96 members in the population and a mutation rate of 0.008. The GA produced essentially the same design as the other methods after 91 generations. It should be noted that the GA requires many more function evaluations, but the number of evaluations is affected more by the desired resolution than by the complexity of the problem. The results, coding information, and a comparison³ for this benchmark case are shown in Table 1.

Value	Range	Bits	GA	ADS	NEWSUMT	IMSL	FUNOPT
x_1	-5.0-5.0	12	0.550672	0.550510	0.550750	0.550510	0.550652
x_2	-5.0-5.0	12	0.101343	0.101021	0.101140	0.101020	0.102817
F			5.60806	5.606121	5.608640	5.606120	5.609337*

Table 1: Results of Benchmark #1. An * denotes slightly infeasible design.

Test Problem #2

This problem is also in two variables, but is non-linear with two non-linear constraints³. Four side constraints are imposed, which in the GA are bounds of the variable used by the chromosome decoding scheme. Since a GA needs variable bounds anyway, side constraints require no extra work on the part of the GA. Shown below are the function and its constraints.

$$F = x_1 \sqrt{1 + x_2^2} \quad (6)$$

$$g_1 = 0.124 \sqrt{1 + x_2^2} \left(\frac{8}{x_1} + \frac{1}{x_1 x_2} \right) - 1 \quad (7)$$

$$g_2 = 0.124 \sqrt{1 + x_2^2} \left(\frac{8}{x_1} - \frac{1}{x_1 x_2} \right) - 1 \quad (8)$$

This problem is interesting due to the presence of non-linear terms. Although the functions themselves are rather uncomplicated, some optimization routines have great difficulty or are unable to work with problems that are not linear. An important feature of the genetic algorithm is that it is a zero-order method, and so the only thing it needs is a set of defined functions. In fact, multi-modal and discontinuous functions work in GA just as well as linear functions. A population size of 80 and a mutation rate of 0.0066 were used for this problem. Coding information, results, and comparisons³ for this case are shown in Table 2.

Value	Range	Bits	GA	ADS	NEWSUMT	IMSL	FUNOPT
x_1	0.2-4.0	10	1.4035	1.4160	1.4395	1.3997	1.3959
x_2	0.1-1.6	10	0.39765	0.35848	0.33409	0.37833	0.42033
F			1.5104	1.5042*	1.5177	1.4965*	1.5142*

Table 2: Results of Benchmark #2. An * denotes slightly infeasible design.

Test Problem #3

A more complicated problem, this benchmark is modeled on the mathematics of a gear reducer system.³ There are seven variables and twenty-five constraints, fourteen of which are side constraints and thus used as variable bounds for the GA. Equations 9-19 show the function and its constraints.

$$F = 0.7854x_1x_2^2(3.3333x_3^2 + 14.9334x_3 - 43.0934) - 1.508x_1(x_6^2 + x_7^2) + 7.477(x_6^3 + x_7^3) + 0.7854(x_4x_6^2 + x_5x_7^2) \quad (9)$$

$$g_1 = \frac{27}{x_1x_2^2x_3} - 1 \quad (10)$$

$$g_2 = \frac{397.5}{x_1 x_2^2 x_3^2} - 1 \quad (11)$$

$$g_3 = \frac{193x_4^3}{x_2 x_3 x_6^4} - 1 \quad (12)$$

$$g_4 = \frac{193x_5^3}{x_2 x_3 x_7^4} - 1 \quad (13)$$

$$g_5 = \frac{A_1}{110x_6^3} - 1$$

$$A_1 = \left[\left(\frac{745x_4}{x_2 x_3} \right)^2 + 16.9 \times 10^6 \right]^{0.5} \quad (14)$$

$$g_6 = \frac{A_2}{85x_7^3} - 1$$

$$A_2 = \left[\left(\frac{745x_5}{x_2 x_3} \right)^2 + 157.5 \times 10^6 \right]^{0.5} \quad (15)$$

$$g_7 = \frac{x_2 x_3}{40} - 1 \quad (16)$$

$$g_8 = 1 - \frac{x_1}{5x_2} \quad (17)$$

$$g_9 = \frac{x_1}{12x_2} - 1 \quad (18)$$

$$g_{10} = \frac{11x_7 + 19}{x_5} - 1 \quad (19)$$

In order to solve the problem, a linear exterior penalty was used with a population size of 240 and a mutation rate of 0.3%. The number of bits assigned to each variable was chosen to achieve a resolution in the thousandths place or better. Like the previous two benchmarks, the GA completed its run in only a few seconds. A feasible "optimum" solution was reached after 140 generations. The results of the run and a comparison to other methods³ are shown in Table 3. All of the methods arrived at essentially the same design, and the design specified by the GA is feasible, with all active constraints on the feasible side. Slightly different results can be obtained using different penalty approaches, but the GA seems to work well regardless of penalty choice. For some problems the selection of penalty function can influence the results, but these benchmarks are very forgiving.

Value	Range	Bits	GA	ADS	NEWSUMT	IMSL	FUNOPT
x ₁	2.6-3.6	9	3.5002	3.5016	3.4982	3.5000	3.5068
x ₂	0.7-0.8	6	0.7000	0.7000	0.6996	0.7000	0.7000
x ₃	17-28	12	17.000	17.000	17.000	17.000	17.000
x ₄	7.3-8.3	9	7.3000	7.3000	7.3000	7.3000	7.3000
x ₅	7.3-8.3	9	7.7188	7.7348	7.7153	7.7153	7.7261
x ₆	2.9-3.9	9	3.3521	3.3533	3.3502	3.3502	3.3516
x ₇	5.0-5.5	8	5.2882	5.2883	5.2866	5.2866	5.2867
F(X)			2995.97	2997.23	2991.79*	2994.30*	2997.63

Table 3: Results of Benchmark #3. An * denotes slightly infeasible design.

The benchmark cases shown above demonstrate that the GA can find designs as good as traditional designs. The disadvantage of the GA is that it requires more function evaluations. The advantages of a GA become apparent in complex problems. A problem suitable for the GA should have a combination of any of the following features: gradients that are not available (or are expensive to compute), a combination of variable types (real, integer, discrete, etc.), discontinuous design space, or multi-modal design space.

Aerodynamic Optimization Problem

The GA was used to investigate aerodynamic planform optimization of a lightweight fighter aircraft. This effort was conducted to show how a GA would be used in a real-world problem, and what sort of results to expect. The study was performed in two parts: the first was to look at QUADPAN (the intended aerodynamics code), investigating the program's behavior and determining what is needed to interface it with another code. The second part of the study was to actually interface QUADPAN with the GA, and do some runs to see how the GA performs with optimization.

Investigating QUADPAN

QUADPAN is a second-order three dimensional panel method aerodynamic analysis tool. As such, it is a steady-state, subsonic, irrotational inviscid code. Though it has compressibility corrections, QUADPAN is not to be used in the transonic range. Also, since the code is inviscid, it can only predict the induced drag, not the total drag for a configuration. This code has advantages over vortex-lattice methods because it uses panels based on geometry, not just planform. Although more computationally intensive than vortex-lattice methods, QUADPAN can accurately describe the effects of wing thickness.

QUADPAN gets input from a data file, which contains flight conditions and surface points of the aircraft configuration. For the wing, these surface points include the scaled airfoil coordinates at both the leading edge and the root, as well as the location of the leading edge, root, and any station where the wing shape changes. Also, data points showing the size and location of control surfaces should be in the input file. The user also specifies the

number of panels to place on the surface. After the run, QUADPAN produces an output file which contains pressures, velocities, and aggregate aerodynamic coefficients. The configuration lift and drag are of interest for this study.

Codes to Simplify QUADPAN

In order to make the use of QUADPAN practical with an optimization code, it was necessary to make the input files work in terms of common design variables such as aspect ratio and sweep. Also, a designer is not necessarily as interested in local surface pressures as in overall design coefficients. To facilitate the use of QUADPAN, two subroutines were written to condense the input and output of the program.

The first subroutine, INQUAD, is designed to create QUADPAN input files. INQUAD takes as arguments the sweep, taper ratio, aspect ratio, wing area, airfoil shape, and incidence angle. From these arguments it determines appropriate chord lengths, positioning and wake data, then writes an input file for QUADPAN. With the modular construction of INQUAD, it would be easy to add additional variables such as wing twist. The primary disadvantage of INQUAD is that it is designed to handle simple trapezoidal wings with no control surfaces. The subroutine would have to be modified heavily to allow more complex geometries.

The second subroutine, OUTQUAD, simply reads the data file output by QUADPAN. It returns values for CL, CD, and CM. This saves the user the trouble of sorting through several hundred lines of output file, and condenses the task into three values. OUTQUAD is intended to work on any output file, regardless of geometrical complexity. The disadvantage of OUTQUAD is the same as the primary advantage: it only returns three numbers. If the designer wants more information, OUTQUAD will not be of practical value.

Finally, a very simple driver program was written to call INQUAD and OUTQUAD. This driver program (QCUT) calls INQUAD, makes a system call to QUADPAN, and then calls OUTQUAD. The user sees only the input of design variables and the output in terms of aerodynamic coefficients.

Investigation of the Design Space

At this point, an investigation of QUADPAN in terms of aircraft design variables could be carried out. It was decided that just the wing planform would be considered, and the effects of design variables on lift-to-drag ratio (L/D) would be explored. The baseline configuration for analysis was the planform of an F-16A [see Table 4 for values]. It was later decided that an additional analysis should be performed with the baseline wing similar to that of the F-16A but with no sweep and no taper (see Fig. 1).

AR	3.0
λ	0.22
Λ	32.0°
Trim α	3.00°
Variable	Value

Table 4: Baseline wing geometry (F-16A)

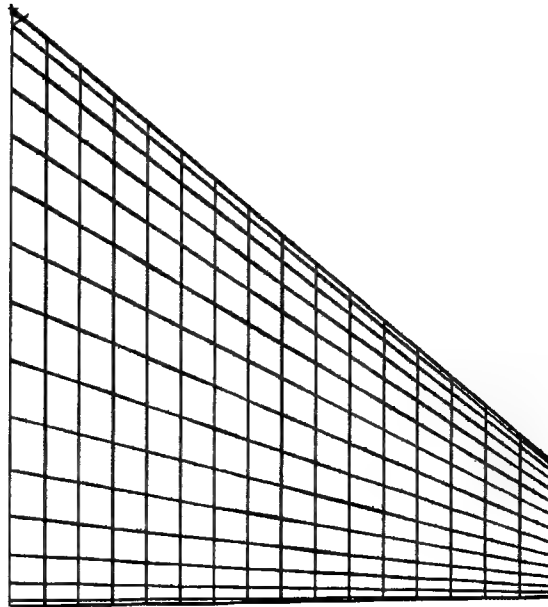
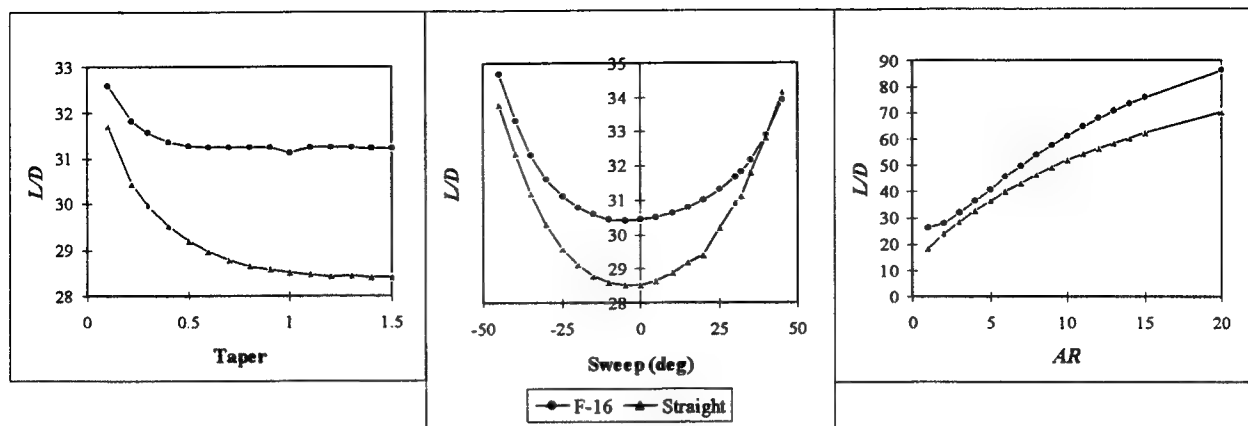


Figure 1: Baseline F-16A planform.

The first part of the study was to determine the amount of panels necessary to achieve an accurate solution. A limited panel convergence study was done to determine the appropriate amount of panels for the problem. The panel number shown is the number of panels in each coordinate on each surface of the wing. That is, a panel number of n corresponds to n panels streamwise on the upper surface, n streamwise on the lower surface, and n spanwise for a total number of panels $2n^2$ plus the panels on the trailing wake. A cosine distribution is used in the streamwise direction.

The resolution showed that with a panel number of less than about 15, the solution depended on the number of panels. With more panels, the solution changed but only very slightly. It was decided that a panel number of 16 was a good compromise between speed and accuracy, as an increase in n causes a quadratic increase in runtime.

With the number of panels set, a parametric study was done to see each variable's effect on the configuration. Each variable was investigated at values on either side of the baseline wing, and the experiments were performed using the F-16A baseline wing and a straight, non-tapered version of the same wing. An arbitrary airfoil section was used for both configurations, and an arbitrary angle of attack ($\alpha = 3^\circ$) was used for all runs. The results are shown in Figures 2-4.



Figures 2-4: L/D vs. Taper, L/D vs. Sweep, L/D vs. AR as determined by QUADPAN.

The effect of changes in the design variables predicted by QUADPAN agrees with aerodynamic theory.⁴ As expected, the effect of aspect ratio is similar between baseline configurations. L/D varies nearly linearly with AR for small values of AR , and then slowly levels out. The effect of quarter-chord sweep was roughly symmetrical about the L/D axis, with minimum L/D occurring at zero sweep. Although both baseline wings show similar trends in the effects of the design variables, it is important to note that the baseline shape influences the aerodynamic effects of each variable. The maximum C_L is obtained at roughly $\Lambda = 37^\circ$ for the baseline F-16A wing, and about $\Lambda = 0^\circ$ for the baseline straight wing. However, the location of maximum drag also changes, allowing for both configurations to have the same trends in L/D . Another interesting effect is that for large aspect ratio and sweep, it is possible for QUADPAN to predict negative drag due to an over-prediction of leading-edge suction.

As with sweep, taper ratio (λ) had different effects on the aerodynamic coefficients of each wing, but again the trends in L/D are the same. An increase in taper ratio on the straight wing seems to have a larger detrimental effect than an increase on the swept F-16A wing.

It should be noted that these studies were performed with a fixed airfoil shape and angle of attack. The trends of the design variables could change slightly due to spanwise flow for different airfoil shapes. Also, for a real engineering problem, a lift coefficient would likely be given instead of an angle of attack thus requiring the use of a trim analysis to determine the appropriate angle of attack for which to calculate L/D .

Planform Optimization Using QUADPAN and GA

Once the design space had been explored, it was possible to interface QUADPAN with a genetic algorithm and have some confidence in the results. It appeared from looking at the simple parametric studies of an F-16A wing that the optimum planform for the given wing area, angle of attack, and airfoil should have a very high aspect ratio, and perhaps a high sweep and low taper ratio. Rather than used a fixed angle of attack, the trim angle of attack was used as a variable, with an equality constraint specifying the lift coefficient $C_L = 0.285$. This step avoids the necessity of performing a complex trim analysis, and allows the GA to determine an appropriate trim angle for an individual. The objective of the optimization was to minimize drag-to-lift ratio, D/L .

The GA was run with 78 members in the population and a mutation rate of 0.006. Bounds on the variables were chosen to reflect a safe evaluating range for QUADPAN. Table 5 shows the variable ranges, coding, and results obtained by the GA.

Value	Range	Bits	GA
Λ	-45° - 45°	8	29.118°
λ	0.2-1.5	6	0.20
AR	1-16	4	16.0
Trim α	-3° - 3°	8	1.235°
D/L			0.00792

Table 5: Results of Aerodynamic Optimization.

The final value obtained by the GA was then used with QCUT for a quick confirmation of the results. Modifying the variable values by hand did not yield any better results. Testing variable values suggested by aerodynamics texts⁵ (such as high AR, no sweep and moderate taper) did not produce better results, either. It was discovered that for several sweep angles, there was an appropriate taper and trim α for best L/D . In many cases, the value of best L/D for a configuration was close to that found by the GA. The reason for this is that a wing is most efficient when it is loaded with an elliptical lift distribution, and modifying Λ and λ change the lift distribution shape.⁴ It follows that there may be several configurations that bring about an elliptical lift distribution, and that a better formulation for the problem may be to minimize the deviation from an elliptical lift distribution. In any event, the L/D of the new configuration is roughly four times as high as the baseline configuration. A picture of the new configuration optimized for L/D is shown in Figure 5. Note that it bears a strong resemblance to transport wings, which have been designed for maximum aerodynamic efficiency.

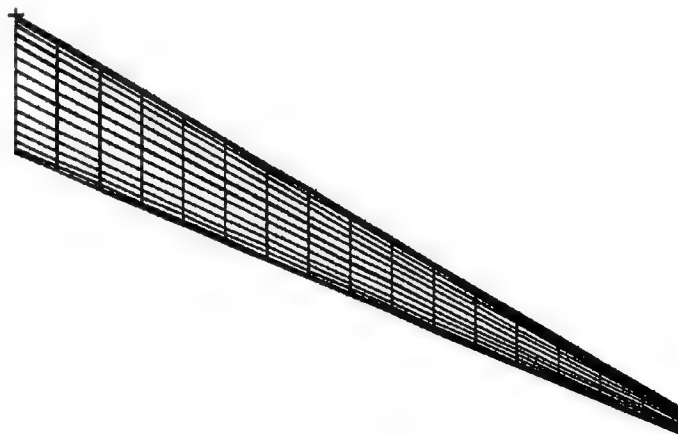


Figure 5: Fighter planform optimized for maximum L/D .

Truss Optimization Problem

Since the GA had performed well on the benchmark problems, it was decided that a more difficult problem be attempted. The ten bar truss problem has long been a severe test of a method's robustness.⁶ The analysis for the optimization was performed by ANALYZE⁷, a small in-house finite-element structural code. With very minimal modification of the code (consisting of a subroutine to interface the fitness evaluation), ANALYZE was coupled with a genetic algorithm and an input deck for the ten bar truss problem.

The ten bar truss problem consists of a series of cylindrical aluminum rods connected in a truss as shown in Fig. 6. Two 100 ksi loads are applied, and the object is to minimize total structural weight subject to a stress constraint and a maximum deflection at any node of 2 vertical inches.

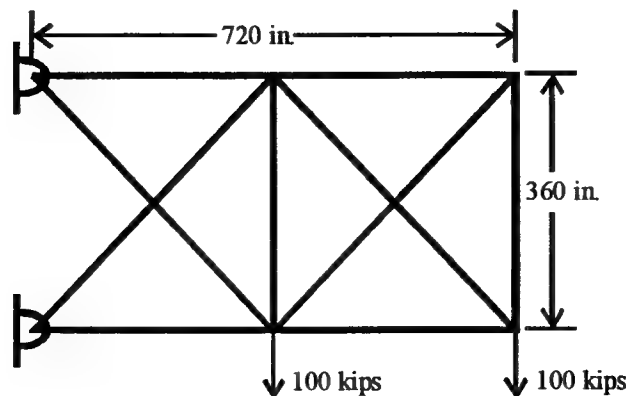


Figure 6: Ten Bar Truss problem description.

Because of the indeterminate nature of the problem, arriving at the “correct” solution is very difficult. The optimal design is extremely sensitive, and is bordered by infeasible regions. There are local minima at 5100 pounds, 5080 pounds, and a published global optimum at about 5062 pounds.⁶ As a result, the ten bar truss problem is an excellent way to discover an optimization method's limitations.

The GA was run a number of times, with various penalty coefficients and different amounts of resolution in the variables. Both of these parameters, selected by the user, proved to be important in determining the best solution. In order to have enough resolution, 10 bits were used for each variable. The corresponding chromosome length was then 100, with a population size of 360 and a mutation rate of 0.0016. Following the problem specifications, the variable bounds were set between 0.1 and 40.0 ft². Several penalty coefficients were investigated with the help of other researchers, and a penalty whose severity varies with the generation number squared was chosen. Using this penalty, a design weight of 5064.3 pounds was obtained. If then the variable bounds were tightened to focus the search area, a design of 5062.1 pounds was obtained. These results shown in Table 6.

Variable	Run 1	Tightened Bounds
x_1	30.45530	30.63170
x_2	0.10000	0.10003
x_3	23.57059	23.44275
x_4	14.65177	15.02485
x_5	0.10000	0.10002
x_6	0.41294	0.51775
x_7	7.45412	7.50241
x_8	21.06706	21.19975
x_9	21.84941	21.25920
x_{10}	0.10000	0.10001
$F(x)$	5064.0	5062.1

Table 6: GA results for the Ten Bar Truss problem.

The results of the GA were fairly good in an absolute sense, being within roughly 0.5% of the accepted optimum. Also, the GA was able to perform better than other commercial codes, such as ASTROS,⁸ which became trapped at the 5100 pound local minima. This is in part due to the fact that the GA starts from a population of points rather than a single point. However, the GA requires many more function evaluations to come to its conclusion. It should be noted that attempts to find the "optimum" design for this problem are purely academic: the 5062 pound designs are so sensitive that building them to tolerance would be very difficult. Slight changes in the design variables in this region of the design space can lead to serious failures. For practical applications, the design at 5100 pounds is much more stable.

Ten Bar Truss, Discrete Material Choice

To demonstrate the capability of a GA to solve problems with discrete variables, a different version of the ten bar truss problem was investigated. This new version was identical to the old, only the material type of each element was a variable. The available materials and associated properties are shown in Table 7.

Material	Young's Modulus (lb/in ²)	Weight Density (lb/in ³)	Yield Stress (lb/in ²)
Aluminum	10.0×10^6	0.101	25.0×10^3
Nickel	28.0×10^6	0.284	20.0×10^3
Steel	30.0×10^6	0.318	13.3×10^3
Titanium	16.5×10^6	0.162	73.3×10^3

Table 7: Material properties for discrete variable problem.

This type of problem could help the designer sort through a host of potential material types, based on the advantages of each. The ability to choose between discrete material choices could save the designer the time it

would take for exhaustive trade studies, and most optimization methods cannot consider discrete variables. Problems of this form also have applications in multi-objective optimizations. For example, a real-world problem might require a trade-off between weight and cost of a structure.

Shown in table 8 are the results of the multiple material optimization. Steel and nickel do not appear in the final design, because although they offer excellent stiffness, they are extremely heavy. Aluminum dominated the design due to its light weight and stiffness. A few members are titanium, which is heavier than aluminum, but also stronger and stiffer. Other researchers were able to get a few dozen more pounds off the weight.

Variable	Area	Material
x_1	27.36305	Aluminum
x_2	0.10000	Aluminum
x_3	15.93519	Titanium
x_4	10.16276	Titanium
x_5	0.10000	Aluminum
x_6	0.10000	Aluminum
x_7	8.68065	Aluminum
x_8	13.24399	Titanium
x_9	12.15191	Titanium
x_{10}	0.10000	Aluminum
$F(x)$		5074.0

Table 8: Results of discrete variable formulation of the Ten Bar Truss problem.

Ten Bar Truss, Multi-objective Formulation

Although the ten bar truss makes a good benchmark problem, it is not likely the best reflection of a real-world design situation. Rather than a fixed deflection constraint, the designer would probably rather be able to quantify the savings in weight gained by allowing a bigger deflection. Rather than one “optimal” design, the designer would require a series of non-dominated designs (for each design, there exists no other design that is better in both objectives). Such a collection of designs is referred to as the “Pareto front” of the design space.

A traditional method for obtaining the Pareto front would be to use a game-theory type approach. The deflection constraint could be set at different values, and the corresponding optimal weight recorded. In this way, a small number of points could be found to approximate the Pareto front. The disadvantage of this technique is that it would require many runs to describe the Pareto front with any reasonable resolution.

An advantage of the genetic algorithm as described previously is that it operates on a population of points. If the selection procedure is structured correctly for multi-objective searches, the entire population should move towards and eventually describe the Pareto front. Dozens of individuals lying on (or close to) the Pareto front could then be obtained in a single run of the GA, requiring an amount of time similar to a single-objective run.

For this effort, a two-branch binary tournament was employed.⁹ The GA is structured similarly to the single-objective version, with most of the changes done in the selection routine. Rather than the whole population being evaluated twice on a single objective, the population is evaluated once on each objective. The surviving members that form the parent pool are then shuffled and randomly mated. This encourages both the development of good designs in each objective, as well as the development of compromise designs in between. The only constraints on the problem are then the material failure constraints.

Since the population moves from generation to generation, the final population may not be the best description of the Pareto front seen during the run. To present the results more efficiently, a linked list data structure was constructed to store the composite Pareto front to date. After each generation, the current Pareto set is compared to the current population, and members are added or removed accordingly. As a result, the Pareto set may contain a different number of individuals than the population itself.

Pareto front movement from a sample run on the ten bar truss problem is shown in Fig. 7. In the first 100 generations, the Pareto front moves toward good designs and increases in size. With 600 generations, the front improves slightly from that of 100 generations, but the number of members it contains is nearly the same.

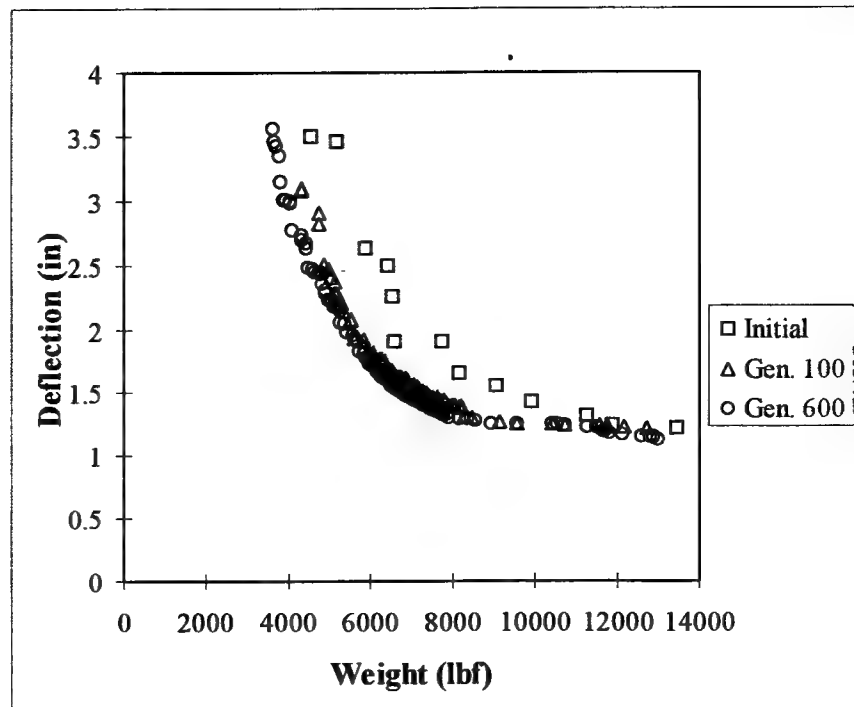
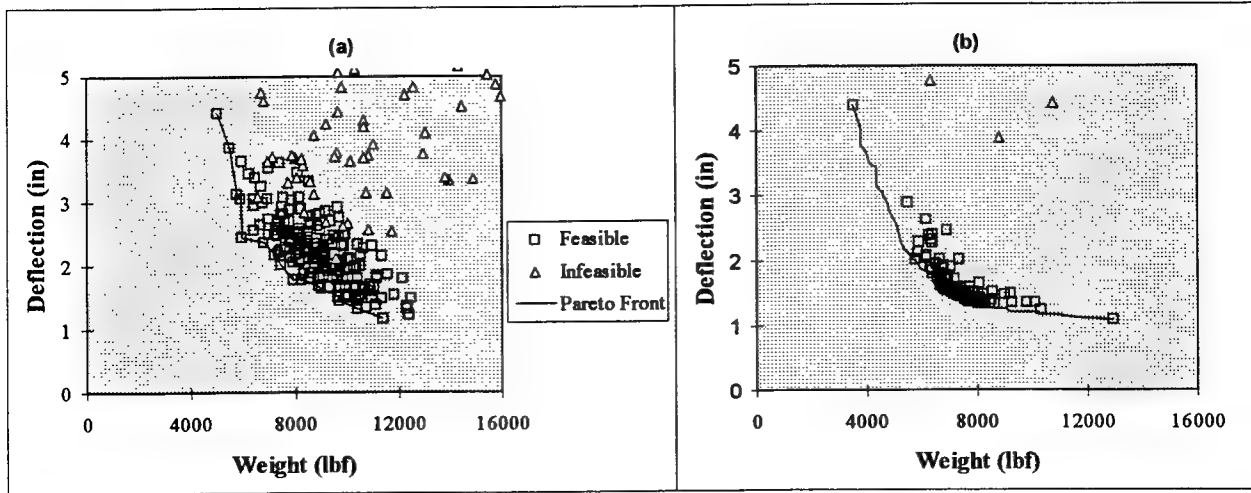


Figure 7: Movement of approximated Pareto front with generations.

Figure 8 shows how the population moves with generations. The initial population is a cloud with one bound formed by the Pareto front. By generation 100, the population is densely packed along the front, tending to gravitate toward the center of the front. As a result of this tendency to compromise, the multi-objective genetic algorithm usually takes more generations to run before a solution is settled upon as compared to the single-

objective version. Note that only a very little overhead is added, so the time to run one generation is roughly the same for each method.



Figures 8: (a) Initial population and Pareto front; (b) population and Pareto front after 300 generations.

Once the GA has determined its approximate Pareto front, it is important to evaluate its success. Since the Pareto front for the ten bar truss is not “known,” it was mapped out using a series of single-objective runs. Each run was done with a different deflection constraint, going from 1” - 4.5” in steps of a half inch. The results of this single-objective approach are plotted with the approximate Pareto front in Fig. 9. The correlation between the two methods is very good, and indicates that the multi-objective approach has merit. The approximate Pareto front produced by the multi-objective method took approximately one eighth of the computational resources as the single objective (traditional) approach, and contains a much larger amount of the designs that lie on the Pareto front.

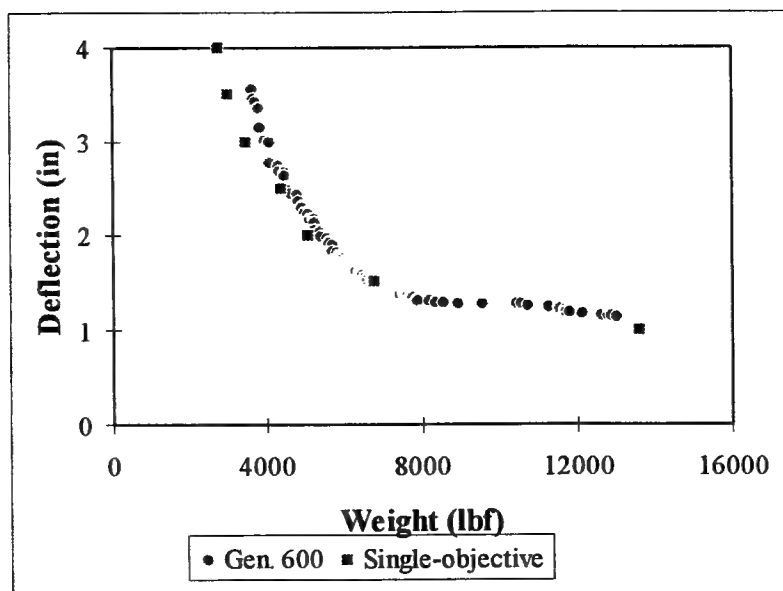


Figure 9: Comparison between multi-objective run and a series of single objective runs.

Conclusions

The Genetic Algorithm has been shown to be an effective tool for use in engineering optimization. It was able to obtain results similar to those found by conventional methods on a series of benchmark cases. The GA demonstrated its ability to avoid local optima by reaching the near-global optimum on the ten bar truss problem. Many traditional methods have difficulty on the ten bar truss problem, and cannot be used for a discrete variable version of the problem, such as the multiple material formulation. In addition, a two-branch tournament was employed in a multi-objective formulation of the ten bar truss problem. This provides the ability to describe an approximation to the Pareto front of non-dominated feasible designs in a single run.

Although it has been shown that the GA can obtain excellent answers on a wide range of problems, it is important to note that genetic algorithms are not the "holy grail" of optimization methods. Like all tools, the GA has drawbacks and is only appropriate for certain problems. The main drawback to the GA is that it requires much more computational time than traditional optimization techniques, approaching two orders of magnitude more computations or more on some problems. In addition, the GA provides no information on the optimality of the solutions it presents.

In conclusion, genetic algorithms are very powerful tools for engineering optimization. However, before a GA is selected as the method of choice, a designer should verify that the problem needs a GA to be solved. The problem should have some combination of the following: discontinuous design space, unavailable or expensive gradients, complex multimodal design space, unknown starting point, or a combination of variable types (real, discrete, integer).

Nomenclature

AR	Aspect Ratio
C_L	Lift coefficient
F	Objective function
g_i	Constraint functions
l	Chromosome length
L/D	Lift to drag ratio
n	Number of panels in aerodynamic model
N_{pop}	Population size
P_{mut}	Mutation probability
x_i	Design Variables
α	Geometric angle of attack
λ	Taper ratio
Λ	Quarter chord sweep angle

References

- ¹ Goldberg, D. E., *Genetic Algorithms in Search, Optimization and Machine Learning*, Addison-Wesley, Reading, MA, 1989.
- ² Williams, E. A., and Crossley, W. A., "Empirically-Derived Population Size and Mutation Rate Guidelines for a Algorithm with Uniform Crossover," WSC2: 2nd On-line World Conference on Soft Computing in Engineering Design and Manufacturing, June 23-27, 1997, URL: <http://isl.cps.msu.edu/GA/wsc2/index.html>.
- ³ Venkayya, V. B., "Benchmark Studies using Various Optimization Algorithms," NATO/DFG Advanced Study Institute University of Essen, Berchtesgaden, Germany, Sept. 23 - Oct. 4, 1991.
- ⁴ Schlichting, H., and Truckenbrodt, E., *Aerodynamics of the Airplane*, McGraw-Hill, New York, NY, 1979.
- ⁵ McCormick, B. W., *Aerodynamics, Aeronautics, and Flight Mechanics*, 2nd Ed., Wiley and Sons, New York, NY, 1995.
- ⁶ Venkayya, V. B., "Design of Optimum Structures," *Computers and Structures*, Vol. 1, 1971, pp. 265-309.
- ⁷ Venkayya, V. B., and Tischler, V. A., "ANALYZE" – *Analysis of Aerospace Structures with Membrane Elements*, Air Force Flight Dynamics Laboratory, Technical Report AFFDL-TR-78-170, Dec. 1978
- ⁸ Johnson, E. H., Neill, D. J., "Automated Structural Optimization System (ASTROS), Volume III – Applications Manual" Air Force Flight Dynamics Laboratory, Technical Report AFWAL-TR-88-3028, Dec. 1988.
- ⁹ Crossley, W. A., "Genetic Algorithm Approaches for Multiobjective Design of Rotor Systems," AIAA Paper 96-4025, *Proceedings of the 6th AIAA/NASA/ISSMO Symposium on Multidisciplinary Analysis and Optimization*, Bellevue, WA, Sep. 4-6, 1996, pp. 384-394.

**COMPARISON OF SELF-ASSEMBLED MONOLAYERS AND CHITOSAN AS
FUNCTIONAL SUBSTRATES FOR DEPOSITION OF ULTRATHIN
PHOTORESPONSIVE FILMS**

**John L. Hazel
Graduate Student
Department of Construction Materials and Industrial Design**

**Western Michigan University
1057 Kohrman Hall
Kalamazoo, MI 49008**

**Final Report for:
Graduate Student Research Program
Wright Laboratory**

**Sponsored by:
Air Force Office of Scientific Research
Bolling Air Force Base, Washington, DC**

And

**Wright Laboratory
MLPJ**

August 1997

August 1997

**COMPARISON OF SELF-ASSEMBLED MONOLAYERS AND CHITOSAN AS
FUNCTIONAL SUBSTRATES FOR DEPOSITION OF ULTRATHIN
PHOTORESPONSIVE FILMS.**

**John L. Hazel
Graduate Student
Department of Construction Materials and Industrial Design
Western Michigan University**

Abstract

Chitosan, an extract from the exoskeleton of arthropoda is compared to a traditionally prepared self-assembled monolayer (SAM) for its suitability as a functional substrate in constructing multilayers of C60-Porphyrin. Measurement of topography, friction, chemical composition, mechanical stiffness and stability of the surface was performed by adaptation of recently developed atomic force microscope (AFM) procedures. While the SAM has a theoretically superior surface character as a substrate for multilayer photoresponsive films, the chitosan was found to be superior in qualities critical for adsorption and mechanical stability. This is due to the different distribution and mechanical stabilization of surface functional amine groups controlled by the helical intramolecular structure of chitosan macromolecules.

COMPARISON OF SELF-ASSEMBLED MONOLAYERS AND CHITOSAN AS FUNCTIONAL SUBSTRATES FOR DEPOSITION OF ULTRATHIN PHOTORESPONSIVE FILMS.

John L. Hazel

Introduction

Siloxane based self-assembled monolayers (SAM) anchored to hydroxyl bearing surfaces were introduced in 1983¹ and are now considered a well established tool for use in surface modification. A typical Siloxane based SAM consists of a Siloxane group for chemically binding the molecule onto the surface and a functional group that has the desired character for the final surface. The two groups are typically connected by a chain of carbon atoms (Fig. 1). The concept of having a majority of the binding groups on the solid substrate and most of the functional groups on the outermost plane of the surface layer is generally accepted. However, in recent work by Hao at WL/MLPJ a comparison of NH₂ terminated silane SAM with chitosan adsorption substrates showed that sulphonated C₆₀ was adsorbed several times greater on the chitosan surface (Fig. 2). The difference in adsorption continued through subsequent electrostatic self-assembly¹ of C₆₀-porphyrin bilayers (Fig 3). These bilayers were of interest for their synergistic enhancement of optical florescence vs. the expected simple arithmetic sum when the two are combined (Fig 4). The greater adsorption on the chitosan is in contradiction with the theoretical density of NH₂ groups on the SAM, $5 \times 10^{14}/\text{cm}^2$, being about 3 times greater. One possible cause of this contradiction is a non-ideal structure in the SAM.

As mentioned earlier, many investigators have demonstrated SAMs. However, reported successful building of well ordered SAMs with functional terminal groups has been rare. A review of the literature reveals several other troublesome observations about

functionalized SAMs that can easily be explained by assuming that the SAM is really a disordered ultrathin layer with only sparse chemical bonding to the substrate: easier mechanical scratching of films deposited on SAMs vs. bare silicon when there is an expected stronger attraction of the film,² little change in composition with respect to XPS takeoff angle,³ smaller than expected water contact angles,⁴ irreversible distortion (wear) of the silane SAM by AFM tips under conditions that do not damage alkanethiol SAMs on gold,⁵ large hysteresis in advancing and retracting contact angle measurements.⁶ In fact, direct report of the difficulty in forming SAMs from silanes having functional termination of NH_2 has been made and an alternative approach of adding the NH_2 after silane and carbon chain surface attachment was proposed and attempted.^{7,8} An additional alternative for the production of gold-alkanethiol directed SAMs involving ultraflat template stripped epoxy surfaces resulting in NH_2 terminated substrates that are transparent enough for optical microscopy has been demonstrated.⁹

Methodology

Surface preparation. NH_2 terminated SAM was produced at MLPJ on glass microscope slides (Fisher finest). 3-aminopropyltriethoxysilane ($\text{C}_9\text{H}_{23}\text{NO}_3\text{Si}$) was added to 95% ethanol 5% milli-Q water for a final concentration of 2% 3-aminopropyltriethoxysilane. This solution was allowed to stand for 15 minutes for hydrolysis of the silanol after which the substrates were immersed in the solution for 30 minutes. The substrates were then removed from the solution and rinsed with ethanol twice and kept overnight in a dry N_2 atmosphere. Before application of C_{60} -porphyrin bilayers the silanized surfaces were protonated by immersion in .01N HCl for 10 minutes.

The chitosan substrates were spin coated onto glass slides. A 2% weight solution of chitosan in water was spin coated at 800 RPM. The samples were then dried overnight in a vacuum oven at 50 degrees C. The resulting films had thickness of about 0.5 μm as measured by AFM across intentional scratches.

Measurements. Surface roughness was measured in contact mode with a Digital Instruments Nanoscope using Digital Instruments “short narrow” V-shaped tips. Scans of 1 μm square were collected at 2-4 Hz scanning rates. Contact forces were minimized during topography scans to avoid damaging the surface being measured. Calculation of roughness was done both on the full 1 μm scan and a smaller area of about 200 nm square as a rapid test of the effect of scale on measured roughness. Friction maps were simultaneously collected with all topography images. Tips were changed when artifacts appeared in the collected images.

Variation of contact forces was exploited to test the mechanical stability of the silane and chitosan layers. A high force contact was established and then several complete scans were made at 20 Hz in an attempt to scratch or plow away the surface layer. The scan force was then reduced and the scan size increased to reveal any damage caused by the previous high rate, high force, scanning.

Tip-surface adhesion was measured by locating the AFM tip out of contact and then extending the piezo tube until contact was detected by deflection of the tip. The piezo tube was then retracted until the spring force of the cantilever pulled the tip off the surface. The maximum negative deflection of the cantilever in this process then indicates surface-tip adhesion. Chemically modified cantilevers produced at WMU¹⁰ with NH_2 functionalized contact points were used to assess the surface chemical and electrostatic

interaction of bare glass, silanized glass and chitosan surfaces. This was used as an indicator of surface coverage by chemically active or charged molecular groups.

The approach-retract cycling of the AFM tip was also employed to assess the mechanical stability of the C₆₀-Porphyrin bilayers. The initial cantilever deflection is smaller on soft samples that allow some penetration of the tip into the surface.¹¹ This method was modified by performing the surface probing under water. The strong capillary attractive forces were thereby eliminated allowing detection of penetration at the initial stages of tip-surface contact. There is a definite difference in the stability or hardness of the bilayers when they are examined this way. Testing mechanical stability of the C₆₀-porphyrin layers by the AFM scratching test mentioned above was not feasible due to the tip destroying abrasiveness of C₆₀. This nanoindentation under fluid was therefore an important technique for mechanical analysis.

Results and Discussion

The bare glass slides showed smooth 100x100 nm areas of about 0.7 nm rms with ~5 nm wide pits and bumps spaced about 100 nm which brought the rms roughness for a 1 µm scan size to 1.2 nm (Fig. 4). Silanized glass showed some smoothing of the bare glass surface with the overall roughness reduced to 0.4 nm rms at the 1 µm scale (Fig 5). The spin coated chitosan surface showed a fine (lateral periodicity ~5 nm) grainy texture with calculated 1 µm rms roughness of 0.9 nm, the 200 nm scale roughness was 0.8 nm (Fig. 6). Neither the silanized glass nor the chitosan surface roughness was significantly changed by the adsorption of the sulphonated C₆₀. This indicates that the C₆₀ layer was not composed of aggregates but was actually adsorption of individual C₆₀.

An AFM wear resistance test on the silanized and chitosan surfaces was performed using the method described above. This test done in air produced similar results for both samples. The high force scanning areas showed only slight changes in topography and friction. However, when this test was repeated with the scanning done under water, the results were dramatically different between the two surfaces. The chitosan showed little damage in the topography image with friction being generally reduced in the high force area (Fig. 7). This large change in friction paired with the small change in topography indicates a slight reordering of the surface layer but no actual displacement of material during the high force scanning. Chitosan has the advantage of being a polymer, so nearly all monomers of this material have their position maintained by at least two chemical bonds. Conversely, the silane layer was completely removed by the high force scanning under water (Fig 8). This is confirmed by the higher friction in the worn area where the tip is in contact with the substrate. This increased susceptibility to wear under water indicates that the water is able to soften or loosen the silanes. However a chemically attached silane would not change its wear resistance so much under fluid. Also of interest are the domains shown in the friction image which are only faintly reflected in the topography. This might be an effect of changes in the surface layer ordering in the silanes.

The adhesive force measurements for an unmodified tip on the two surfaces showed nearly identical values (Fig 9). With an AFM tip having NH_2 terminated surface modification, the adhesive forces are much smaller on the chitosan surface which indicates that the surface density of NH_2 groups is much greater than the silanized surface or that the contact area is much larger (Fig 10). Note that the scales in each figure are

identical but the scale of figure 10 is not identical to that of figure 11 due to uncertainty of spring constant in the AFM cantilevers.

In tests using a stiff cantilever, the relative hardness of the chitosan-porphyrin bilayers were tested as the number of bilayers were added. Note the point where the tip makes contact in the one bilayer force curve for each surface (Fig 11,12). The chitosan surface shows a larger penetration by the AFM tip in the initial contact. This can be seen by the large radius of the "corner" formed as the tip deflection begins during initial contact of the chitosan surface. This result is expected since the chitosan layer is much thicker than the silane. Note also the presence of a "jump to contact" evident in the silane layer. Moving to the force curves for 3 bilayers, the radius of the initial contact is much smaller on the chitosan surface. In fact the change is very sharp indicating almost no penetration by the AFM tip. In contrast, tip penetration of the 3 and 5 bilayers on silane samples is apparent. This indicates that chitosan adsorbs the bilayers and packs them closely enough that they support each other at or before the 3rd set of bilayers are deposited. Bilayers on the silane substrate do not display this until after more than five bilayers are applied. The force curve for the 10 bilayer sample of the silanized substrate indicates the surface penetration is minimal so there is some self reinforcement of the adsorbed material before the tenth bilayer. These comparative results are consistent with the adsorption data provided by Hao at WL/MLPJ. Surface hardness increases with the number of bilayers much more quickly in samples with chitosan substrates.

Conclusion

If the SAM studied in this work is indeed a disordered layer then the explanation for lower adsorption of sulphonated C_{60} is fairly straightforward. Most of the NH_2 groups are buried inside the SAM and therefore less likely to attract a C_{60} . Many of the NH_2 that are exposed at the surface will be part of silane groups that have not made a chemical attachment to the surface. Each C_{60} that adsorbs to the surface could then draw nearby NH_2 terminated molecules. This would further reduce available adsorption sites and also mask some or all of the SO_2 sites on the adsorbed C_{60} inhibiting attachments of the subsequent porphyrin molecules. This reduction in adsorption and the masking of C_{60} sulphonates explains the propagation of the reduced adsorption to subsequent bilayers.

The obvious solution to these problems is to expose more NH_2 groups at the surface and keep them from moving around. Chitosan is a good candidate for achieving this solution. The chitosan used here is a polymer with a helical backbone and molecular weight of about 70,000. The helical backbone is beneficial in this situation because it insures that some NH_2 is exposed at the surface. The backbone of the polymer also provides a relatively regular spacing and orientation of the active groups thus insuring that a fairly homogeneous distribution of favorably oriented NH_2 appears at the surface. This spacing is enforced by the bonds along the chitosan polymer. When the sulphonated C_{60} is adsorbed the chitosan polymer bonds prevent adjacent NH_2 groups from migrating to it. The NH_2 is then available to attract sulphonated C_{60} and is also keeping active adsorption sites on already deposited C_{60} available for adsorbing porphyrin in the next step of the electrostatic assembly process. The stable location of the NH_2 then adsorbs the C_{60} in a more tightly packed layer which also contributes to the mechanical stability.

Data from the application of various atomic force microscope (AFM) techniques such as chemical force microscopy (CFM), friction force microscopy (FFM) to this problem indicate that the most straightforward explanation for the discrepancy is that the SAMs used in these experiments are very disordered ultrathin coatings. Additionally the chitosan substrate showed a superior tendency to stabilize bilayers of C₆₀-porphyrin.

References

1. Netzer L., Sagiv J.; J. Am. Chem. Soc. 105 674 (1983)
2. Lvov Y. M., and Decher G.; Crystallography Reports 39 696 (1994)
3. Ararwal M., DeGuire M. R., and Heuer A. H.; Appl. Phys. Lett. 71 891 (1997)
4. Trevor J. L., Mencer D. E., Lykke K. R., Pellin M. J. and Hanley L.;
Anal. Chem. 69 4331 (1997)
5. Laibinis P. E. and Whitesides G. M.; J. Am. Chem. Soc. 114 1990 (1992)
6. Xiao X, Hu J. Charych, and Salmeron M.; Langmuir 12 235 (1996)
7. Wasserman S. R., Tao Y., Whitesides G. M.; Langmuir 5 1047 (1989)
8. Balachander N. and Sukenik C. N.; Langmuir 6 1621 (1990)
9. Wagner P., Hegner M., Guntherodt H., Semenza G.; Langmuir 11 3867 (1995)
10. Tsukruk V. V. and Bliznyuk V. N.; Langmuir accepted.
11. Vanlandingham M. R., McNight S. H., Palmese G. R., Elings J. R., Huang X.
Bogetti T. A., Eduljee R. F., and Gillespie J. W. Jr.; J. Adhesion 64, 31 (1997)

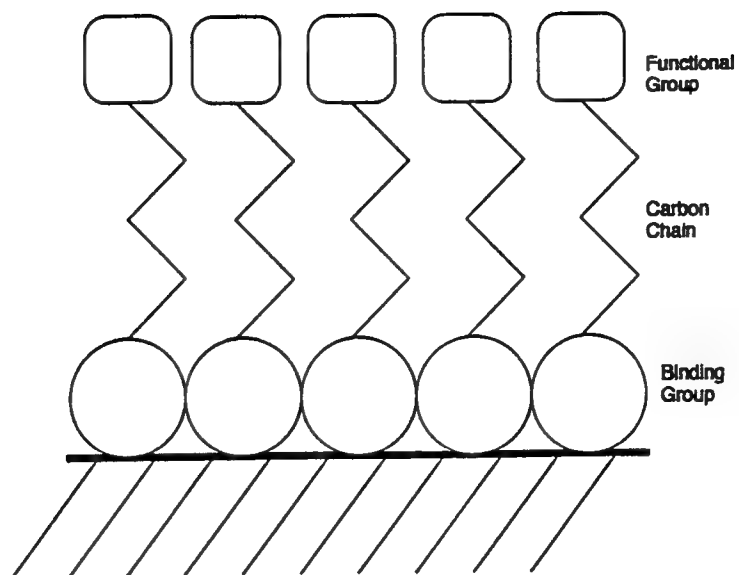


Figure 1 Typical SAM conceptual illustration.

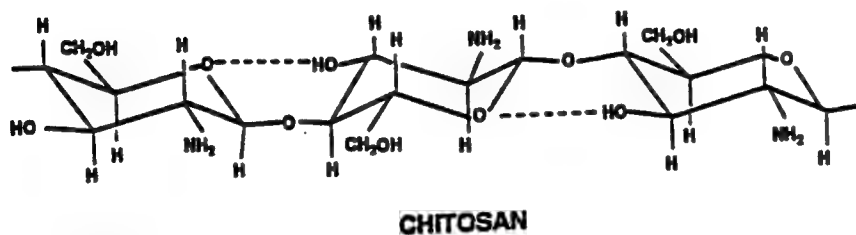


Figure 2

Comparison of Chitosan to Silanized glass
(5 mins dipping in C60-porphyrin)

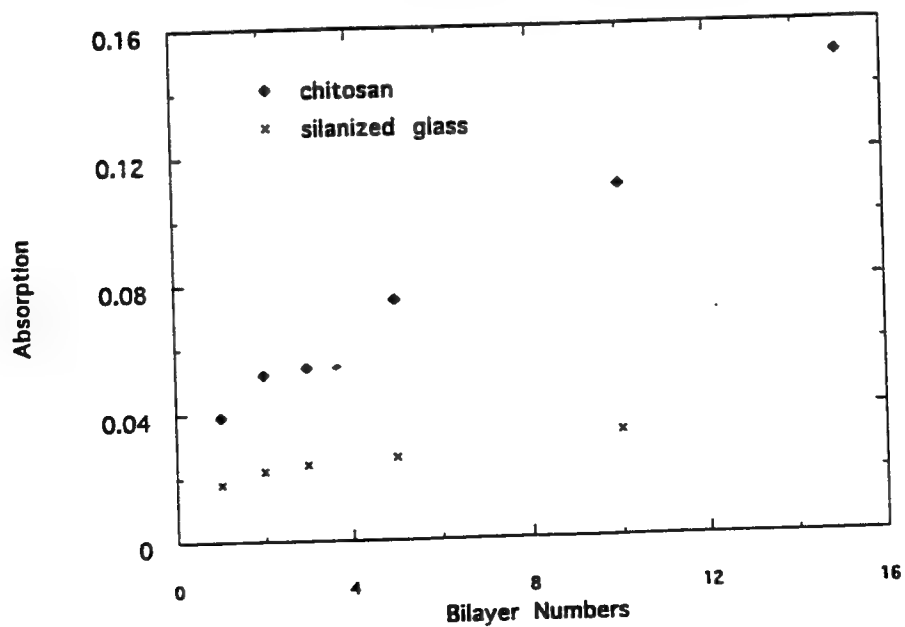


Figure 3

Supplied by Hao

Supplied by Hao

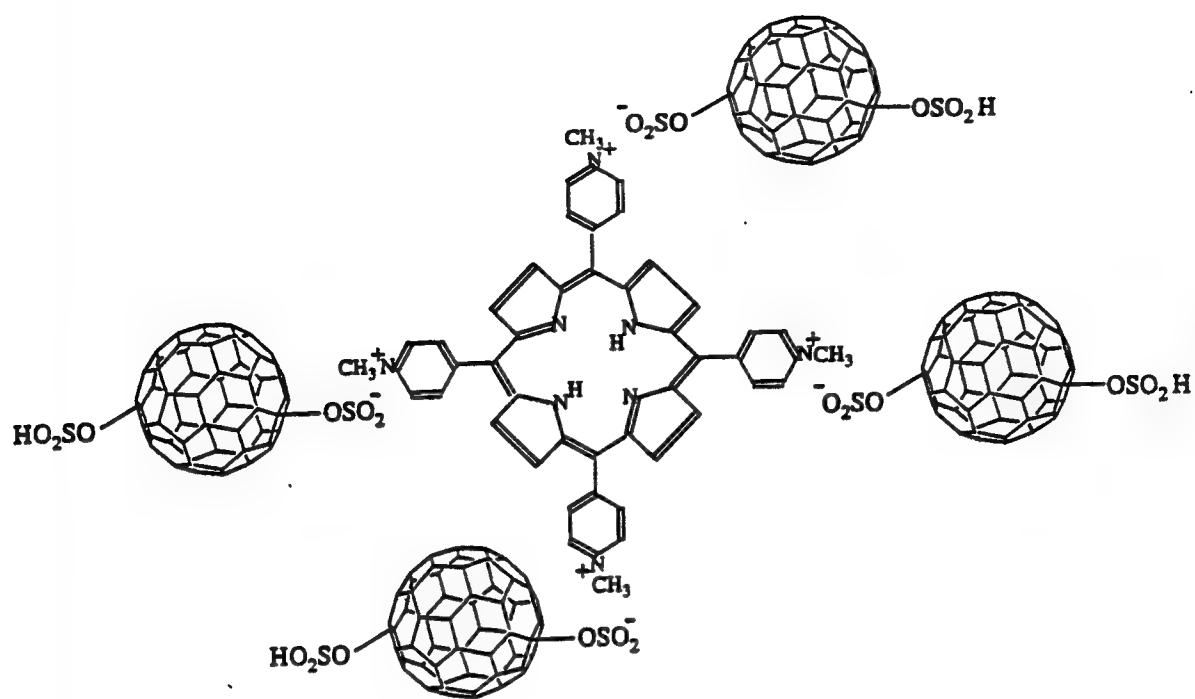


Figure 4

Supplied by Hao

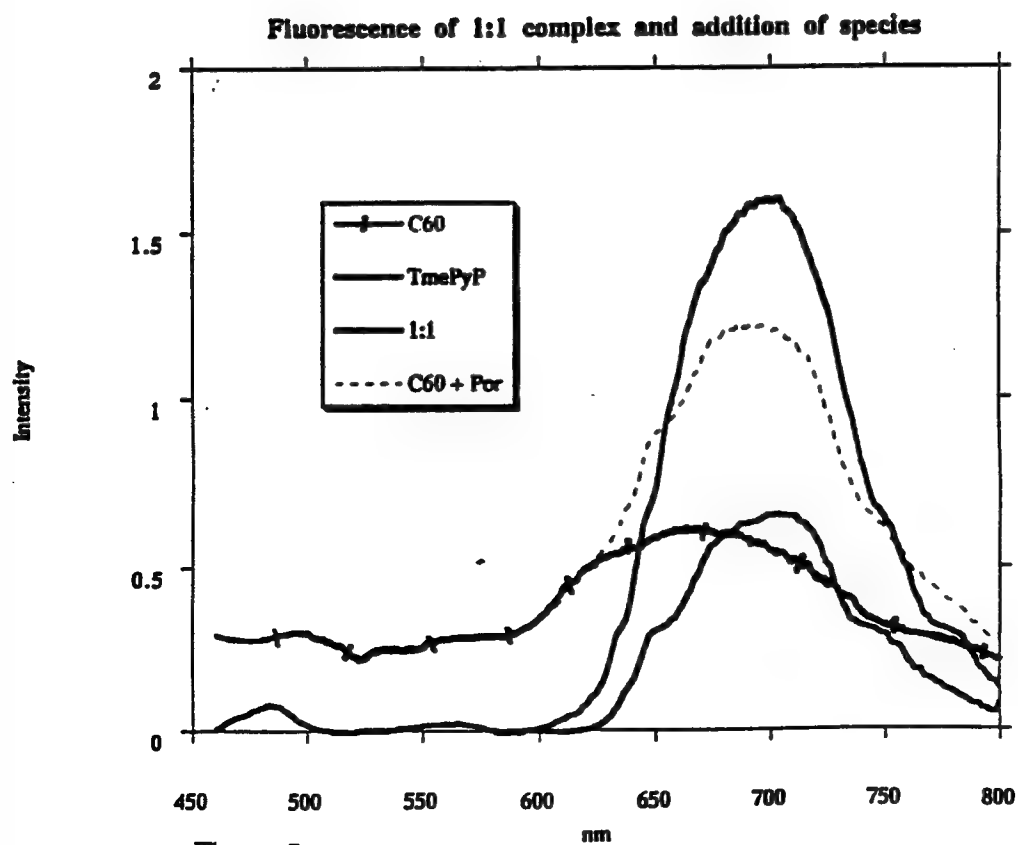


Figure 5

Supplied by Hao

Roughness Analysis

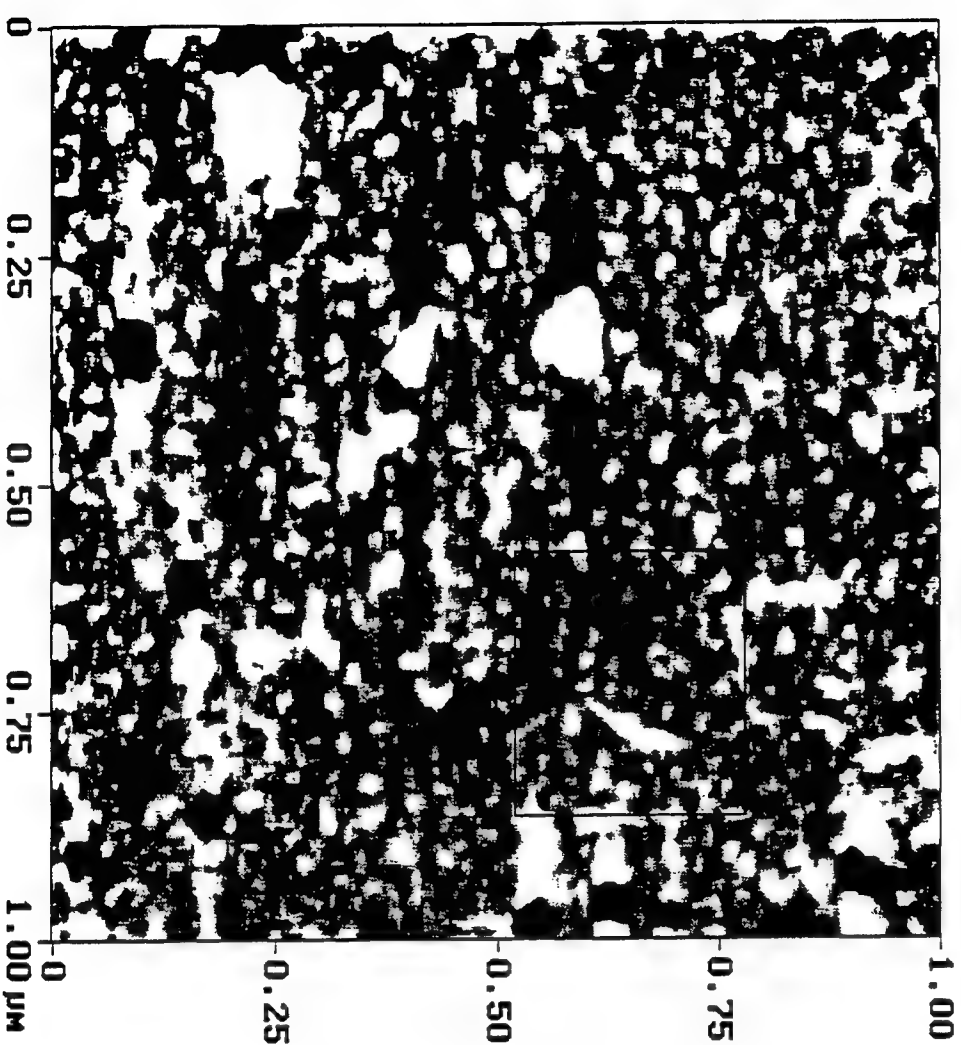


Image Statistics

Img. Z range 17.946 nm
 Img. Mean -0.000000 nm
 Img. Raw mean 7.486 nm
 Img. Rms (Rq) 1.171 nm
 Img. Ra 0.731 nm

Box Statistics

Z range 8.298 nm
 Mean -0.085 nm
 Raw mean 3.605 nm
 Rms (Rq) 0.687 nm
 Mean roughness (Ra) 0.478 nm
 Box x dimension 290.20 nm
 Box y dimension 258.82 nm

Figure 6

Peak Surface Area Summit Zero Crossing Stopband Execute Clear

Roughness Analysis

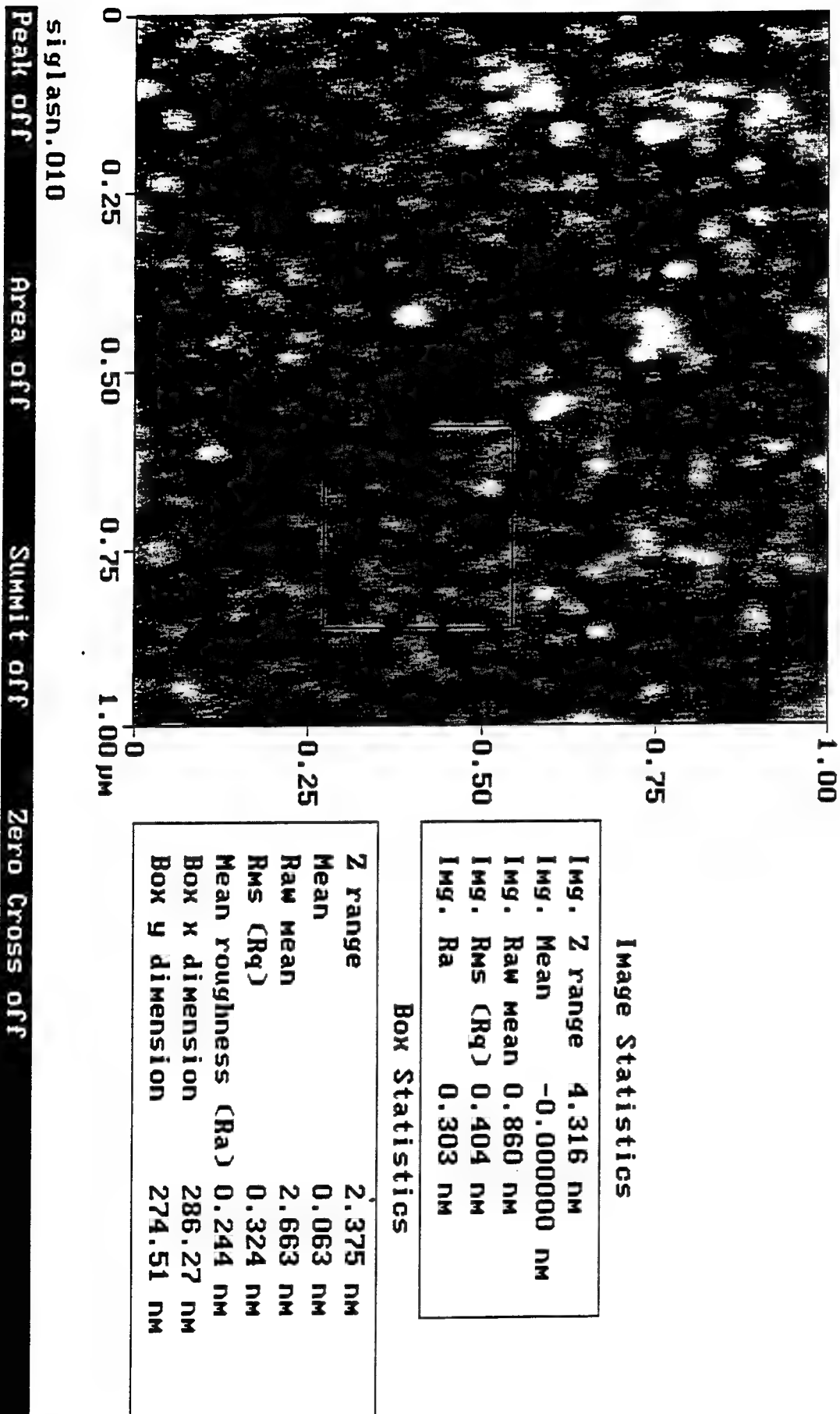


Figure 7

Peak Surface Area Summit Zero Crossing Stopband Execute Clear

Roughness Analysis

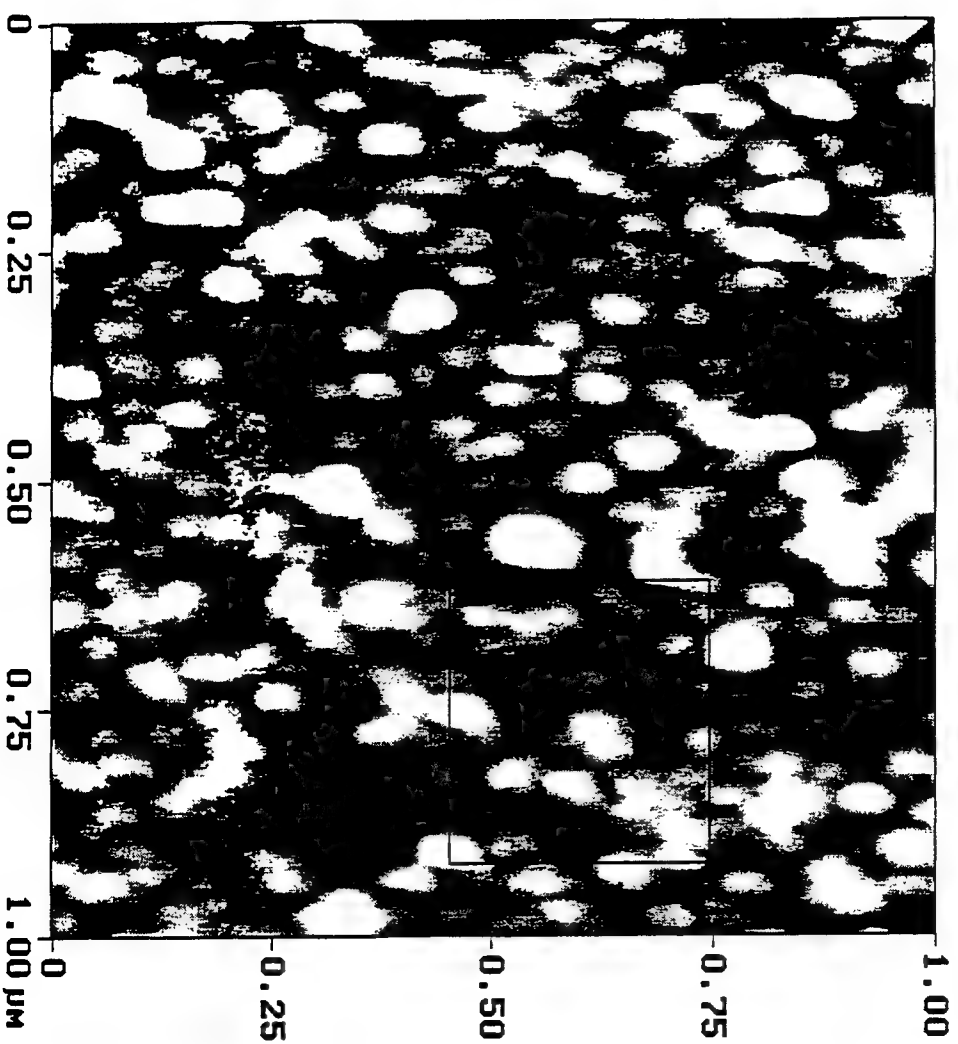


Image Statistics

Img. Z range 6.456 nm
Img. Mean 0.000000 nm
Img. Raw mean 0.396 nm
Img. Rms (Rq) 0.882 nm
Img. Ra 0.705 nm

Box Statistics

Z range 4.510 nm
Mean -0.091 nm
Raw mean 8.446 nm
Rms (Rq) 0.788 nm
Mean roughness (Ra) 0.639 nm
Box x dimension 309.80 nm
Box y dimension 294.12 nm

chiton.004

Peak off Area off Summit off Zero Cross off

Figure 8

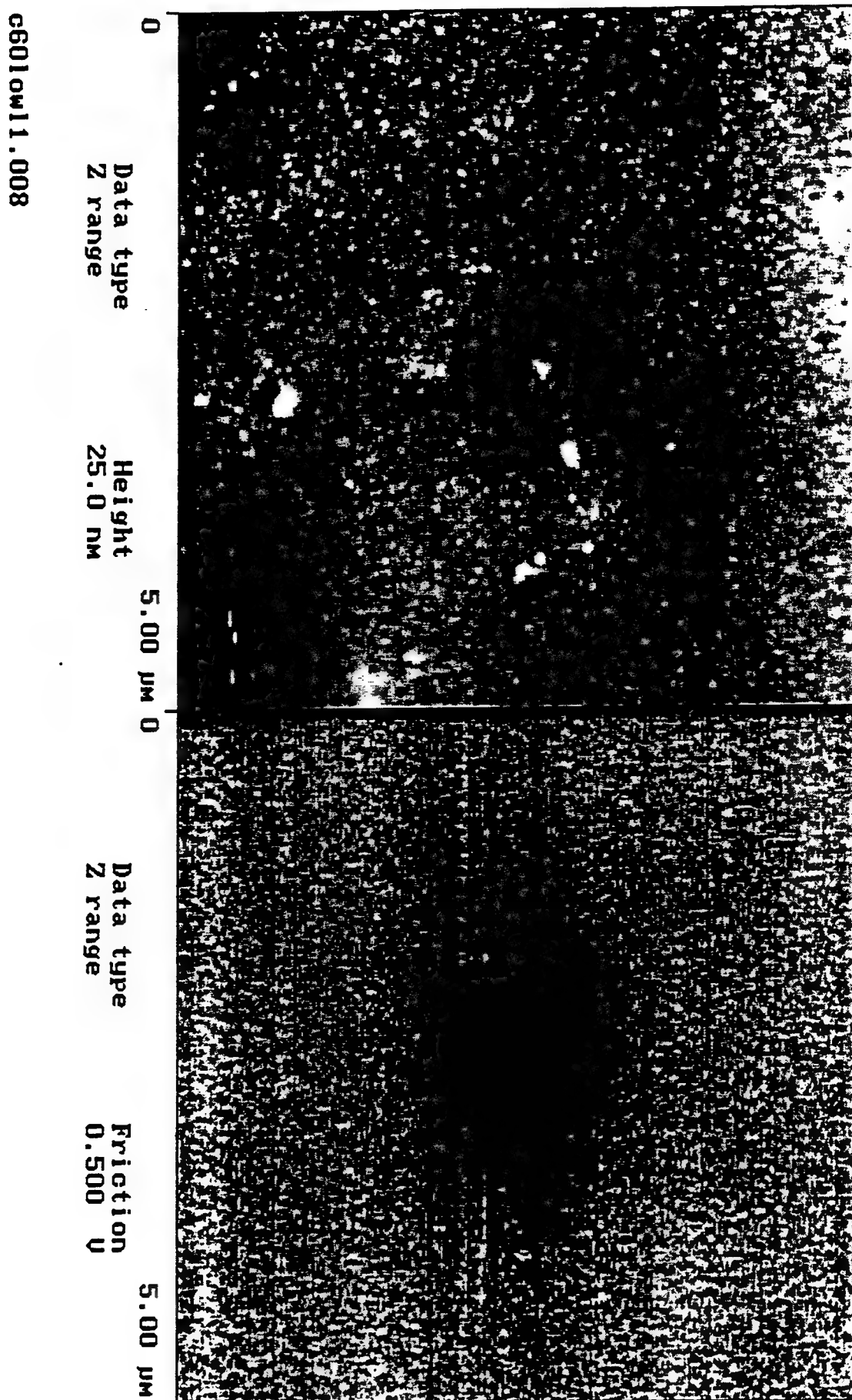
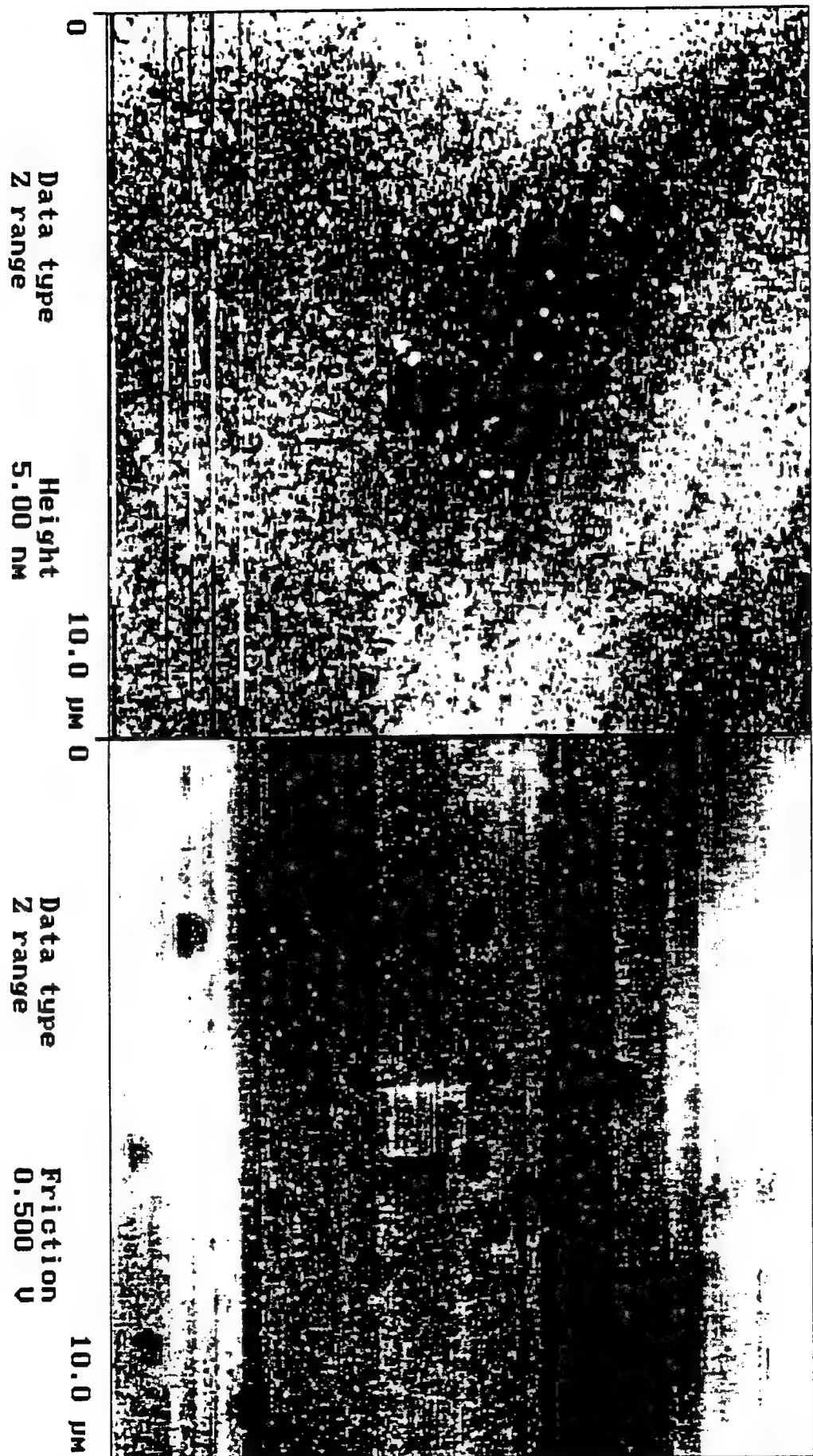


Figure 9

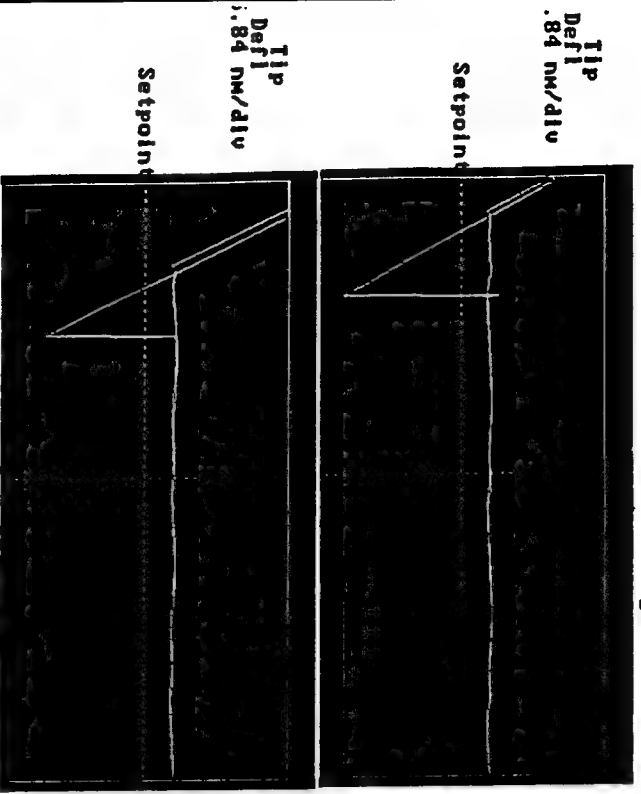


si.009

Figure 10

Force Calibration Plot

← Extending
→ Retracting



Z position - 0.05 $\mu\text{m}/\text{div}$

PLAIN TIP IN AIR

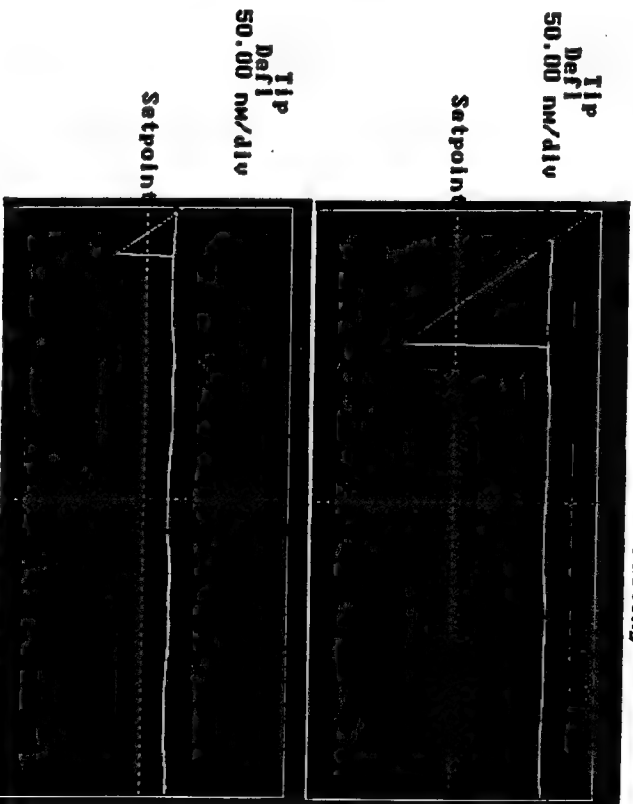
NanoScope
Z scan size
Setpoint
Z scan rate
Z range

Contact AFM
1.000 μm
-1.875 V
9.788 Hz
258.4 nm

Figure 11

Force Calibration Plot

← Extending
→ Retracting



Tip Defl
50.00 nm/div

Setpoint

Z position - 0.05 $\mu\text{m}/\text{div}$

NH_2 MOP TIP

NanoScope
Z scan size
Setpoint
Z scan rate
Z range

Contact AFM
1.000 μm
-0.2500 V
4.883 Hz
500.0 nm

Figure 12

Silanized
GLASS

1 bilayer

3

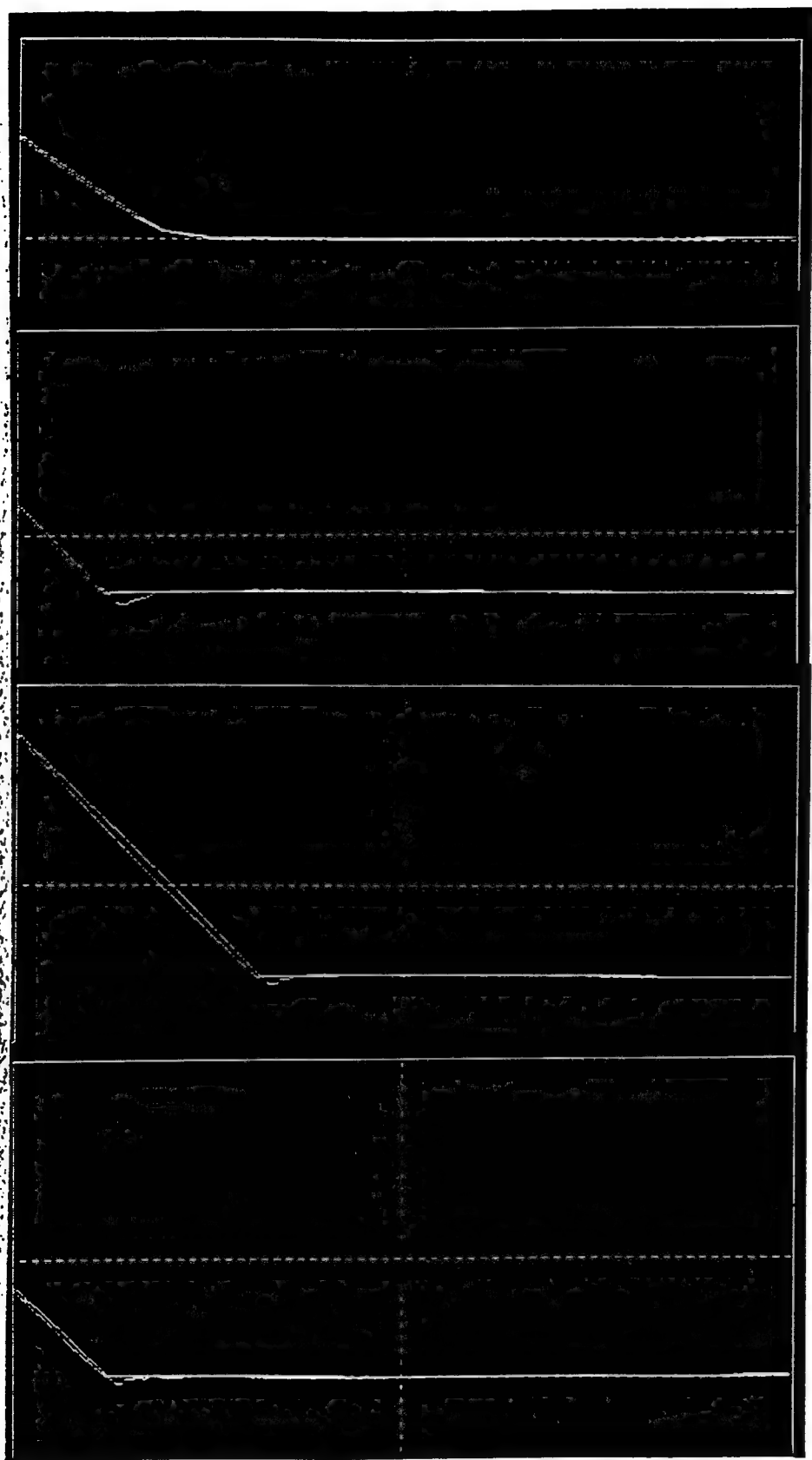
5

10

Figure 13

12-19

SCAN IN H₂O



CHITOSAN

1 bilayer

3

5

10

Figure 14

12-20

SCAN IN H₂O

SIMILARITY MEASURES
FOR
PATTERN RECOGNITION

Carl C. Hoff
Graduate Student
Department of Computer Science & Engineering

Wright State University
Dayton, Ohio

Final Report
for the
Graduate Student Research Program
of
Wright Laboratory

Sponsored by
Air Force Office of Scientific Research
Bolling Air Force Base, DC

and

Wright Laboratory
Wright Patterson Air Force Base, Ohio

September 1997

SIMILARITY MEASURES FOR PATTERN RECOGNITION

Carl C. Hoff
Graduate Student
Department of Computer Science & Engineering
Wright State University

ABSTRACT

What similarity is and how it is measured is fundamental to pattern recognition. A survey of recent literature resulted in this report's description of similarity measures for many types of data representations. These include:

- Points
- Point Sets
- Contiguous Point Sets (Shape and Texture)
- Attributed Relational Graphs (Parameterized Structural Descriptions)

For these data representations, what makes two patterns similar is that they are alike as concerns some significant characteristic. Unfortunately for the designer of pattern recognition algorithms, significant characteristics are problem dependent and may be hidden within the data, unknown to the algorithm designer. Thus the designer should consider many different problem and data representations, along with their accompanying similarity measures.

SIMILARITY MEASURES FOR PATTERN RECOGNITION

Carl C. Hoff

1. INTRODUCTION.

Similarity is fundamental to recognizing patterns, and yet frequently not explicitly defined. For example, consider neural networks being used for classification. Here the definition of similarity is consciously avoided. One puts a pattern into the neural network, and then trains the network according to whether it produced a correct or incorrect answer. How the network “reasoned” to generate the answer is not of interest, only the correctness of its response is important. In contrast, there are situations in which the designer of a pattern recognition algorithm needs to explicitly consider similarity.

Thus this effort’s objective has been to gain insight into what similarity is and how it is measured for pattern recognition and image understanding.

The approach taken was to survey recent literature. First, a dissertation on the meaning of similarity as applied to fuzzy logic was studied. Then databases of conference papers and journal articles were searched for words in their titles and abstracts that indicated a paper or article might be applicable to this effort. A typical search was “similarity “ and (“image” or “pattern”) and (“recognition” or “understanding”). Using this query, the Compendix Plus database was by far the most responsive. However, many of the articles and papers identified did not explicitly define similarity or distance measures. In contrast, the articles and papers which did explicitly define such measures did not consistently use a common set of key words in their titles and abstracts. As a result, identifying relevant literature takes time. This report is a beginning.

The nature of similarity and the four categories of similarity measures are addressed in the next two sections of this report. This establishes a basis for the most important sections, those describing the application of similarity measures to various data representations. These representations include points, point sets, contiguous point sets (shapes and textures) and attributed relational graphs (parameterized structural descriptions).

2. NATURE OF SIMILARITY.

The nature of similarity is not obvious, even though we humans measure similarity of visual, auditory and other patterns all day. Usually we do it unconsciously.

Similarity is the degree to which two things are alike as concerns some significant characteristic. Which characteristics are significant depends on the problem or situation. Unfortunately, sometimes the significant characteristics are not obvious. Even though the designer of a pattern recognition algorithm may understand the overall problem, the identity of the significant characteristics may remain hidden within the data. Thus the designer faces a challenge.

The nature of similarity involves a number of other notions, many of which are addressed in [Cross - 1993].

a. Dissimilarity -- Although dissimilarity is frequently treated as the complement of similarity, the two can have a very different focus. The common features we humans emphasize for similarity judgments differ substantially from the distinctive features we emphasize for dissimilarity judgments. Thus, one might define "dissimilarity" as the similarity of complements, and the complement of similarity as "non-similarity". For fuzzy sets, these are not the same.

b. Symmetry -- Although symmetry is frequently considered a desirable property for a similarity measure, this is not always the case. For example, in the question "How similar are X and Y?", the roles of X and Y appear the same. In contrast, in the question "How similar is X to Y?", the roles are different. X is the subject and Y the referent. We humans tend to choose the more salient object as the referent. In other words, we tend to choose as the object which has a better goodness of form, or when that goodness is equivalent, the object which is more complex. This can be very important because it amounts to deciding what is the basis for comparison.

c. Relativity -- Deciding what is the scale for comparison is a relative decision. That is when we humans judge the similarity of two values of an attribute, we make the judgment within the context of the distribution of the attribute's values. Given a nonlinear distribution, we are likely to use a nonlinear scale.

d. Multi-dimensional versus Multi-attribute -- Color, with its dimensions of hue, brightness and saturation, is an example of an attribute which we humans perceive as one stimulus despite its multiple dimensions. Comparing the similarity of two colors would be a perceptual activity, done without apparent thought. In such cases, similarity measures are relatively straight forward. In contrast, determining the similarity of two airplanes could require considerable thought. Tradeoffs between the planes' many different attributes (mission, payload, speed,

altitude, range and maneuverability) would require a highly cognitive activity. Such multi-attribute comparisons can involve all the delicate problems of attitude and strategy that characterize decision making in general. These complicated similarity measures are in the realm of "data fusion".

3. FOUR CATEGORIES OF SIMILARITY MEASURES

Of the multitude similarity measures, each may generally be categorized as one of the following:

- Distance - based measures
- Sets theoretic measures
- Logical co-implication measures
- Information theoretic measures

Although these categories come from different perspectives, the resulting similarity measures are NOT disjoint. The same similarity measure may result from considering the data as members of a set, as the components of a vector, or as the members of a string. The important point is that designers should consider their data from each of the four perspectives since each may provide a different insight into the problem.

Many examples of the functions used to compute these measures, along with analyses of their mathematical properties, are included in [Cross-1993] and [Van Cutsem - 1994].

3.1 Distance - Based Measures

Distance-based similarity measures differ from the distance measures on which they are based. While similarity measures range from 0 to 1, distances range from 0 to infinity. This distinction is frequently unimportant. Usually the ordering of a set of measurements is important, not their magnitude.

When a similarity magnitude is needed, a variety of functions can be defined that will convert a distance measurement. One common example is to define similarity as the reciprocal of (1 plus the distance). Another example is to define similarity as the reciprocal of a constant raised to the distance. If the distances are periodic, then trigonometric functions may be used.

A large variety of distance measures exist. Distances between points are frequently measured using a Minkowski r -metric, the most common of which are the one, two and infinity norms (i.e. the city-block, Euclidean and maximum norms). There are also distance measures between intervals, distance measures in hyper-spherical spaces, distance measures of fuzzy set properties, and more.

3.2 Set Theoretic Measures

There are also a variety of set-theoretic measures, each of which measures a different type of similarity. For example, for one type, sets may be similar only to the extent they share members. In contrast, another type of similarity may measure both the common sharing of members and the common lack of other members. For some problems, different members may differ in their importance. This may result in their presence being weighted more or less heavily. Thus different set-theoretic measures involve different bases and scales of comparison.

Three common set theoretic measures are listed below. In all three cases, they are the ratio of the cardinality of the intersection of two sets to the cardinality of some basis.

- Inclusion -- $I(A,B) = \text{intersection cardinality} / \text{cardinality of set A.}$
- Partial Matching -- $P(A,B) = \text{intersection cardinality} / \text{cardinality of the smaller of A and B.}$
- Similarity -- $S(A,B) = \text{intersection cardinality} / \text{cardinality of the union of A and B.}$

In other words, two sets are similar to the extent they share members (and possibly to the extent they share the lack of other members) as compared to some basis of possible membership.

3.3 Logical Co-Implication Measures

Two logic statements are similar to the extent the truth of statement A implies the truth of statement B, and vice versa. Measuring this similarity is straight-forward for crisp, binary logic. In contrast, for fuzzy, multi-valued logic, there are various ways of measuring the extent of co-implication. For example, does one also include the extent to which the compliments imply each other. (This is analogous to the question for set theoretic measures of whether to consider the common lack of members between sets.)

3.4 Information Theoretic Measures

Two groups of data are similar to the extent the information in group A is redundant with that in group B, and vice versa. This similarity is related to two types of distance.

The first distance is based on Kolmogorov complexity theory as described in [Li & Vitányi - 1997]. This information distance is measured relative to a universal computer, that is a theoretical computer capable of simulating any other computer. On such a computer, the minimum information distance between A and B is the size of the largest of two algorithms: (1) the smallest algorithm that will translate from A to B, and (2) the smallest that will translate from B to A.

The second distance is based on Shannon's communication theory as described in [Shannon - 1948]. This information distance is measured relative to entropy. Entropy is a measure of the change in uncertainty caused by the receipt of a message. Thus the information distance between A and B is the sum of the uncertainty about A given B, and the uncertainty about B given A.

4. APPLICATIONS OF SIMILARITY MEASURES

The remaining sections of this report describe the use of similarity measures for various data representations. These representations include points, point sets, contiguous point sets (first shape, then texture), and attributed relational graphs (parameterized structural descriptions).

5. POINTS

Frequently for classification and clustering, the similarity and dissimilarity of a point with one or more other points is measured. These measurements may be made using a probabilistic model or various distances, including the Mahalanobis distance.

5.1 Probabilistic Models

One measure of the similarity of two points is the likelihood that one represents the other. This concept has been applied to speech recognition and to optical character recognition using hidden Markov models. Examples include [Rabiner - 1989] and [Sin & Kim - 1997]. These examples use a set of learned conditional probabilities to determine the probability of all possible classifications of a data point. The resulting probabilities range from 0 to 1, and thus may be considered similarity measures.

5.2 Clusters

In [Young - 1996], a new algorithm based on a weighted Mahalanobis distance is used to cluster data. Like other clustering algorithms, the algorithm seeks to maximize inter-cluster distances and minimize intra-cluster distances. Frequently Euclidean distances have been used. However, the use of Euclidean distances assumes clusters may be separated by enclosing each in a hyper-sphere. This would be true if the coordinates of each datum in a cluster were independent and thus equally important. Because this assumption is not always true, the Mahalanobis distance measure is useful. In Young's algorithm, covariance of the data within each cluster is used to create a space in which each cluster's data coordinates are independent. In the original data space, this corresponds to allowing each cluster to be shaped and oriented as a hyper-ellipsoid. To inhibit

large clusters from unduly attracting members of neighboring clusters, the Mahalanobis distances are weighted by the ratio of the cluster size to the size of the training set. The resulting algorithm was tested along with some other well-known algorithms on classical data sets, and used for image encoding. For all the algorithms, MATLAB code is furnished in an appendix.

6. POINT SETS

Measures of distances between point sets fill multiple needs. One is to match image features in stereoscopic vision (as with a median-based distance). Others are to align point sets (as with affine transformations) and to classify sets (as with the Hausdorff distance).

6.1 Median - Based Distance Measures

Median-based distance measures may fill a need for robust statistics in computer vision. Like other applications of statistical estimation processes, computer vision involves the reduction of large amounts of noisy data to a small amount of information. However, Gaussian noise may not be the only source of error. For example, a program which estimates a 3-dimensional position from two 2-dimensional images may have errors due to incorrect matching of features within the images. These errors may be very large, and not fit the normal distribution on which many statistical measures are predicated. For this reason, [Stein & Werman - 1992] advocates use of the median over a mean. They also suggest forms of the equations for straight lines and 2-dimensional conic sections which are more appropriate than other forms. Their suggested forms maintain translation and rotation equivariance while using the more robust median measure.

Although some authors have suggested a median-based distance measure is natural for computer vision, [Boninsegna & Rossi - 1994] argue no such natural measure exists. Instead, they argue the most suited distance measure critically depends on the problem and its data. For example, when comparing a gray-level image to a template, the image may have Gaussian noise, as well as other larger errors due to geometric transformations. To accommodate both sources of error, they proposed a parametric class of distance measures which varies from a median measure at one extreme to a Euclidean measure at the other extreme. In between, their distance measure combines the benefits of both median and Euclidean measures. The Euclidean measure is applied to smaller distances, and the median to the larger distances. This approach works when the Gaussian noise for which the Euclidean distance is appropriate is smaller than the larger non-Gaussian errors.

6.2 Affine Transformations

To align sets of points from two images, [Werman & Weinshall - 1995] use the Frobenius norm. In essence, this norm is the sum of the Euclidean distance between corresponding points in the two sets. Before this norm can be applied, the planes containing the points must be tentatively aligned. This alignment may entail a scaling, translating, rotating and tilting the planes containing the point sets. (In this context, "tilting" is about an axis in the image plane, where as "rotation" is about the axis normal to the plane.) Once the images are aligned, the Frobenius norm is used to calculate distances. Three distance measures were found useful. One, "D_sim", excluded any tilting in contrast to the second, "D_aff", which included tilting. The third distance, "D_mix", measured the difference between a point set which had be tilted and another which had not. When D_mix was minimized, the images were considered properly aligned. As examples, this method was used to align images of a cube and of a toy tiger. In [Weinshall, Werman & Tishby - 1994], the method was used to analyze the stability and likelihood of two dimensional images of three dimensional objects.

6.3 Hausdorff Distance

The Hausdorff distance is the maximum nearest-neighbor distance between two sets of points. The distances between the points in one set and their nearest neighbors in the other set may be measured using any distance metric. Usually, the Euclidean distance is used.

The Hausdorff distance is used by the neural network in [Rosandich - 1997] to recognize binary images. This contrasts with many current networks which use Hamming, dot product or Euclidean distance metrics. Those metrics require that the two-dimensional input patterns be converted to multi-dimensional vectors before training and recognition is done. Unfortunately, for patterns that appear very similar to a human, the resulting behavior of those metrics can be counter-intuitive. In contrast, the Hausdorff distance decreases gracefully as the pattern deviates further from the ideal. This behavior is more representative of human performance. As an example, the Hausdorff distance is used with a neural network to recognize hand-written English characters.

Because of its usefulness, a series of articles address efficient computation of the Hausdorff distance when an image and a model are translated and rotated in respect to one another. The most recent is [Huttenlocher, Klanderman & Rutledge - 1993].

7. CONTIGUOUS POINT SETS -- SHAPES

There are three basic approaches for measuring how well the shape of a real-world, 2 dimensional (2D) image corresponds to that of a 3 dimensional (3D) model:

- 1 -- Image distance -- Project the 3D model on to a 2D surface, thereby creating a 2D model. Then measure the similarity of that 2D model to the 2D image.
- 2 -- Transformation distance -- Measure the deformations that must be applied to the 3D model in order to produce the 2D image.
- 3 -- Model distance -- Inversely project the 2D image into a 3D volume, thereby creating a 3D image_model. Then measure the similarity of that 3D image_model to the original 3D model.

Note that both the second and third approaches may involve the first to some degree. For example, for the second, if no transformation can produce an exact copy of the 2D image, then the desired transformation is that which minimizes the distance between the image and the transformed model. In the case of the third, the algorithm generating the 3D pseudo-image may iteratively generate trial image_models, whose projection on a 2D surface is then compared to the original 2D image.

7.1 Image Distances

Image distances are the first of three approaches for comparing a 2D image with a 3D model. Most image distances can be divided into two groups: (1) those which are based on the shape boundary and (2) those using the whole shape.

An example of those based on the boundary is described in [Arkin, Chew, Huttenlocher, Kedem & Mitchell - 1991]. This article is frequently cited because it argues a measure of shape similarity should have four properties: (1) be a metric, (2) be invariant under translation, rotation and scale changes, (3) be reasonably easy to compute and (4) be consistent with human intuitive notions of shape resemblance. These four properties are present in the article's similarity measure for polygonal shapes. Each polygon may be described by the orientation of its sides as a function of the distance around its perimeter. Thus the first step is to normalize the length of the polygon perimeters. Then the square of the difference between the orientation of the sides of the polygons is integrated around the perimeter. The value of this integral may vary depending on the relative orientation of the polygons. Thus one polygon is rotated until the integral is a minimum. The square root of that integral is the distance.

Among the image distances using the whole shape are those based on mathematical morphology. The following papers are both based on the morphological skeleton transform. Like many morphological papers, both were written for binary images. However, the concepts are equally applicable to images of higher dimensionality, for example, gray-scale images and 3D shapes.

To express the distance between two binary shapes, [Trahanias - 1992] conceptually overlays one shape's skeleton on the other's. Then each point in both skeletons is matched with the nearest point in the other skeleton. The distances between these nearest points are each given a weight based on the difference, if any, in the significance of each point to its skeleton. These weighted inter-point distances are then summed to measure the distance between the shapes. Use of this distance measure was illustrated with a variety of binary shapes.

[Sahasrabudhe & Banerjee - 1990] and [Banerjee & Sahasrabudhe - 1994] define the similarity (or "closeness") of two binary shapes. The first shape is used as a morphological structuring element to create a skeleton of the second. The index stored at each point in the skeleton indicates the number of dilations by the structuring element which are needed to recover the second shape. The points with the largest index identify the shape's fundamental shape. This is so because the skeleton is formed so that dilations of its points will not overlap. Skeleton points with less than the largest index represent distortions of the second shape from that of the first. A weighted sum of the distortions may be defined as the similarity of the two shapes. ([Banerjee & Sahasrabudhe - 1994] is a more complete explanation than [Sahasrabudhe & Banerjee - 1990].)

Note: Related to similarity measurement with morphological transforms is the idea of morphing between two shapes. However, these two operations have very different emphases. While the former seeks to summarize in one number a global abstraction of how the shapes are related, the latter seeks a local, point-by-point transformation between the two shapes. An example is the morphing technique described in [Ranjan & Fournier - 1996]. That technique decomposes each shape into a set of circles (or spheres for three dimensional shapes) such that the circle centers form the skeleton of each shape. The points in each skeleton are then matched with the points in the other. By interpolating between the circle positions, radii and orientations, one may morph from one shape to the other. However, although the two shapes have been related, that relationship is not described in a single number, a similarity measure.

7.2 Transformation Distances

Transformation distances are the second of three approaches for comparing a 2D image with a 3D model. An example is described in [Basri & Weinshall - 1996]. Their method seeks to minimize the difference between the image and the best possible view of the model under a rigid transformation. With the assumption that the image is an affine transformation of the model, this is equivalent to minimizing the difference between rigid and affine transformations. The rigid transformations are a subset of the affine transformations, which also include reflection, stretch and shear. Thus the minimization results in a transformation metric which measures how much the

model must be deformed in order to produce the image. This metric is shown to be equivalent to the Euclidean image metric in that they bound each other from above and below. Use of the transformation metric is illustrated by recognizing some chairs and by obtaining the dimensions of a battery charger.

7.3 Model Distances

Model distances are the third of three approaches for comparing a 2D image with a 3D model. Examples include the use of range data, shading data and stereoscopic data to create 3D image_models. These models have taken various forms, some of which are in terms of superquadric equations. The image_models may in turn be used to access a model base.

7.3.1 Superquadrics

By using a gradient descent method to minimize a cost function, [Solina & Bajcsy - 1990] formed 3D superquadric image_models from range data. The cost function depended both on the distance of the range data points from the model surface and on the overall size of the model. During minimization, all the model's parameters were simultaneously adjusted, thereby recovering position, orientation, size, and shape. Because this parameter space had many local minima, a stochastic technique was used. The parameters also had to be constrained to a subspace because otherwise the symmetry in some images would have caused multiple acceptable solutions. The resulting solutions were superquadric models with parametric deformations (bending, tapering, and cavity deformations).

The use of shading data to generate a shape is described by [Saito & Kimura - 1996]. That shape is defined in terms of superquadric equations whose parameters are evolved by a genetic algorithm. The fitness of those parameters is determined by creating a 2D image of the shape and measuring its similarity to the original image. This similarity is measured by two cross-correlations, one of gray scale images and the other of edge images.

A method for accessing a 3-D shape database with descriptive words or 2-D images is described by [Horikoshi & Kasahara - 1990]. All the database shapes are characterized in terms of superquadric equations. Thus each shape is characterized by a set of parameters. Using an Euclidean distance measure, these parameters are compared to those generated by the database user inquiry. The shape with the closest parameters is selected as the shape about which the inquiry was made. The inquiry may be made in terms of words or rough images of the shape.

7.3.2 Other 3D Methods

In [Sato & Honda - 1983], the distance between two 3D objects is a weighted sum of five pseudo-distances: elongatedness, horizontal strain, section shape, torsion and displacement. These pseudo-distances are defined for objects which are modeled as a stack of horizontal sections. Among those objects used to test the distance measures were models of an elephant, pig, lion, giraffe and human. The human model was observed in standing, jumping (bending) and walking (twisting) positions.

In [Okada, Sano & Kaneko - 1994], the similarity between 3D shapes is measured by comparing sets of surfaces. Each surface is represented by a vector whose magnitude is proportional to the surface area and whose direction is normal to the surface. Spherical correlation of the vectors then results in a measure of similarity. Use of the metric was demonstrated with various polyhedrons.

In [Shum, Hebert & Ikeuchi - 1995/1996], the distance between 3D shapes is measured in terms of the local curvature in a mesh which has been deformed from a sphere. More precisely, a closed, curved or polyhedral 3D shape without holes is covered by deforming a semi-regularly tessellated sphere. On the sphere, each mesh node is connected to its three nearest neighbors. These connections are preserved as the mesh is deformed so that each node approaches a point on the original 3D shape. The result is a spherical representation of the shape's local curvature at each mesh node. Thus, by comparing the curvature distributions of two shapes, the similarity or distance between the shapes may be measured. As examples, this distance metric was used to compare various polyhedrons, and to compare a dog with a sha.

Note: For a brief description of additional shape similarity measures, see section 1 of [Shum, Hebert & Ikeuchi - 1995/1996].

8. CONTIGUOUS POINT SETS -- TEXTURES

A texture is a large ensemble of elements that resemble each other to a great extent and that have a rough kind of order, such that no one element is perceived in a special way. When looking at a texture, a human gets the impression of uniformity. The three most important perceptual dimensions for humans are "repetitiveness", "directionality" and "granularity and complexity".

To identify which texture in a database is most similar to a prototype texture, [Liu & Picard - 1996] use a texture model based on Wold random field decomposition theory. They order the database based on a weighted sum of two preliminary orderings. One of those orderings is based on each

texture's random, indeterministic nature and the other on its harmonic, deterministic nature. For the deterministic ordering, the similarity of harmonic patterns is measured by convolving the prototype texture with every database texture. The indeterministic ordering is based on the Mahalanobis distance between two vectors. Those vectors are formed from the parameters of a second order, symmetric, multi-resolution, simultaneous autoregressive model of each texture. A weighted sum of these two preliminary orderings is used to create the final ordering. The weights are based on the relative contribution of the deterministic and indeterministic components to the autocovariance energy. This method was tested using the Brodatz texture database.

9. PARAMETERIZED STRUCTURAL DESCRIPTIONS & ATTRIBUTED RELATIONAL GRAPHS

A parameterized structural description may be represented by an attributed relational graph. The graph describes a scene in which objects are represented by nodes and the relations among objects by arcs. Just as each object's attributes are represented node parameters, so to can arc parameters represent the attributes of relationships. For example, objects with the attribute Shape (cube, sphere) may have a relationship Position (in_front_of, on_top_of). The relationships could include is_a_part_of, in which case the graph may represent a hierarchy of objects. For example, one or more lines may form an English character, one or more of which may form a word, one or more of which may form a sentence, etc. Thus the graph may contain information at several levels of abstraction.

Similarity measures for attributed relational graphs are useful in many cases. One case is when the objects and relationships derived from an image are to be compared to a model. Another case is for stereopsis when the graphs from two images are compared.

Similarity measures for attributed relational graphs have been studied for many years. In [Tsai & Fu - 1979], the first journal article for this type of graph, patterns were classified using a combination of both statistical methods and structural techniques. In other words, patterns were first represented as relational graphs. Then deformation probabilities and a maximum-likelihood decision rule were used to find the most likely isomorphism between the graphs for the observed and model patterns. Because deformation probabilities are not always known, alternative forms of the algorithm were presented that use a weighted distance measure or a weighted least squared error measure. After this initial article, many more articles and papers by King-Su Fu and his students have followed, among which are [Sanfeliu & Fu - 1983] and [Eshera and Fu - 1984].

Typically the similarity measures are expressed as distances. [Sanfeliu & Fu - 1983] grouped the conventional graph distance measures as follows:

1) Distances Using Feature Vectors - Extract the principal features of each graph (for example, the quantity of vertices with various degrees, quantity of triangles, etc.). Then represent those features as n-dimensional vectors, and compute the Euclidean distance between vectors.

2) Distances Using Transformation Cost - Associate a cost with each graph modification and then compute the minimum cost required to transform one graph into another. This can be done in two ways: (a) by computing the transformations from an external reference (for example, a grammar), or (b) by computing the transformations using only the input and reference graphs.

For patterns that contain "noise" or minor deformations, both a similarity measure and related distance measure are defined by [Wong & You - 1985]. These measures are based on "random" graphs in which both object attributes and relationship attributes are considered random variables. As such, Shannon's entropy may be used as a measure of graph variability. The distance between random graphs is then defined as the minimum change in entropy required to merge the graphs, where the minimization is over all possible structural isomorphisms between the two graphs. The authors suggest this concept may be extended to both random hierarchical graphs and hypergraphs. (In a hypergraph, an arc may connect more than two nodes.) As a test, the concept was used to recognize hand-written lower-case English letters.

For models of colored solids, a tunable distance measure described by [Aisbett and Gibbon - 1994] mimics the way humans judge the relative similarity of objects. The distance is based on the lowest cost map among object representations. Those representations use a boundary representation scheme that reflects human visual segmentations of color + physical space. The distance includes three measures: (1) a geometric measure of the smooth deformation of edges and faces, (2) a feature measure based on visually significant singular points, and (3) a topological measure based on the correspondence between significant vertices, edges and faces. Tunable features of this distance include the relative cost of ignoring parts of objects; the treatment of color; and whether or not the distance measure is rotationally invariant. As an example, this distance is applied to the recognition of lower case, English letters.

For stereopsis, [Boyer & Kak - 1988] match objects and relationships in the left image with those in the right image by minimizing an information-theoretic distance. In other words, the description

of one image most closely corresponds to that of the other when little additional information is provided by the second. This correspondence may be measured in terms of the conditional probability that the existence of features in one image's description would indicate the existence of corresponding features in the description of the other. Thus, this is a probabilistic problem of consistent labeling between the parameterized structural descriptions of the two images. Because the problem is probabilistic, some noise and distortion can be handled. These may arise because of difficulties in primitive detection and extraction, geometrical distortions induced by the perspective, optical distortions, etc. Although a great many probabilities must be estimated, computed or supplied by the user, these probabilities allow the distance measure to be sensitive to the characteristics of the problem domain. Indeed, the probabilities may be adjusted as new data becomes available or the situation changes. Using this approach, a robot was able to identify and manipulate four rods which were initially lying on top of one another on a table.

For organizing large structural modelbases, [Sengupta and Boyer - 1995] defines two information-theoretic distance measures. (These measures are called "dissimilarity measures" by the article, but are really distance measures in that their range is from zero to infinity, not zero to one.) In any case, the approach is similar to that in [Boyer & Kak - 1988] above. When the information in one parametric structural description is highly redundant with that in another, then the two descriptions are judged to be similar. This concept is used to define both distance measures. One measure is used to cluster the models within the modelbase. This clustering facilitates use of the other distance measure to determine which model most closely corresponds an image's description. To test this approach, it was applied to 1000 synthetically generated descriptions, 50 descriptions of real household objects and 100 descriptions of 3-D computer aided design (CAD) objects.

10. CONCLUSION

Similarity is fundamental to recognizing patterns, but takes on many guises: distance, set membership, etc. In any guise, what makes two things similar is that they are alike as concerns some significant characteristics. What is significant is problem dependent. This poses two challenges for the designer of pattern recognition algorithms. The first is that there are many different problems. The second is that for some problems the designer does not know which characteristics are significant. Their significance is hidden within the data. Thus the algorithm designer should consider many problem and data representations. Each representation may provide its own insight into the problem. Hopefully, this insight will lead the designer to discovering those significant data characteristics which must be the basis of that problem's similarity measure.

11. REFERENCES

[Aisbett & Gibbon - 1994]

A tunable distance measure for coloured solid models

-- Jane Aisbett and Greg Gibbon

-- Artificial Intelligence, volume 65 (1994), pages 143 - 164

[Arkin, Chew, Huttenlocher, Kedem & Mitchell - 1991]

An Efficiently Computable Metric for Comparing Polygonal Shapes

-- Ester M. Arkin, L. Paul Chew, Daniel P. Huttenlocher, Klara Kedem and Joseph S. B. Mitchell

-- IEEE Transactions on Pattern Analysis and Machine Intelligence, volume 13 number 3 (March 1991), pages 209 - 216

[Banerjee & Sahasrabudhe - 1994]

C-Factor: A Morphological Shape Descriptor

-- Sujata Banerjee and S. C. Sahasrabudhe

-- Journal of Mathematical Imaging and Vision, volume 4 number 1 (February 1994), pages 43 - 55

(Available from "ftp://violettele.pitt.edu/pub/Telecom_Faculty/Banerjee/Papers/JMIV-94.ps" which may be accessed via "http://www2.pitt.edu/~sujata/pubs_year.html".)

[Basri & Weinshall - 1996]

Distance Metric Between 3D Models and 2D Images for Recognition and Classification

-- Ronen Basri and Daphna Weinshall

-- IEEE Transactions on Pattern Analysis and Machine Intelligence, volume 18 number 4 (April 1996), pages 465 - 470

(Related to MIT AI Memo 1373, "Distance Metric Between 3D Models and 2D Images for Recognition and Classification", which is available from DTIC as ADA260069 and "ftp://publications.ai.mit.edu/ai-publications/1000-1499/AIM-1373.ps.Z".)

[Boninsegna & Rossi - 1994]

Similarity Measures in Computer Vision

-- M. Boninsegna and M. Rossi

-- Pattern Recognition Letters, volume 15 (December 1994), pages 1255 - 1260

[Boyer & Kak - 1988]

Structural Stereopsis for 3-D Vision

-- K. L. Boyer and A. C. Kak

-- IEEE transactions on Pattern Analysis and Machine Intelligence, volume 10 number 2 (March 1988), pages 144 - 166

[Cross - 1993]

An Analysis of Fuzzy-Set Aggregators and Compatibility Measures

-- Valerie Veltri Cross

-- Ph.D. dissertation, Wright State University, 1993

[Eshera & Fu - 1984]

A Similarity Measure between Attributed Relational Graphs for Image Analysis

-- M. A. Eshera and K. S. Fu

-- IEEE International Conference on Pattern Recognition -- 1984, pages 75 - 77

- [Horikoshi & Kasahara - 1990]
 3-D Shape Indexing Language
 -- T. Horikoshi and H. Kasahara
 -- Phoenix Conference on Computers and Communications -- 1990, pages 493 - 499
- [Huttenlocher, Klanderman & Rutledge - 1993]
 Comparing Images using the Hausdorff Distance
 -- Daniel P. Huttenlocher, Gregory A. Klanderman and William J. Rucklidge
 -- IEEE Transactions on Pattern Analysis and Machine Intelligence, volume 15 number 9
 (September 1993, pages 850 - 863)
- [Li & Vitányi - 1997]
 An Introduction To Kolmogorov Complexity and Its Applications
 -- Ming Li and Paul Vitányi
 -- Springer-Verlag, first edition - 1993, second edition - 1997
- [Liu & Picard - 1996]
 Periodicity, Directionality, and Randomness: World Features for Image Modeling and Retrieval
 -- Fang Liu and Rosalind W. Picard
 -- IEEE Transactions on Pattern Analysis and Machine Intelligence, volume 18 number 7 (July 1996), pages 722 - 733
- [Okada, Sano & Kaneko - 1994]
 Three-Dimensional Object Recognition Using Spherical Correlation
 -- Takashi Okada, Mutso Sano and Hiroshi Kaneko
 -- Systems and Computers in Japan, volume 25 number 7 (1994), pages 48 - 58
 (As translated from Denshi Joho Gakkai Ronbunshi, volume J75-D-II, number 12 (December 1992, pages 2027 - 2037))
- [Rabiner - 1989]
 A Tutorial on Hidden Markov Models and Selected Applications in Speech Recognition
 -- Lawrence R. Rabiner
 -- Proceedings of the IEEE, volume 77 number 2 (February 1989), pages 257 - 286
- [Ranjan & Fournier - 1996]
 Matching and Interpolation of Shapes using Unions of Circles
 -- V. Ranjan and A. Fournier
 -- Computer Graphics Forum, volume 15 number 3 (3 September 1996), pages 129 - 142
- [Rosandich - 1997]
 HAVENET: A New Neural Network Architecture for Pattern Recognition
 -- Ryan G. Rosandich
 -- Neural Networks, volume 10 number 1 (1997), pages 139 - 151
- [Sahasrabudhe & Banerjee - 1990]
 Morphological Shape Descriptor
 -- S. C. Sahasrabudhe and Sujata Banerjee
 -- SPIE volume 1350, Image Algebra and Morphological Processing (1990), pages 56 - 67

[Saito & Kimura - 1996] ---- The following two papers are essentially the same.
Superquadrics Modeling of Multiple Objects from Shading Images using Genetic Algorithms
-- Hideo Saito and Makoto Kimura
-- IEEE International Conference on Industrial Electronics, Control and Instrumentation -- 1996,
pages 1589 - 1593

Shape Modeling of Multiple Objects from Shading Images using Genetic Algorithms
-- Hideo Saito and Makoto Kimura
-- IEEE International Conference on Systems, Man and Cybernetics -- 1996, pages 2463 - 2468

[Sanfeliu & Fu - 1983]
A Distance Measure Between Attributed Relational Graphs for Pattern Recognition
-- Alberto Sanfeliu and King-Sun Fu
-- IEEE Transactions on Systems, Man and Cybernetics, volume SMC-13 number 3 (June 1983),
pages 353 - 362

[Sato & Honda - 1983]
Pseudodistance Measures for Recognition of Curved Objects
-- Yukio Sato and Ikuji Honda
-- IEEE Transactions on Pattern Analysis and Machine Intelligence, volume PAMI-5 number 4
(July 1983), pages 362 - 373

[Sengupta and Boyer - 1995]
Organizing Large Structural Modelbases
-- Kuntal Sengupta and Kim L. Boyer
-- IEEE Transactions on Pattern Analysis and Machine Intelligence, volume 17, number 4 (April
1995), pages 321 - 332

[Shannon - 1948]
A Mathematical Theory of Communications
-- C. E. Shannon
-- Bell Systems Technical Journal, volume 27 (July - October 1948), pages 379 - 423 and 623 -
656

[Shum, Hebert & Ikeuchi - 1995/1996]
On 3D Shape Similarity
-- Heung-yeung Shum, Martial Hebert and Katsushi Ikeuchi
-- (1) Carnegie Mellon University report CMU-CS-95-212 (November 1995)
(Available from <http://www.dtic.mil/stinet/str> in full text as ADA303243)
(2) IEEE Computer Society Conference on Computer Vision and Pattern Recognition, 1996,
pages 526 - 531

[Sin & Kim - 1997]
Ligature Modeling for Online Cursive Script Recognition
-- Bong-Kee Sin and Jin H. Kim
-- IEEE Transactions on Pattern Analysis and Machine Intelligence, volume 19 number 6, June
1997, pages 623 - 633

- [Solina & Bajcsy - 1990]
Recovery of Parametric Models from Range Images: The Case for Superquadrics with Global Deformations
-- Franc Solina and Ruzena Bajcsy
-- IEEE Transactions on Pattern Analysis and Machine Intelligence, volume 12 number 2 (February 1990), pages 131 - 147
- [Stein & Werman - 1992]
Robust Statistics in Shape Fitting
-- Andrew Stein and Michael Werman
-- IEEE Computer Society Conference on Computer Vision and Pattern Recognition (CVPR) - 1992, pages 540 - 546
- [Trahanias - 1992]
Binary Shape Recognition Using The Morphological Skelton Transformation
-- P. E. Trahanias
-- Pattern Recognition, volume 25 number 11 (1992), pages 1277 - 1288
- [Tsai & Fu - 1979]
Error-Correcting Isomorphisms of Attributed Relational Graphs for Pattern Analysis
-- Wen-Hsiang Tsai and King-Sun Fu
-- IEEE Transactions on Systems, Man, and Cybernetics, volume SMC-9 number 12 (December 1979), pages 757 - 768
- [Van Cutsem - 1994]
Classification and Dissimilarity Analysis
-- Bernard Van Cutsem, editor
-- Springer-Verlag, Lecture Notes in Statistics (LNS) 93, 1994
(See chapter 3, particularly the table at the end of that chapter, for many similarity functions.)
- [Weinshall, Werman & Tishby - 1994]
Stability and Likelihood of Views of Three Dimensional Objects
-- Daphna Weinshall, Michael Werman and N. Tishby
-- European Conference on Computer Vision (ECCV) - 1994, pages 24 - 35
- [Werman & Weinshall - 1995]
Similarity and Affine Invariant Distances between 2D Point Sets
-- Michael Werman and Daphna Weinshall
-- IEEE Transactions on Pattern Analysis and Machine Intelligence, volume 17 number 8 (August 1995), pages 810 - 814
- [Wong & You - 1985]
Entropy and Distance of Random Graphs with Application to Structural Pattern Recognition
-- Andrew K. C. Wong and Manlai You
-- IEEE Transactions on Pattern Analysis and Machine Intelligence, volume PAMI-7, number 5 (September 1985), pages 599 - 609
- [Young - 1996]
Weighted Mahalanobis Distance for Hyper-Ellipsoidal Clustering
-- Khaled S. Young
-- Air Force Institute of Technology report AFIT/GE/ENG/96D-22 (December 1996)
(Available from "<http://www.dtic.mil/stinet/str>" in full text as ADA321151)

EVALUATION AND INTEGRATION OF ELECTRODYNAMIC SIMULATION PACKAGES FOR MADMEL PROGRAM

Adam R. Hoffman
Graduate Student
Department of Electrical Engineering

Wright State University
3640 Colonel Glenn Hwy.
Dayton, Ohio 45435-0001

Final Report for:
Graduate Student Research Program
Wright Laboratories

Sponsored by:
Air Force Office of Scientific Research
Bolling Air Force Base, DC

And

Wright Laboratory

August 1997

EVALUATION AND INTEGRATION OF ELECTRODYNAMIC SIMULATION PACKAGES FOR MADMEL PROGRAM

Adam R. Hoffman
Graduate Student
Department of Electrical Engineering
Wright State University

Abstract

In order to study various electromagnetic effects pertaining to the More Electric Aircraft Initiative a package of simulation software was assembled by Honeywell Technology Center under the contract of Wright Laboratory's Aerospace Power Division, Aerospace Propulsion and Power Directorate. The main objective was to establish a relatively easy to use, workstation based simulation package that could be used together or singly to simulate a wide variety of real world problems. This report consists of an evaluation of the software, a brief description of how the software works and can interact with one another and, as an added appendix available in building 450 at Wright Patterson Air Force Base Area B, a simplified user's manual for each program.

EVALUATION AND INTEGRATION OF ELECTRODYNAMIC SIMULATION PACKAGES FOR MADMEL PROGRAM

Adam R. Hoffman

Introduction

The More Electric Aircraft program recently undertaken by the Air Force calls for many of the mechanical systems of military aircraft to be replaced with electrical systems, as well as improving existing electrical systems and even new standards on the aircraft's electrical power supply and distribution. A major concern under this program is that the new and existing systems do not have adverse effects on each other or the basic performance of the aircraft. By studying and simulating the various systems of an aircraft on a computer prior to actual physical testing can save a considerable amount of time and energy, not to mention money, by running tests only on the aspects of the problem that are shown by the computer to be important, as opposed to running a test repeatedly just to determine the areas that are important and call for more testing. It was with these thoughts in mind that a contract was awarded to Honeywell to develop a package that would accomplish the above tasks.

Honeywell's contract consisted of three main points: construct the simulation package, run a sample simulation for both example and validation, and finally, upon delivering said system to Wright Labs, hold a training session on the programs assembled.

In order to assure wide applicability and compatibility, Honeywell chose several 'off the shelf' software programs, as opposed to writing problem specific code. The programs that were decided upon were Analog's Saber and Design Star, EMA's Mharness and EMA3d, and FEG's FAM. Saber and its' graphical design capture program Design Star are widely used circuit simulation programs. Mharness is a program to simulate cable and wire configurations. EMA3d is a three-dimensional Maxwell's equation solver with FAM as its pre and post processor. These programs and various utilities were bundled on a Sun SPARCstation 20 running SUN OS 4 and OpenWindows.

EVALUATION AND INTEGRATION OF ELECTRODYNAMIC SIMULATION PACKAGES FOR MADMEL PROGRAM

Adam R. Hoffman

The sample project undertaken by Honeywell consisted of a multifaceted simulation of an electro-hydrostatic actuator operating in an aircraft environment. This simulation shows how the programs can interact with each other; the results of one simulation can be used as inputs for the other programs.

Having completed the test project and obtaining results that seemed to validate the function of the simulation packages, the computer system with software pre-installed was delivered to Wright Laboratories. It was at this point that Wright Laboratories researchers were able to get some time learning the programs in preparation for the training.

A few weeks after the workstation arrived, Dr. Rodney Peralá, president of EMA Inc., arrived with Fred Malver, a research scientist with Honeywell, to begin the training. Dr. Peralá gave a weeklong class on his company's Mharness, EMA3d and also the FAM graphical interface. This training consisted of a theoretical background, basic use of the software, worked examples, and several on-the-spot realistic simulations from the attendees' areas of interest.

Evaluation

Before I begin a quick evaluation of the software itself I would like to address some of the concerns raised by Lt. Col. Steven Davidson in his memo 'Comments on the Honeywell More Electric Aircraft Program.' He raises several points about the validity of the project. I would first like to make clear that all the possible problems he raises are problems with Honeywell's EHA simulation, not necessarily with the software used. The EHA simulation was to be merely an example of how to run a simulation; it was not to be used for design specifications.

EVALUATION AND INTEGRATION OF ELECTRODYNAMIC SIMULATION
PACKAGES FOR MADMEL PROGRAM

Adam R. Hoffman

The first concern raised was the equation used to convert the interior shield current, given as output from Mharness, to exterior shield voltage, needed as input to EMA3d. The equation used by Honeywell was:

$$V_s = I R_t + L_t \frac{dI}{dt},$$

Where:

V_s is external shield voltage

I is internal shield current

dI/dt is time derivative of current

R_t and L_t are the shield resistance and inductance, respectively.

He claims the correct equation to be used is:

$$dV = Z_t I dx$$

where:

dV is voltage per unit length

Z_t is the impedance of the shield

I is the internal current

dx is the unit length

He then also gives a very complex definition of Z_t , including thickness, radius and a frequency dependent current skin depth. If you take a look at what is actually happening you can see that $Z_t * dx$ really equals R_t although a more accurate R_t than the one that Honeywell used. The two competing equations become $V_s = I * R_t + L_t \frac{dI}{dt}$ and $V_s = I * R_t$. Both of these equations have assumptions implicit in them and I highly doubt that there is any appreciable difference in the end result. One more thing to be said on this topic; the calculation of the voltage is done external to the simulation software, so, if we decided that it would be better to use a different equation we could do that with out making any real changes to the heart of the simulation.

The next issue is the cable model used in the Mharness simulation. The problem is that the value of the resistance for the connectors and terminations of the various cables are not given any correspondence to the actual hardware and in some cases seem quite arbitrary. I will admit that just reading the report that the values chosen are not explained

EVALUATION AND INTEGRATION OF ELECTRODYNAMIC SIMULATION PACKAGES FOR MADMEL PROGRAM

Adam R. Hoffman

in detail but the values in the important section of the problem, the termination to the motor of the excited cable, do match well enough. As for the other values spread throughout out the model, these more than likely are arbitrary in the sense that they do not correspond to actual values for the cable but are instead used to give stable results. If a large resistor is needed use 10 MegaOhm, if a small resistor is needed use 10 milliOhm. While the results obtained from this portion of the simulation are not going to be exact, the data is acceptable for the confines of this example problem.

Number three has several concerns about the power cables connecting the actuator and controller. The first is concerning the number of wires in the power cable itself. There are six wires in the power cables - there are two for each phase of the motor. Honeywell made the simplification that, for Saber analysis, it was just as plausible to have only three. The other wires that are brought into question are not important to the problem at hand and, so, can be ignored. The three control lines (ia, ib, ic) are external to the cable that is under examination. The 'thetarm' is a line running from a tachometer on the actuator to the control logic, again external to the cable. It is also mentioned that there is no cable for return current and that all return current flows through the grounded shield. The concern seems to be that the system ground is not the same as the aircraft ground. This seems to be because there is no way to implement a true aircraft ground in the simulation at the moment and in a real case situation the system ground would always be the same as the aircraft ground. His final conclusion is that the results for the current are erroneous because the current flowing through aircraft structure is not taken into account. Perhaps I am wrong but I highly doubt the amount of current that would flow through the aircraft structure would be anywhere near the amount flowing through the grounded shield.

At the end of the report Colonel Davidson makes several conclusions and recommendations. The majority of the conclusions are that EMC simulation is important to the MEA program and that Honeywell's package is a step in the right direction and also includes a comment on the problems discussed above. The recommendations really

EVALUATION AND INTEGRATION OF ELECTRODYNAMIC SIMULATION PACKAGES FOR MADMEL PROGRAM

Adam R. Hoffman

are two: Do not use Honeywell MEA and Pursue better analysis tools. I agree fully with the latter. A research lab should always be on the look out for better tools and simulation software is no different. As computers become more powerful and the algorithms used are refined, the equipment available can only improve. The recommendation to not use Honeywell MEA is a little more complicated. If by 'do not use Honeywell MEA program' the Colonel means do not use the data obtained for design purposes or other consequential uses then I would agree. The results, although seemingly plausible, are questionable enough that I would not recommend them to be used without further study. But again I would like to emphasize that Honeywell's EHA study was a test of the software; an example of possible uses for the programs they supplied. If, on the other hand, the Colonel means that the work Honeywell did in its' entirety, software and all, should be thrown out then I can not agree with him. The programs are merely tools and it is up to the user to apply them efficiently and accurately. I see no reason on the basis of the Honeywell report or the memorandum to suggest that the software is invalid. My recommendation would be, if the EHA simulation is deemed important, have the evaluation redone without the approximations that the original report used.

Description and Evaluation of Software

As said before, Honeywell put together a package consisting of three programs: a circuit simulator, a cable simulator and a field solver. In this section I will give a brief description of each program's function and use.

Saber is a very simple to use program to simulate lumped element circuit models. Systems for study are input as a circuit diagram via the Design Star schematic capture program. Design Star is a window based program with a wide range of pre-programmed digital and analog components for use in a click and drag design process. Saber also has the ability to define completely new user components. Design Star then generates a net-list for use by Saber, which it automatically invokes. The Saber portion of the system simulates and solves the design and allows the user to obtain graphical or tabular results. Both Saber and Design Star have drop down menus and easy to use interfaces. Anyone

EVALUATION AND INTEGRATION OF ELECTRODYNAMIC SIMULATION PACKAGES FOR MADMEL PROGRAM

Adam R. Hoffman

familiar with SPICE type simulators should have no problem using this program. Saber is a widely used program and has been shown to be very accurate.

Mharness is used to simulate a series of wires or cables; this can include a complex geometry of many sets of wires grouped with individual shields and insulators in an overall shield. Connectors, splits, terminations and various other cable properties can be defined. The program uses a finite differencing of the basic transmission line equations to solve for induced currents as well as cable inductance and various other parameters of interest. This program has no graphical user interface; the inputs are a text file for the geometry and physical properties of the cable harness and a tabular excitation file. The outputs include a diagnostic file which will include inductance calculations, etc, and text files for the probe points of interest for use with an external graphing program. This program seems fairly powerful and gives what appear to be consistent results. Owing to the text file input it is somewhat difficult to use and can be hard to see where you had made mistakes. Overall it will take an investment of time to get reliable data out of this program.

The final program is EMA3d and its' graphical user interface FAM. EMA3d allows for basically any geometry and material property for its problems. It uses a finite difference of Maxwell's equations to solve for the electric and magnetic fields in the entirety of the problem space.

First a quick discussion on how this is implemented: The space is gridded into cubic sections with each vertex given an electric field and the midpoints of each line given a magnetic field value. At each iteration the fields surrounding the point of interest are used to calculate the next time steps' field value. All points in the problem space are given values and calculated in the same manner except for the edge cells. In order to satisfy whatever boundary conditions the problem specifies it is necessary to treat the cells close to the edge in an appropriate manner. If edge conditions are ignored, the very last cells look outside of the problem space for it's calculation, which are effectively zero.

EVALUATION AND INTEGRATION OF ELECTRODYNAMIC SIMULATION PACKAGES FOR MADMEL PROGRAM

Adam R. Hoffman

This causes the boundary to act as a perfect conductor and reflect all fields back into the problem space. This can actually be used as a boundary condition if so desired. In order to simulate unbounded space it is necessary to use specially developed algorithms that allow the edges to pass travelling waves out. One caveat though: none of the algorithms used are perfect, i.e., there is always some reflection, albeit very small it may be important depending on the problem. The other thing to keep in mind is that the fields are the driving force in the calculations; any other output, voltage, surface current, etc., must be extrapolated from the fields.

In order to specify to EMA3d the geometry, material properties and excitation of the problem one uses the FAM pre-processor. Although being a graphical user interface, FAM is a command line driven program; there are few mouse commands but there are pull down menus and hot buttons. In order to make a body, such as a solid rectangle, one must go through the process of specifying coordinates for each point, using the points to define lines, use the lines to define surfaces and finally, using the surfaces to define a body. If it is a complex geometry or there are many bodies this can be quite time consuming. FAM does allow for the use of macros; small external files that have lists of commands for FAM that will automatically do often used processes. FAM comes with several macros for common functions or you can define your own, either type can be put in a pull down menu toolbox for easy use. For example instead of making the rectangle by the method above you could use one of the macros included with FAM, simply by inputting the desired lengths. After defining the geometry of the problem you then need to give properties to the lines, surfaces, or bodies. This is most easily done with the built in macros. If a piece of geometry does not have material properties EMA3d does not know it exists. The next step is to set the grid size and time step. This is set in order to resolve the smallest wavelength or geometrical feature of the problem. The time step and grid size are tied together by a numerical stability condition described in the manual that can not be violated. Having set the grid you must now 'mesh' the problem. This step is where the space is gridded to cubes needed for the simulation, with each vertex being called a node. These nodes are needed to specify where an excitation is to be applied or

EVALUATION AND INTEGRATION OF ELECTRODYNAMIC SIMULATION PACKAGES FOR MADMEL PROGRAM

Adam R. Hoffman

where to probe for various parameters. Both excitation and probes are easiest done with macros. When geometry, material properties, mesh, excitation and probes are completed the model is saved and, from the UNIX prompt, run through a filter and then into EMA3d. EMA3d will give a brief description of the problem it is about to run, including any errors or possible errors, and ask you if you wish to continue. EMA3d does the actual calculations and saves the values at the probe points at the specific time steps desired. When complete you can either use a utility program to turn desired output at single nodes into tables or use a filter to bring the results back into FAM. FAM as a post-processor is quite powerful. It allows time plots of an individual node to be made, or, all values at a specific time can be shown in a color, three-dimensional plot.

After having used EMA3d and FAM for a considerable length of time I can say it takes a considerable amount of time to become familiar with EMA3d and FAM. This is not the sort of program which anyone with windows experience can come in and learn in an hour. There are also several problems that I have run into that need to be put forward. The first and most threatening concerns the current on a curved surface. After several simulations using a curved metallic surface that is excited in various ways, I noticed that the surface current, the desired output, was not acting the way that physical reality suggested. Overall the values were several orders of magnitudes lower than they should have been and the maximas and minimas were in the completely wrong places. I got in contact with EMA and after jointly trying several fixes, it was finally admitted that this was a problem with the software, not the numerical method, or the geometry. This problem is currently being fixed and EMA says by the next release it will be fixed. The other problems are mostly related to the complexity and difficulty of the program itself. In order to get the resolution one desires for the geometry one has to choose such a tiny time step that the program will take several days to run. I once filled up the remaining one gigabyte of the hard drive when running a simulation. There are many other examples of problems that can arise when setting up a problem but most can be taken care of with a knowledge of the software.

EVALUATION AND INTEGRATION OF ELECTRODYNAMIC SIMULATION PACKAGES FOR MADMEL PROGRAM

Adam R. Hoffman

Conclusions

The conclusions included here are only regarding the Honeywell software bundle and not the EHA simulation. Simulation of electrodynamic effects with the use of a computer is important to the development of a modern lab and, I believe, will eventually become an integral part of the research process. The package put together by Honeywell is a step closer to the wide ranging, easy to use, efficient package needed for a research lab. The programs put together by Honeywell are able to be used for a wide variety of problems, unfortunately their complexity makes that almost unreachable to anyone who can not give the serious amount of time it takes to become proficient. Saber and Mharness both seem to give reliable results, consistent with common sense and physical reality. EMA3d, on the other hand, does not always give results that mesh with reality. Aside from the curved surface problem stated above, most errors can be overcome by slight changes in the way the problem is laid out. I think the main thing this shows is that one still needs to be smarter than the tools he is using in order to get anything worthwhile from them. My final recommendation would be to open the programs up to other researchers, put them on the network, so that, they can be evaluated by people with real world problems. I would also recommend always being on the look out for new packages that come closer to the ease and accuracy desired by a research lab.

Exploding Foil Initiator Flyer Velocity Measurement Using VISAR

George W. Jarriel Jr.

Research Assistant

Department of Electrical Engineering

Auburn University

200 Broun Hall

Auburn, AL 36849-5201

Final Report for:

Summer Faculty Research Program

Wright Laboratory

Sponsored by:

Wright Laboratory, Eglin AFB, FL

August 97

George W. Jarriel Jr.
Research Assistant
Department of Electrical Engineering
Auburn University

Abstract

Exploding Foil Initiators (EFI) flyer plate velocities were the focus of this research. Using laser velocity interferometer system for any reflecting surface (VISAR), a procedure for measuring EFI flyer plate velocities was developed to complement existing procedures for measuring electrical characteristics. The VISAR velocity data combined with electrical characteristics will be incorporated into an existing numerical model predicting the electrical behavior of the EFI. This unified model will then be able to predict EFI mechanical performance as a function of the electrical parameters. This model can then be used to predict the behavior of more complicated systems such as air bag initiation devices utilizing a particular EFI device..

Exploding Foil Initiator Flyer Velocity Measurement Using VISAR

George W. Jarriel Jr.

1. Introduction

Exploding foil initiators (EFI) have long been used to detonate explosives in various applications. The basic principle (see Figure 1) involves a large current driven through a metal bridge foil. The foil is quickly vaporized due to ohmic heating and expands quickly. The expanding plasma will shear off a small section of the material coating the bridge, such as kapton. This material, or some material deposited on it, becomes a flyer plate which will then strike an explosive pellet at speeds in the kilometer per seconds range. The resulting shockwave will then initiate the explosive pellet.

Assuming a EFI fabrication process controlled well enough that the flyer plate mass and dimensions can be determined, a simple empirical model can be created in PSpice. This model requires the accurate measurement of the electrical parameters and mechanical parameters of the EFI in actual use. Previous research presented a procedure for treating the electrical parameters of an EFI in a spice model. This research focuses primarily on the mechanical parameters, specifically, the velocity and displacement with respect to time of the EFI flyer plate in order to integrate flyer plate velocity into existing models.

In order to make these measurements, a velocity interferometer for any reflecting surface (VISAR) was used. The VISAR is an instrument which measures velocity of a target by determining the Doppler shift of a beam of coherent light directed at the target. While the technology for such measurements has been available for some time and accepted by the physics community, it is not widespread, and expensive.

2. Experimental Apparatus and Procedure

There are three main components in the VISAR system used for these experiments: a continuous wave laser, a target/probe assembly, and a Valyn VISAR. Show in Figure 2 is a rough block diagram of

the VISAR apparatus. The following section describes the function of each major section with brief descriptions of problems encountered during actual operation.

The heart of the VISAR system is a 514 nm [green] continuous wave argon ion laser in the 5 watt range.

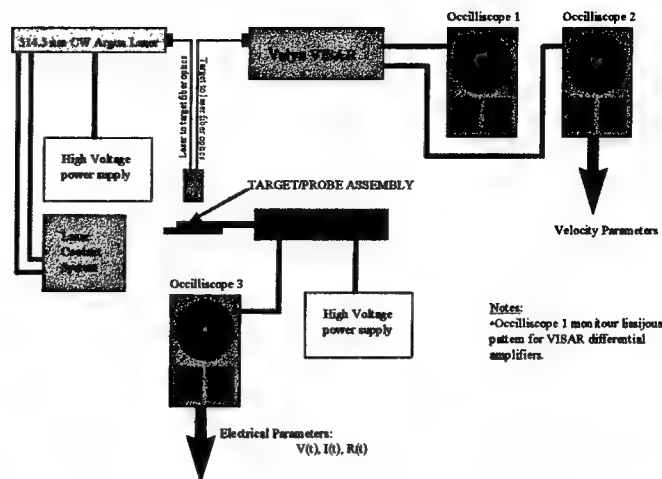


Figure 1 VISAR Experimental Apparatus Arrangement

This laser provides the coherent light to illuminate the target. In practical use, the laser can produce an adequate return signal using less than 350 mW of incident laser power. Some, less reflective targets (i.e. tarnished copper, nickel) may require a greater incident power. In these experiments, the incident laser intensity was never greater than 500 mW. At these intensities, no discernible damage to the target was observed. Future experiments with greater incident laser intensities must be preceded by a determination of the possible effects of higher intensities on the thin (~1000 nm thick) targets.

It is important to note at this stage that the Lexel laser used in these experiments must be tuned regularly to insure a strong 514.4 nm mainline. The laser tuning is very sensitive and will move out of tune with time if not on an absolutely stable surface. Even on a stable surface, a slight bump on the laser casing or tuning knobs can result in a great reduction of laser output. This can even result in a failure to lase the gas. Laser tuning should include adjustments at the adjustment ports in the front as well as the tuning knobs in the rear for maximum power output from the laser.

The laser coupled into a fiber optic cable by a coupler which must be carefully placed in the beam path. Placing the focusing fixture (a 20x microscope objective) 53 mm from the laser output lens ring produced maximum observable coupling between the laser and the cable, resulting in maximum power

transfer. The fiber optic coupler must also be adjusted regularly to insure it is aligned properly with the rest of the laser beam.

The laser light is guided with 50/125 fiber optic cable (the orange one) to the target/probe assembly. The fiber is mounted in a probe which also contains the signal or return fiber which leads to the VISAR (see Figure 2) and an integrated

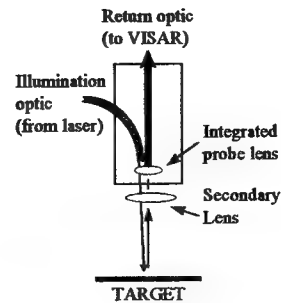


Figure 3 Laser probe assembly.

focusing lens with a focal length of 12 mm. In order to focus the beam on an even tighter region of the flyer plate, this probe is modified by mounting a small lens in the beam path. This has three results: 1) the probe is closer to the target and therefore easier to focus and align, 2) the return light gathered by the probe is increased, and 3) the amount of incoherent light due to the foil plasma driving the event collected at the probe is reduced due the eclipsing effect of the flyer.

Several different lens/probe combinations have been attempted, with 4.5X4.5 and 4.5X9.0 lens yielding the best results. It is important to note at this point that the flyer plate from the slappers cause significant damage to the focusing lens on the probe. Therefore, the lens (which are very cheap) provide some protection for the probe (which are less cheap), but must be replaced routinely (every fifth or sixth "shot") in order to minimize signal degradation.

The probe is mounted directly on a fixture for modifying the probes pitch and yaw. Because there are two fiber optics in the probe, the probes do not generally provide maximum return to the VISAR when mounted normal to the target. Slight adjustments in pitch and yaw are required

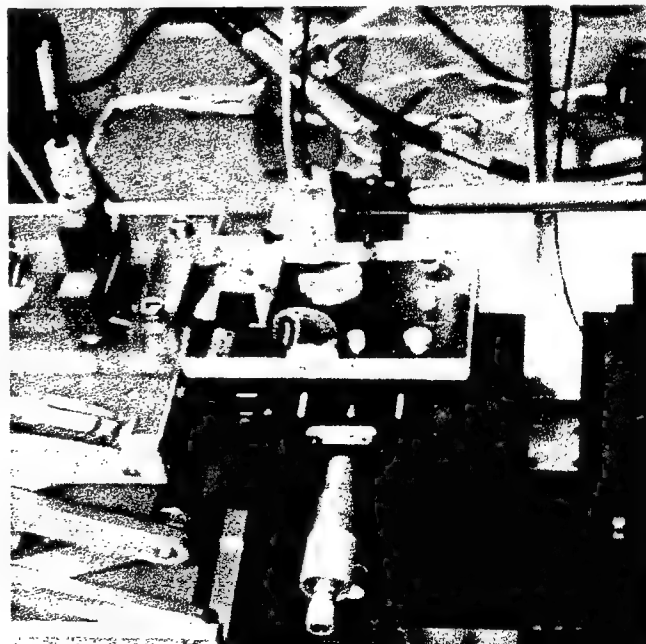


Figure 2 Target/Probe assembly

in order to maximize signal return. This is especially important for targets which tend to disperse or absorb the incident signal.

The probe assembly with yaw/pitch adjustment is then mounted onto an XYZ BLOCK which can be used to quickly adjust the probe over the center of the target.

The target itself is mounted securely using kapton tape to a piece of 1/2" Plexiglas in order to isolate it electrically from the rest of the assembly.

The final piece of equipment in the target/probe assembly is a "swamp" lamp. Due to the rough surface, and therefore dispersive quality of many of the targets, it is generally necessary to focus a bright lamp on the target area in order to "swamp out" much of the reflected laser light. This will allow the experimenter to easily see the exact point on the target where the laser beam is focused. Even though the VISAR is equipped with a narrow band filter to attenuate light other than the 514 nm mainline, it is still prudent to turn the swamp lamp should be turned off prior to a shot in order to reduce ambient light traveling to the VISAR.



Figure 4 - Chipping and fracturing of secondary lens due to flyer plate impact.

The Valyn VISAR receives the return signal via a low loss fiber optic cable. Using essentially the same technique as described by Barker [3], the VISAR produces a series of fringes whenever the target is displaced normal to the probe. These fringes are derived from the Doppler shift in the reflected light, and can be analyzed to generate accurate velocity and displacement curves for the target.

Generally, only a few fringes are generated during a single shot, with each fringe representing a specific change in the velocity of the target. The velocity a single fringe represents is dependent on the thickness of the delay etalon in the VISAR. For flyer plate measurements with peak velocities measured in kps, an etalon yielding roughly 1.2 km/fringe was found to produce the smoothest results. Other,

thicker etalon combinations tried thus far in an attempt to increase the number of fringes received during the event have failed due to fringe skipping.

More information on the function of the VISAR, including a brief discussion on how to choose which etalon to use, consult the Valyn VISAR handbook. A list of helpful idiosyncrasies of the Valyn VISAR at Eglin AFB is included here however:

- the quarter wave plate which is vital to the operation of the VISAR must be carefully set to insure it lies normal to the path of the light path.
- the left hand signal of the VISAR can be observed to be weaker, and must be compensated for using the PMU polarizers.
- whenever possible, maximize lissajous amplitude by increasing the laser intensity and not the PMU voltage.
- lissajous patterns should not exceed 250 mV peak value (500 mV peak to peak) in order to protect the differential amplifiers. (This will operate the amplifiers at approximately 75-80% peak and result in quite data output results well above the noise threshold.)

3. Data Analysis

Once a successful shot is fired, the data from the VISAR can be used to directly determine the velocity of the flyer plate with time which also tells the observer the displacement of the flyer. Fringe analysis is accomplished by a program provided by Valyn. It returns velocity and displacement data with respect to time derived by the formula:

$$v(t) = F(t) * VPF$$

where $F(t)$ is the fringe count and VPF is the velocity per fringe constant:

$$VPF = \lambda / [2 \tau (1 + \Delta v/v_o)(1 + \delta)]$$

where:

λ = incident light wavelength (514.4 nm mainline in this case)

$1 + \delta$ = etalon refractive correction factor

$(1 + \Delta v/v_0)$ = refractive index of window correction factor (normally unity)

When this data has been analyzed, the following information is known:

Flyer velocity vs. time

Flyer displacement vs. time

Current through EFI vs. time

Voltage across EFI vs. time

which can then be used to calculate the following information:

Flyer energy and momentum vs. displacement

EFI efficiency

and by inference the electrical energy required for target explosive initiation.

The experiments in this work focused primarily on generating an efficient procedure for measuring the first four parameters. Sample curves of typical shots are shown in Appendix A. Other calculations (momentum, efficiency, ect.) will be left for future research. The results shown here are for a typical EFI device, where all information has been normalized.

3. Conclusions

A complete empirically derived model of EFI behavior can be derived using the electrical and interferometer data presented here. This model can then be used to directly calculate the force necessary to initiate the explosive as well as for the prediction electromechanical EFI behavior in more complex circuits than simple test sets without actually having to build them. This model is still dependent however on empirical data gathered from VISAR experimentation and therefore new data must be collected for each new EFI design. Future work must include efforts to make these models "scaleable" in the manner of Furnberg, et al [2] in order to maximize their usefulness.

Acknowledgments

Special thanks to Dr. Keith Thomas, Lt. Jeff McGuirk, Lt. Dan and Steve Smith and all the personnel at the Fuzes Branch, WL-MN/MF for their hospitality and for the use of their facilities.

Bibliography

1. Keith A. Thomas, Michael E. Baginski and Edward Shaeffer, *A Characterization of the Electrodynamics of Metals under the Action of Large Electric Currents*. *International Journal on Electromagnetics*, in preparation.
2. C. M. Furnberg, G. R. Peevy and S. G. Barnhart, *Slapper Detonator Modeling Using the Pspice Electrical Circuit Simulator*. Sandia National Laboratories Report, 1993.
3. L. M. Barker and R. E. Hollenbach, *Laser Interferometer for Measuring High Velocities of Any Reflecting Surface*, 1972.
4. Roger F. Harrington, *Electromagnetic Fields*. New York: McGraw-Hill, Inc, 1961.

Appendix A

The following plots show normalized data of a successful EFI shot.

Figure A.1 - Voltage, current vs. Time for EFI

Figure A.2 - Displacement, velocity vs. Time for EFI

Figure A.3 - Displacement vs. Velocity for EFI

Figure A.4 - Instantaneous power absorbed vs. Time

Figure A.5 - Total energy absorbed vs. Time

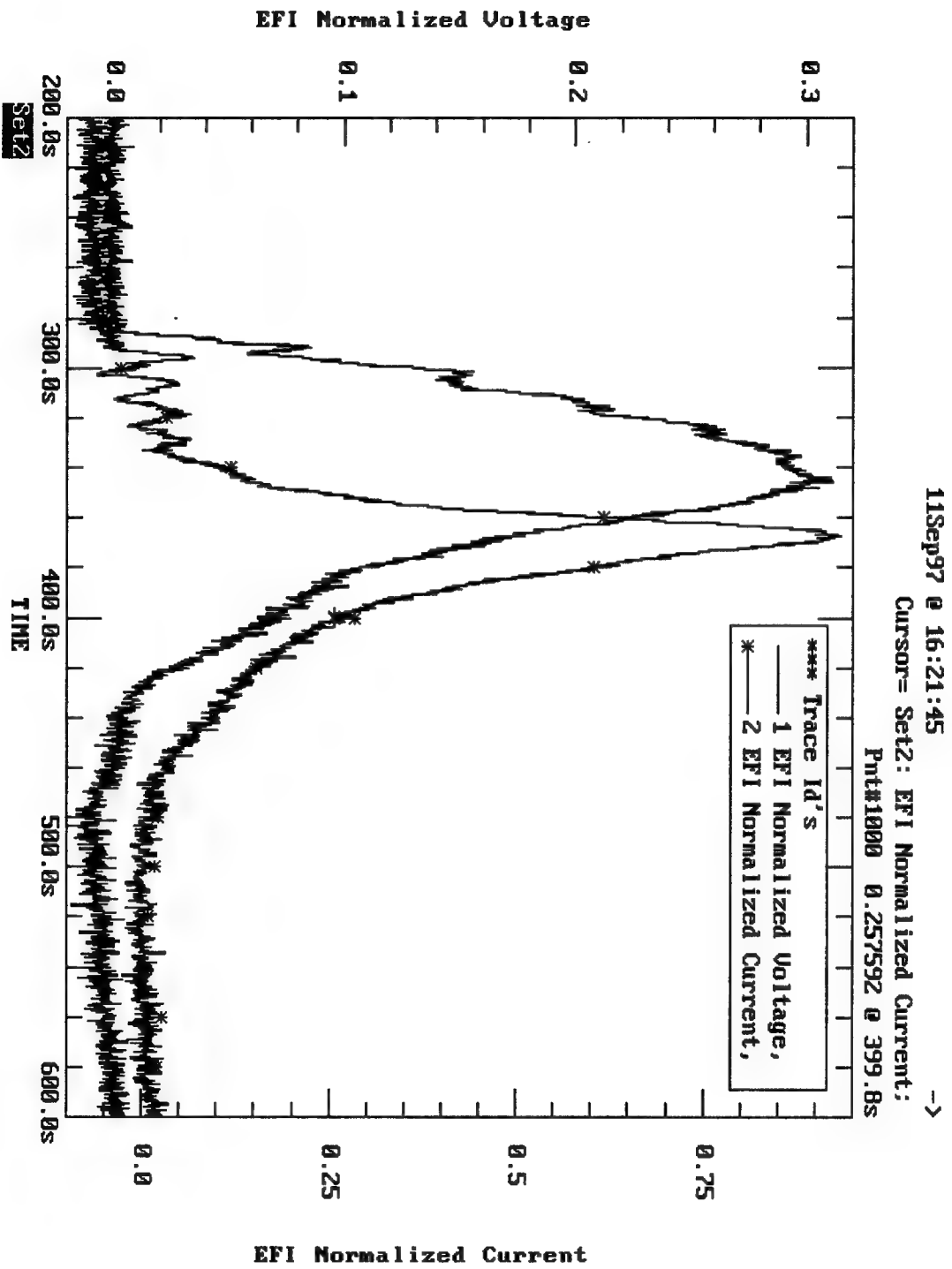


Figure A.1 Voltage, current vs. Time for EFI

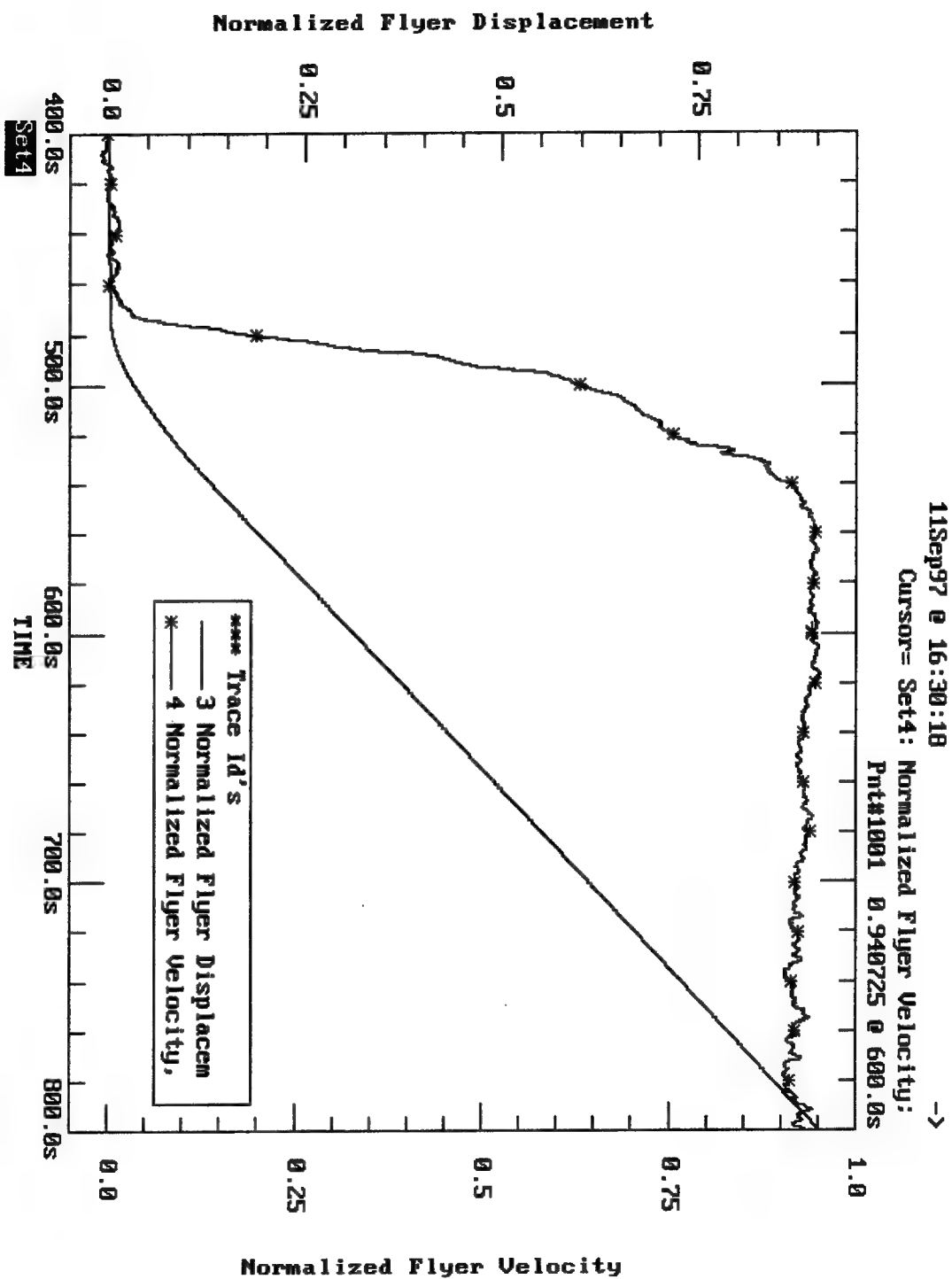


Figure A.2 Displacement, velocity vs. Time for EFI

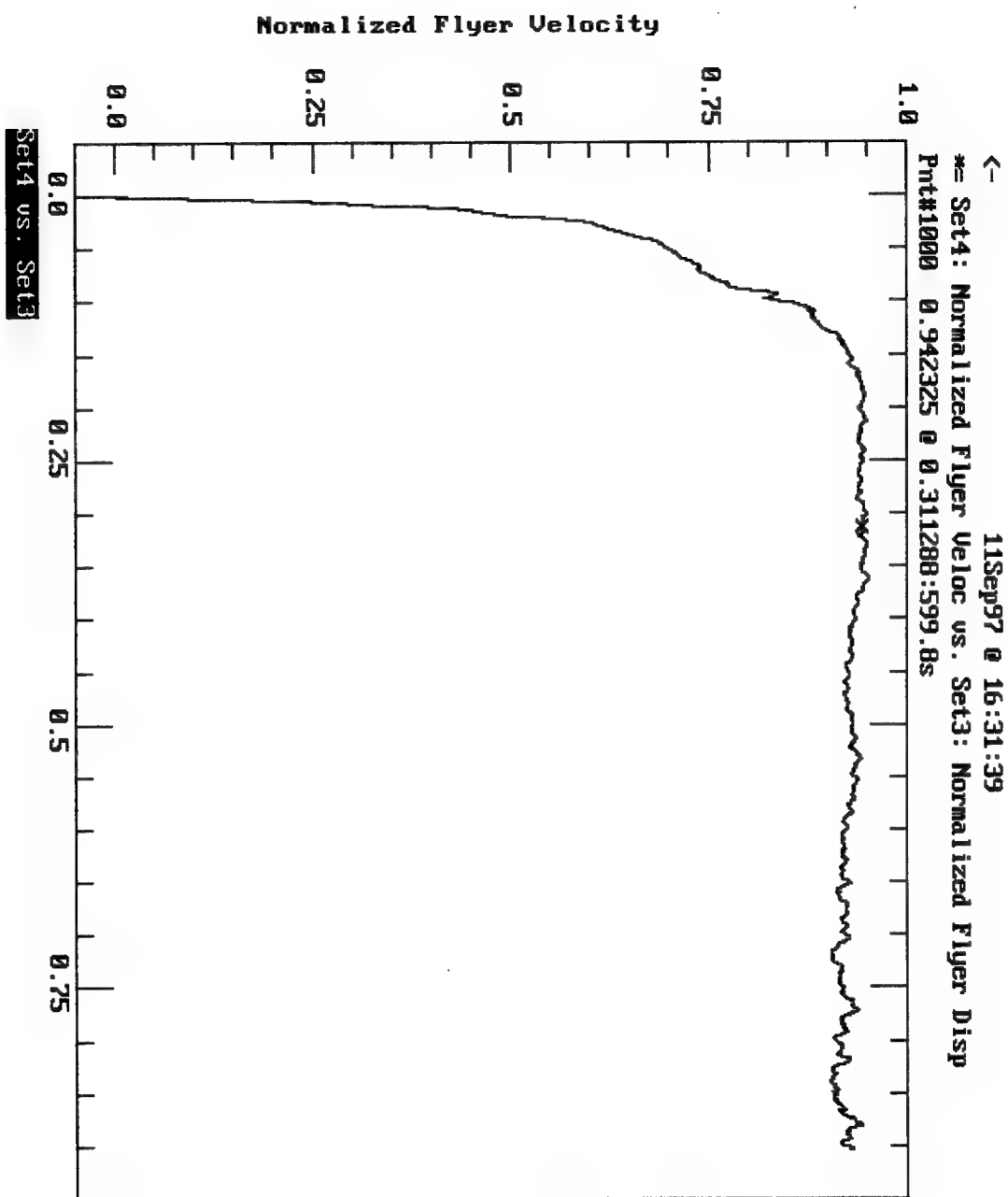


Figure A.3 Velocity vs. Displacement for EFI

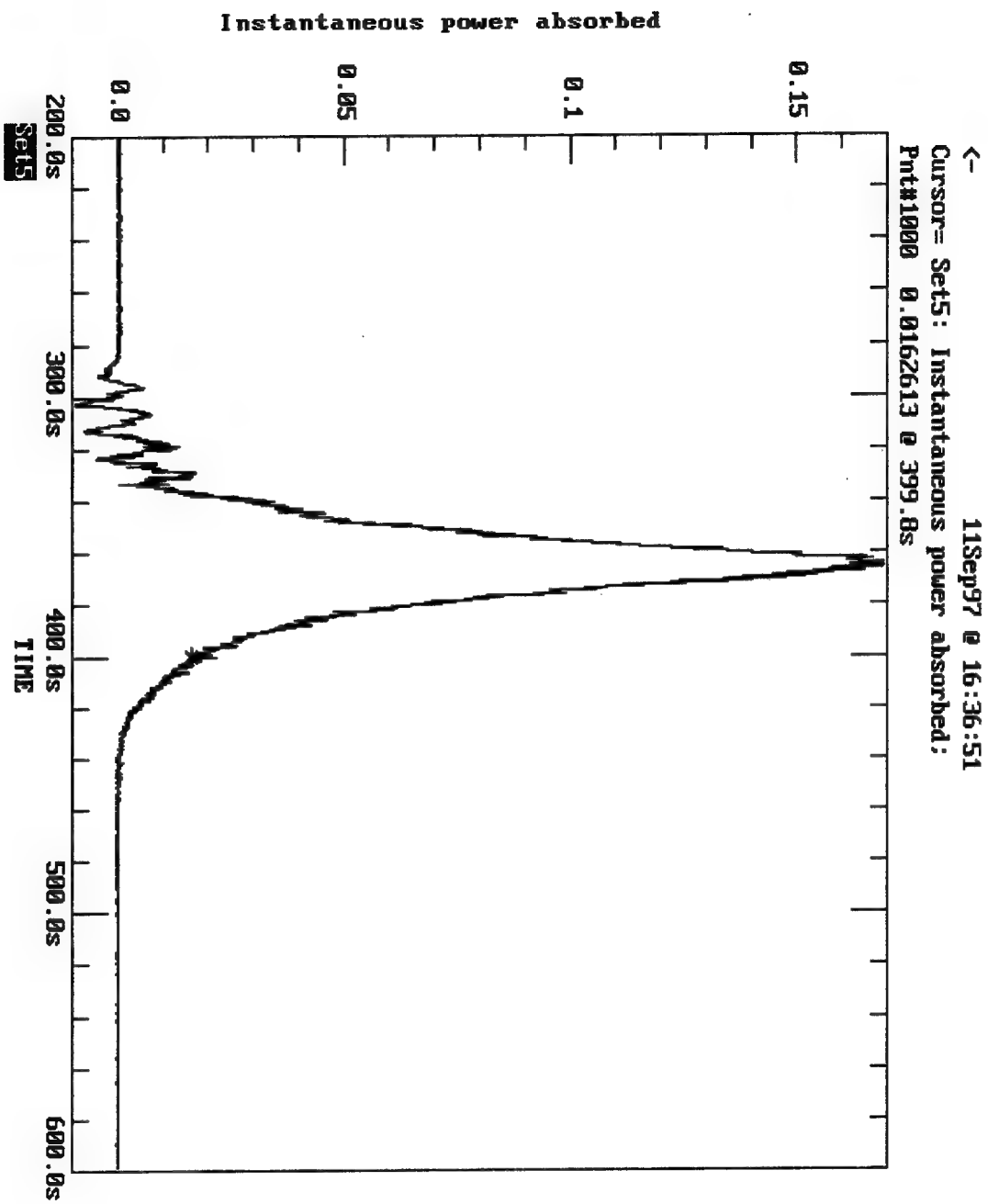


Figure A.4 Instantaneous power absorbed vs. Time

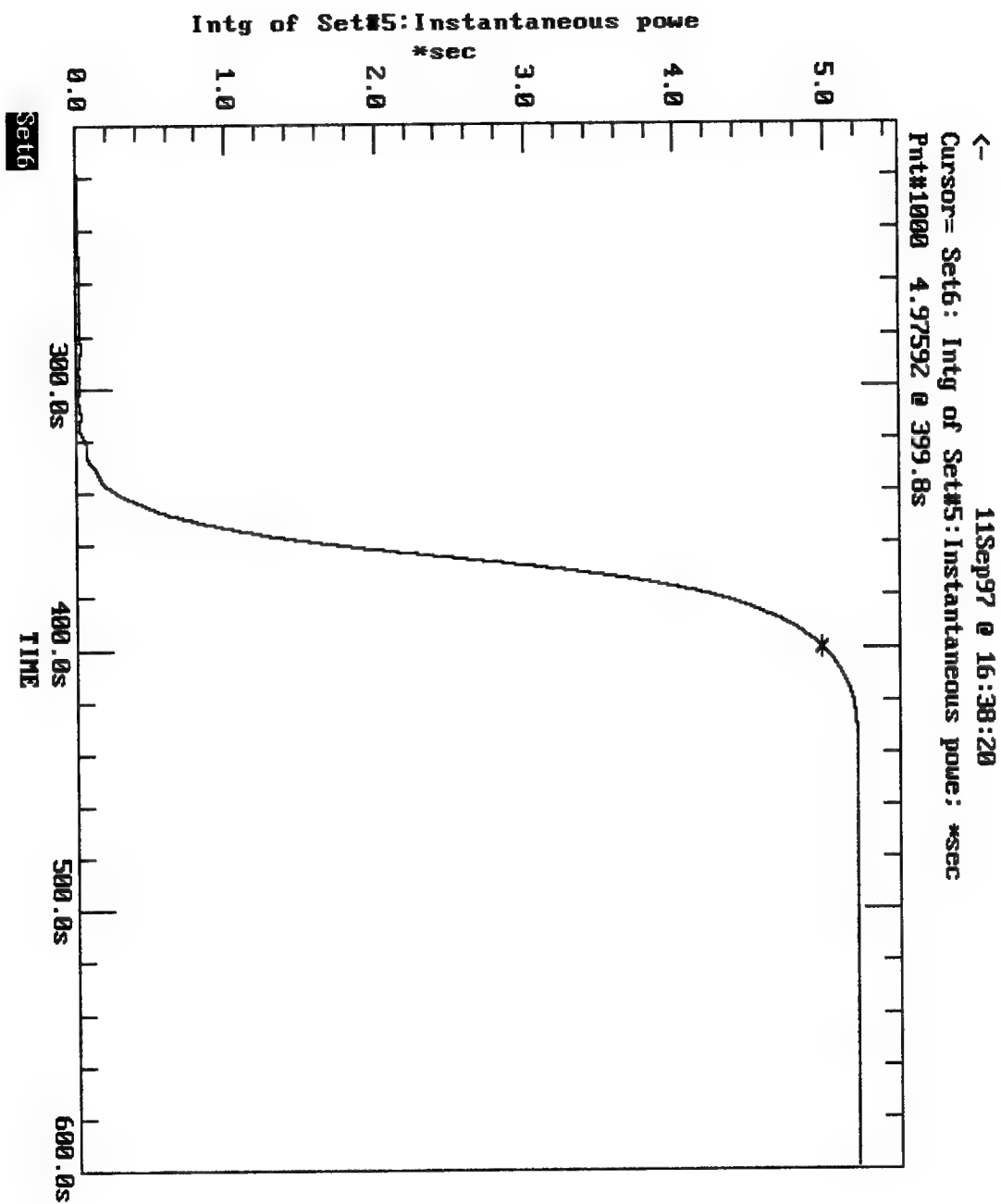


Figure A.5 Total energy absorbed vs. Time

CAPACITOR BASED DC BACKUP POWER SUPPLY WITH INTEGRATED CHARGING CIRCUIT

Brett A. Jordan
MSEE Student
Department of Electrical Engineering

Wright State University
3640 Colonel Glenn Hwy.
Dayton, Ohio 45435-001

Final Report for:
Graduate Student Research Program
Wright Laboratory

Sponsored by:
Air Force Office of Scientific Research
Bolling Air Force Base, DC

and

Wright Laboratory

August 1997

CAPACITOR BASED DC BACKUP POWER SUPPLY WITH INTEGRATED CHARGING CIRCUIT

Brett A. Jordan

MSEE Student

Department of Electrical Engineering

Wright State University

Abstract

A capacitor based DC backup power supply with an integrated charging circuit was studied. The design utilized the relatively new 10-F 2.5V capacitors as the energy storage units. The constant output voltage was maintained by a Pulse Width Modulated (PWM) boost converter with both feedforward and negative feedback control.

CAPACITOR BASED DC BACKUP POWER SUPPLY WITH INTEGRATED CHARGING CIRCUIT

Brett A. Jordan

I. Introduction

The double-layer capacitor is a recent innovation that combines high surface area electrode materials with the high capacitance per unit area of the chemical double layer. Commercially available devices with a capacitance of 1500 F are now available [1]. This improvement in rated capacitance has presented opportunities for the use of double layer capacitors in high power and/or high energy storage applications [2]. The main goal of this research effort was to construct and test an independent power supply capable of providing critical energy during a primary power supply failure. The capacitors mentioned above provided the energy storage required for such a system, and also had the advantages of superb durability and low internal resistance.

Four distinct sections of the backup power supply were identified for proper operation: Energy storage units, charging circuit, boost circuit, and the controller circuit. The controller circuit was further divided into two areas: Feedforward control and negative feedback control.

II. Methodology

The voltage chosen for our energy storage system was 25 volts. This system was intended to be placed in an aircraft whose bus voltage was a nominal 28 volts. Current-technology backup systems operate at 25 volts, and this capacitor based system is intended to be retrofitted into airframes with the older design.

A charging circuit was integrated into the completed design. Some basic operating modes were established to satisfy certain requirements. In the standby mode, it was assumed that the primary power supply was operating normally, and that the backup power supply was not needed. At that time, it was most important for the charging circuit to maintain the capacitor bank at its full voltage. In the event that the primary power supply failed, the boost circuit went into backup mode. In this mode, it was very

important that the charging circuit be disabled so that energy would not be wasted recharging the capacitors. After primary power was restored, the charger circuit would enter the charging mode and begin the process of recharging the capacitor bank. This process was repeated in order to demonstrate the ability of the backup power supply to handle an intermittent main power failure.

A Pulse Width Modulated (PWM) boost circuit was used to provide a constant output voltage at the load. This boost converter was governed by Equation (1):

$$\frac{V_o}{V_i} = \frac{\eta}{(1-D)} \quad (1)$$

where η is efficiency, and D is the duty cycle. Constant output voltage was required as part of the design criteria. Intended loads for this system were unable to run effectively on less than 24 volts. Capacitor bank voltage was used as the input voltage to the boost converter. The boost converter increased this voltage throughout the capacitor discharge cycle for a constant output of 25 volts. The amount of boost required to do this was determined by utilizing both feedforward and negative feedback control. The use of a PWM boost converter with proper controls assured constant voltage to the load instead of the continuously decreasing voltage inherent in capacitors being used as power supplies.

The boost converter in this project used feedforward control for determining the magnitude of the duty cycle (see Fig. 1). The level of the capacitor voltage (V_i) was used for the reference voltage to determine the duty cycle. Simply put, as the capacitor was discharged, the duty cycle was increased proportionally.

It was determined that feedforward control alone was not suitable for high power applications. Since current demand became greater for heavy loads, the voltage drop caused by the various parasitic losses became larger. A feedforward design could not predict this voltage drop from the parasitic elements and thus the duty cycle was less than what was required. For this reason, limited negative feedback was introduced into the system to help compensate for these losses.

III. CONSTRUCTION AND OPERATION

The capacitor type chosen was an Elna Dynacap (2.5 V 10 Farad). By arranging 10 of these units in series, the voltage rating of the system was increased from 2.5 volts (the rating on each capacitor) to 25

volts. The total capacitance of this series string was then 1 Farad. But, by placing 10 of these capacitor groups in parallel the capacitance was restored to the 10 Farads of the single 2.5 volt capacitor. These capacitors were able to provide a total energy storage found from Equation (2):

$$E_c = \frac{1}{2} CV^2 \quad (2)$$

The energy storage of this system was found to be 3125 Joules. The rated ESR of each of these capacitors was less than 100 mΩ [3].

A simplified block diagram of the entire system including the charging circuit, capacitor bank and boost circuit is shown in Fig. 2.

It was assumed that the first operation of the backup power supply would be to charge the capacitor bank. However, the current entering a fully discharged capacitor bank was limited only by the on-resistance of the IRF 530 MOSFET (or any type of voltage regulator chosen), which was on the order of 100mΩ. The input current can be found from Equation (3):

$$I_I = \frac{V_I}{R_{DS}} \quad (3)$$

Total input current for this configuration would have been 280 amps. Therefore, a series resistor was required to reduce the current to a value which would not damage the MOSFETs. An 18Ω resistor was chosen, with the resulting input current reduced to 1.55 amps as found from Equation (4):

$$I_I = \frac{V_I}{R_{DS} + 18\Omega} \quad (4)$$

Since the feedforward control reference voltage was a multiple of capacitor voltage, the duty cycle for a fully discharged capacitor bank was 100%. Under these conditions, the MOSFET located in the boost circuit would have been on continuously, which would cause all of charge current to be shunted to ground. The solution was to temporarily disable the feedforward and negative feedback control, thus leaving the switch in the boost circuit in the always-off position. This stage of the charging cycle is shown in Fig. 3.

In order to shorten the charging time, the second stage of the charging cycle would begin. At approximately $V_c=21$ volts, the charging circuit would short out the 18Ω resistor and the capacitor would

then charge through the on resistances of the two IRF 530 MOSFETs. The feedforward control was enabled at this point, owing to the fact that the duty cycle would be approximately 20% and the charger could provide enough energy to enable the boost circuit to begin switching and to finish charging the capacitor bank. This stage of the charging cycle continued until the capacitor bank reached the full voltage of 24 volts. This stage of the charging cycle is shown in Fig. 4. The final stage of the charging cycle was the voltage regulation stage. At this stage, the LM 1458 dual operational amplifier behaved as a voltage regulator and maintained the voltage of the capacitor bank at 24 volts.

The charger circuit was assembled using two IRF 530 n-channel MOSFETs, two zener diodes (21 volt and 24 volt), an LM 1458 dual operational amplifier chip, two resistors ($5K\Omega$ and $7K\Omega$), and an 18Ω 60W resistor. This circuit is shown in Fig. 5.

A diagram of the controller circuit can be seen in Fig. 6a. The controller circuit had the function of controlling the pulse length and frequency applied to the boost circuit's IRF 530 MOSFET. The sawtooth waveform required for the PWM boost circuit was generated by a Harris ICL 8036 waveform generator chip. The chip was configured to provide a 100 MHz sawtooth with a minimum voltage of 7 volts and a peak of 14 volts. Because the duty cycle was directly proportional to capacitor voltage, the duty cycle for a fully charged capacitor bank would be nearly 0%. However, when the capacitor was at half voltage, the reference voltage was at 7 volts corresponding to a 100% duty cycle for the sawtooth with the 7 volt offset. This sawtooth waveform was altered to have a minimum voltage of 0 volts and a maximum of 7 volts, which eliminated the nonlinearity.

The reference voltage was provided by the capacitor voltage. A voltage divider was used to allow the full capacitor voltage of 24 volts to correspond to approximately 7 volts as applied to the LM 311 comparator. Since this 7 volts corresponded with the sawtooth's peak of 7 volts, the duty cycle for the boost circuit with a fully charged capacitor was approximately 0%. This configuration, along with the diode isolation prevented the boost circuit from providing energy to the system while the primary power supply was operating.

While in the standby mode, the controller circuit was providing a duty cycle of nearly 0% to the MOSFET in the boost circuit. This was due to the fact that the main power supply was providing the

required energy, and the boost converter was required to idle. Upon failure of the main power supply however, the controller circuit would begin to alter the duty cycle to correspond to the requirements of the capacitor bank voltage and the output voltage.

Later, after increasingly heavy loads were used, it became apparent that parasitic voltage drops were becoming a problem. The duty cycle needed to be increased a small amount to correct for these problems, but with the feedforward control no such correction was readily available. The solution was to place a transistor across one of the resistors in the feedforward control's voltage divider (see Fig. 6b and 6c.) When the load voltage would begin to drop, the transistor would begin to conduct, and this would drop the reference voltage being compared to the sawtooth. This had the effect of increasing the duty cycle and thereby correcting the voltage drop.

After the charging cycle was completed, the circuit was considered to be in the standby mode. In the event of a main power supply failure, the output voltage would drop from the nominal value of 28 volts DC to the 25 volt DC value of the boost converter (see Fig. 7). At the time of primary power system failure, the controller circuit would disable the charging circuit to prevent energy from circulating from the output of the boost converter through the charger and back into the capacitor bank. Without this feature, there would have been serious efficiency problems in the completed backup power supply circuit.

The backup power supply would continue operating in this mode until the main power supply began providing power again or the capacitors ran out of energy. In the event the main power supply became active again, the boost circuit's diode isolation would prevent current from flowing into the converter circuit from the load. Also, the charging circuit would begin charging the capacitor again from the energy provided by the main power supply.

The sizes of components used in the boost converter were determined from Equation (5) and Equation (6) [4]:

$$L_{\min} = \frac{2}{27} \frac{R_L}{f} \quad (5)$$

$$C_{\text{filter}} = \frac{D_{\text{MAX}} V_O}{f R_L V_C} \quad (6)$$

The boost circuit, as shown in Fig. 8, was constructed with a 56 μH inductor, an MBR 10100 diode (10 amp maximum capacity), an 86 μF capacitor, and an IRF 530 MOSFET switch (14 amp maximum). The values selected were of greater capacity than what was required in order to permit maximum flexibility of the backup power supply.

IV. Performance

Initially, the circuit was designed to use feedforward control only. As the load resistance was lowered from an initial 55Ω to 18Ω , it became necessary to add a small level of negative feedback to the circuit to prevent a steady output voltage drop. Table 1 shows many of the critical measurements such as input voltage, input current, output voltage, and efficiency for one discharge cycle without negative feedback enabled. After a limited amount of negative feedback was added to the circuit, the output voltage remained relatively constant throughout most of the discharge cycle as compared to the design with feedforward control only. This data is shown in Table 2. Fig. 9 shows the input and output voltages from Table 1 and Table 2. Correspondingly, this graph illustrates the continuously decreasing voltage drop inherent to the purely feedforward design as opposed to the circuit with negative feedback control which maintained its output voltage consistently.

During the testing, the efficiency of the system was typically greater than 85 percent, except at the end of the discharge cycle. However, the efficiency would drop continuously from a peak of about 90% throughout the discharge cycle because the input current was increasing as the input voltage dropped. The efficiency was calculated using Equation (7):

$$\frac{P_o}{P_i} * 100 = \eta \% \quad (7)$$

The typical response to main power supply failure is shown in Fig. 10. This test simulated the effect of the primary power supply failing momentarily, and then being restored to full voltage after a short time. Under the conditions simulated in the lab, the circuit maintained the output voltage within the required amounts.

The final test performed on the circuit was to observe the effects of switching the load from 45Ω to 18Ω while the input voltage was at different levels. This was intended to simulate a load change while the circuit was operating in the backup mode. Figs. 11 through 14 show the input voltage, output voltage (offset by -20 volts), and input current for an input voltage varying from 23 volts to 14 volts. This object of this particular group of tests was to observe the response of the circuit with feedforward control only versus the same circuit with negative feedback. Figs. 15 through 18 show the response of the circuit with negative feedback enabled. These figures illustrate the improved performance inherent in the circuit with the negative feedback, as opposed to the circuit with feedforward control only.

V. Conclusions

In this investigation a capacitor-based DC backup power supply was successfully designed, built and tested. The backup system was able to provide the proper voltage to the load quickly enough to prevent the switching problems inherent in changing to secondary power systems. The circuit also demonstrated the ability to operate independently of any external devices such as function generator or an external power supply. This circuit may be integrated into systems which presently utilize a battery-based backup power system, thereby reducing weight and size while increasing reliability.

VI. References

- [1] *Technical Guide of Electric Double Layer Capacitors*, Matsushita Electronic Components Co., Ltd., 1992
- [2] Spyker, R.L. and Nelms, R.M., 1997, "Discharge Characteristics of High Energy Storage Double Layer Capacitors", Proc. IECEC, Vol. 1, pp. 292-296.
- [3] *Dynacap Electric Double Layer Capacitors*, Elna America, Inc., 1996.
- [4] Mohan, N., Undeland, T., and Robbins, W.P., 1989, *Power Electronics: Converters, Applications and Design*, New York. John Wiley & Sons. pp. 75-81.

Capacitor Voltage

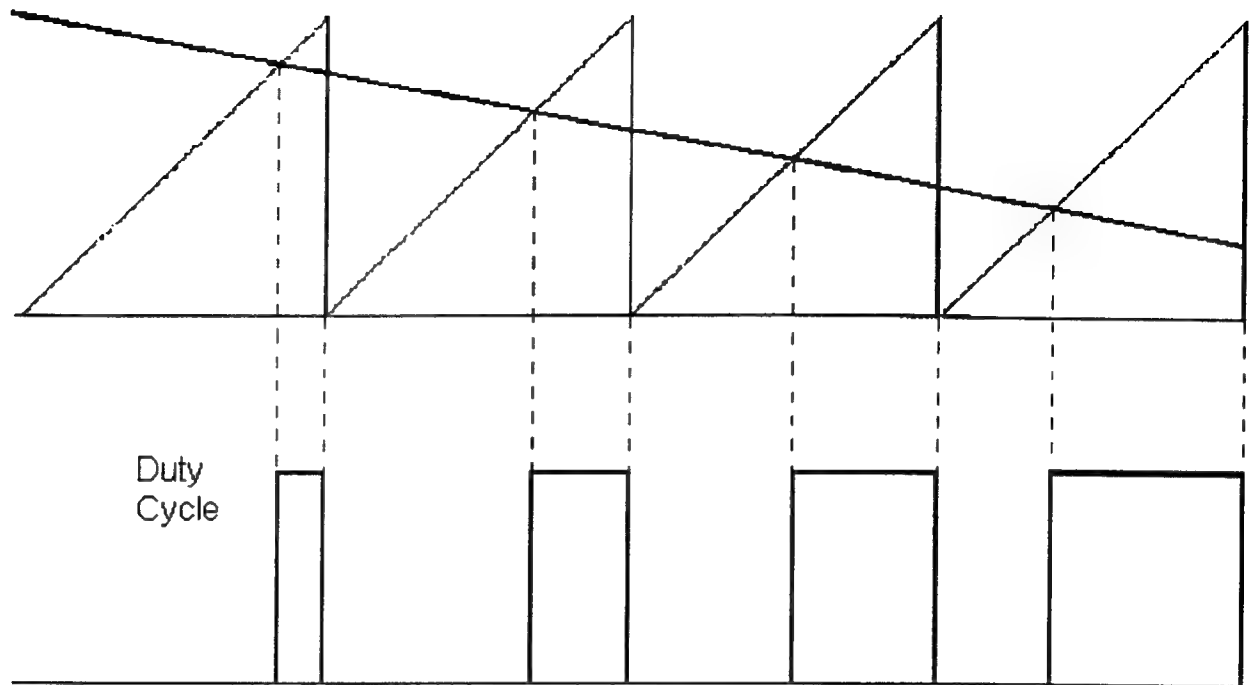


Fig. 1: Illustration of PWM feedforward operation.

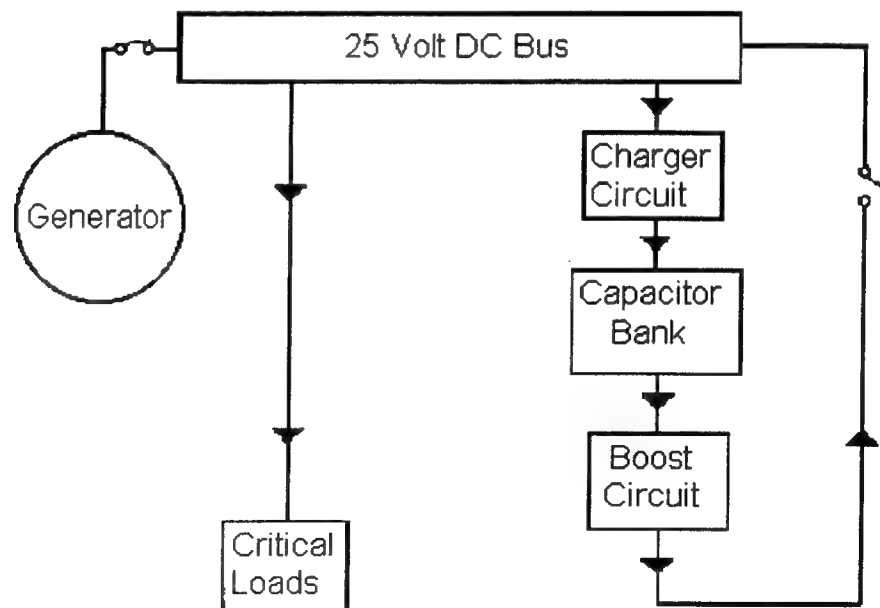


Fig. 2: Capacitor based DC backup power supply with integrated charger circuit

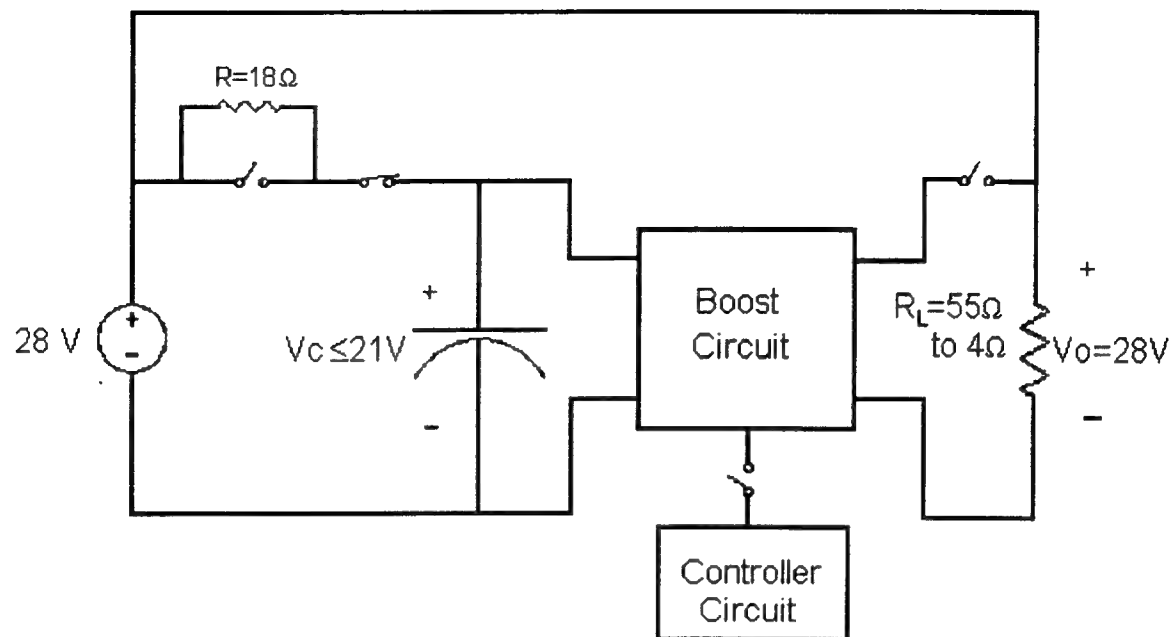


Fig. 3: Backup circuit while charging the capacitor bank.

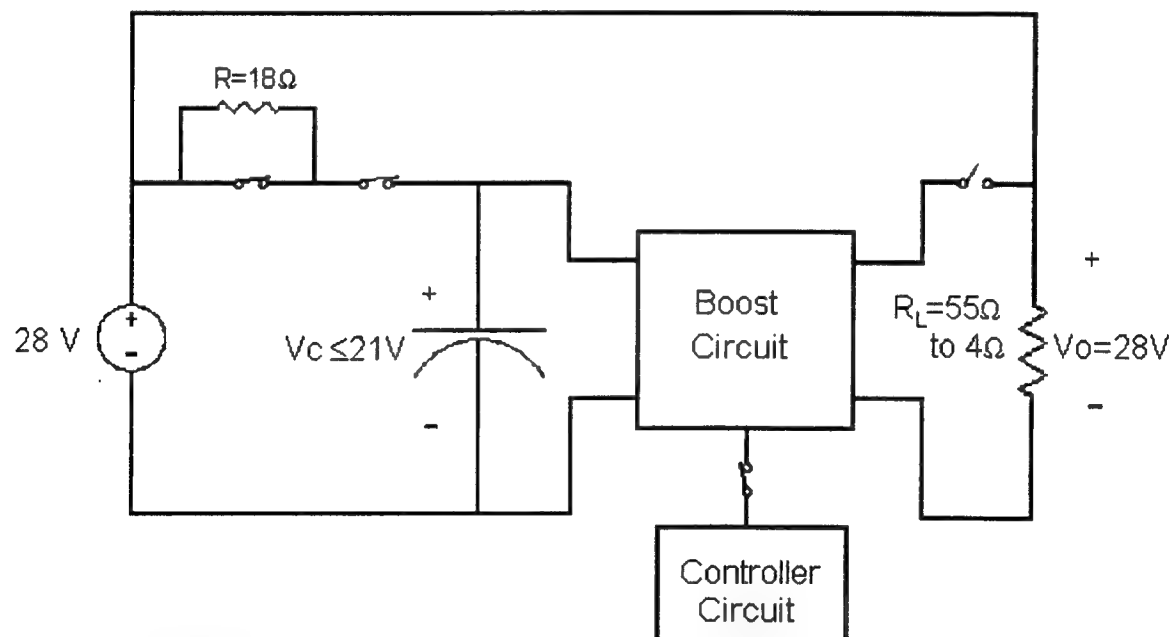


Fig. 4: Backup circuit upon completion of the charging cycle.

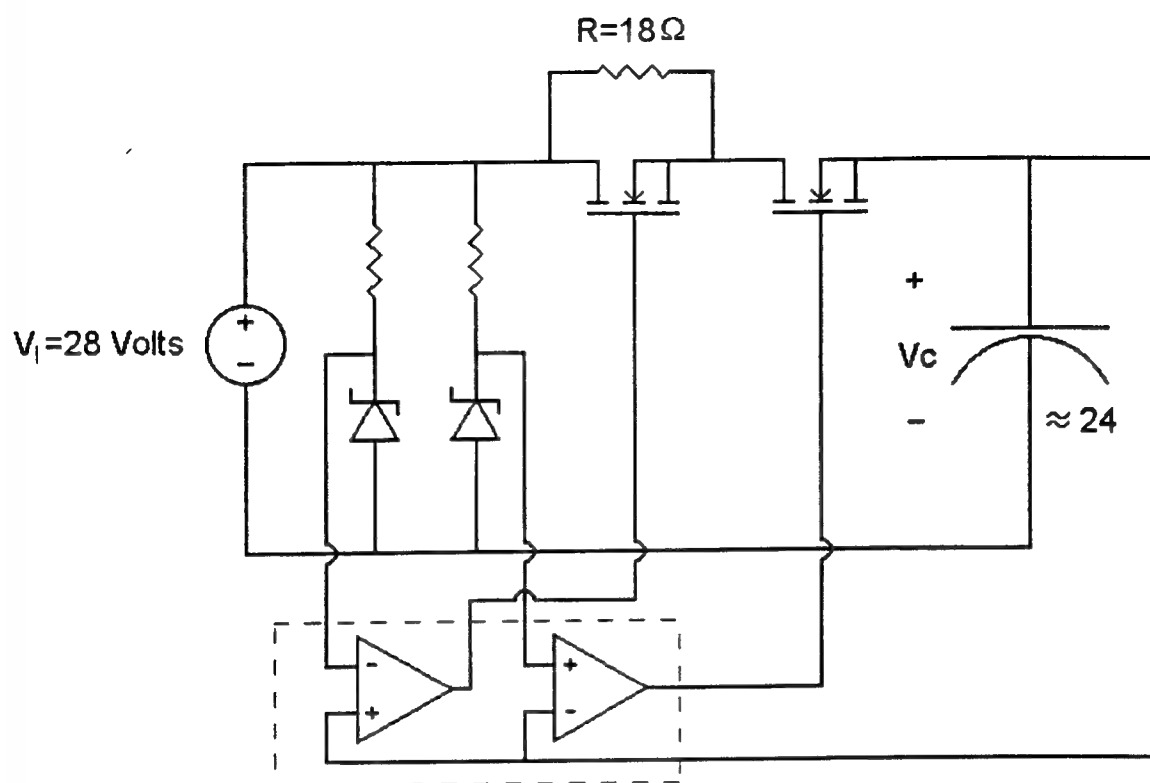


Fig.5: Capacitor charger circuit

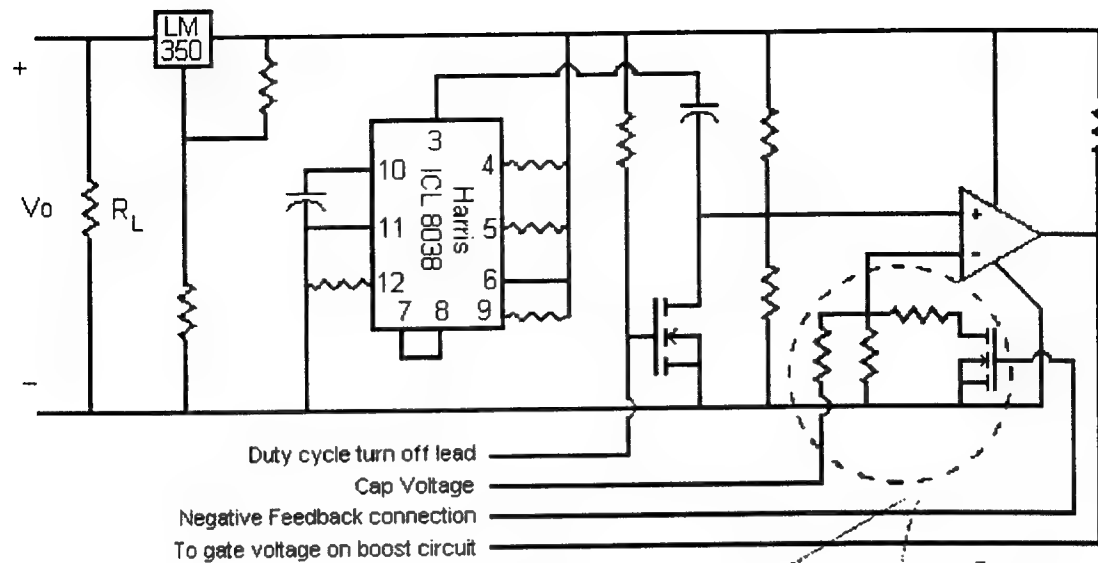


Fig. 6a

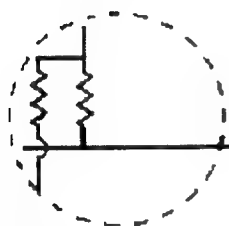


Fig. 6b: Without negative feedback

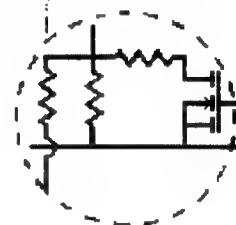


Fig. 6c: With negative feedback

Figs. 6a-c: Controller circuit

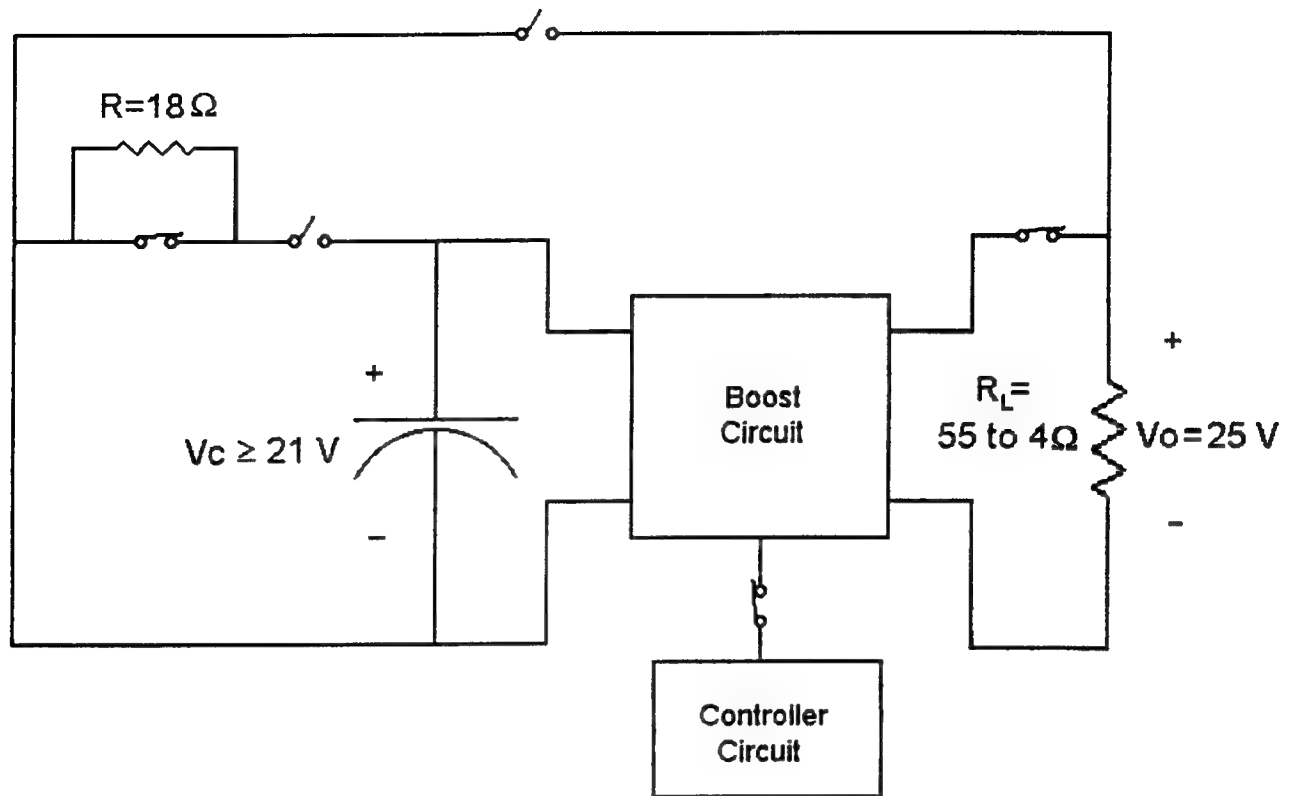


Fig. 7: DC power supply in backup mode.

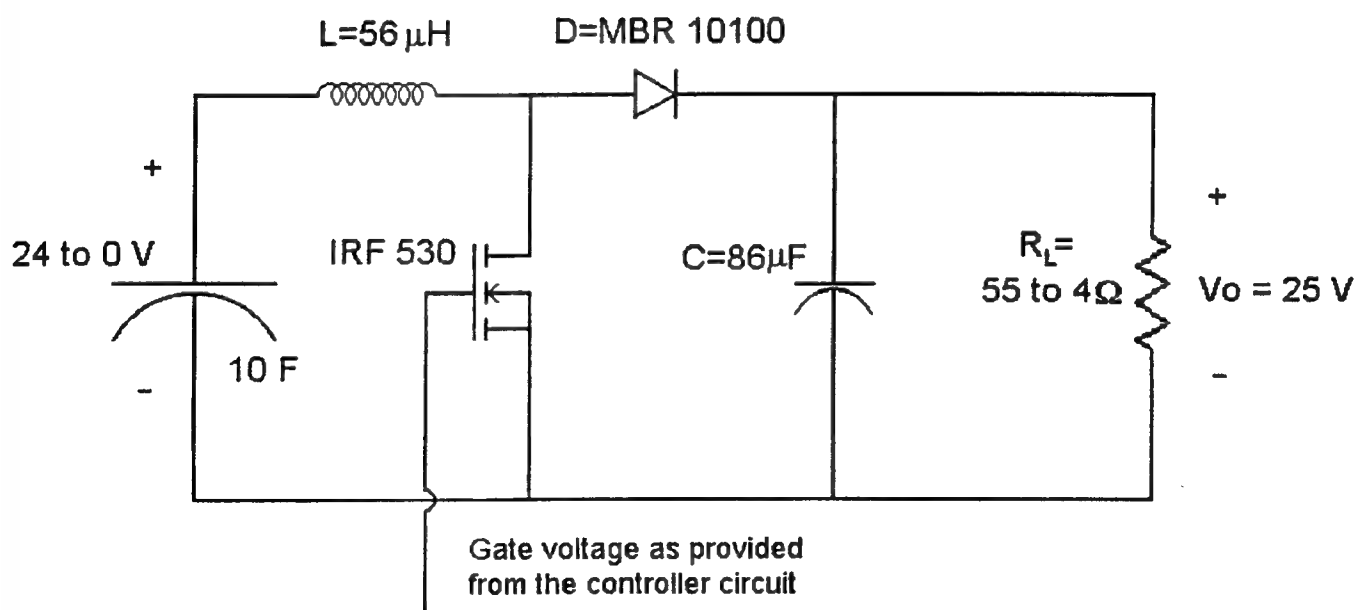


Fig.8: PWM Boost Circuit

Time (sec)	Input volts (v)	Input Current (A)	input power (w)	Output volts (v)	Output Current (A)	Output Power (W)	Efficiency η	Duty Cycle
0	23.33	0.68	15.86	25.27	0.55	13.94	87.89%	0.189
20	22.23	0.70	15.56	25.15	0.55	13.81	88.75%	0.216
40	21.25	0.74	15.73	25.14	0.55	13.80	87.76%	0.258
60	20.11	0.78	15.69	25.04	0.55	13.69	87.28%	0.299
80	18.93	0.81	15.33	24.82	0.54	13.45	87.72%	0.331
100	17.66	0.85	15.01	24.56	0.54	13.17	87.74%	0.369
120	16.36	0.91	14.89	24.20	0.53	12.79	85.89%	0.419
140	14.91	0.98	14.61	23.73	0.52	12.30	84.14%	0.471
160	13.29	1.10	14.62	23.54	0.51	12.10	82.76%	0.533
180	11.34	1.31	14.86	23.27	0.51	11.82	79.59%	0.612

Table 1: Circuit without negative feedback.

Time (sec)	Input volts (v)	Input Current (A)	input power (w)	Output volts (v)	Output Current (A)	Output Power (W)	Efficiency η	Duty Cycle
0	23.45	0.68	15.95	25.22	0.55	13.89	87.09%	0.190
20	22.42	0.71	15.92	25.22	0.55	13.89	87.24%	0.224
40	21.33	0.74	15.78	25.20	0.55	13.87	87.84%	0.256
60	20.12	0.79	15.89	25.26	0.55	13.93	87.65%	0.302
80	18.87	0.85	16.04	25.28	0.55	13.95	87.00%	0.351
100	17.50	0.90	15.75	25.06	0.55	13.71	87.06%	0.392
120	16.01	1.01	16.17	25.08	0.55	13.73	84.93%	0.458
140	14.25	1.14	16.25	25.01	0.55	13.66	84.07%	0.521
160	12.15	1.36	16.52	25.01	0.55	13.66	82.65%	0.598
180	9.58	1.59	15.23	23.85	0.52	12.42	81.54%	0.672

Table 2: Circuit with negative feedback.

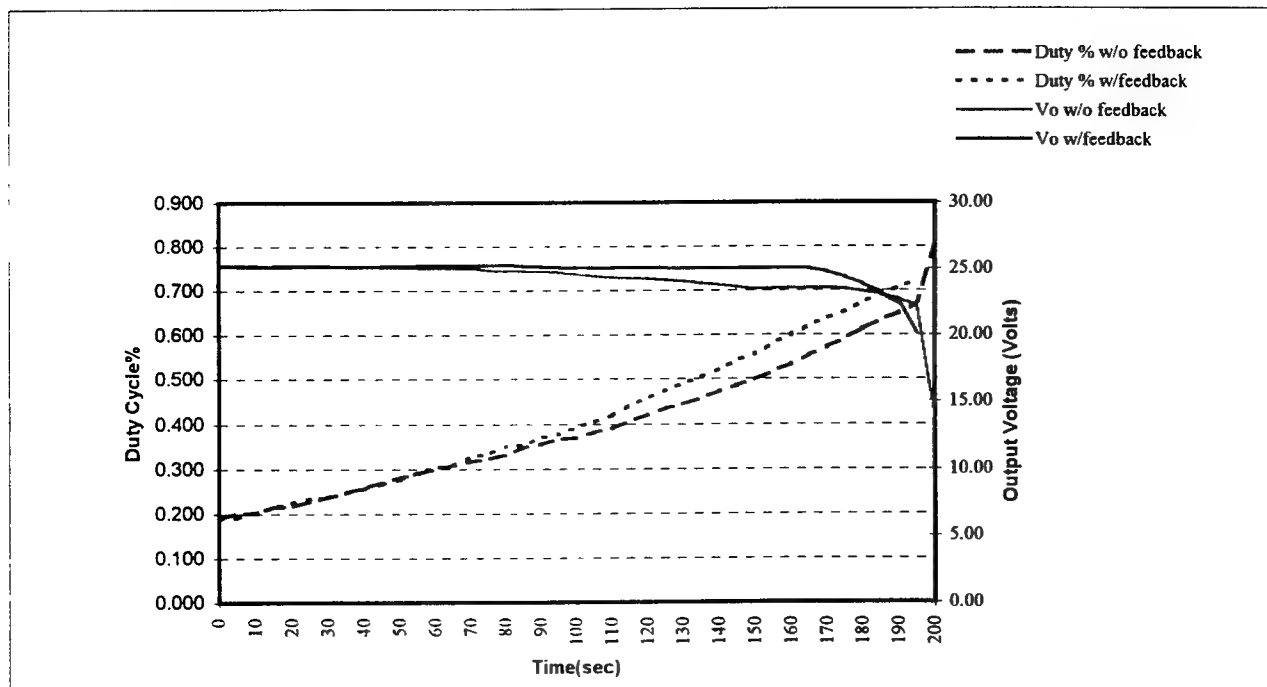


Fig. 9: Graph illustrating the improved performance with limited negative feedback enabled.

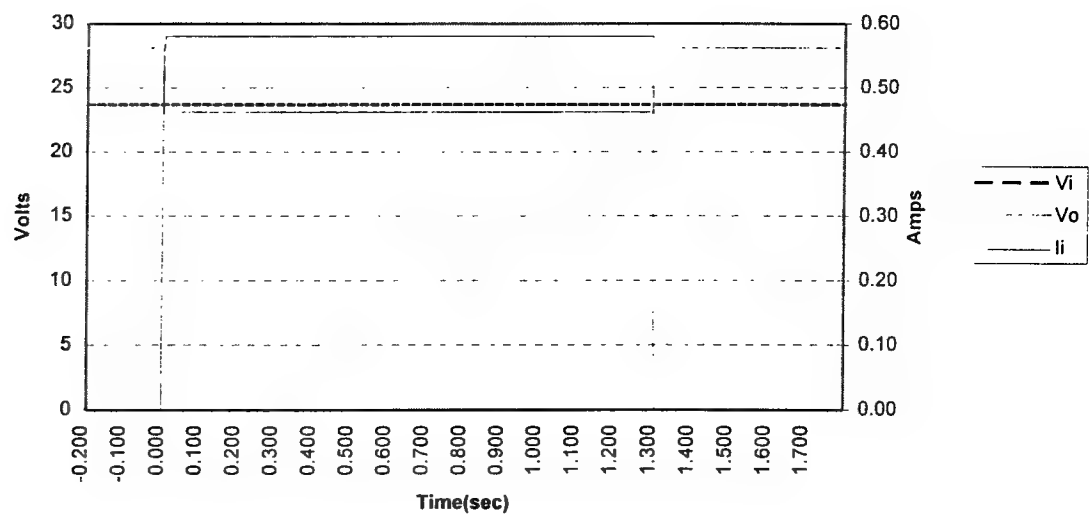


Fig. 10: Waveforms of the backup power supply during a primary power supply failure.

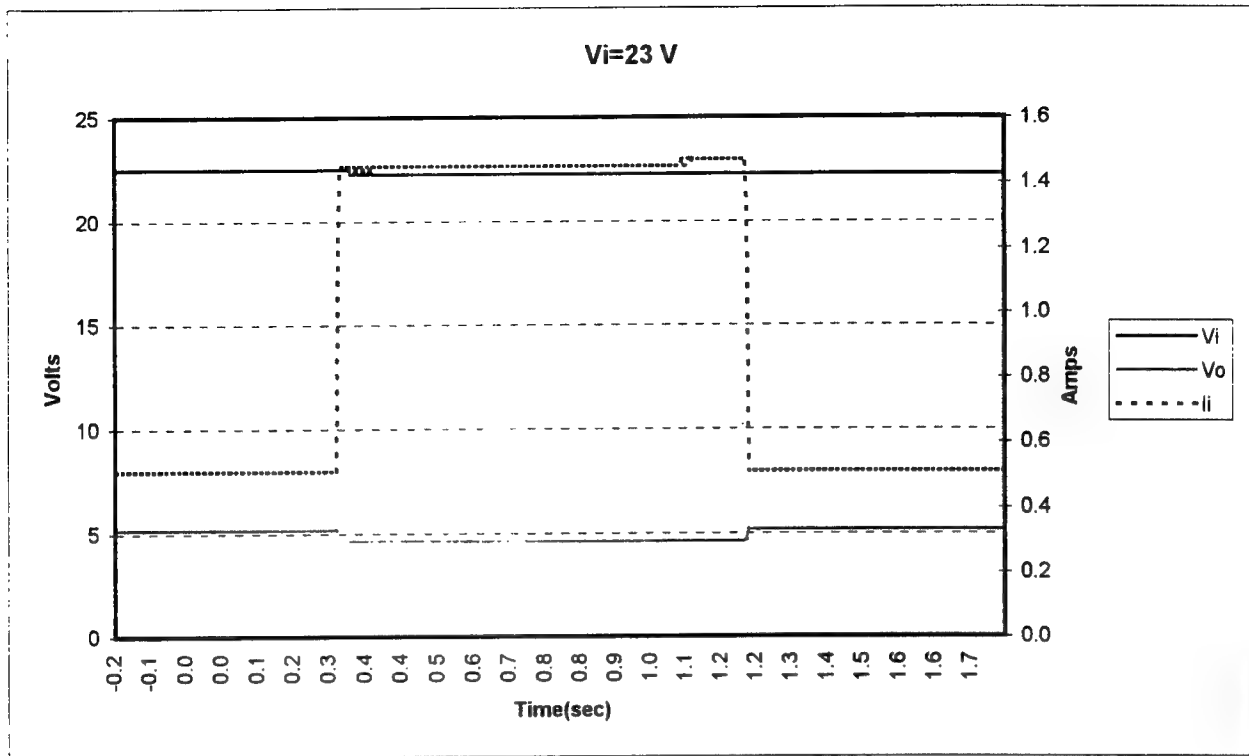


Fig. 11: Step load change as applied to the backup power supply with $V_c=23\text{ V}$

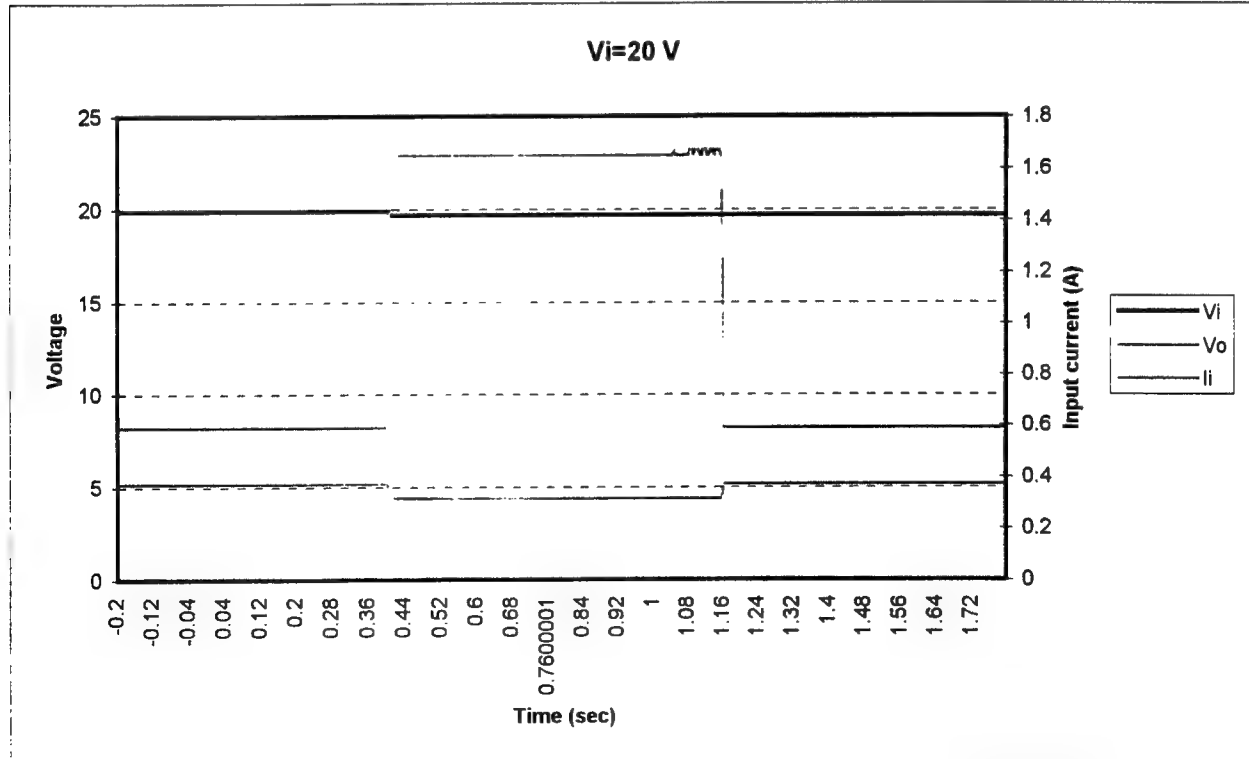


Fig. 12: Step load change as applied to the backup power supply with $V_c=20\text{ V}$

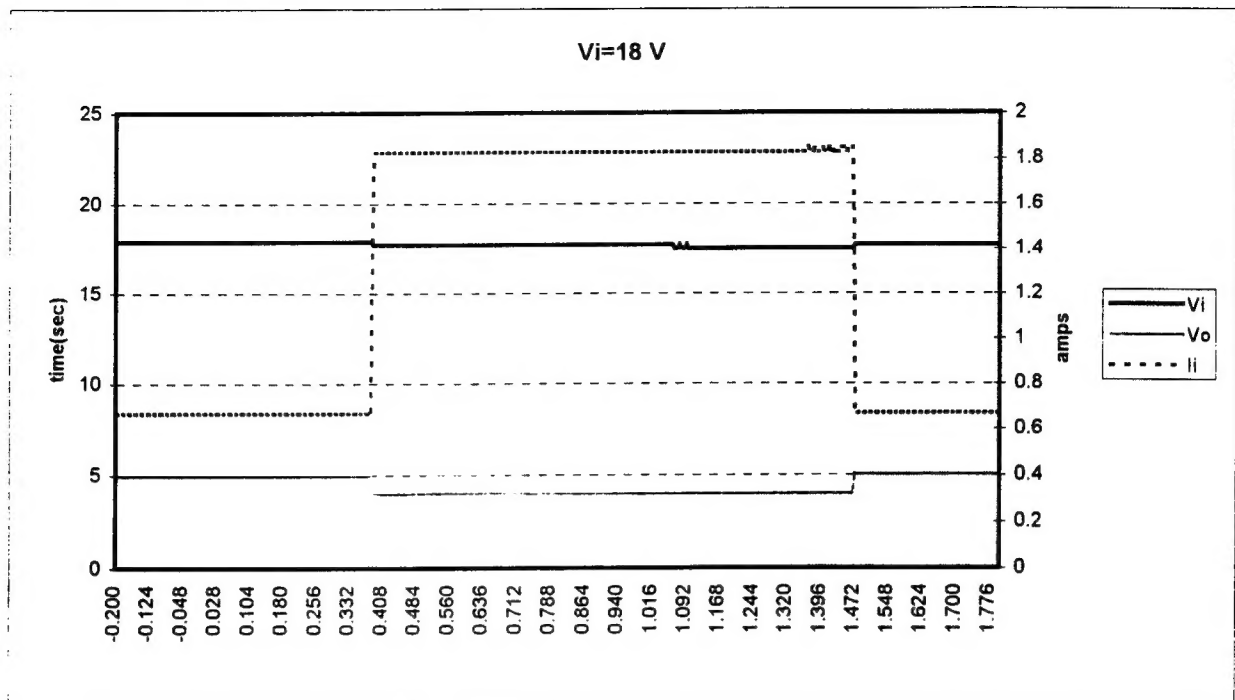


Fig. 13: Step load change as applied to the backup power supply with $V_c=18$ V

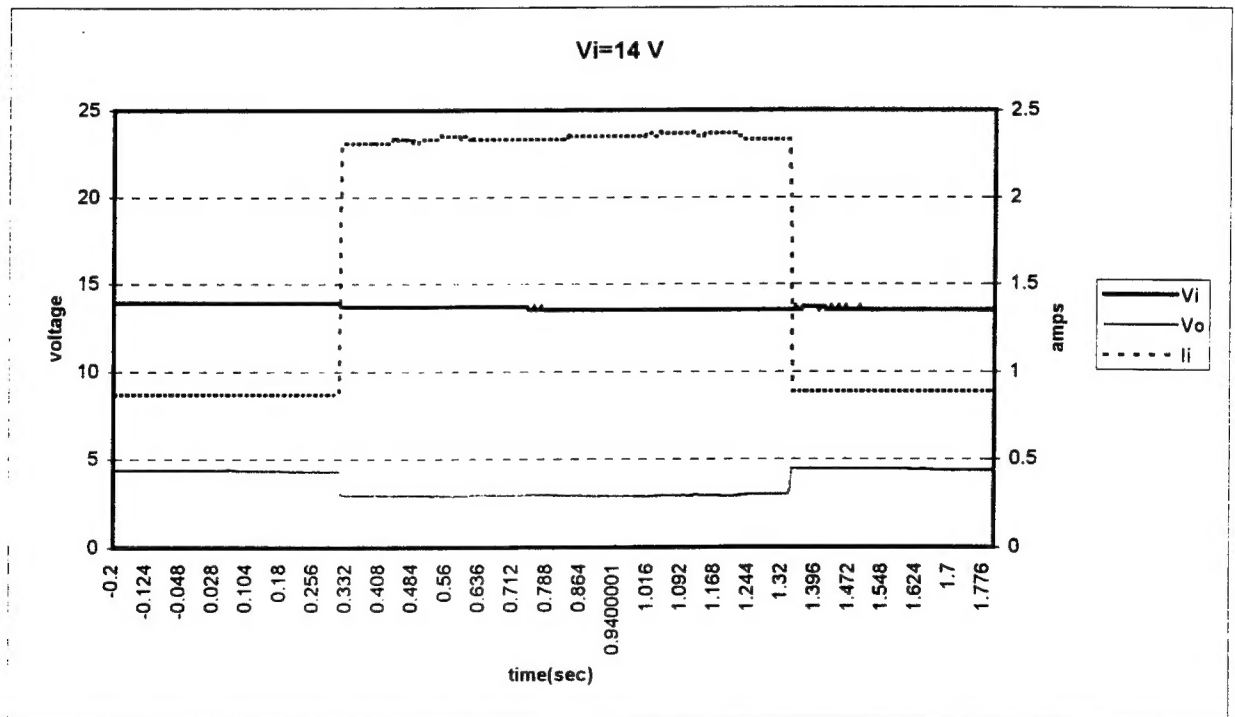


Fig. 14: Step load change as applied to the backup power supply with $V_c=14$ V

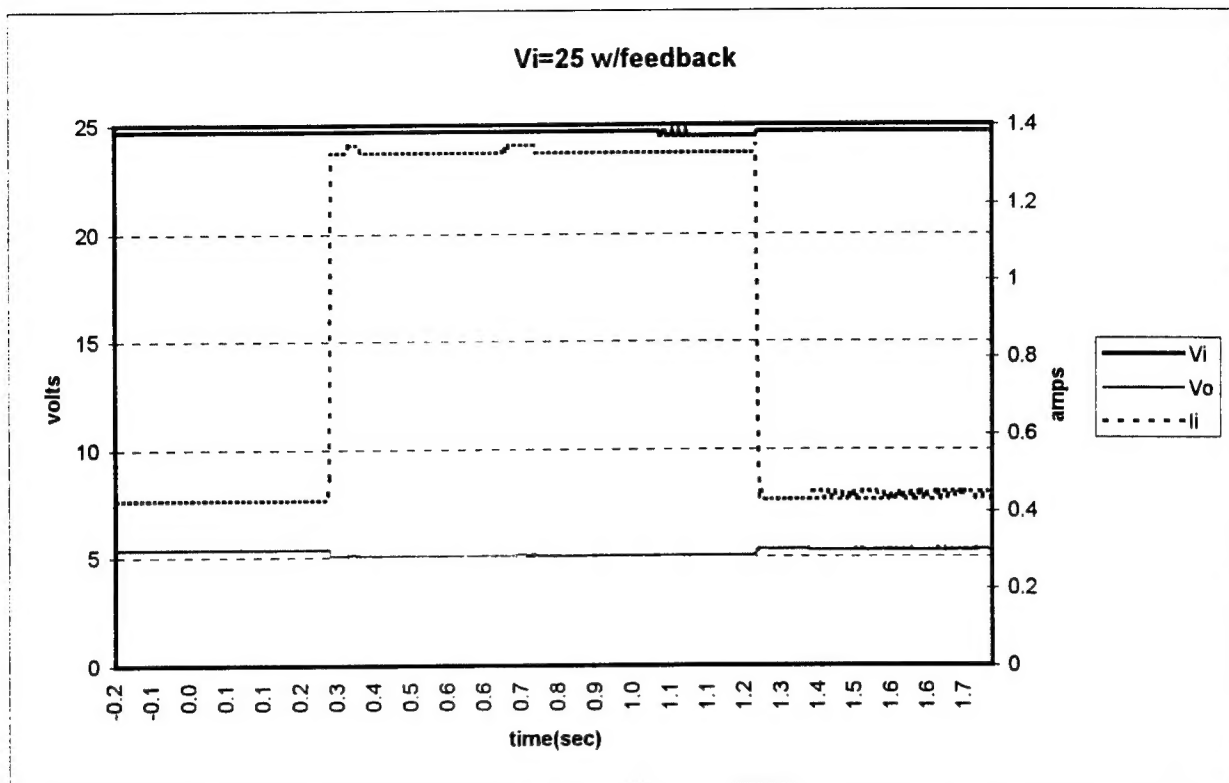


Fig. 15: Step load change as applied to the backup power supply with $V_c=25$ V

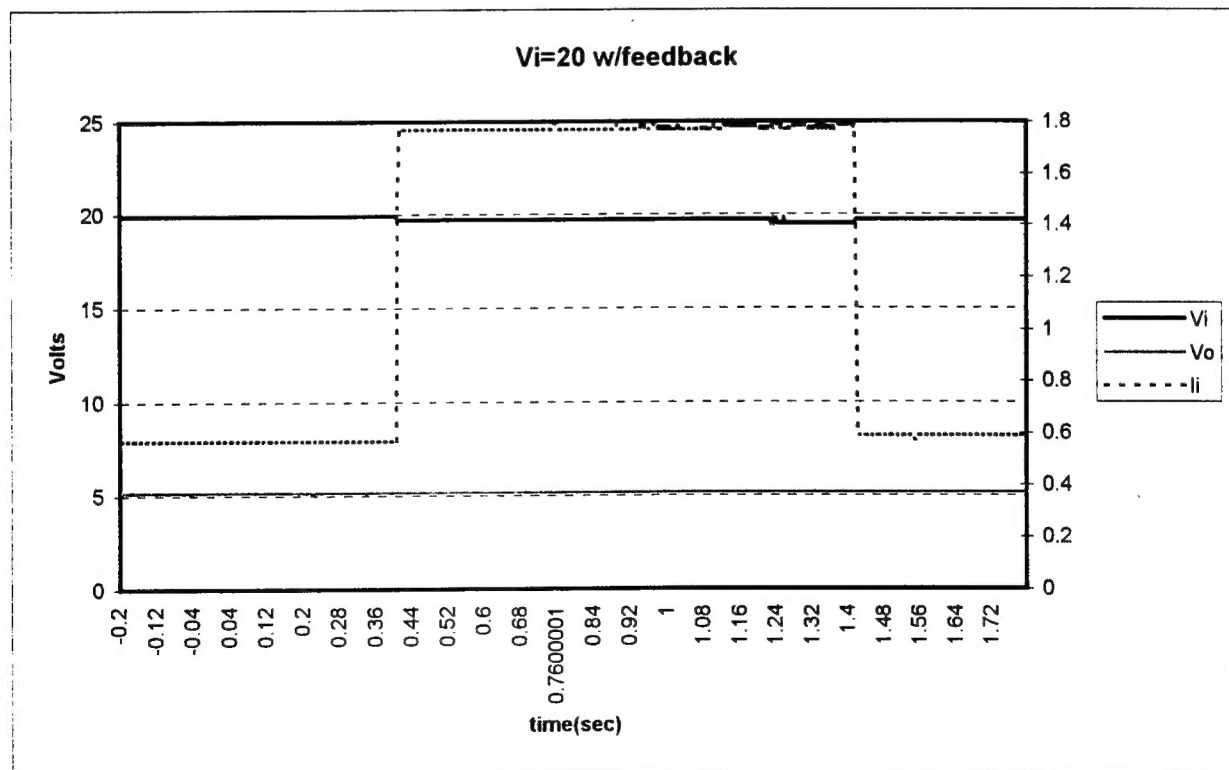


Fig. 16: Step load change as applied to the backup power supply with $V_c=20$ V

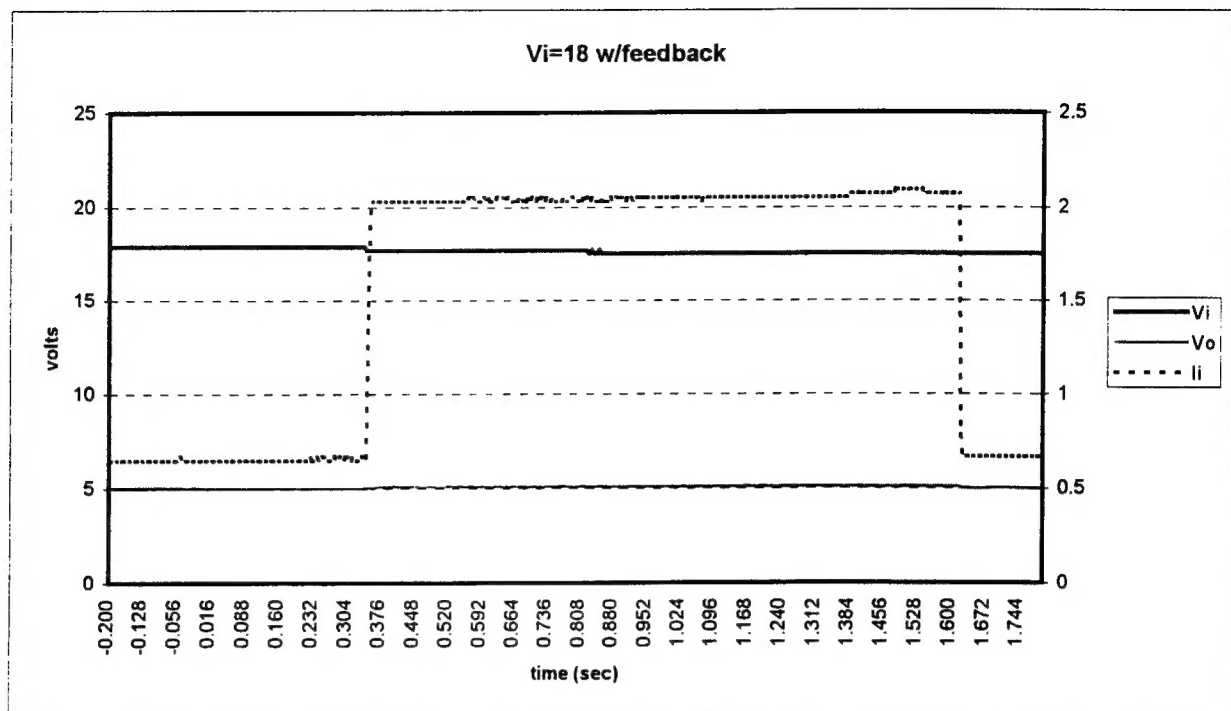


Fig. 17: Step load change as applied to the backup power supply with $V_c=18$ V

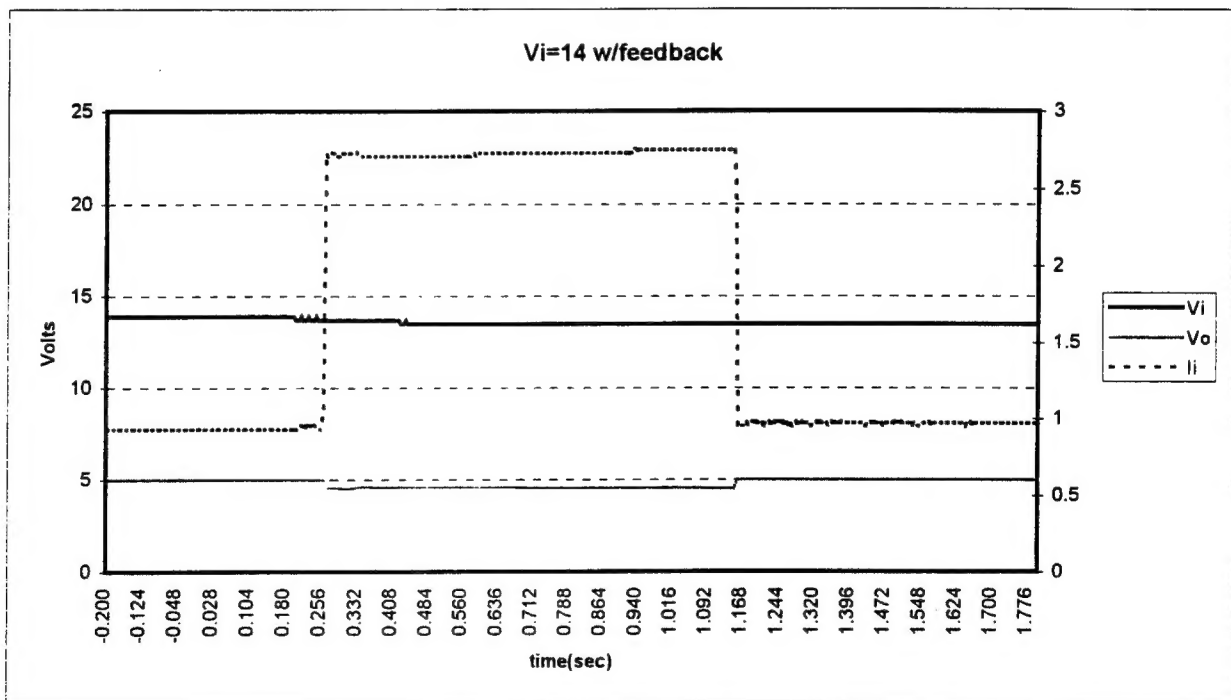


Fig. 18: Step load change as applied to the backup power supply with $V_c=14$ V

Associate did not participate in program.